



Vrije Universiteit Brussel

FACULTY OF ENGINEERING

Dynamic strain analysis with micro-structured fiber optic strain sensors embedded in structural components

Sidney Goossens

Dissertation submitted in partial fulfillment of the requirements to obtain the degree of
Master of Science in Photonics Engineering

Promotor: Prof. Dr. Ir. Francis Berghmans
Co-promotor: Prof. Dr. Ir. Steve Vanlanduit
Supervisor: Dr. Ir. Thomas Geernaert
Supervisor: Ir. Alfredo Lamberti

Academic Year 2014-2015



Preface

During my Master thesis I came into contact with a lot of interesting people, whom I would like to thank. Without these people this thesis would not have been possible.

First, I would like to thank my promotors, prof. Francis Berghmans and prof. Steve Vanlanduit. You gave me the opportunity to do a master thesis according to my own ambitions and input. I appreciated working on a multidisciplinary level, combining photonics with mechanics, and learning much from both aspects. It were your innovative ideas that that have put this thesis in motion and kept it going. I would like to thank you for your professional advice and steering me in the right direction whenever needed, but also letting me know when good work was delivered.

I would also like to show my gratitude to my supervisors Thomas Geernaert and Alfredo Lamberti. You always had time for me to help me out or to answer my questions. Although this sometimes was multiple times a day, your enthusiasm of helping your students remained ever so great. You made me see things I accomplished if I wasn't even aware of them yet, and showed believe in my capabilities, whenever I needed it. After a meeting with you it seemed I always went back to my work with great motivation.

Whenever I went to the Department of Materials Science and Engineering of the UGent to do the embedding or orientation analysis I was assisted with great enthusiasm by Geert Luyckx and Gabriele Chiesura, although I once forgot a UV-light. I would like to thank you for your efforts and assistance for helping me out. I would also like to thank Mathias Kersemans for performing the ultrasound scans of the composite plates.

I would like to thank Karima Chah of the Université de Mons and Martin Becker of the Leibniz Institute of Photonics Technology for helping me with the inscription of the FBGs. Also thanks to Tigran Baghdasaryan from B-phot for accompanying me to Mons and helping me with the inscription of the gratings.

My gratitude also goes to Jean-Paul of the technical assistance for helping me with technical issues of the impact setup. You were always very enthusiastic for helping me in finding a solution. Also Sanne Sulejmani from B-Phot I would like to thank for her help in the lab, whenever a splice failed for the 50th time. Ben De Pauw is also thanked for the explanation of the scripts used. Thanks also to Martin Virte from B-phot for helping me with the French translation of the abstract, you can find it on the next page.

Of course my family is to thank for their support during the year (and way longer before that). Thanks to my parents, my grandparents and my brother for their moral motivations that kept me going during this though year.

The last weeks of my thesis I spend close to my fellow students. We worked together, complained together and laughed together. Thank you Gregory Boeckmans, Jorn Jacobs and Nick Spooren.

Last but not least I want to thank my friends of KSA Lommel- Centrum. You have also showed a lot of mental support during the year, even if that included listening to me trying to explain you the principle of a fiber Bragg grating.

Abstract

Name: Sidney Goossens

Master Degree: Master of Science in de ingenieurwetenschappen: Fotonica

Master thesis title: Dynamic strain analysis with micro-structured fiber optic strain sensors embedded in structural components

Year: 2014-2015

Keywords: Fiber Bragg grating (FBG), Microstructured optical fiber (MOF), Optical sensors, Structural components, Strain, Dynamic measurements

Abstract

In my Master thesis, we combine the potential of fiber Bragg gratings (FBGs) and microstructured optical fibers (MOFs) into microstructured optical fiber Bragg grating (MOFBG) sensors. These innovative sensors enable 3D strain measurements once embedded inside a carbon fiber reinforced polymer (CFRP) composite material. The main goal of the thesis was to demonstrate the ability to perform dynamic strain measurements with these embedded MOFBG sensors for the first time. To do so, we made measurements of the MOFBG spectrum when the composite plate with the embedded sensors was exposed to an impact on its surface and we processed the reflection spectra with an innovative peak detection algorithm. With this approach we were able to detect and quantify the three-dimensional strain field in the composite plate during impact. Additionally an interrogator based on a VCSEL, with the potential of being miniaturized and produced at low-cost, was shown to be able to carry out full-spectrum measurements of the MOFBG reflection spectrum for the first time.

Samenvatting

In mijn masterthesis combineren we het potentieel van Bragg rooster sensoren (fiber Bragg gratings, FBG) and microgestructureerde optische vezels (MOV) in microgestructureerde optische vezel Bragg rooster sensoren (microstructured optical fiber Bragg gratings, MOFBG). Deze innovatieve sensoren maken het mogelijk 3D rekmetingen te doen, eenmaal ze ingebed zijn in een koofstofvezel versterkte polymeer (cabon fiber reinforce polymer, CFRP) composiet materiaal. Het hoofddoel van deze thesis was het voor de eerst keer demonstreren van de mogelijkheid tot het doen van dynamische metingen met deze ingebedde sensoren. Daartoe maakten we metingen van het reflectiespectrum van de MOFBGs, terwijl de composiet plaat met de ingebedde sensoren onderhevig was aan een impact op het oppervlak. We verwerkten de data met een innovatief piek detectie algoritme. Met deze aanpak hebben we het opmeten en kwantiseren van het 3D rekveld in de composietplaat tijdens een impact verwezenlijkt. Bovendien werd een VCSEL-gebaseerde interrogator, met de mogelijkheid tot miniaturisatie en productie aan lage kost, gebruikt om voor de eerste keer volledige spectrale metingen te doen van de reflectiespectra van de MOFBGs.

Résumé

Dans cette thèse de master, nous combinons le potentiel des fibres à réseaux de Bragg (Fiber Bragg Gratings, FBGs) et des fibres optiques micro-structurées (Microstructured Optical Fiber, MOFs) pour former des fibres optiques microstructurées à réseaux de Bragg (Microstructured Optical Fiber Bragg Grating, MOFBGs). Lorsqu'ils sont intégrés dans des matériaux composites à base de polymères renforcés par fibres de carbone (Carbon Fiber Reinforced Polymer, CFRP), ces capteurs innovants permettent la mesure des tensions internes du matériau en trois dimensions. Le principal objectif de cette thèse était de démontrer pour la première fois que ces capteurs MOFBG intégrés permettent de réaliser des mesures de tension dynamiques. Pour ce faire, nous avons effectué des mesures de spectre optique à partir de ces capteurs MOFBGs lorsque la plaque en matériaux composite est soumise à un impact à sa surface, et nous avons exploité le spectre en réflexion en utilisant un nouvel algorithme de détection de pic. Par cette approche, nous avons pu détecter et quantifier le champ de déformation tridimensionnel à l'intérieur de la plaque en composite lors de l'impact. De plus, nous avons pu démontrer pour la première fois qu'un interrogateur basé sur une diode laser de type VCSEL, et donc montrant un fort potentiel de miniaturisation et de production à bas cout, avait l'entière capacité d'effectuer ces mesures en exploitant l'entièreté du spectre en réflexion des capteurs MOFBG.

Content

Preface.....	I
Abstract	II
Content.....	IV
1. Introduction.....	1
1.1. Outline.....	2
2. Theory of 3D MOFBG sensors	1
2.1. Fiber optical sensors.....	2
2.2. Working principle of a step-index FBG	3
2.3. FBG fabrication methods.....	5
2.3.1. Phase mask technique.....	5
2.3.2. Interferometric technique.....	6
2.3.3. On-tower FBG inscription	7
2.4. FBG sensor principle.....	9
2.4.1. Temperature changes.....	9
Axial strain.....	9
2.4.2. Multi-axial strain field.....	11
2.5. Introduction to PCF and MOF.....	11
2.5.1. Index guiding microstructured optical fibers	11
2.5.2. Fabrication of microstructured optical fibers	12
2.5.3. MOF used in this thesis	14
2.6. CFRP Composites.....	15
2.6.1. Introduction to composite materials and structural health monitoring.....	15
2.6.2. Composite materials.....	15
2.6.3. Cure cycle of CFRP	17
2.6.4. Structural health monitoring: monitoring composite materials with embedded sensors	19
2.7. FBG sensor theory in 3D MOFBGs.....	19
2.7.1. Theory of 3D strain transfer	20
2.7.1.a Simplifications	21
2.7.2. Theoretical formulation of the sensitivity.....	23
2.8. Conclusion	28
3. Preparation of the 3D MOFBGs strain sensors.....	29

3.1.	First samples (UMons).....	30
3.1.1.	Splicing the samples	30
3.1.2.	Inscription of the gratings in butterfly MOF.....	32
3.2.	Second samples (IPHT)	35
3.3.	Sensor layout and orientation.....	37
3.3.1.	Orientation procedure.....	38
3.3.1.a	Orientation of the MOF fiber	43
3.3.1.b	Micro-CT scan	44
3.4.	Embedding the fiber sensors in composite material	47
3.5.	Cure monitoring	53
3.6.	End result.....	56
3.7.	Post-mortem analysis.....	58
3.7.1.	Ultrasound C-scans.....	58
3.7.2.	Orientation of fibers by polishing and microscope examination	61
3.7.2.a	Orientation of butterfly PCFs	66
3.8.	Conclusion	69
4.	Interrogation methods	71
4.1.	OSA/ASE Interrogation	72
4.2.	FBGS FBG-scan 700/704D interrogation	73
4.3.	Micron Optics Optical Sensing Interrogator SM125.....	75
4.4.	VCSEL-interrogator	75
4.4.1.	VCSEL-interrogator Setup.....	77
4.4.1.a	Vertical-cavity surface-emitting laser (VCSEL)	77
4.4.1.b	Photodiode (PD)	78
4.4.1.c	MATLAB script and VCSEL control.....	78
4.4.2.	VCSEL-characterization.....	78
4.5.	Conclusion	82
5.	3D strain Measurements with MOFBGs sensors.....	83
5.1.	Impact setup.....	84
5.2.	Fast phase correlation algorithm	85
5.3.	Impact on MONS-samples with FBG-scan.....	86
5.3.1.a	Setup.....	86
5.3.1.b	Peak shifts during the impact.....	88
5.3.1.c	Force calibration.....	90

5.3.1.d	Measurements on MOFBG 1	91
5.3.1.e	Measurements on MOFBG 2	92
5.3.1.f	Measurements on MOFBG 3	93
5.3.1.g	Strain transfer.....	95
5.4.	Impacts on IHPT-samples with FBG-scan	98
5.5.	Impacts on IHPT-samples with VCSEL-interrogator	103
5.5.1.	Full spectrum measurements.....	105
5.5.2.	Future prospect: edge filtering.....	107
5.6.	Conclusion	108
6.	Conclusion and future prospects.....	110
6.1.	Accomplishments	111
6.1.1.	Preparing the 3D strain MOFBGs for embedding.....	111
6.1.2.	Embedding the MOFBGs in CFRP composite materials	111
6.1.3.	Dynamic 3D strain sensors	111
6.1.4.	Miniaturized VCSEL-based interrogator	111
6.2.	Future prospects	111
6.2.1.	Orientation of MOFBGs in composite materials	111
6.2.2.	Custom VCSEL-based interrogator	112
6.2.3.	Further impact measurements.....	112
6.2.4.	Industrial prospects.....	112
References.....		113
Appendix 1: MATLAB script for OSA READOUT.....		115
Appendix 2: MATLAB script Impact Measurements with FBG-scan (700/704D) and the Piezotronics 208B02 Force Sensor		118
Appendix 4: Automatic Reading Out of VCSEL-spectra with the OSA.....		128
Appendix 4: MATLAB script for the Phase Correlation Algorithm		133

1. Introduction

Sensors are everywhere in our everyday engineering world. They are playing crucial roles in a broad range of industrial applications. In most cases conventional electro-mechanical sensors do the job of measuring many process parameters such as temperature, pressure and mechanical strain and stress.

In this thesis we will use optical fiber sensors (OFS) instead, and exploit their advantages when compared to their electric counterparts. The most important advantage is their immunity to electromagnetic interference. In addition, optical fiber based sensors are small and do not carry much weight, meaning that they can be integrated within materials and structures in a minimally intrusive or disturbing manner. Finally optical fiber sensors can be extremely temperature and chemically resistant and operate in harsh circumstances.

The optical fiber sensors used in this thesis combine the properties of fiber Bragg gratings with the highly birefringent features of a microstructured optical fiber. A fiber Bragg grating (FBG) is a small wavelength selective filter inside the core of an optical fiber. The inscription of an FBG exploits the photosensitivity inside a fiber core to alter the refractive index locally with an interferometric UV-light pattern. Whenever a strain or temperature change is applied to the FBG, this will be noticed by the change in reflected wavelength. By relating this wavelength to the stress and/or temperature in a correct way, a sensor is created. A microstructured optical fiber (MOF) is not a conventional step-index fiber. A MOF is an optical waveguide that holds a microscopic structure of air holes in its cross section that runs over the entire fiber length. By designing the MOF in such a way that the cross section shows a high anisotropy in two perpendicular directions, the MOF can measure axial as well as transversal strain. A fiber Bragg grating fabricated in a microstructured optical fiber will be named 'MOFBG' throughout the text.

In this thesis we will exploit the unique properties of MOFBGs in a domain called structural health monitoring (SHM). Structural health monitoring uses sensors to measure damage inside structures and predict failure of the components in question. It is mostly used in structures which experience stresses, strains and pressures during their operation like the wings of an airplane or the blades of a wind turbine. An increasing amount of such structures are built with composite materials. Composite materials are very light, but very stiff and strong materials which can be fabricated in the form of the finished component. The type of composite material used in this thesis is called carbon fiber reinforced polymer (CFRP) composite and consist out of epoxy plies with reinforcement fiber, which are stacked together and temperature cured to form a strong and stiff finished component.

The fact that they are built by stacking plies before the hardening of the component allows embedding a MOFBG inside the component. The function of the sensor is to measure strain changes inside the composite component, which may either warn that the occurrence of damage is imminent or that it has already occurred.

The objective of this thesis is to combine the properties of fiber Bragg gratings (FBGs) with those of microstructured optical fiber (MOF) to create a sensor that is capable of measuring strain in the three dimensions of space when embedded within a carbon fiber reinforced polymer (CFRP) composite component, and to use it to enable dynamic measurements of impacts on the structure.

1.1. Outline

In the second chapter of the thesis we explain the theory behind the 3D MOFBG sensors used in this work. A short overview of optical fiber sensors is given with an emphasis on the FBG. The operation principle of a fiber Bragg grating is explained followed by the fabrication techniques of these gratings. We used both the phase mask technique as the interferometric technique in this work to fabricate the gratings of the MOFBGs. We explain how the fiber Bragg grating can be used to measure temperatures, axial and multi-axial strains. An introduction to MOF is given and their added value to FBGs for multi-axial strains. Especially the Butterfly MOF is explained here, for we used it extensively during the thesis. In the last section of the chapter we explain the theory behind composite materials and structural health monitoring, with emphasis on the prepreg CFRP composite used in this work. Also the cure process is explained here, as we did a monitoring with the embedded MOFBGs during the curing. As a last paragraph we explain the theory behind the transformation from measured wavelength shifts to actual 3D strains.

Chapter three contains the elaboration on the preparation of the embedded 3D MOFBG sensors. First we explain the preparation of the samples before embedding. This includes the layout with the embedding in mind, the unique splice program used to splice the fibers, the orientation of the microstructure and the inscription of the gratings with a scanning phase mask technique. We then come to the embedding of the MOFBGs into the CFRP composite plates. The MOFBGs were interrogated during the entire process to perform a cure monitoring of the CFRP plates. As last, we explain the post-mortem analysis performed on the CFRP plates to determine the actual orientation of the MOFBGs.

In the fourth chapter we illustrate all the interrogation methods used in this thesis. This chapter includes the setup used to characterize the samples with an optical spectrum analyzer (OSA) and a light source using amplification by spontaneous emission (ASE). We explain the commercially available interrogation method by FBGS International, the FBG-scan 700/704D and the custom made MATLAB script to operate it at 4000 Hz, which allowed it doing dynamic interrogation. We also used the Micron Optics Optical Sensing interrogator (SM125-500) for the cure monitoring the CFRP composites, as will be explained. Last in this chapter we discuss a custom built VCSEL-based interrogator for doing dynamic strain measurements.

In the fifth chapter we present the results of the dynamic measurements. We build a custom made impact setup to excite composite plates in a dynamical way. The reflection spectra of the MOFBGs spectra were processed with a phase correlation algorithm that is also explained. A transfer matrix method was applied to convert the wavelength shifts into a 3D strain field. As a last section of this chapter we explain how we a built VCSEL-based interrogator and use it to do full-spectrum measurements of the MOFBGs reflection spectra.

In the sixth and last chapter we conclude on the work carried out as part of this Master thesis. We summarize the obtained results and we conclude on the potential for dynamic measurements with a 3D MOFBG sensor. We also provide a number of hints to solutions for problems which could not yet be solved as part of our Master research.

2. Theory of 3D MOFBG sensors

In this chapter we explain the sensor technology used in this thesis. It lies at the cross roads of fiber Bragg gratings (FBGs) and microstructured optical fibers (MOFs). Together they give rise to the so called MOFBGs. By choosing the sensor layout intelligently, two MOFBGs allow measuring 3D strain. [1]

This chapter is structured as follows: First, in section 2.1, a summary of possible fiber sensors is given. In section 2.2 the principles of a fiber Bragg grating are explained. In section 2.3 we discuss different techniques used to fabricate FBGs. The phase mask, interferometric and draw-tower techniques are explained here. Section 2.4 explains the principle of using a FBG as a sensor for measuring temperature, axial and multi-axial strains. In section 2.5 an introduction to microstructured optical fibers and photonic crystal fibers is given. We discuss their index guiding properties and the ways of manufacturing them. Next, in section 2.6 we explain the concept of carbon fiber reinforced polymer (CFRP) composites. The principle of composite materials is explained as well as their cure cycle and their contribution to structural health monitoring (SHM) with integrated MOFBGs. Finally a conclusion concerning FBGs in MOF to create 3D MOFBG strain sensors in CFRP for SHM is given.

2.1. Fiber optical sensors

Optical fiber sensors include a variety of many sensor types. Table 1 gives an overview of the different possibilities divided into point sensors, distributed sensors and quasi-distributed sensors. The table gives the name of the sensor, the typical measurands, which property of the light is used to perform the measurement (light modulation), if the response of the sensor is linear with changes in the measurand, and finally the typical spatial resolution over which a measurement can be performed. [1], [2]

Table 1: A summary of all optical fiber sensor methods, divided into three classes of point, distributed and quasi-distributed sensors. The table gives each sensor type, the main typical measurands of this sensor, which property of the light is modulated by the measurands, if the response of the sensor is linear to a change in measurand and the spatial resolution over which a measurement can be performed. [1], [2]

Distribution	Sensor	Measurands	Light property	Linear	Spatial resolution
Point	Fabry-Perot interferometric sensor	- Strain - Temperature	Phase	Yes	Sub-mm to mm
	Long gage	- Displacement	Phase	Yes	Sub mm to mm
Distributed	Raman/Rayleigh scattering (ODTR)	- Fiber loss - Damage location - Temperature - Strain	Intensity	No	cm
	Brillouin scattering (BOTDR)	- Temperature - Strain	Intensity	No	m
Quasi-distributed	Fiber Bragg gratings	- Temperature - Strain - Pressure	Wavelength	Yes	Sub-mm to mm

Point sensors are sensors that only measure at a specific point in space. They usually make use of an interferometric setup, which measures the difference in optical path length between the sensor arm and a reference arm. They can be very precise, but because they only measure at one point, and cannot be straightforwardly multiplexed, they are not suitable candidates for structural health monitoring as many fibers would be needed to equip an entire structure. [2], [3]

Distributed sensors send out an optical pulse and measure the light intensity returning to the device due to Rayleigh scattering in the fiber itself or Fresnel reflections at connectors or at imperfections. They are therefore mostly used in telecom applications to investigate defects in an optical fiber

network. They can also be used to do temperature measurements according to the principle of Raman scattering. A different type of distributed sensors makes use of Brillouin scattering to measure temperature and strain inside a fiber. Distributed fiber sensing definitely finds its use in sensing applications, but is not suited for dynamical structural health monitoring. Firstly they need a complex (and expensive) demodulation system and secondly, their spatial resolutions are the lowest of the fiber sensing methods (although mm-resolution cases exist). Lastly, because the returning light intensity is very weak, a lot of averaging is needed, meaning a measurement can easily take up to minutes or even longer. This means they are definitely not suited for high speed interrogation techniques required to measure dynamic strain changes inside composites. [2], [3]

This leaves the last type of sensors, being Fiber Bragg Gratings (FBGs). They are very versatile sensors. They can be used as point sensors, but by wavelength multiplexing, a quasi-distributed sensor chain can be obtained. This allows the sensor to be minimally intrusive (only one fiber in the composite) and yet to measure at many precise (known) locations. The sensor modulates the reflected Bragg wavelength when a change in strain or temperature is applied. The sensor modulates the light in real time (no averaging necessary), so if the interrogation allows it, it is possible to do dynamical measurements. Traditional FBGs in single mode fiber (SMF) allow only axial measurements. However, to measure a 3D strain field, stresses need to be measured in multi-axial directions. By inscribing an FBG into a microstructured fiber (MOF), axial as well as transverse strain can be measured with fiber Bragg gratings.

In the next section we will explain the working principle of such FBGs, their fabrication methods and their sensor principle.

2.2. Working principle of a step-index FBG

As mentioned in the introduction, there are many advantages to a fiber Bragg grating or FBG implemented as a strain or temperature sensor. They can be extremely temperature and radiation resistant, for operation in harsh circumstances. The gratings are part of the transmission medium, which means they have a low insertion loss. Also multiplexing is very easy, because one fiber can be inscribed with many gratings. As long as their Bragg wavelengths do not overlap, wavelength division multiplexing is possible. A last very important advantage is that they are immune to electromagnetic radiation, where their electric counterparts are not. [1], [2], [4], [5]

Fiber Bragg gratings have been around from the 1980's and were accidentally discovered in 1978 by Hill et al [6]. They have proven themselves in areas of telecommunication and sensing as wavelength sensitive filters. Filters of which the filter wavelength seems to change when a temperature change or strain is applied.

As shown in Figure 1, a FBG is a periodic refractive index modulation written into an optical fiber. When a light wave of a broadband light source enters the fiber and reaches the grating, light will be slightly reflected ($R \approx 10^{-7}$) at each interface [2]. However, only the light that satisfies the Bragg condition will interfere constructively and form a back traveling wave at a narrow wavelength range centered around λ_B . The light that does not satisfy this condition will be out of phase with other reflected waves and interfere destructively. This light will simply be transmitted. The transmission spectrum will show a dip around the wavelength λ_B , because this light is reflected. [4]

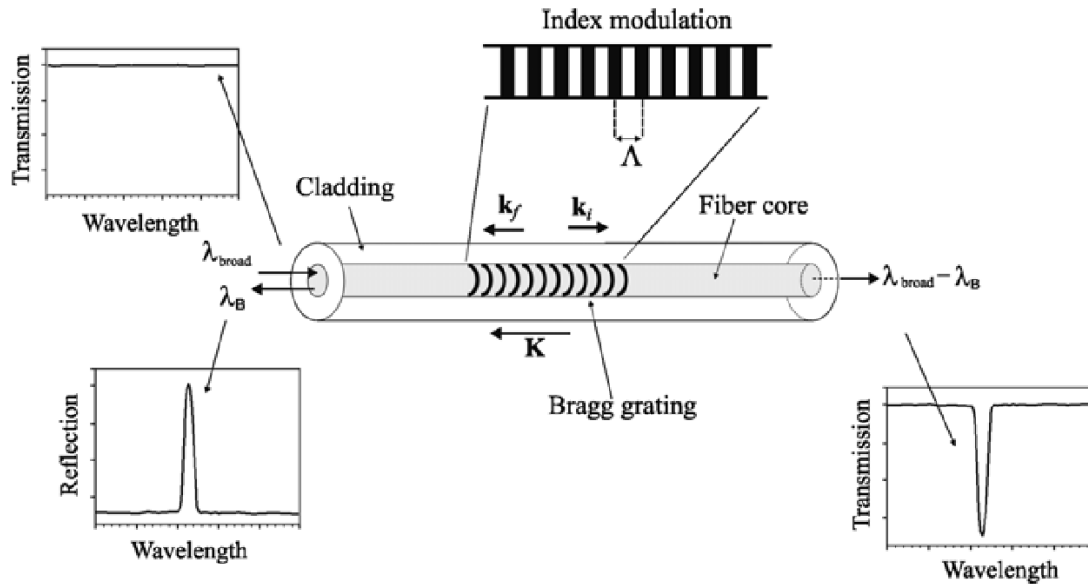


Figure 1: Working principle of an FBG [4] The figure shows the index modulation in a fiber core and the effect on a brought light λ_{broad} source transmitted into the fiber. Inside the grating, the light will experience reflection at each reflective index change. Only the light with the right wavelength (λ_B) for encountering constructive interference will be reflected. The transmitted light shows a dip around the Bragg wavelength.

The Bragg condition itself is a result from conservation energy and conservation of momentum. Energy conservation dictates the conservation of frequency (ν) in reflected and incident wave: $h\nu_r = h\nu_i$, where h is Plancks constant. Conservation of momentum dictates the following wave vector sum

$$\vec{k}_i + \vec{K} = \vec{k}_f \quad (1)$$

Here \vec{k}_i , \vec{K} and \vec{k}_f are the wave vectors of the incident wave, grating and reflected wave respectively. The direction of the vectors in shown in the figure above. The magnitude of the vectors is given by equation (at wavelength λ_B).

$$|\vec{K}| = \frac{2\pi}{\Lambda} \quad (2)$$

$$|\vec{k}_f| = \frac{2\pi n_{eff}}{\lambda_B} \quad (3)$$

At this wavelength the wave vector of the reflected wave becomes

$$|\vec{k}_i| = -|\vec{k}_f| = -\frac{2\pi n_{eff}}{\lambda_B}. \quad (4)$$

n_{eff} is the effective refractive index over the grating (taking the high and low refractive index into account). If (2)-(4) are filled back into (1), this gives

$$\frac{2\pi}{\Lambda} = 2 \left(\frac{2\pi n_{eff}}{\lambda_B} \right), \quad (5)$$

which, written differently, results in the Bragg condition (6) for reflection on a fiber Bragg grating.

$$\lambda_B = 2\Lambda n_{eff} \quad (6)$$

An example of a Bragg peak, measured with an optical spectrum analyzer (OSA) when illuminated with an ASE source through a circulator (see section 4.1) is shown in Figure 2.

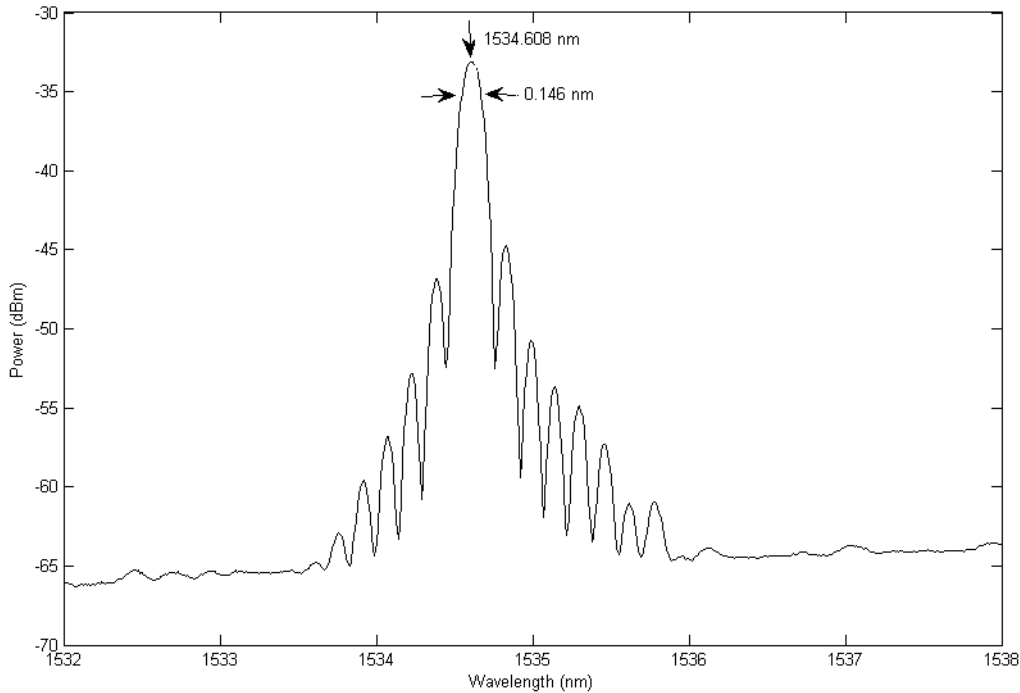


Figure 2: Example the reflected power of a fiber Bragg grating. The grating was illuminated by and ASE source and the reflected spectrum was measured with an optical spectrum analyzer (OSA) through a circulator. The Bragg wavelength was 1534.608 nm and the full width at half maximum 0.146 nm.

2.3. FBG fabrication methods

There are different possible methods available for writing gratings in the core of an optical fiber. These methods exploit photosensitivity. By illuminating the fiber core with UV light, the properties of the fiber material are locally altered. In this way a periodical structure in the form of a grating is obtained.

2.3.1. Phase mask technique

The first method that will be discussed here is the phase mask technique. The ± 1 diffraction order of a UV laser light creates an interference pattern along the fiber core. The periodic fringe pattern writes the grating into the fiber core because of the photosensitivity of the core as explained above. This is schematically shown below in Figure 3 [7]. The period of the grating Λ_{PM} depends on the fringe pattern, which is determined by the wavelength of the light λ_{UV} and the angle of the diffracted orders φ :

$$\Lambda_{PM} = \frac{\lambda_{UV}}{\sin(\varphi)} \quad (7)$$

The phase mask is constructed to diffract most of the optical energy in the ± 1 diffraction orders.

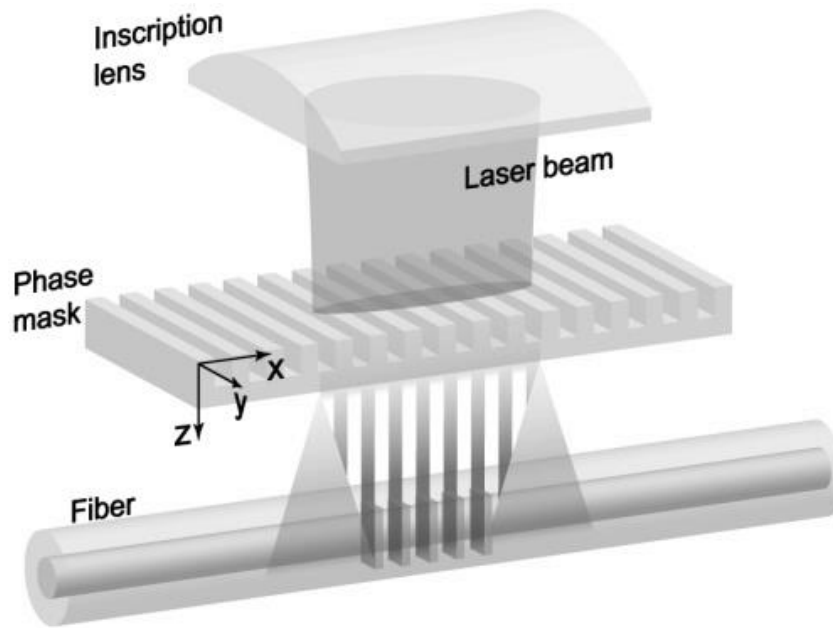


Figure 3: Schematic representation of the phase mask technique. The optical fiber is illuminated by a UV laser source through a phase mask. The interference fringes of the ± 1 diffraction orders create a grating pattern which will be written into the photosensitive fiber core. [8]

The phase mask is a simple and robust technique. Because the setup is stable, long writing times can be achieved, which increases the refractive index difference and so the reflected power.

One of the limitations of this setup, however, is that the Bragg wavelength is fixed for a given phase mask. Also spatial coherence of the UV beam is required, and the larger the distance between the fiber and the mask, the shorter the length of the FBG. A second limitation is the fact that phase masks are very fragile and can be easily damaged.

I used a phase mask technique for inscribing the gratings in the first set samples, as will be explained later in section 3.1.2.

2.3.2. Interferometric technique

A first version of the interferometric inscription techniques is called amplitude splitting. Here a UV laser beam is split into two UV beams with equal amplitudes. They propagate along different optical pathways and recombine on the core of an optical fiber, where they will interfere. By changing the angle of recombination φ the Bragg wavelength can be tailored by:

$$\lambda_B = \frac{n_{eff} \lambda_{UV}}{\sin \varphi}. \quad (8)$$

An interferometric Talbot configuration is shown in Figure 4. The UV beam passes through a beam splitter, and is divided in two beams with equal amplitude. The beams then are directed towards two mirrors which reflect the light towards the optical fiber. The UV laser light will interfere and form an interference pattern that is copied into the fiber core by the refractive index changing effect of the photosensitivity.

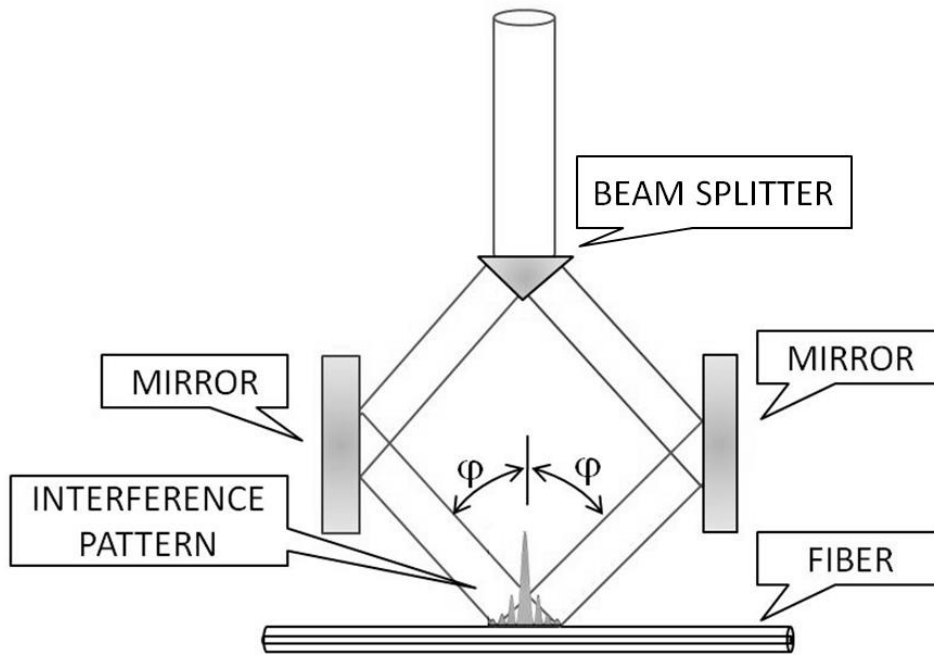


Figure 4: Amplitude splitting interferometric FBG inscription method. A laser beam is split into two parts of equal amplitude and is later recombined over the fiber core. By changing the angle of recombination, the wavelength of the grating (and so the Bragg wavelength) can be altered. (a) In the right picture an extra mirror is added to the setup to ensure the same number of reflections and an equal path length for both arms. This ensures spatial and temporal coherence respectively. [2]

A second type of interferometric interference inscribing is called wave front splitting. Interference is created by splitting a beam into two wave fronts, and letting both interfere. This can be done inside a prism, or with a vertical mirror. The first method is called a prism interferometer and is optically stable, because the optical path difference occurs completely inside the prism. The second method is respectively called a Lloyd interferometer.

Advantages of wave front splitting are the fact that the Bragg wavelength can be changed. Also, because only few components are present, and because the difference between the two interferometer arms is smaller, the system will be less sensitive to errors in alignment or vibrations. Drawbacks are the limited coherence length, because half the beam is folded on its other half.

The FBGs inscribed at the IPHT were fabricated with such a Talbot interferometer, because custom wavelengths were required.

2.3.3. On-tower FBG inscription

To show that inscribing gratings can be put into mass production, on-tower FBG inscription is shortly described here and displayed in Figure 5 [9]. The image shows an standard draw tower setup, where a fiber is drawn from the heated preform. However an interferometric grating inscription system is added to the tower. The system allows for systematic inscription of gratings while the fiber is drawn. The advantages of this method are of course speed and the ability to mass produce, but also the fact that the coating of the fiber can be applied after the grating is inscribed is a large advantage for the mechanic strength of the grating. A drawback is the lower efficiency of the technique. Because a single short pulse is used (20 ns) for the inscription a steady continuous illumination is not always possible.

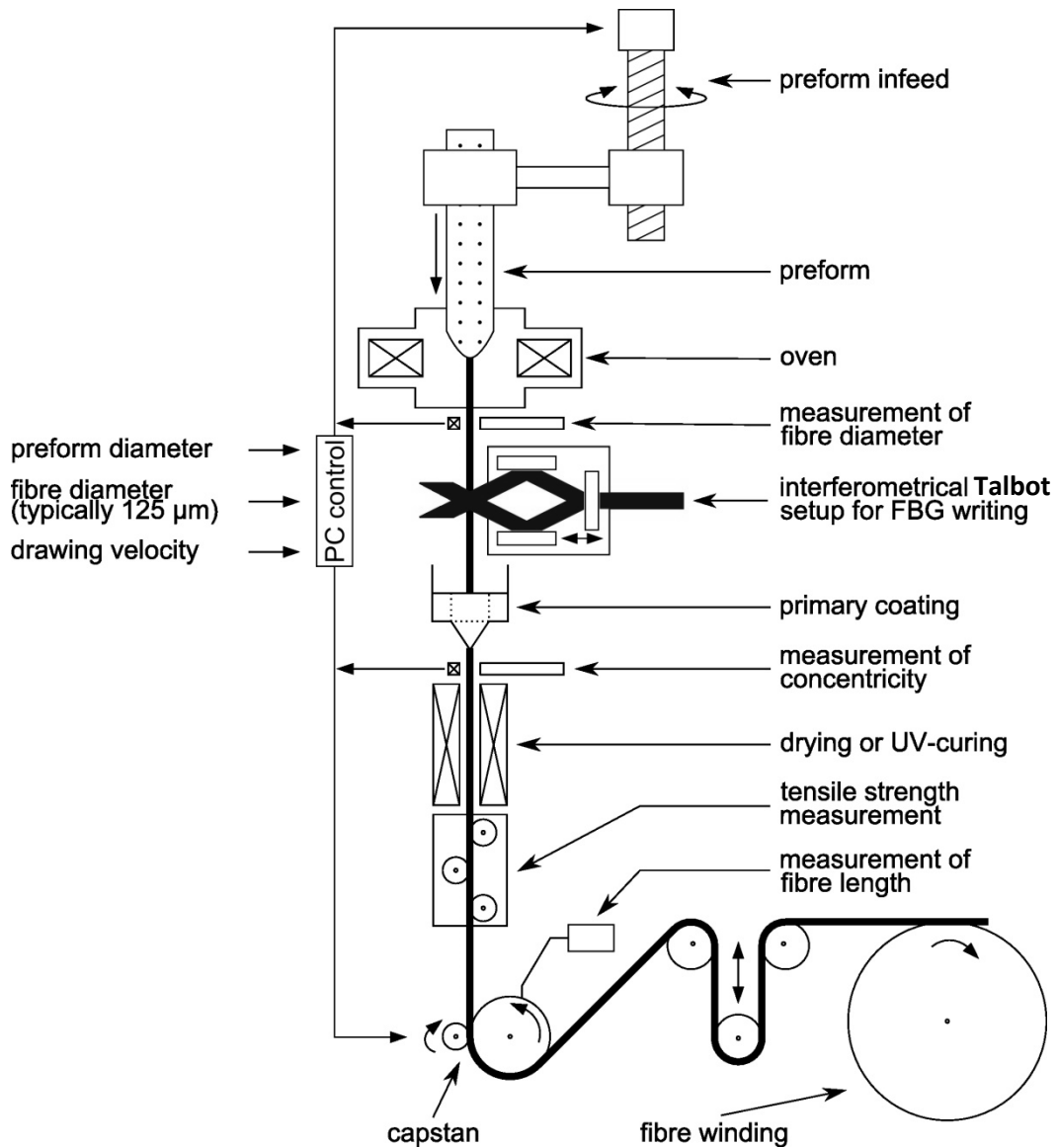


Figure 5: On-tower FBG inscription technique: gratings are inscribed in the fiber while the fiber is drawn. By adding an Talbot interferometric UV system, before the fiber coating is applied. [9] © FBGS technologies

Figure 6 shows the reflection spectrum of 80 FBGs written into a single optical fiber with the draw tower gratings (DTG) technique by FBGS [9]. The figure shows that variations in reflections of such FBG-arrays can be limited.

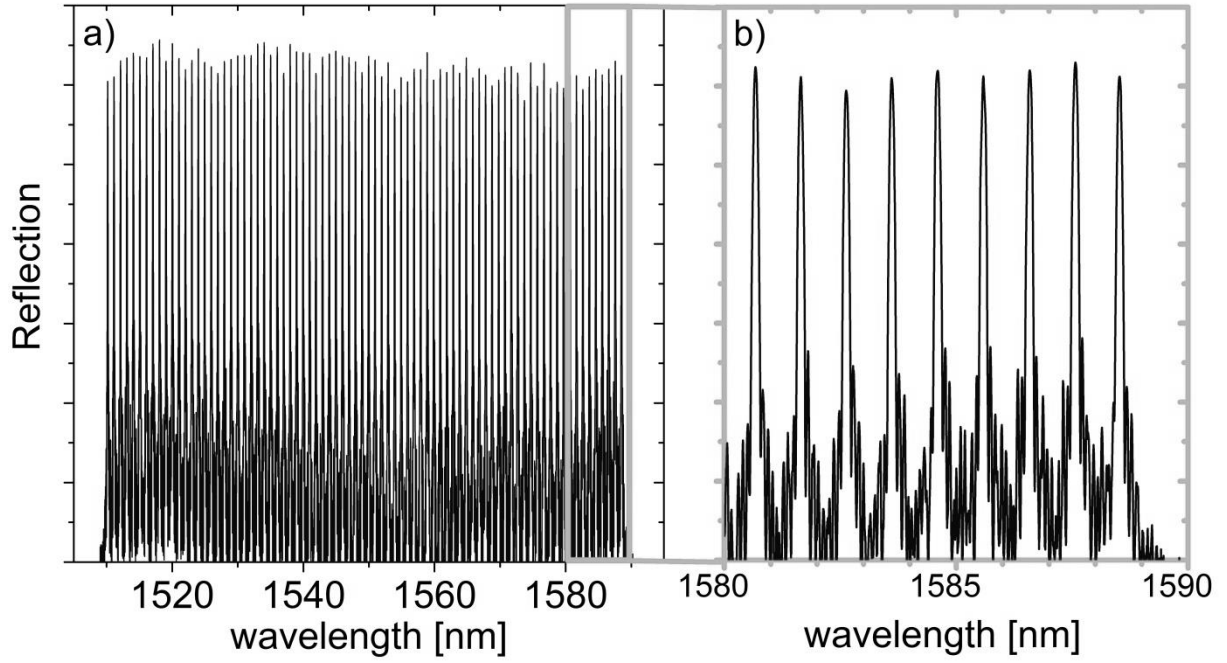


Figure 6: 80 FBGs written into a single fiber with the DTG technique by FBGS a) and a zoom of the reflection spectrum for 1580 - 1590 nm b)

2.4. FBG sensor principle

As can be seen in (6) the only factors able to change λ_B are Λ and n_{eff} , as shown in (9).

$$d\lambda_B = 2n_{\text{eff}}d\Lambda + 2\Lambda dn_{\text{eff}} \quad (9)$$

2.4.1. Temperature changes

Assuming no strain the change in reflected wavelength, due to the change in temperature is given by (10).

$$\frac{d\lambda_B}{dT} = 2 \left(\frac{dn_{\text{eff}}}{dT} \right) \Lambda + 2 \left(\frac{d\Lambda}{dT} \right) n_{\text{eff}} = \lambda_B \left[\frac{1}{n_{\text{eff}}} \left(\frac{dn_{\text{eff}}}{dT} \right) + \frac{1}{\Lambda} \left(\frac{d\Lambda}{dT} \right) \right] = \lambda_B (\xi + \alpha) \quad (10)$$

Here α is the thermal expansion coefficient, and ξ is the thermo-optic coefficient of the fiber. Both depend on type of silica and dopant concentration used.

For a grating at 1550 nm, this corresponds to a shift in Bragg wavelength of

$$\frac{d\lambda_B}{dT} = 1550 \text{ nm} \cdot (\xi + \alpha) = 1550 \text{ nm} \cdot (9.2 + 0.55) \cdot 10^{-6} \text{ }^\circ\text{C}^{-1} = 15.1 \text{ pm}/^\circ\text{C}. \quad (11)$$

With $\alpha = 0.55 \cdot 10^{-6} \text{ }^\circ\text{C}^{-1}$ the thermal expansion coefficient for SiO_2 and $\xi = 9.2 \cdot 10^{-6} \text{ }^\circ\text{C}^{-1}$ the thermal expansion coefficient for 2.4 mol% GeO_2 doped SiO_2 [5]

2.4.2. Axial strain

Also axial strain gives rise to changes in Λ and n_{eff} , as is shown in (12).

$$\frac{d\lambda_B}{d\epsilon} = 2 \left(\frac{dn_{\text{eff}}}{d\epsilon} \right) \Lambda + 2 \left(\frac{d\Lambda}{d\epsilon} \right) n_{\text{eff}} = \lambda_B \left[\frac{1}{n_{\text{eff}}} \left(\frac{dn_{\text{eff}}}{d\epsilon} \right) + 1 \right] \quad (12)$$

A change in applied strain gives rise to a different index ellipsoid of the fiber material, as can be seen from (13) [10]:

$$\Delta \left(\frac{1}{n^2} \right)_i = \sum_{j=1}^6 p_{ij} S_j \quad (13)$$

Where p_{ij} are the elements of the strain-optic tensor, which strongly simplifies because of the isotropic and homogeneous character of the fiber, as seen in (14).

$$\bar{p} = \begin{bmatrix} p_{11} & p_{12} & p_{12} & 0 & 0 & 0 \\ p_{12} & p_{11} & p_{12} & 0 & 0 & 0 \\ p_{12} & p_{12} & p_{11} & 0 & 0 & 0 \\ 0 & 0 & 0 & \frac{1}{2}(p_{11} - p_{12}) & 0 & 0 \\ 0 & 0 & 0 & 0 & \frac{1}{2}(p_{11} - p_{12}) & 0 \\ 0 & 0 & 0 & 0 & 0 & \frac{1}{2}(p_{11} - p_{12}) \end{bmatrix} \quad (14)$$

\bar{S} is the strain vector, as shown in (15), of which the elements relate to the longitudinal strain ϵ and in the radial directions to the Poisson ratio ν times this strain.

$$\bar{S}^T = [\epsilon \quad -\nu\epsilon \quad -\nu\epsilon \quad 0 \quad 0 \quad 0] \quad (15)$$

No shear strain is assumed. Solving (13) with the given material properties (14) and (15), yields (16):

$$\Delta \left(\frac{1}{n^2} \right)_{2,3} = \epsilon(1 - \nu)p_{12} - \nu\epsilon p_{11} \quad (16)$$

A small change in indicatrix can be related to a small change in refractive index by (17):

$$\Delta \left(\frac{1}{n^2} \right)_{2,3} = -2 \left(\frac{\Delta n}{n^3} \right) \quad (17)$$

Together, (16) and (17) give (18) for n_{eff} :

$$\Delta n_{\text{eff}} = -\frac{1}{2} n_{\text{eff}}^3 [\epsilon(1 - \nu)p_{12} - \nu\epsilon p_{11}] \quad (18)$$

According to (6), a change in the Bragg wavelength can be related to both a change in grating spacing as in refractive index by (7). The change in the period of the grating is given by

$$\Delta \Lambda = \epsilon \Lambda \quad (19)$$

Inserting (19) and (7) into (18) and filling in λ_b for $2n\Lambda$ gives, finally (20):

$$\Delta \lambda_B = \epsilon \lambda_B - \frac{\epsilon \lambda_b n_{\text{eff}}^2}{2} [p_{12} - \nu(p_{12} + p_{11})] = \epsilon \lambda_B (1 - p_{\text{eff}}) \quad (20)$$

with

$$p_{\text{eff}} = \frac{n_{\text{eff}}^2}{2} [p_{12} - \nu(p_{12} + p_{11})]. \quad (21)$$

From (20) the change in wavelength can be related to the strain applied to the fiber grating, with p_{eff} the effective photo-elastic coefficient. Using the values $p_{11} = 0.113$ and $p_{12} = 0.252$ [11] a normalized strain response at constant temperature can be obtained as in (22).

$$\frac{1}{\lambda_B} \frac{d\lambda_B}{\epsilon} = 0.798 \cdot 10^{-6} \mu\epsilon^{-1} \quad (22)$$

For a grating at 1550 nm, this corresponds to a shift in Bragg wavelength of 1.24 pm/ $\mu\epsilon$.

2.4.3. Multi-axial strain field

When the strain applied to the fiber Bragg grating is not isotropic (ie. $\epsilon'_1 \neq \epsilon'_2 \neq \epsilon'_3$), the strain field present in the optical fiber will induce a refractive index difference along the two transversal axes of the fiber. The propagating light will see this index difference and will form two different polarization modes, along the slow axis and the fast axis of the fiber. The axes are called this way, because the phase velocities in both modes are different ($v_\varphi = c/n_{\text{eff},x,y}$), ie. one mode will be fast, the other slow. The light reflected by the Bragg grating, will also be different for both modes. This means the simplification made to come to equation (20) are no longer valid, and two different conditions for the two distinct modes arise. These conditions are shown in equations (23) and (24).

$$\frac{\Delta\lambda_{B,1'}}{\lambda_{B,1'}} = \epsilon_{3'}^m - \frac{1}{2} n_{\text{eff},1'}^2 [p_{11}\epsilon_{1'}^m + p_{12}(\epsilon_{2'}^m + \epsilon_{3'}^m)] \quad (23)$$

$$\frac{\Delta\lambda_{B,2'}}{\lambda_{B,2'}} = \epsilon_{3'}^m - \frac{1}{2} n_{\text{eff},1'}^2 [p_{11}\epsilon_{2'}^m + p_{12}(\epsilon_{1'}^m + \epsilon_{3'}^m)] \quad (24)$$

Instead of one reflection peak, two Bragg peaks will now be visible in the reflected grating spectrum.

2.5. Introduction to PCF and MOF

To increase the resolution of the transverse strain measurements, a new kind of optical fiber was developed, called photonic crystal fiber (PCF) or microstructured optical fiber (MOF). This fiber has an in advance created refractive index difference along two perpendicular transversal axes. By creating a larger difference in the refractive indices, the difference between the two Bragg peaks will also be larger, and transversal strains can be better distinguished.

2.5.1. Index guiding microstructured optical fibers

Because the term photonic crystal fiber tends to refer to a periodic microstructure, fibers without a periodic structure are also called microstructured optical fibers (MOF), although the term PCF is still used as well. The microstructure allows for better mode confinement of the light. The principle is comparable with that of a step-index fiber, where the light is confined by total internal reflection (TIR). In step-index fibers higher order modes are rejected by respecting the V-number for the fiber as in (25).

$$V = \frac{2\pi}{\lambda} r_{\text{core}} \sqrt{n_{\text{core}}^2 - n_{\text{cladding}}^2} < 2.405 \quad (25)$$

Here λ is the wavelength of the light used, r_{core} is the radius of the core and $n_{\text{core}}, n_{\text{cladding}}$ are the refractive indices of the core, respectively cladding of the single mode fiber.

The principle in MOFs uses a different method to exclude these higher order modes. The light is still confined in the solid core region of the fiber by the surrounding air holes, which have lower refractive index. The difference is in the “modal sieve” created by the air holes. As can be seen in Figure 7, the dimensions of higher order modes are small enough to ‘leak’ through the spaces between the holes [12]. The largest mode is too large to leak and will stay inside this core region. By choosing the spacing of the air holes, more modes could be trapped.

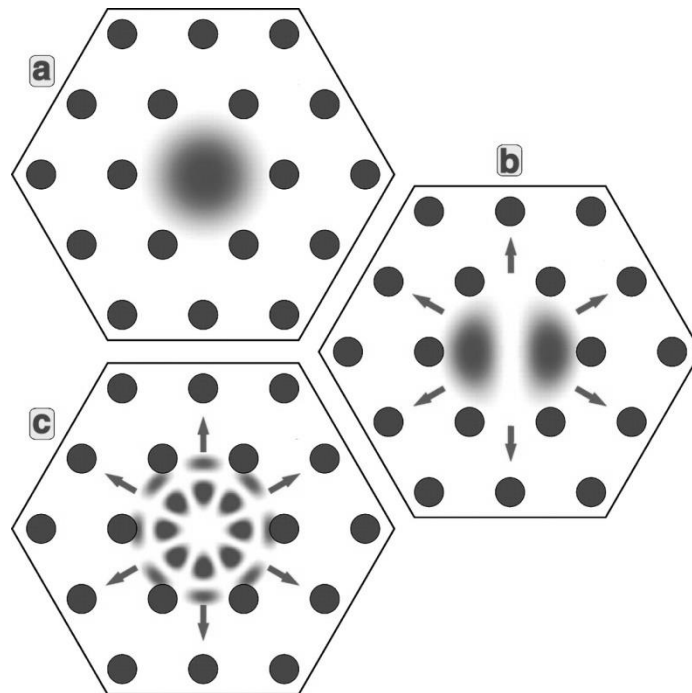


Figure 7: Modal sieve in microstructured optical fibers largest mode is confined (a) higher order modes are smaller and are able to leak out (modal sieve) (b),(c) [12]

A second type of light guiding in MOFs is photonic band gap guiding. Here a periodic refractive index is required around the core region. Now the core region itself is left hollow (air hole), and is in this way lower than the index of the surrounding material. Due to the periodic air holes in the transverse plane of the fiber, light traveling in nonaxial directions will experience a Bragg grating structure. This alternating refractive index structure can create a photonic band gap. This means that light which has a frequency in this band gap range, will not be able to propagate in the direction of the grating. The core region hole acts as a defect where the light propagates through. The surrounding periodic holes act as cladding and keep the light guiding confined in the core region defect as explained above. As can be expected by this guiding method, low confinement losses have been reported. [13][14]

2.5.2. Fabrication of microstructured optical fibers

The most common technique for fabricating microstructured optical fibers is called the ‘stack-and-draw’ technique, and is illustrated in Figure 8. The targeted microstructure is replicated in a macroscopic preform stack. Unlike the conventional fiber preform it is not created by modified

chemical vapour deposition (MOCVD) or vapour-phase axial deposition (VAD), but consists of many rods. Each MOF type has its own specific preform. Figure 8 shows an example of such a preform. The rods can be hollow, to create air holes, or absent (b) to create larger air holes. It is possible to create birefringent cores (a), solid isotropic cores (c) or doped cores (d).

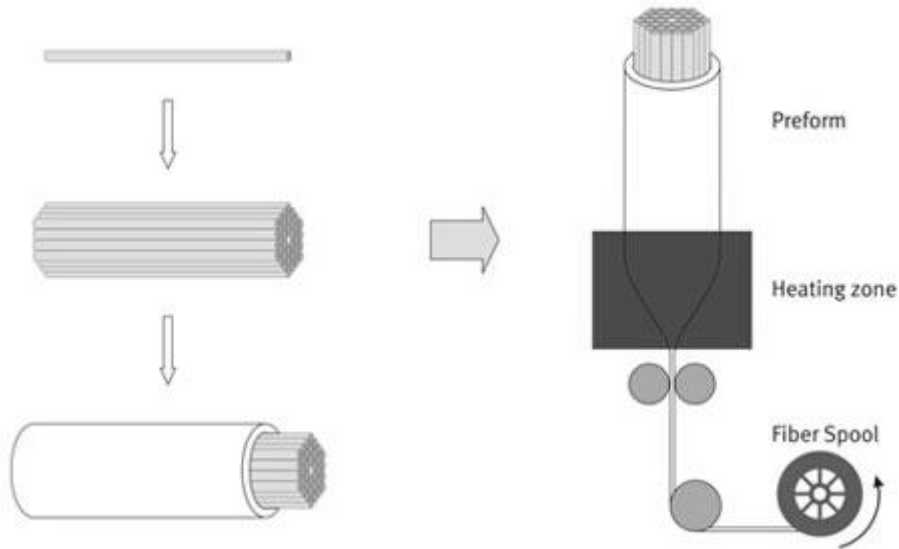


Figure 8: Draw process of a MOF. Silica rods are stacked in the designed way to form a preform. Analogous to a SMF fiber drawing, they are heated and wound on the fiber spindle. [15]

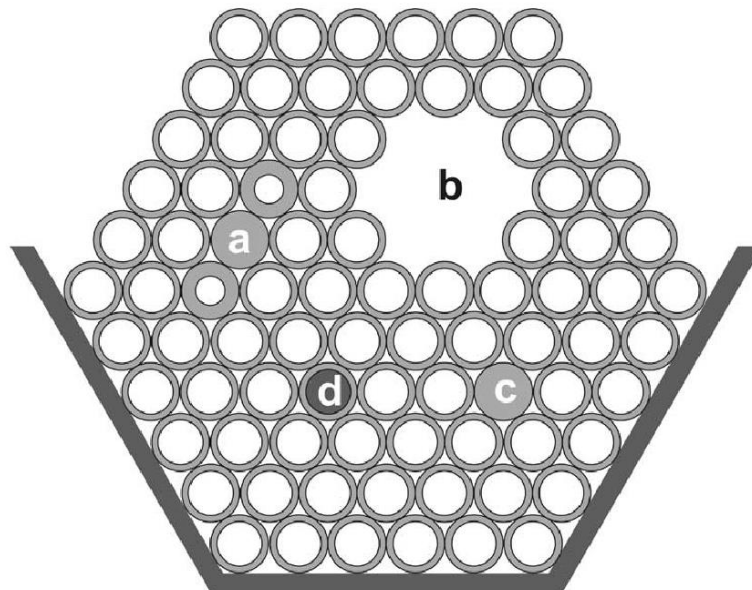


Figure 9: Different types of capillaries are possible: a) a birefringent solid core b) a hollow core (7-cell) c) a solid isotropic core and d) a doped core [16]

The challenge in fabricating MOFs is to maintain this macrostructure pattern through the collapsing of the preform to the microstructure of the fiber itself. This is done by placing the rods into a larger tube, called a preform jacket. The drawing of the MOF is done in two stages. The first stage reduces the diameter of the entire structure. This intermediate stage is called the cane. The preform jacket keeps the stability of the structure during this process. At this point a vacuum is applied between the jacket and the rods (now called capillaries) to make interstitial holes between the capillaries collapse.

This intermediate cane is then again put into a preform jacket to define the final geometry of the MOF. While drawing the final form of the fiber, air pressure is applied into the air holes. This prevents them from collapsing during the drawing. A thorough control of the drawing parameters as temperature, pressure and drawing speed determine the final form of the MOF. The fiber is then drawn through a furnace heating the materials above their glass transition temperature (between 1750 °C and 2100 °C), although a little lower than conventional fibers to prevent the air holes from deforming. In a very last step a protective polymer coating is applied around the MOF.

2.5.3. MOF used in this thesis

In this work a special type of fiber is used to guide the light to the FBG, and allow measurements of axial as well as transversal strain measurements with an inscribed FBG [5]. The power of this type of fiber lies in the microstructure design. It is not a step-index fiber, optimized for telecommunication, and used for local to global data transfer. As can be seen in Figure 10, this type of fiber inherits a special microstructure formed by two types of materials in its inner part [17]. In this case the grey material in Figure 10 is glass (SiO_2), the main material of most optical fibers. The black dots are air holes.

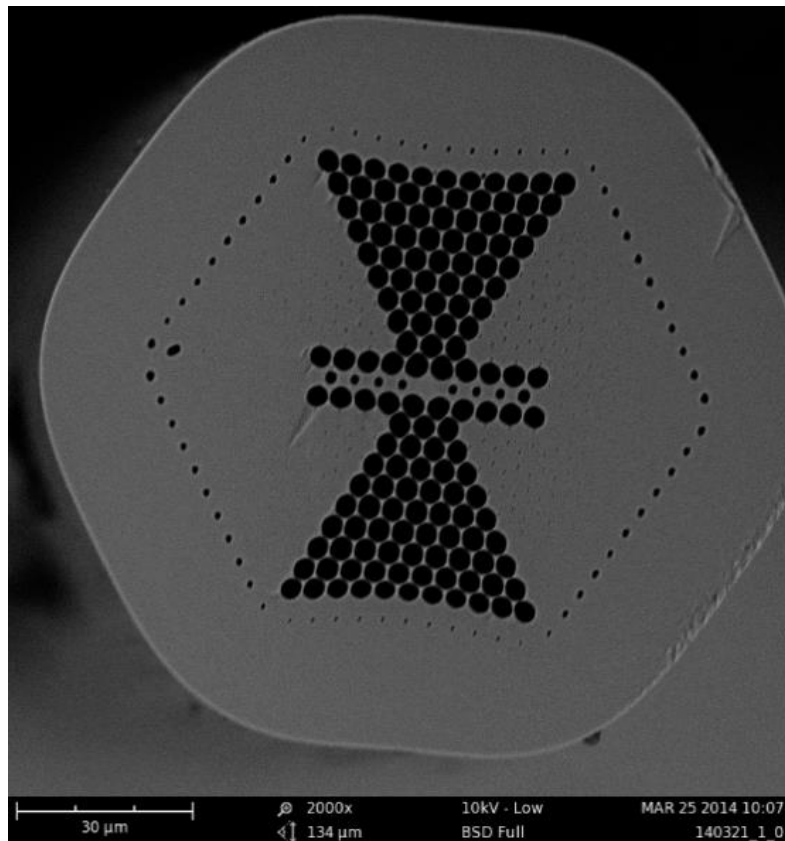


Figure 10: SEM image of the cross section of the butterfly MOF used in this work. The fiber clearly shows two distinct transversal axes. The black holes are air holes in between the silica of the glass fiber. Strain along the direction of the air holes or along the direction of the solid silica will have a different effect on the reflected wavelength.

This MOF is of the type 100321/1/0-100 and is called butterfly MOF as the air hole structure in the cross section looks like the top view of a butterfly. It was this fiber type that was heavily relied on during this work.

Figure 11 shows a detailed view of the core of the MOF. The core is doped with 2.4 mol% GeO_2 . It are the properties of the GeO_2 -bonds that will change when illuminated with UV light and create a permanent local refractive index change.

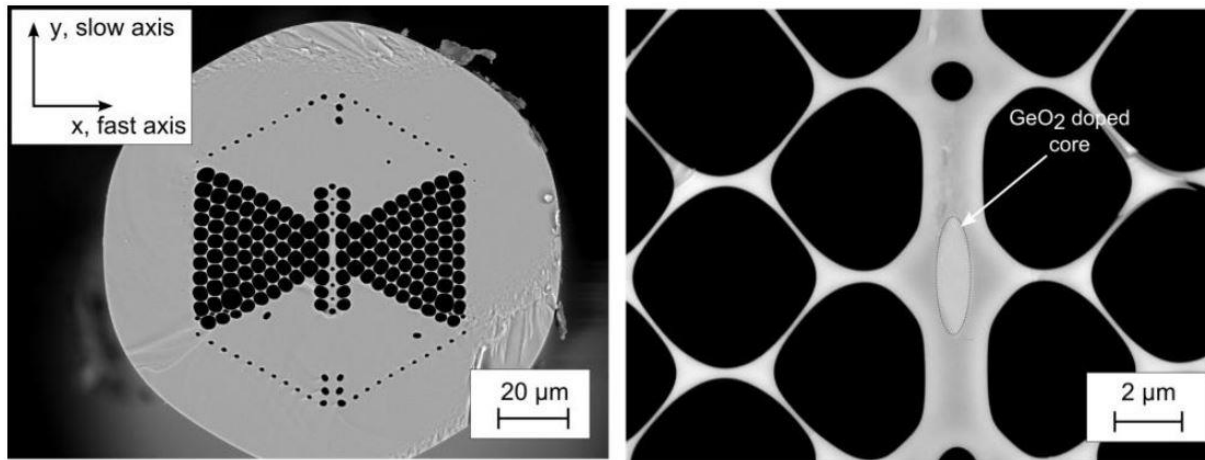


Figure 11: The second designed fiber, and the one used in this work. The left image shows the cross section of the MOF, the right zooms in to the GeO_2 doped core.

2.6. CFRP Composites

2.6.1. Introduction to composite materials and structural health monitoring

The knowledge acquired in the previous chapters on MOFBGs will be extended here to a sensor embedded in a composite material. As hinted before, a right choice of fiber orientation can lead to multi-axial strain measurements, measuring the strain along all three of the principal axes of a composite material.

2.6.2. Composite materials

Composite materials normally consist of two types of distinct constituents. The first constituent is a strong and stiff reinforcement, called the array. Around this array the second constituent forms a matrix that binds the reinforcement and gives form to the material. The matrix usually forms a continuous phase throughout the composite component, and transfers an applied load to the reinforcements and protects the reinforcements against harsh environments. The advantages of composite materials are their strength and their stiffness in comparison with their low density, called a high structural efficiency. This allows them to be used in applications where mass is a factor, i.e. space and aeronautics as well as construction, but also other electrical, thermal, tribological and environmental, structural and mechanical applications [18].

There are three main kinds of composites, depending on the kind of matrix used, to bind the reinforcements. There are matrixes made of polymer or other organic components, called organic-matrix composites (OMCs). Also a metal matrix is possible, leading to metal-matrix composites (MMCs). And lastly there are ceramic-matrix composites (CMCs). [1], [18]

The first type of composites (OMCs) has the lowest strength and stiffness of the three. The second type (MMCs) have little higher strength and stiffness, but deforms under tensile stress. The last type (CMCs) has the highest strength and stiffness, but is the most brittle. [1], [18]

The reinforcements are usually stiffer and stronger than their matrix counterparts, and will provide strength and stiffness to the finished component. Figure 12 shows different kinds of reinforcements [19]. The first type is continuous fiber reinforcements. The term continuous fiber is used when the reinforcements have a very high aspect ratio, ie. if their length is much larger than their diameter. As is shown in the picture, a sequential stacking of layers (called plies) of different orientations is possible. This can give the finished piece changeable properties. Such a finished ply stack is called a laminate. It is this type of reinforcement that will be used in this thesis.

Discontinuous reinforcements are also possible. Reinforcements are called discontinuous when their aspect ratio is between 20 and 100. These reinforcements are shown in the figure as short fibers and include spheres, rods, flakes and whiskers. The last type of possible reinforcements is called particle reinforcements and is shown in the bottom right of the figure. All their dimensions have roughly the same size.

To be complete also woven reinforcements composites are mentioned, but not displayed in the picture below. They include braided and knitted fiber designs.

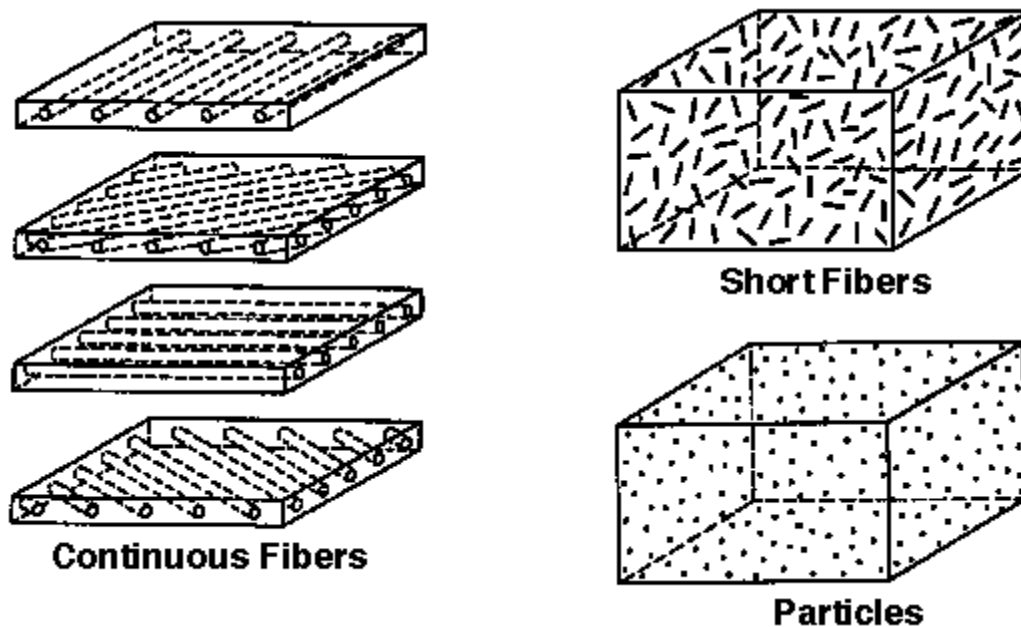


Figure 12: Types of composite reinforcements: continuous fibers are present along the entire composite matrix, short fibers are randomly organized inside the composite and so are particle reinforcements [19]

Because of the many matrices and reinforcements available, there are also numerous combinations possible. The best composition of the composite is however determined by the application of the finished part. The main reason for using composite materials is their increased structural efficiency relative to the material they are to replace. The strength and stiffness of a composite are mainly determined by the kind of reinforcement and the volume fraction with respect to the matrix. Usually volume fractions between 10% and 70% are required.

In continuous fiber reinforced composites the material has the highest structural efficiency when loaded along the fiber orientation. **The lowest strength is however felt when the load is applied perpendicular to the orientation of the fibers.** This because then the matrix has to carry the loads, and not the reinforcements. This means that fiber reinforced composites exhibit a large anisotropy,

which has to be taken into account when designing a composite structure for a certain application. One way to make a continuous fiber composite less anisotropic is to orient certain plies differently than the ply beneath or on top of it. In this way the amount of fibers in a direction where more load is expected, can be increased and vice versa. An example was already given in Figure 12 (left), where a quasi-isotropy is achieved in plane by orienting the successive laminate layers at angles of 0° , 45° , 90° and -45° .

The orientation of the fibers can be tailored in a way to achieve the highest strength and stiffness in a given load direction. Because the shape of the composite part can be chosen during fabrication, this can reduce assembly costs because less detail parts and fasteners are required. This is why the fields of construction and transportation make most use of composite materials, but also aerospace, marine applications, sporting materials and infrastructure use composites.

Also a drawback is the high cost of raw materials and the high assembly costs. Impact damage and, when using laminated composites, ply separation are also problems encountered when using composites. Lastly also temperature changes and moisture can affect the composite parts. When strength and stiffness are necessary and material cost is less of a problem, high efficiency continuous carbon fiber composites are used. This is for example the case in aeronautics, where the total cost of ownership (TCO) can be reduced by using composite components. In this way they save on component weight, leading to less fuel consumption.

One particular kind of fiber-reinforced composite is used in the rest of this thesis. It is a prepreg composite and used an epoxy resin as matrix and carbon fiber as continuous fibers. This kind of composite is called carbon fiber reinforced polymer (CFRP).

2.6.3. Cure cycle of CFRP

The reinforcements of the CFRP composites used are found in the plies of matrix epoxy in a monomer state. These plies will be stacked together to form the wanted component. When the stack formation is cured in an autoclave chamber where temperature and pressure can be adjusted, the epoxy matrix thermoset will undergo the process that is schematically displayed in Figure 13. Monomer molecules start connecting with their neighbors to form linear chains. These chains also branch out and form a gelled, but still incomplete crossed-linked network. This means the number of molecules reduces, but the mass per molecule increases, creating a higher viscosity liquid. The next, more noticeable, transition is when a fully cured thermoset is formed. The molecular mass theoretically goes to infinity and the thermoset is said to be at the gel point. The gelation time is very important as of this moment the material will be no longer a liquid, so can no longer be manipulated. Continuing the cure process will form an infinite network of connected chains. Macroscopically this leads to different elastic properties than were present in the monomer epoxy stage. [1], [3], [20]–[22]

A last transition is the vitrification phase. In this stage the material (in this case an elastic gel) turns into a glassy stage, when the temperature of the resin meets the glass transition temperature.

During the curing process, there are two main transitions (gelation and vitrification) leading to considerable changes in density and thereby creating stresses or distortions inside the composite. Three main phenomena following these changes are listed below: [1], [3], [20]–[22]

- When the monomers form a network, the total volume of the epoxy resin tends to shrink about 7%. This mainly leads to in-plane stress, curvature of composite parts and distortions in laminates.
- The thermal expansion coefficients of the matrix and the reinforced fiber are not the same. So does the reinforcement fiber have a negative thermal expansion coefficient in the axial direction ($-0.5 \cdot 10^{-6}$ to $-1.3 \cdot 10^{-6} \text{ } ^\circ\text{C}^{-1}$) and a slightly higher expansion coefficient in the radial direction ($10 \cdot 10^{-6}$ to $30 \cdot 10^{-6} \text{ } ^\circ\text{C}^{-1}$), but the matrix has a higher thermal expansion coefficient (isotropic). This results in compressive stresses along the fibers and tensions in the matrix along the fiber direction.
- When a mold is used the interaction between mold and matrix also influences the residual stresses. When a metal mold is used eg. aluminum ($69 \cdot 10^{-6} \text{ } ^\circ\text{C}^{-1}$) or steel ($35 \cdot 10^{-6} \text{ } ^\circ\text{C}^{-1}$), the larger expansion coefficient of the mold can create tension at the surface of the cured epoxy thermoset. This will result in in-plane stress gradients through the whole thickness of the composite, creating in turn distortions and bending of the complete composite part.

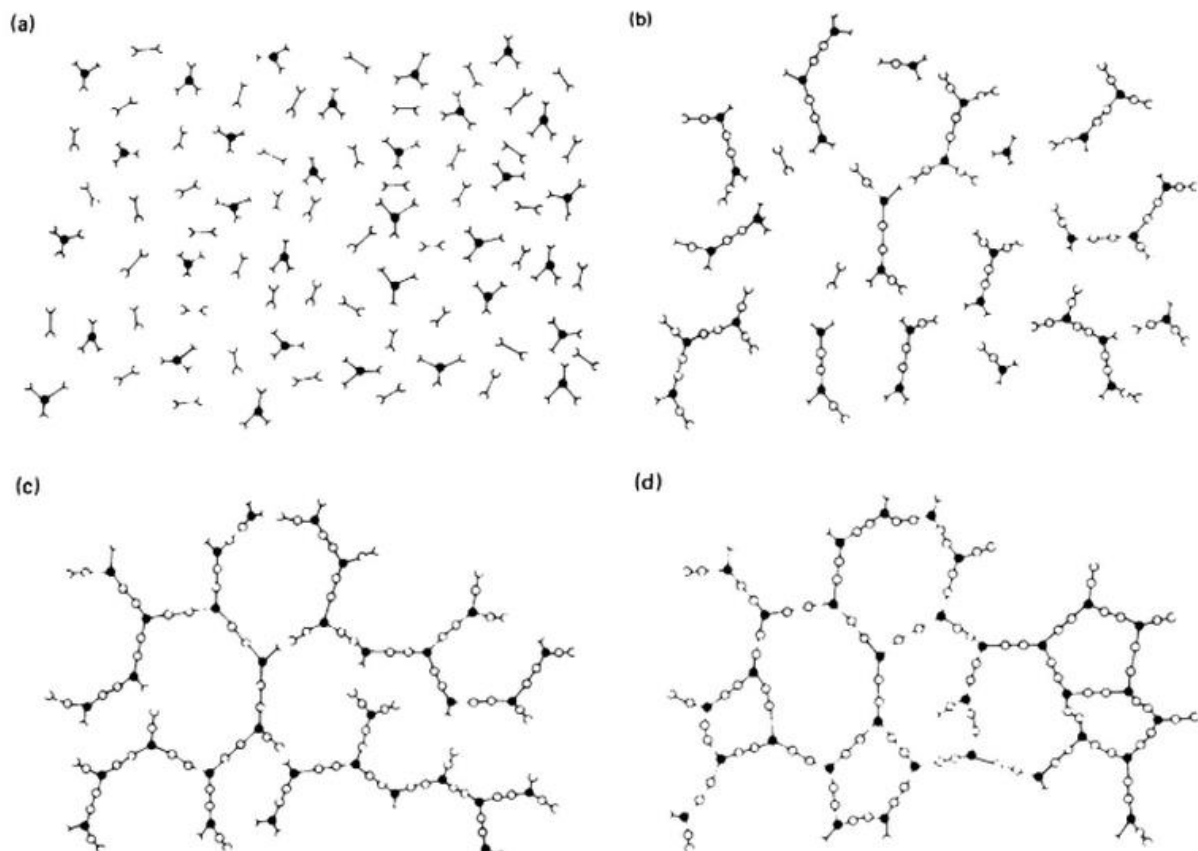


Figure 13: The four different steps during a thermoset curing cycle. The matrix starts in a monomer stage (a) linear growth and branching forms a material below gel point (b) formation of a gelled, but incomplete cross-linked network (c) fully cured, cross-linked thermoset.

Keeping these three points in mind, a monitoring of the curing process can be done to predict curvature, delamination and distortion inside the finished composite part. Measuring strains and stresses during the process with the optical fiber sensors can help to optimize the process and minimize previously mentioned problems. This will prolong the lifetime of the finished part and make it more reliable. Optimizing the cure cycle may also give knowledge about the amount of resin

necessary and the temperature needed, leading to cost and energy savings during curing cycle and material production.

We performed such a cure cycle monitoring with our MOFBGs, as is explained in section 3.5.

2.6.4. Structural health monitoring: monitoring composite materials with embedded sensors

Because reinforced composites have high structural efficiency they were originally used in military and aeronautic application. In these applications a high reliability of the materials is also required. It is for that reason a lot of research effort has been invested into real time monitoring of the state of the internal structure. Structural health monitoring refers to the monitoring of structures while in service. Measurands are strain, vibration, pressure, temperature or moisture. The main purpose of structural health monitoring is to determine damage in structures that is not visible at the exterior. **Predicting damage is an even better objective, and it is also here that dynamic measurements come into play.** The sensor measuring these quantities of course need to intrude the structure as less as possible, for themselves not to create a weakness in the composite component. Optical fibers are the ideal candidate for this job. They are very small (diameter of 125 μm), and it is possible to have many sensors in only one fiber (so no extra electrical wires are required inside the composite). There are many more advantages of optical fiber sensors for structural health monitoring, as listed below [23]–[26]:

1. The material they are built of is silica, which can withstand large tensile elongations of 5%, this makes sure they are durable materials with long life cycles
2. Optical fiber sensors have a large temperature measuring range. They can measure from -200 °C to 800 °C and even higher for fibers with a special doped core
3. They are versatile: they are flexible and can be used on complex surfaces and can be used locally ($\sim \text{mm}$) and distributed ($\sim \text{km}$)
4. They are immune to electromagnetic radiation, something their electronic counterparts are not
5. The fibers are also capable of withstanding harsh chemical environments (like a temperature curing epoxy bath)
6. Their small diameter and no extra connections ensures a minimal intrusiveness in the composite material
7. Defining gratings at different Bragg wavelengths allows for wavelength multiplexed distributed sensors that can sense along a larger structure with only one fiber
8. Due to the developments in mass production of fibers in optical telecom, optical fiber sensors exhibit the same price decrease. Their cost-competitiveness will increase as the market grows. The optical sensor market has an annual growth rate of 20% and will reach a expected market share of \$ 4.10⁹ in 2017 [27]

2.7. FBG sensor theory in 3D MOFBGs

As explained before, the Bragg wavelength of an FBG in a fiber is given by $\lambda_B = 2\Lambda n_{eff}$. Here n_{eff} was the effective refractive index. In the MOF used in this thesis, the effective index seen by the light depends on the polarization. As can be seen in Figure 10 (b), the transverse layout of the structure has two different axes. If light is polarized along the fast axis ($\alpha = 0^\circ$ in Figure 7 (b)), it will

experience more influence of the air holes, and see a smaller refractive index n_{fast} . The opposite explanation explains the higher index n_{slow} seen by light polarized along the slow axis ($\alpha = 90^\circ$ in Figure 7 (b)). The two different polarization modes that exist due to this difference in fast and slow axis refractive index, give rise to a birefringence

$$B = n_{slow} - n_{fast} = \frac{1}{k_0} (\beta_y - \beta_x). \quad (26)$$

Here $k_0 = 2\pi/\lambda$ is the wavenumber and $\beta_{x,y}$ are the propagation constants along the fast and slow axis respectively. Because there are now two refractive indices instead of just one (n_{eff}), this means there will be two Bragg wavelengths $\lambda_{B,x,y}$. The separation between these wavelengths is given by (27).

$$\Delta\lambda_B = 2\Lambda B \quad (27)$$

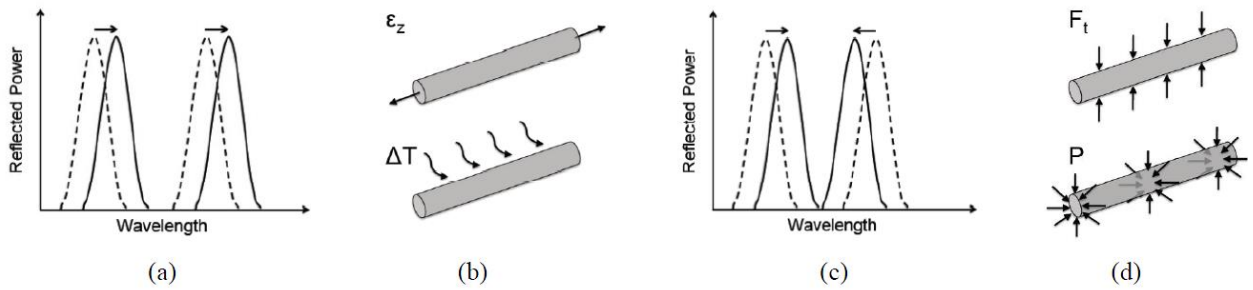


Figure 14: Change in the Bragg wavelengths due to different perturbation. (a, b) Axial strain and a change in temperature move both peaks in the same wavelength direction, and the difference stays constant. (b, c) A transverse force or pressure changes the wavelength separation of both peaks. [5], [28]

2.7.1. Theory of 3D strain transfer

The whole idea of a 3D strain measurement with fiber Bragg gratings is to translate the measured wavelength shift into the total strain immediately around the MOFBG. In the next chapter, we will discuss these immediate surroundings, as the fibers will be embedded in industrial composite materials.

The strains which are measured, are not necessarily the strains present in the composite, but those present in the fiber core itself. For relating these stresses a transfer matrix is necessary. This matrix will transform the stress and strain components measured in the fiber to stress and strain components at the same position inside the composite, as if the fiber were not present.

$$\begin{bmatrix} \epsilon_1^h \\ \vdots \\ \epsilon_6^h \\ \Delta T^h \end{bmatrix} = \begin{bmatrix} TC_{11} & \cdots & TC_{17} \\ \vdots & \ddots & \vdots \\ TC_{71} & \cdots & TC_{77} \end{bmatrix} \begin{bmatrix} \epsilon_1^{m,s} \\ \vdots \\ \epsilon_6^{m,s} \\ \Delta T^s \end{bmatrix} \quad (28)$$

Here the transfer matrix is a seven by seven matrix transforming the mechanical sensors stress and strain components $\epsilon_i^{m,s}$ into the stress and strains components at the same location, but as if the fiber was not intruding the composite. This is schematically show in Figure 15 [1].

A second conversion that needs to be done, if relating the measured wavelength shifts to the strains inside the composite material. A general equation for doing so is given in (29).

$$\begin{bmatrix} \varepsilon_1^h \\ \varepsilon_2^h \\ \varepsilon_3^h \\ \Delta T^h \end{bmatrix} = [TC] \cdot [K]^{-1} \cdot \begin{bmatrix} \Delta\lambda_{B1,1'}/\lambda_{B1,1'} \\ \Delta\lambda_{B1,2'}/\lambda_{B1,2'} \\ \Delta\lambda_{B2,1'}/\lambda_{B2,1'} \\ \Delta\lambda_{B2,2'}/\lambda_{B2,2'} \end{bmatrix} \quad (29)$$

Here the ε_i^h 's are the strains in the three axes of the surrounding material, $[TC]$ here is the transfer coefficient matrix for the strains. This matrix converts the strains and stresses in the core of the fiber to the strains and stresses in the material embedding the fiber. $[K]^{-1}$ is a transfer matrix for relating the strains and stresses in the optical fiber core to $\Delta\lambda_{B2,1'}/\lambda_{B2,1'}$, the normalized wavelength shift of the first peak of the second grating, respectively. This matrix is called the sensitivity matrix. As can be seen from this equation, four peak shifts are needed to find the four unknowns being the strains and temperatures.

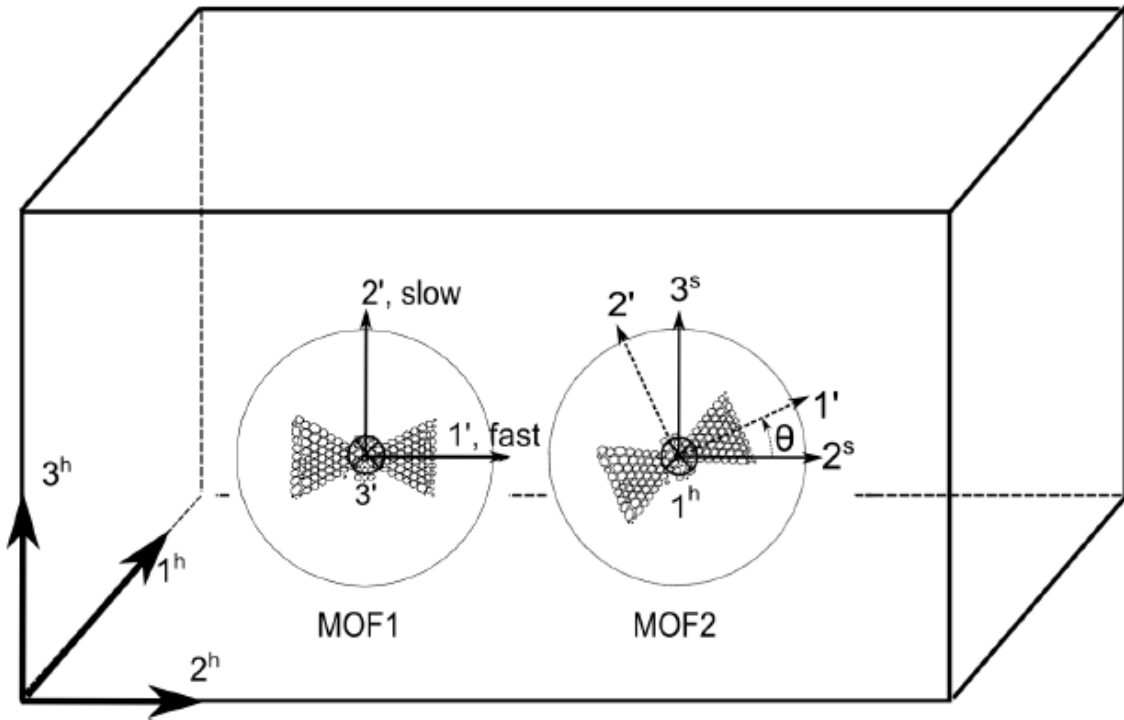


Figure 15: Two MOF fibers inside a composite material are shown. The picture denotes the principal axes of the composite material (h) and the principal axes of the fibers (') embedded therein. The first MOF has the same principal axes as the surrounding composite where the second one (MOF2) is rotated along its axis with an angle θ .

2.7.1.a Simplifications

To further simplify equation (28) it can be taken into account that an FBG is not sensitive to shear strain components $\varepsilon_4^{m,s}$ and $\varepsilon_5^{m,s}$ [29]–[31]. Also the shear component $\varepsilon_6^{m,s}$ can be neglected, because this component influences the cross coupling between the modes of orthogonal polarization and the change of Bragg peak sensitivity varies only between 2 and 10% in function of the orientation of the fiber. This simplification leads to a TC-matrix as in (30) [30].

$$\begin{bmatrix} \varepsilon_1^h \\ \varepsilon_2^h \\ \varepsilon_3^h \\ \Delta T^h \end{bmatrix} = \begin{bmatrix} TC_{11} & TC_{12} & TC_{13} & TC_{14} \\ TC_{21} & TC_{22} & TC_{23} & TC_{24} \\ TC_{31} & TC_{32} & TC_{33} & TC_{34} \\ TC_{41} & TC_{42} & TC_{43} & TC_{44} \end{bmatrix} \begin{bmatrix} \varepsilon_{1'}^{m,s} \\ \varepsilon_{2'}^{m,s} \\ \varepsilon_{3'}^{m,s} \\ \Delta T^s \end{bmatrix} \quad (30)$$

Furthermore we assume that the temperature inside the core of the fiber is the same as in the surrounding composite material. If $\Delta T^h = \Delta T^s$, this induces the following equalities for the TC-matrix components: $TC_{41} = TC_{42} = TC_{43} = 0$ and $TC_{44} = 1$. These can be added as third simplification to the TC-matrix, as is done in equation (31).

$$\begin{bmatrix} \varepsilon_1^h \\ \varepsilon_2^h \\ \varepsilon_3^h \\ \Delta T^h \end{bmatrix} = \begin{bmatrix} TC_{11} & TC_{12} & TC_{13} & TC_{14} \\ TC_{21} & TC_{22} & TC_{23} & TC_{24} \\ TC_{31} & TC_{32} & TC_{33} & TC_{34} \\ 0 & 0 & 0 & 1 \end{bmatrix} \begin{bmatrix} \varepsilon_{1'}^{m,s} \\ \varepsilon_{2'}^{m,s} \\ \varepsilon_{3'}^{m,s} \\ \Delta T^s \end{bmatrix} \quad (31)$$

When referred back to Figure 15, the axes $1', 2'$ denote the radial axes of the fiber and $3'$ denotes the axial axis. $\varepsilon_i^{m,s}$ are the mechanical strain components along these axes and ΔT^s is the temperature change inside the fiber.

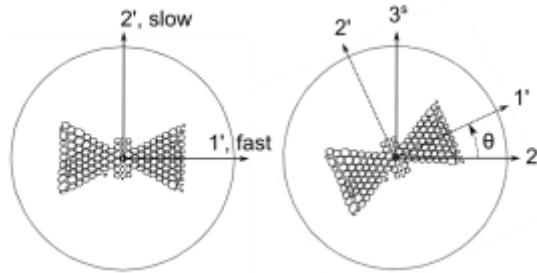


Figure 16: Radial orientation of the axes of the MOF ($1', 2'$) with respect to the principal axes of the material surrounding it ($1s, 2s$)

Dr. Camille Sonnenfeld acquired the numerical values of the TC-components with a finite element simulation in her PhD. For θ being the angle as defined in Figure 16, different TC-matrices are shown in Table 2. θ is the angle between the fast axis of the MOF and the in-plane axis of the surrounding composite material. [1]

Table 2: TC-matrices calculated numerically with finite element simulations: 0° for the first fiber and different axial orientations of the second fiber (0, 25, 45, 60 and 90°).

Angle of orientation	TC-matrix
0°	$\begin{bmatrix} 1.00 & 0.00 & 0.00 & 0 \\ 4.74 & 26.2 & 4.53 & 0 \\ -0.716 & -3.33 & 0.0473 & 0 \\ 0 & 0 & 0 & 1 \end{bmatrix}$
25°	$\begin{bmatrix} 1.00 & 0.00 & 0.00 & 0 \\ 1.88 & 12.8 & 4.36 & 0 \\ -0.616 & -3.29 & 1.10 & 0 \\ 0 & 0 & 0 & 1 \end{bmatrix}$
45°	$\begin{bmatrix} 1.00 & 0.00 & 0.00 & 0 \\ 0.145 & 4.82 & -1.57 & 0 \\ 0.090 & -2.30 & 3.73 & 0 \\ 0 & 0 & 0 & 1 \end{bmatrix}$
60°	$\begin{bmatrix} 1.00 & 0.00 & 0.00 & 0 \\ -0.488 & 2.03 & -3.11 & 0 \\ 1.37 & -0.592 & 9.95 & 0 \\ 0 & 0 & 0 & 1 \end{bmatrix}$
90°	$\begin{bmatrix} 1.00 & 0.00 & 0.00 & 0 \\ -0.487 & 0.825 & -1.96 & 0 \\ 4.32 & 3.67 & 22.8 & 0 \\ 0 & 0 & 0 & 1 \end{bmatrix}$

2.7.2. Theoretical formulation of the sensitivity

There is also a need for a conversion between the measured wavelength shifts and the physical strains experienced in the core. Therefore a second conversion matrix will be used. This matrix is called the sensitivity matrix, or K-matrix. The derivation of this K-matrix starts from equations (32)

and (33), which give the relative wavelength shift in function of the strain $(\varepsilon_{1'}^{m,s}, \varepsilon_{2'}^{m,s}, \varepsilon_{3'}^{m,s})$, and the temperature change ΔT in the fiber core.

$$\frac{\Delta\lambda_{B,1'}}{\lambda_{B,1'}} = \varepsilon_{3'}^{m,s} - \frac{1}{2} n_{eff,1'}^2 [p_{11}\varepsilon_{1'}^{m,s} + p_{12}(\varepsilon_{2'}^{m,s} + \varepsilon_{3'}^{m,s})] + (\alpha_0 + \zeta_{0,1})\Delta T \quad (32)$$

$$\frac{\Delta\lambda_{B,2'}}{\lambda_{B,2'}} = \varepsilon_{3'}^{m,s} - \frac{1}{2} n_{eff,2'}^2 [p_{11}\varepsilon_{2'}^{m,s} + p_{12}(\varepsilon_{1'}^{m,s} + \varepsilon_{3'}^{m,s})] + (\alpha_0 + \zeta_{0,2})\Delta T \quad (33)$$

Here $\varepsilon_{1',2',3'}^{m,s}$ are the mechanical strain components in the core of the fiber sensor, along the optical axes as defined before (Figure 16). The other three (shear) components $\varepsilon_{4',5',6'}^{m,s}$ are usually neglected compared to the first three strain components [31]. $n_{eff,1'}$ and $n_{eff,2'}$ are the effective refractive indices of the fiber core in the polarization modes along the axes 1' and 2' respectively. The elasto-optic coefficients are p_{11} and p_{12} and are also called the Pockels coefficients. Thermal constants are α_0 , $\zeta_{0,1}$ and $\zeta_{0,2}$, being the thermal expansion coefficient and the thermo-optic coefficient in radial directions respectively.

A change in these physical quantities gives rise to a change in reflected Bragg wavelength $\Delta\lambda_{B,1'}$ and $\Delta\lambda_{B,2'}$ along the polarization modes corresponding to $n_{eff,1'}$ and $n_{eff,2'}$ respectively. They are expressed relative to the Bragg wavelength in a calibrated situation $\lambda_{B,1'}$ and $\lambda_{B,2'}$.

The idea is now to get these formulas in a matrix notation. For a 3D strain measurement two gratings are required, resulting in four wavelength shifts. A general representation is given in equation (34).

$$\begin{bmatrix} \frac{\Delta\lambda_{B1,1'}}{\lambda_{B1,1'}} \\ \frac{\Delta\lambda_{B1,2'}}{\lambda_{B1,2'}} \\ \frac{\Delta\lambda_{B2,1'}}{\lambda_{B2,1'}} \\ \frac{\Delta\lambda_{B2,2'}}{\lambda_{B2,2'}} \end{bmatrix} = \begin{bmatrix} K_{11} & K_{12} & K_{13} & K_{14} \\ K_{21} & K_{22} & K_{23} & K_{24} \\ K_{31} & K_{32} & K_{33} & K_{34} \\ K_{41} & K_{42} & K_{43} & K_{44} \end{bmatrix} \begin{bmatrix} \varepsilon_{1',MOFBG1}^{m,s} \\ \varepsilon_{2',MOFBG1}^{m,s} \\ \varepsilon_{3',MOFBG1}^{m,s} \\ \Delta T'_{MOFBG1} \end{bmatrix} \quad (34)$$

The first wavelength subscript refers to the MOFBG, where the second subscript refers to the peak of this grating. The strain components and temperature change are those of the first grating. Each K-coefficient depends on the properties of the sensor used, and on the configuration of this sensor. Because wavelength shifts are measured, and strains are the required physical quantity, it is advised to reformulate this relation with the inverse of the sensitivity matrix, as shown in equation (35).

$$\begin{bmatrix} \varepsilon_{1',MOFBG1}^{m,s} \\ \varepsilon_{2',MOFBG1}^{m,s} \\ \varepsilon_{3',MOFBG1}^{m,s} \\ \Delta T_{MOFBG1}' \end{bmatrix} = K^{-1} \begin{bmatrix} \frac{\Delta\lambda_{B1,1'}}{\lambda_{B1,1'}} \\ \frac{\Delta\lambda_{B1,2'}}{\lambda_{B1,2'}} \\ \frac{\Delta\lambda_{B2,1'}}{\lambda_{B2,1'}} \\ \frac{\Delta\lambda_{B2,2'}}{\lambda_{B2,2'}} \end{bmatrix} \quad (35)$$

At constant temperature, this equation simplifies to equation (36).

$$\begin{bmatrix} \varepsilon_{1',MOFBG1}^{m,s} \\ \varepsilon_{2',MOFBG1}^{m,s} \\ \varepsilon_{3',MOFBG1}^{m,s} \end{bmatrix} = K^{-1} \begin{bmatrix} \frac{\Delta\lambda_{B1,1'}}{\lambda_{B1,1'}} \\ \frac{\Delta\lambda_{B1,2'}}{\lambda_{B1,2'}} \\ \frac{\Delta\lambda_{B2,1'}}{\lambda_{B2,1'}} \end{bmatrix} \quad (36)$$

To yield a rigorous description the strain inside the composite, the strain in the first MOFBG has to be linked with the strain inside the second MOFBG. This can be done by a simple rotational matrix, which will be called the ROT-matrix. The general form of this matrix is shown in equation (37).

$$\begin{bmatrix} \varepsilon_{1',MOFBG1}^{m,s} \\ \varepsilon_{2',MOFBG1}^{m,s} \\ \varepsilon_{3',MOFBG1}^{m,s} \end{bmatrix} = \begin{bmatrix} n_{11} & n_{12} & n_{13} \\ n_{21} & n_{22} & n_{23} \\ n_{31} & n_{32} & n_{33} \end{bmatrix} \begin{bmatrix} \varepsilon_{1',MOFBG2}^{m,s} \\ \varepsilon_{2',MOFBG2}^{m,s} \\ \varepsilon_{3',MOFBG2}^{m,s} \end{bmatrix} \quad (37)$$

As will be seen later the two MOFBGs will be oriented parallel with each other, so will axially feel the same strain. This simplifies equation (37) to (38).

$$\begin{bmatrix} \varepsilon_{1',MOFBG1}^{m,s} \\ \varepsilon_{2',MOFBG1}^{m,s} \\ \varepsilon_{3',MOFBG1}^{m,s} \end{bmatrix} = \begin{bmatrix} n_{11} & n_{12} & n_{13} \\ n_{21} & n_{22} & n_{23} \\ 0 & 0 & 1 \end{bmatrix} \begin{bmatrix} \varepsilon_{1',MOFBG2}^{m,s} \\ \varepsilon_{2',MOFBG2}^{m,s} \\ \varepsilon_{3',MOFBG2}^{m,s} \end{bmatrix} \quad (38)$$

According to equations 28 and 29 the wavelength shift of the second grating MOFBG2 can be written in function of the strains inside the core of the fiber. By using equation 33 this can be linked with the strains inside the first sensor MOFBG1. This is done in equation (39) and (40).

$$\frac{\Delta\lambda_{B,1'}}{\lambda_{B,1'}} = \varepsilon_{3',MOFBG2}^{m,s} - \frac{1}{2}n_{eff,1'}^2 \left[p_{11}\varepsilon_{1',MOFBG2}^{m,s} + p_{12} \left(\varepsilon_{2',MOFBG2}^{m,s} + \varepsilon_{3',MOFBG2}^{m,s} \right) \right] \quad (39)$$

$$\begin{aligned}
= \varepsilon_{3',MOFBG1}^{m,s} & \left[1 - \frac{1}{2} n_{neff,1'}^2 (p_{11} n_{13} - p_{12} (n_{23} + 1)) \right] \\
& + \varepsilon_{2',MOFBG1}^{m,s} \left(-\frac{1}{2} n_{neff,1'}^2 \right) (p_{11} n_{12} \\
& + p_{12} n_{22}) \\
& + \varepsilon_{1',MOFBG1}^{m,s} \left(-\frac{1}{2} n_{neff,1'}^2 \right) (p_{11} n_{11} + p_{12} n_{21})
\end{aligned} \tag{40}$$

From equation (39) and(40), the relation as suggested in equation (35) can be derived in equation (41)

$$K = \tag{41}$$

$$\left[\begin{array}{ccc}
-\frac{1}{2} n_{neff,1'}^2 p_{11} & -\frac{1}{2} n_{neff,1'}^2 p_{12} & 1 - \frac{1}{2} n_{neff,1'}^2 p_{12} \\
-\frac{1}{2} n_{neff,2'}^2 p_{12} & -\frac{1}{2} n_{neff,2'}^2 p_{11} & 1 - \frac{1}{2} n_{neff,2'}^2 p_{12} \\
-\frac{1}{2} n_{neff,1'}^2 \left(\begin{array}{c} p_{11} n_{11} \\ + p_{12} n_{21} \end{array} \right) & -\frac{1}{2} n_{neff,1'}^2 \left(\begin{array}{c} p_{11} n_{12} \\ + p_{12} n_{22} \end{array} \right) & 1 - \frac{1}{2} n_{neff,1'}^2 \left(\begin{array}{c} p_{11} n_{13} \\ + p_{12} (n_{23} + 1) \end{array} \right)
\end{array} \right]$$

Equation (41) is the theoretical representation of the sensitivity or K-matrix. It states the proportionality between the wavelength shifts of a MOFBG due to strains present in the fiber core.

Because, however, there is an anisotropy in the shape of the photonic crystal of the fiber and thus the core of the sensor, there will be a non-uniform strain field transfer to the core of the fiber. It is therefore that the relation between the strain components along the optical axes of the two fibers, cannot be solved analytically with a simple rotation matrix as proposed in equation 33. The coefficients of the ROT-matrix (and so the K-matrix) will have to be determined numerically. In her work, Camille Sonnenfeld, proposed a finite element (FE-) approach for different fiber orientations. The possibilities are shown in Figure 17 and are a combination of these three angles.

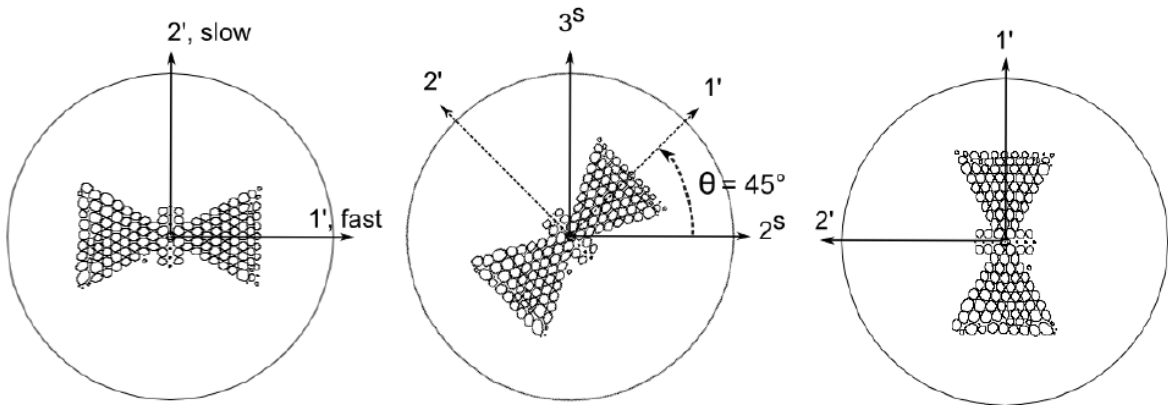


Figure 17: Orientations of the MOF used for the FE approach. Orientations of 0, 45 and 90° are shown and all three combinations of these are used to calculate the ROT- and K-matrices.

The results of this numerical simulation with the finite element method are shown in Table 3 below [1].

Table 3: summary of the ROT- and K-matrices following from a FE-numerical simulation performed by C. Sonnenfeld for three orientation combinations $\theta_1 = 0^\circ, \theta_2 = 90^\circ$; $\theta_1 = 45^\circ, \theta_2 = 90^\circ$ and $\theta_1 = 0^\circ, \theta_2 = 45^\circ$ [1].

Orientation angles	ROT-matrix	K-matrix
$\theta_1 = 0^\circ, \theta_2 = 90^\circ$	$\begin{bmatrix} -3.869 & -0.646 & -0.913 \\ 22.877 & 4.065 & 4.246 \\ 0 & 0 & 1 \end{bmatrix}$	$\begin{bmatrix} -0.115 & -0.256 & 0.744 \\ -0.257 & -0.115 & 0.743 \\ -5.421 & -0.968 & -0.240 \end{bmatrix}$
$\theta_1 = 45^\circ, \theta_2 = 90^\circ$	$\begin{bmatrix} 0.667 & 6.738 & 1.038 \\ -2.771 & -31.706 & -5.800 \\ 0 & 0 & 1 \end{bmatrix}$	$\begin{bmatrix} -0.115 & -0.256 & 0.744 \\ -0.257 & -0.115 & 0.743 \\ 0.633 & 7.354 & 2.111 \end{bmatrix}$
$\theta_1 = 0^\circ, \theta_2 = 45^\circ$	$\begin{bmatrix} 7.44 & 1.25 & 1.22 \\ 2.18 & 0.907 & 0.375 \\ 0 & 0 & 1 \end{bmatrix}$	$\begin{bmatrix} -0.115 & -0.256 & 0.744 \\ -0.257 & -0.115 & 0.743 \\ -1.42 & -0.376 & 0.507 \end{bmatrix}$

As repeated in equation (42), the proportionality between the wavelength shifts and the strains inside the composite material is given by the transfer (TC) matrix and the inverse sensitivity (K) matrix.

$$\begin{bmatrix} \varepsilon_1^h \\ \varepsilon_2^h \\ \varepsilon_3^h \\ \Delta T^h \end{bmatrix} = [TC] \cdot [K]^{-1} \cdot \begin{bmatrix} \Delta\lambda_{B1,1'}/\lambda_{B1,1'} \\ \Delta\lambda_{B1,2'}/\lambda_{B1,2'} \\ \Delta\lambda_{B2,1'}/\lambda_{B2,1'} \\ \Delta\lambda_{B2,2'}/\lambda_{B2,2'} \end{bmatrix} = [P] \cdot \begin{bmatrix} \Delta\lambda_{B1,1'}/\lambda_{B1,1'} \\ \Delta\lambda_{B1,2'}/\lambda_{B1,2'} \\ \Delta\lambda_{B2,1'}/\lambda_{B2,1'} \\ \Delta\lambda_{B2,2'}/\lambda_{B2,2'} \end{bmatrix} \quad (42)$$

Because these matrices were both determined numerically, this means their product is also easily determined. And will be called the proportionality matrix P. The products P were also calculated for the different orientations as before and displayed in Table 4 [1].

Table 4: P-matrices for different orientation possibilities, as used before. The P-matrix is the product between TC- and inverse K-matrix and stand for the proportionality between wavelength shifts and strains active in the composite.

Orientation angles	P-matrix
$\theta_1 = 0^\circ, \theta_2 = 90^\circ$	$\begin{bmatrix} -0.547 & 1.87 & -0.077 \\ -1.11 & 5.85 & -5.08 \\ -6.08 & 5.28 & 0.494 \end{bmatrix}$
$\theta_1 = 45^\circ, \theta_2 = 90^\circ$	$\begin{bmatrix} 1.90 & -0.715 & 0.054 \\ 5.89 & -0.952 & -5.28 \\ 5.91 & -11.7 & 5.47 \end{bmatrix}$
$\theta_1 = 0^\circ, \theta_2 = 45^\circ$	$\begin{bmatrix} -0.410 & 1.98 & -0.324 \\ 7.99 & 13.0 & -21.5 \\ -6.96 & 4.58 & 2.09 \end{bmatrix}$

2.8. Conclusion

In this chapter we explained the basic principles behind a fiber Bragg grating. We show the theory behind two of the fabrication methods of fiber Bragg gratings (phase mask and interferometric) that will both be used in this thesis. We also explain how the Bragg wavelength of an FBG changes when a temperature or strain is applied to the grating and how this can be used to create a sensor.

We elaborate on the theory of MOFs and show why they gave an added value to fiber Bragg gratings. Their birefringence allows doing multi-axial strain measurements and thus create a MOFBG. Also the fabrication methods of these fibers are explained.

In this thesis we will do dynamic measurement on MOFBGs embedded in composite plates. Composite plates have some special properties with respect to conventional structural components, regarding their strength, stiffness and light weight. We elaborate on this by explaining the composition and curing process of these materials.

Last in this chapter we explain the theory of strain transfer. This theoretical model relates the Bragg wavelength shift to a strain inside the fiber core, which is in its turn related to a strain inside the composite materials. For different orientation of the MOF different of these transfer matrices are obtained.

3. Preparation of the 3D MOFBGs strain sensors

In this chapter we will elaborate the procedures followed to create the 3D MOFBG strain sensors. Two sets of such sensors were created. The first set uses FBGs inscribed at the Université de Mons (UMons), with a phase mask technique. These gratings were written in one day, so measurements could start while the second gratings were being inscribed. The second set uses FBGs inscribed at the Leibniz-Institut für Photonische Technologien (IPHT), with a Talbot interferometric setup. This allowed the Bragg wavelength to be customized in order to be in the wavelength range of the interrogator.

This chapter is structured as follows: in the first section (3.1) the preparation of the FBGs for the UMons inscription is described. We discuss the process of splicing the MOF to SMF, inscribing at UMons with a phase mask technique and characterizing the FBGs. Next, in section 3.2 we discuss the layout, splicing, inscribing and characterizing of the IPHT FBGs. Both sample sets needed to be oriented in order to predict the orientation of the internal microstructure. This procedure is explained in section 3.3. The practical embedding of the MOFBGs into CFRP composite plates is explained in section 3.4. During the cure cycle of this embedding a cure monitoring was performed, which is elaborated in section 3.5. The end result of the embedded MOFBGs 3D sensors in CFRP composite plates is shown and explained in section 3.6. Finally, in section 3.7, a post-mortem analysis is done on a used CFRP plate to determine the precise orientation of the MOFBGs in the CFRP.

3.1. First samples (UMons)

The first FBGs were inscribed at the Université de Mons (UMons). Seven samples were prepared with a layout as shown in Figure 18. The gratings were inscribed in the center of 1 meter of MOF. Both ends of the MOF were spliced to step-index SMF, for being able to measure both reflection and transmission during splicing.

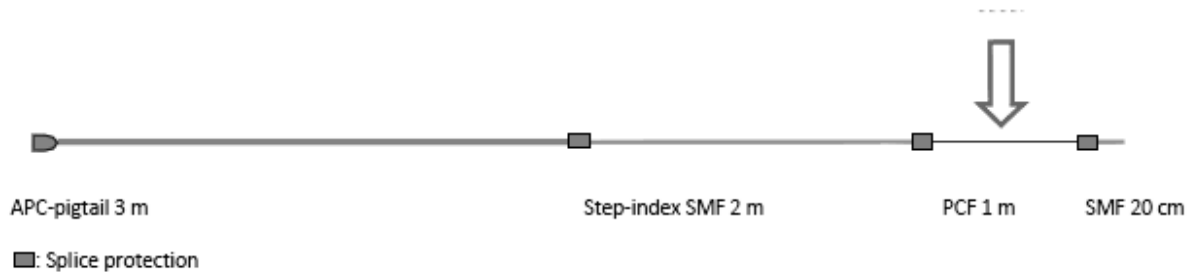


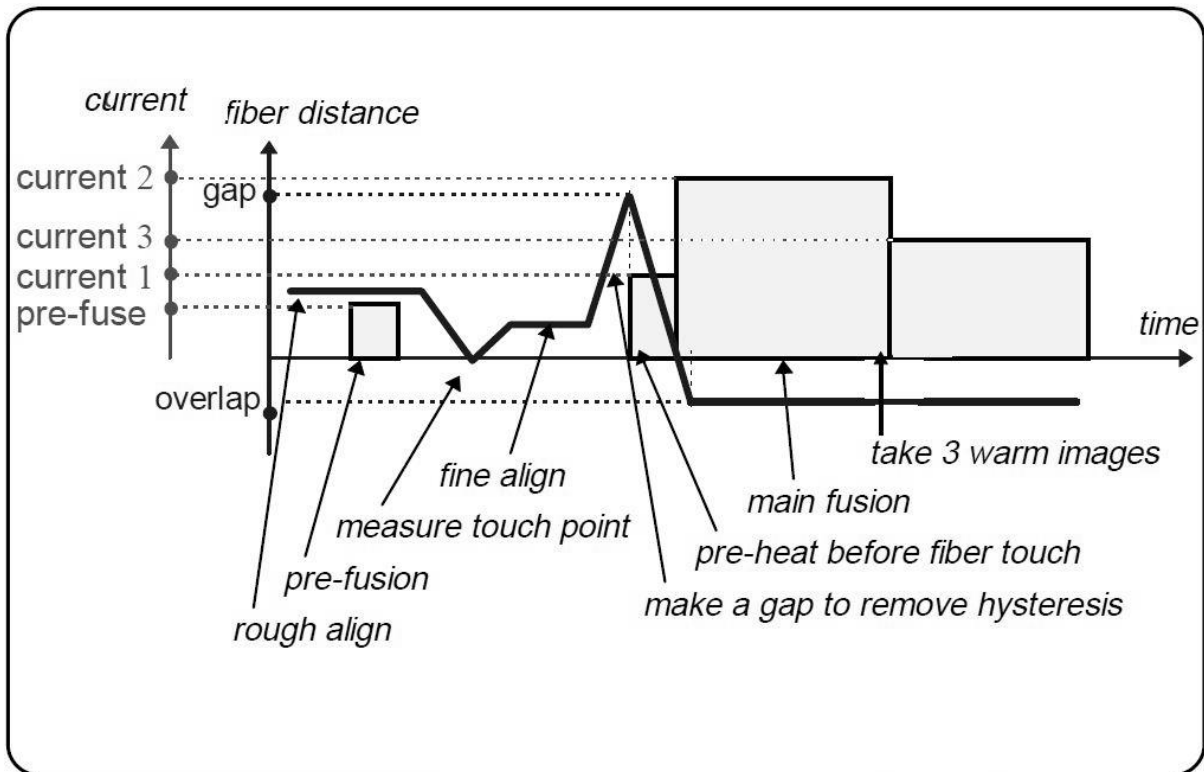
Figure 18: Schematical representation of the first (UMons) samples. The grating was inscribed in the center of a meter of MOF. Spliced to that was step-index SMF and an APC pigtail at the reflection end. All splices were protected by a reinforced splice cover.

3.1.1. Splicing the samples

The splicing process was performed with an Ericsson FSU 975 fusion. Because splicing a butterfly MOF to a step-index SMF is not a standard foreseen splice setting, homemade splice programs were used. The settings of these programs are shown in Table 5. Figure 19 shows these currents and time durations in a graph form. When the fibers are roughly aligned, a prefuse is performed. This prefuse is done to clear all dirt from the fiber ends before splicing. A spark is created between the two electrodes of the splicer and a current is applied for a given time. When the prefusing is done, the fibers are made to touch, to afterwards align them precisely next to each other. When the fibers are spliced together, three currents (I_1 , I_2 and I_3) are applied for times (t_1 , t_2 and t_3). During this splicing the fibers are pressed together with a preset overlap with respect to the touch position. The first fuse spark (I_1, t_1) is to preheat the fiber ends. The second fuse (I_2, t_2) is the main fuse and usually had the highest current. The third fuse (I_3, t_3) is an afterfuse to ensure a good splice.

Table 5: Ericsson FSU 975 fusion splicer splice settings. A prefuse of 10 mA is used to clean dirt of the fiber ends and after that three fuses are performed of different time and current relative to the program in use.

Program	Prefuse time (t)	Prefuse current (I) (mA)	Gap (μm)	Overlap (μm)	t_1 (s)	I_1 (mA)	T_2 (s)	I_2 (mA)	t_3 (s)	I_3 (mA)
01	0.2 s	10	50	10	0.3	10.5	2	14.3	2	12.5
11	0.5 s	10	5	5	0.5	8.5	0.7	10.3	1.3	12.5
12	0.2 s	10	50	6	0.3	10.5	0.5	16.3	0.5	11.5



A typical splicing sequence for the normal splicing process

Figure 19: A typical splice process of the Ericsson FSU-975 fusion splicer. The bar diagrams denote the currents used during the entire (standard) splice process. A pre-fuse, and three fuses of different timing and current are distinguished. The line graph shows the distance between the fiber end. During the actual fuse, the ends make an overlap. [32]

Before splicing two fiber ends together the fiber ends were stripped of their coating with a fiber stripper, remaining dirt or coating was washed off with IPA. Lastly their edges were cleaved with a fiber cleaver (Fujikura CT-30) and carefully put into the splicer. If the display of the splicer showed a clean cleave, one could proceed. If not, the stripping, cleaning and cleaving needed to be repeated. A clean splice and some defects that can occur during cleaving are shown in Figure 20.

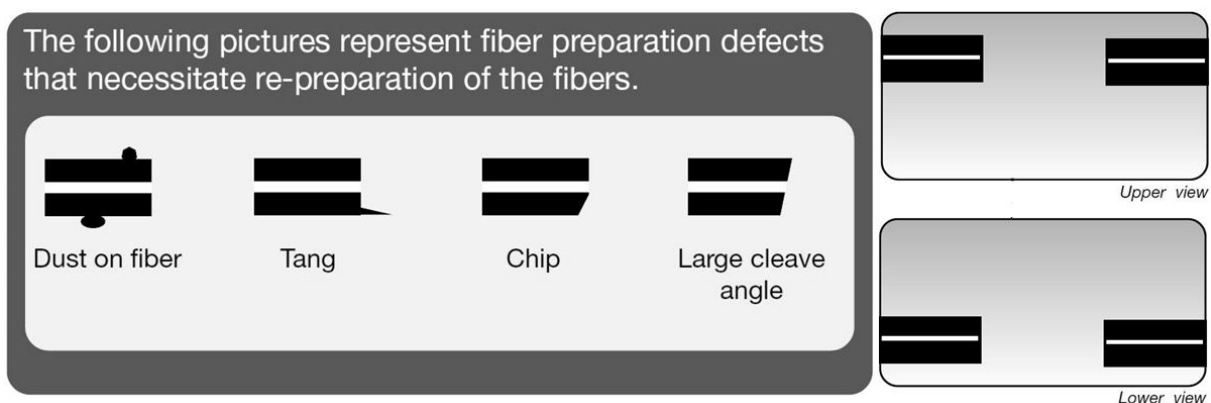


Figure 20: Cleave quality. A Bad cleave can consist of many things: too much dust on the fibers, a tang a chip or a too large cleave angle at one of the fiber ends (left). A good cleave shows two straight cleaves in both the upper and lower view of the fibers (right). [32]

For step-index single mode fiber (SI-SMF) program 01 was used on automatic splicing. It means also the aligning of the two fiber ends was done by the FSU-975. For splicing MOF to SI-SMF a different program was needed, typically with lower splicing times. Therefore program 11 or 12 was used,

depending on the quality of the splice. Because the cross sections of a SI-SMF and a MOF are not at all the same, manual aligning is advised here. This was done by first splicing an SI-SMF end of 20 cm to the MOF and hitting the splice button a few times more, to ensure transmission.

After this a second piece of SI-SMF (2 m) was added to the other side of the MOF. Here the alignment was done manually. The transmission of this splice was monitored by splicing an APC pigtail to both SI-SMF ends. Later the pigtail at the 20 cm SI-SMF end would again be removed.

An ASE-FL7002 light source by Thorlabs was connected to the first pigtail (in front of the splice), and a photodetector was connected to the second pigtail (after the splice). The fibers were then manually aligned until the power measured by the detector was maximum. Program 12 was then used to splice both ends together. Sometimes more fusion events were needed to have transmission. When no light seemed to reach the detector, the splice needed to be broken and the process needed to be redone. If the power of the light source (18.8 mW, directly measured) was compared to the power after the splices¹ an average loss of 12,47 dB, with a standard deviation of 2.63 dB was achieved. This being the overall loss for both splices. After a splice, a plastic protection with steel reinforcement was slid over the splice and was heated to make it collapse around the fiber and protecting the fragile splice.

3.1.2. Inscription of the gratings in butterfly MOF

The fiber Bragg gratings were inscribed into the MOF by the phase mask technique as explained in section 2.3.1, at the Université de Mons.

A picture of the setup, together with the schematical representation can be found in Figure 22. The light of a continuous wave Argon (Beamlock) laser is sent through a frequency doubler (Spectra Physics iTrain 244), dividing the wavelength into two, resulting in $\lambda_{UV} = 244 \text{ nm}$. This light is focused through a cylindrical lens onto the photosensitive fiber core. The +1 and -1 diffraction orders are nicely visible on the paper screen behind the setup. During the inscription the FBG reflection was monitored with a FiberSensing BraggMETER and the growing of the peaks could be followed in real time on a PC. When the peak height stagnated or was found to be high enough, the process was stopped and the next fiber was stripped and clamped in place behind the phase mask. The inscription time was a minute up to a few minutes, depending on the orientation of the fiber. Figure 21 shows the dependence of the inscription time on the orientation of the MOF. Light entering the fiber and encountering a lot of air holes is scattered, and so it will take longer for the grating to be inscribed as compared to inscribing a grating with light entering the fiber at a side where less air holes are present. [33]

These samples were made for being able to start doing measurements on them as soon as they were embedded (see next chapter), and for having the experience of witnessing a phase mask inscription technique in a real setup.

¹ Mind the fact that the first splice was done automatically and was only there to insure the ability of measuring the maximum transmitted power.

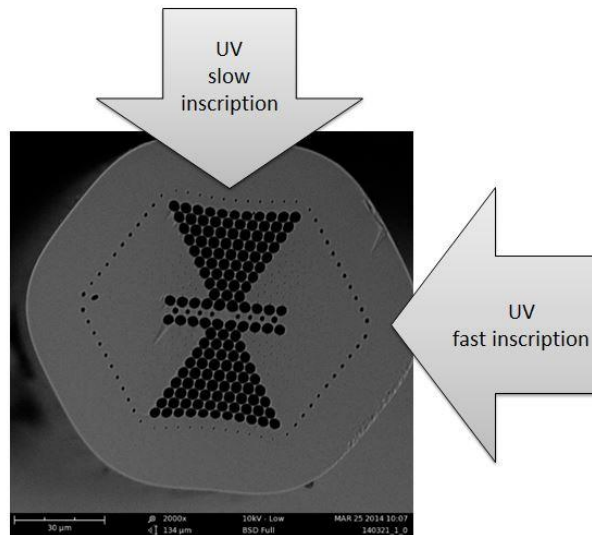


Figure 21: If the UV light is incident on the fiber side along which the air holes are present a lot of light is scattered, and the inscription time is longer as compared to UV light entering the MOF along the side of the fiber where mostly glass is present.

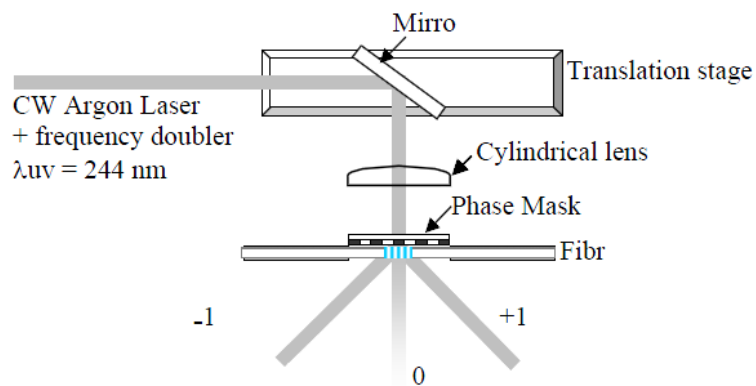
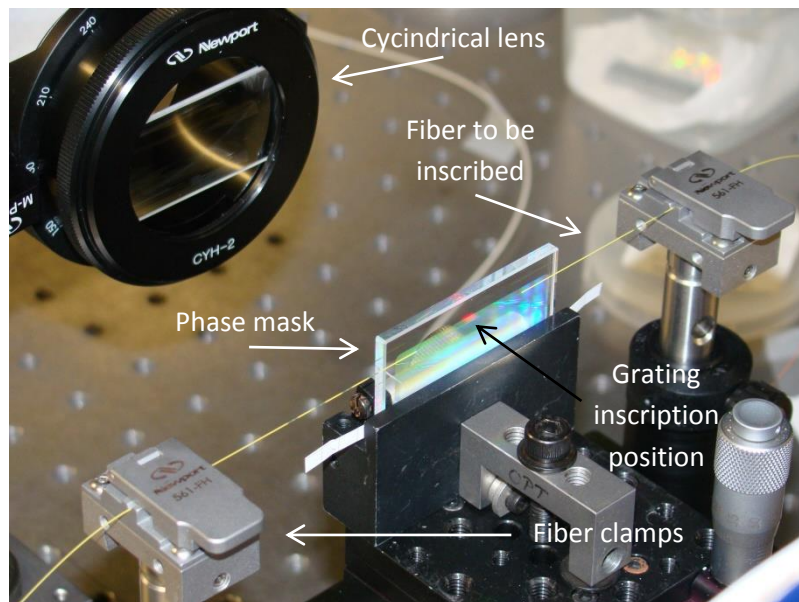


Figure 22: Picture of the UMons “phase mask scanning” FBG inscription setup (top) and schematical representation (bottom) [33]

The reflection spectra were afterwards measured with an optical spectrum analyzer (OSA). An example of such a spectrum can be seen in Figure 23. Two peaks are definitely visible. Data for the two peaks of the different samples is shown in Table 6. The first peak has an average value of 1567.14 nm, and the second peak and average of 1567.87 nm. The standard deviation on these values is 0.20. The average peak separation is 0.738 nm with a standard deviation of $9.35 \cdot 10^{-3}$ nm. The average maximum power of the first six samples is -55.29 dB, with a signal to noise ratio (SNR) of 18.86 dB. Standard deviations on these values are 1.54 and 3.91 dB respectively. The last sample has lower peak power, and so was kept as reserve sample.

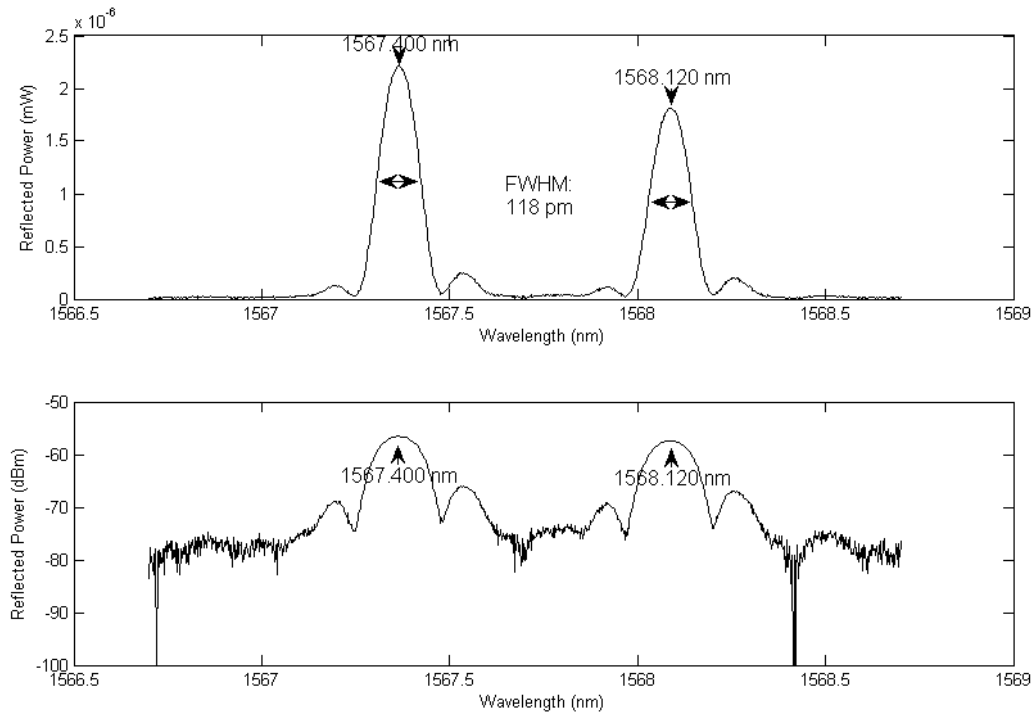


Figure 23: Reflection spectrum of an UMons phase-mask inscribed FBG in MOF in linear power scale (top) and dB-scale (bottom). The spectra were read out with an ASE/OSA-interrogation.

Table 6: Peak values of the seven inscribed FBGs into MOF. Central wavelength, Peak separation, peak power and signal to noise ratio are displayed.

Number of the grating	Peak	Centroid Wavelength nm	Peak Separation nm	Max Power dBm	SNR dB
1	1	1567.244	0.730	-54.00	20.08
	2	1567.974		-54.50	19.58
2	1	1566.740	0.748	-56.83	17.10
	2	1567.488		-57.60	16.33
3	1	1567.244	0.720	-56.84	19.44
	2	1567.964		-57.53	18.75
4	1	1567.140	0.728	-54.04	18.93
	2	1567.868		-54.70	18.27
5	1	1567.400	0.720	-55.13	19.18
	2	1568.120		-55.88	18.43

6	1	1567.298	0.720	-52.95	20.39
	2	1568.018		-53.50	19.84
7	1	1566.948	0.732	-64.16	8.35
	2	1567.680		-64.66	7.85

3.2. Second samples (IPHT)

As mentioned before, the first (UMons) samples were samples constructed to start measuring while a second set of samples was being inscribed in the Leibniz-Institut für Photonische Technologien (IPHT) in Jena. These samples were necessary, because the Bragg wavelength of the phase mask constructed gratings is not changeable, as explained before. As will become clear in the chapter on the interrogation methods, there was a need for gratings at specific Bragg wavelengths different from 1567.14 nm and 1567.87 nm.

The preparing of these IPHT samples for inscription was the same as the UMons samples, so the explanation of the splicing process will not be repeated here. The layout of the samples was different however, and is shown in Figure 24. This time two gratings should be inscribed into one piece of MOF of 2 m. Both ends of the MOF were sealed with a meter of SI-SMF. Eleven samples of this kind were spliced together. The average transmission loss of this construction was 12.47 dB, with a standard deviation of 2.63 dB.

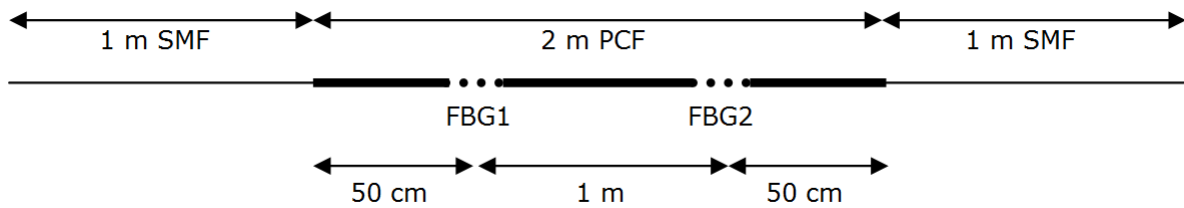


Figure 24: layout of the IPHT samples. This time two gratings had to be written in a two meter MOF, which was on both ends terminated by a meter of SI-SMF.

The prepared samples were sent to IPHT in Jena (Germany) for the inscription of two gratings per sample. The Bragg wavelengths were asked to be 1541 and 1543.5 nm with a tolerance of 200 pm.

The samples were there firstly hydrogen loaded for several days at 100 bar in an 80 °C hydrogen chamber.

Figure 25 shows the reflection spectrum of such a sample, measured with the OSA. All peak values are displayed in Table 7. The first grating has peaks at on average 1540.417 and 1541.054 nm with standard deviations of 0.298 and 0.314 nm respectively. The second grating reflects at 1542.967 nm and 1543.549 nm on average, with standard deviations of 0.279 and 0.340 respectively. Peak separations were on average 637 pm for the first grating and 582 pm for the second grating, with standard deviations of respectively 0.0407 and 0.168. Reflectivities are on average 66.69 %, but have large standard deviation in the order of 18 %.

Table 7: Peak data for the two grating in all of the eight returned IPHT samples. Shown are the four peaks and the reflectivity per grating.

3.2 Second samples (IPHT)

#	PK1@FBG1	PK2@FBG1	PK2- PK1	PK3@FBG2	PK4@FBG2	PK2- PK1	R(1)	R(2)
	nm	nm	nm	nm	nm	nm	%	%
1	1540.635	1541.302	0.667	1543.179	1543.701	0.522	32	95
2	1540.918	1541.592	0.674	1543.350	1543.978	0.628	99	97
3	1540.169	1540.836	0.667	1542.984	1543.650	0.666	78	60
5	1540.606	1541.169	0.563	1543.293	1543.916	0.623	59	63
6	1540.236	1540.880	0.644	1542.784	1543.430	0.646	67	65
8	1539.976	1540.551	0.575	1542.484	1543.196	0.712	63	54
10	1540.189	1540.837	0.648	1542.733	1542.894	0.161	51	87
11	1540.606	1541.267	0.661	1542.925	1543.625	0.700	48	49

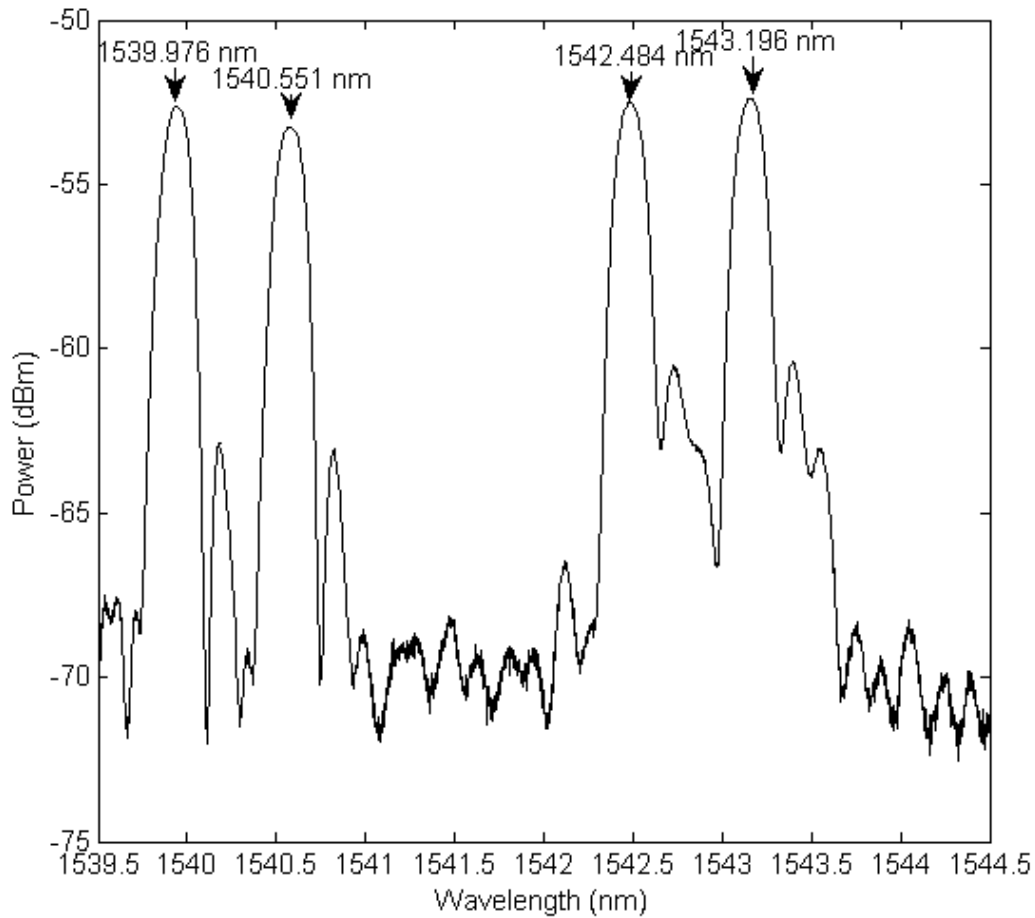


Figure 25: Reflection spectrum of the sample Sidney8 measured with the ASE/OSA-interrogation. Two peaks for each inscribed grating are clearly visible.

The UMons spectra show a slightly larger peak separation of 738 nm compared to the separations of the IPHT samples at 637 nm and 582 nm. The closer the peaks are together the more difficult it will be for interrogation processing software to distinguish between them. However small, the peak separation of the IPHT samples is still large enough to process the data, if the peaks do not shift too much toward each other. FWHM and SNR of the two samples seemed to be in the same order.

3.3. Sensor layout and orientation

The FBGs constructed in MONS with a phase mask technique, need to be embedded in composite plates in an intelligent way in order to be able doing dynamical 3D strain measurements. The orientation of the photonic crystal fiber is of great importance, as was explained in the theory about strain transfer. To have the minimal strain difference between two FBGs in adjacent fibers, they need to be placed as close together as possible.

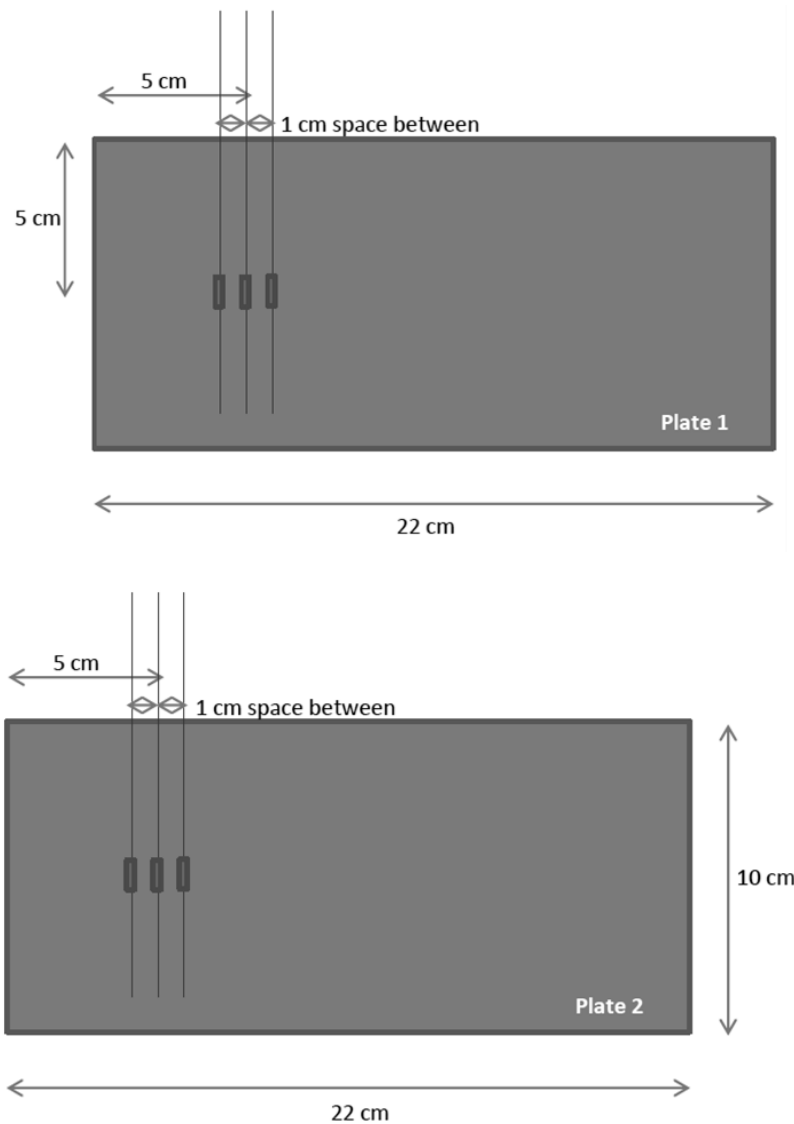


Figure 26: The schematical proposal of the 3D strain sensor, embedded in a composite plate. The plate is 10 by 22 cm, to fit in the dynamic excitation setup, explained later on. The load will be applied at about 1/4 of the long side of the plate, where the FBG's are positioned. Three gratings are placed close to each other (~1 cm), but at different axial orientations with respect to the butterfly structure of the MOF. The orientation angles are shown, and refer to the same orientation as used in the previous chapter. Two of these plates were manufactured.

3.3.1. Orientation procedure

MOF orientation is of great importance for the working principle of a 3D strain sensor constructed with FBGs. Two different, favorably perpendicular, orientations are required in order to do a 3D measurement. Some methods for investigating the orientation and structure of a MOF were investigated in this work.

We started by characterizing the cross section of a photonic crystal fiber with a microscope setup, as shown in Figure 27. The microscope used was a DinoLite Premier AM3113T USB microscope. It allowed a simple and fast setup in order to have an easy to visualize, yet reliably measurement. By cutting or cleaving the fiber and putting it between the rotation stages which are on a translation rail, the microscope can be moved towards the fiber on the translation rail and on the 3D microstage it is mounted on. The microscope is in this way moved right in front of the fiber,

until the fiber cross-section is in focus on the computer screen. The microscope has an own light source to illuminate the sample.

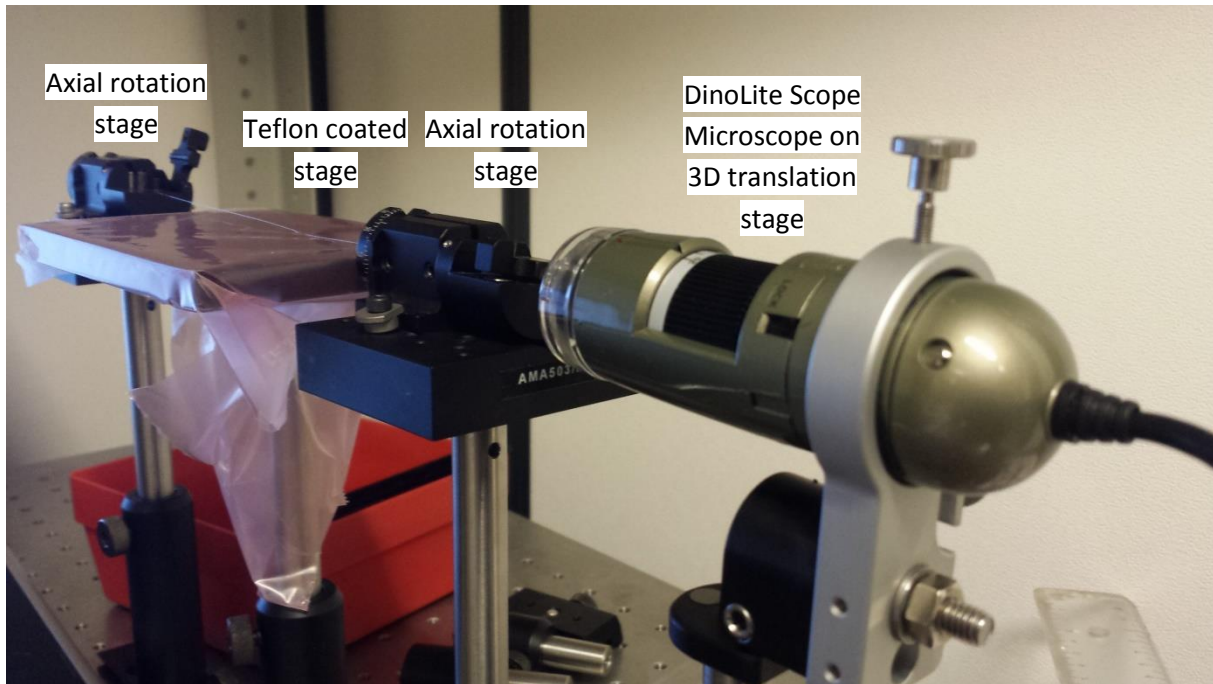


Figure 27: The microscope setup. From left to right: a rotation stage, a teflon coated stage, a second rotation stage and the DinoLite microscope on a 3D microstage. The fiber is clamped between the two rotation stages and rotated around its axis in that way.

The magnification of the microscope was set to maximum in order to have a clear image of the fiber. The microscope software allowed doing a length calibration from a known distance. We used Corning SMF-28 to do the calibration. The Corning fiber as a cladding diameter of $125.0 \pm 0.7 \mu\text{m}$. [34]

The calibration fiber was put into the setup of Figure 27 and put into focus by translating the microscope. The result of the microscope image is seen in Figure 28. With the microscope software a perfect circle is drawn over the circumference of the Corning fiber. The diameter of the circle is calibrated to be $125 \mu\text{m}$.

When the magnification of the microscope is not changed, this calibration can be used to measure the diameter of the MOF used in this thesis. An example of a stripped and cleaved MOF seen by the microscope is shown in Figure 29. Also here a perfect circle is fitted around the, now hexagonal, cross-section of the MOF. From this fit the diameter of the MOF can be estimated to be $125,0 \pm 0.7 \mu\text{m}$. Hereby we neglect the fitting error.



Figure 28: The Corning SMF-28 fiber as visualized by the DinoLite Scope and calibrated to a fiber diameter of $d=125$ μm . A perfect circle was fitted around the fiber circumference in order to determine the diameter. A and C stand for the surface and circumference of the circle respectively.

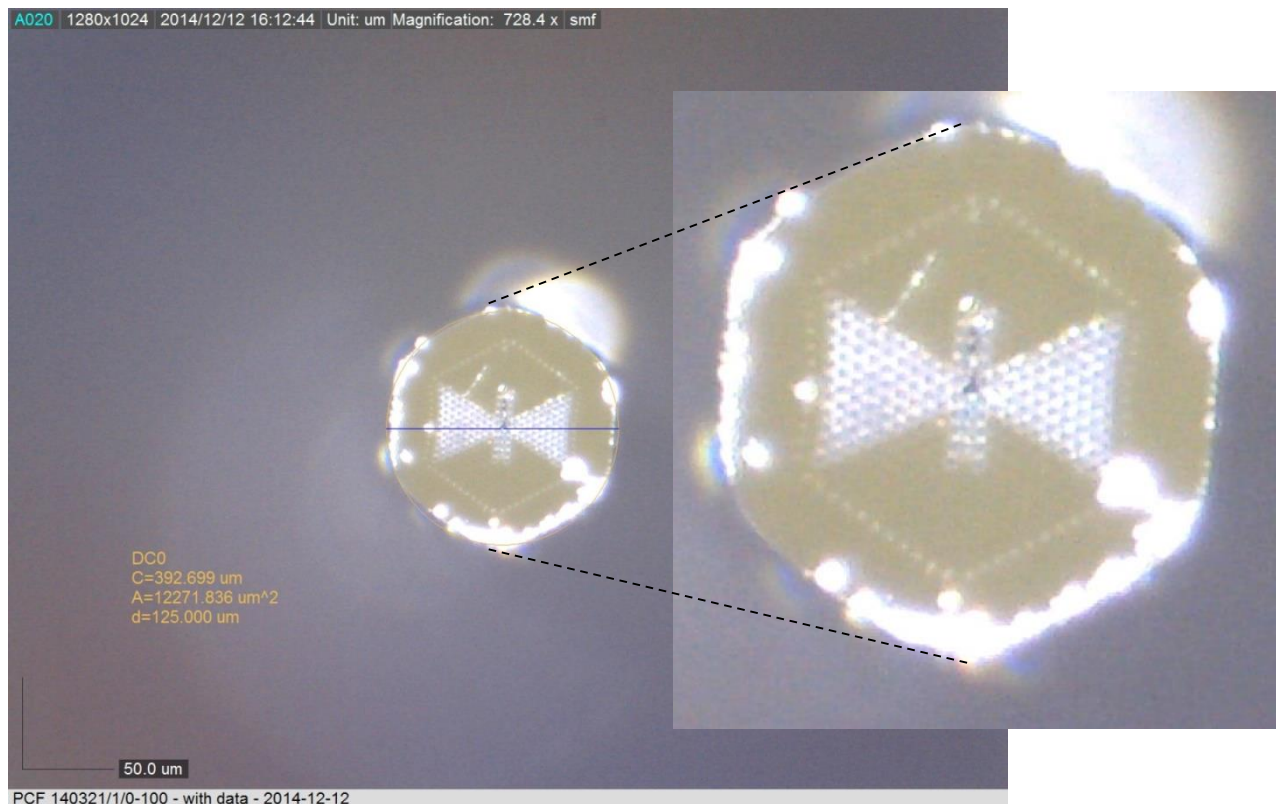


Figure 29: A MOF sample mounted in the same microscope setup (same magnification as before). A perfect circle is fitted around the hexagonal shape of the MOF. From this circle the diameter of the MOF is estimated to be 125 μm . The zoomed image shows that a the butterfly structure of the MOF is clearly visible when the MOF is stripped and cleaved.

Interesting to look at is the MOF with the coating around it. To do this, the MOF cannot be stripped, and as such it can also not be cleaved, it can only be cut. When putting the cut MOF in the setup, the light source of the microscope itself can sometimes cause too much reflection, making the image of the cross-section unclear. Therefore external lighting was used, but still had to be positioned very carefully in order to recognize the fiber, the fiber coating and the butterfly microstructure. Figure 30 gives an example of this, and shows the butterfly structure is still recognizable.

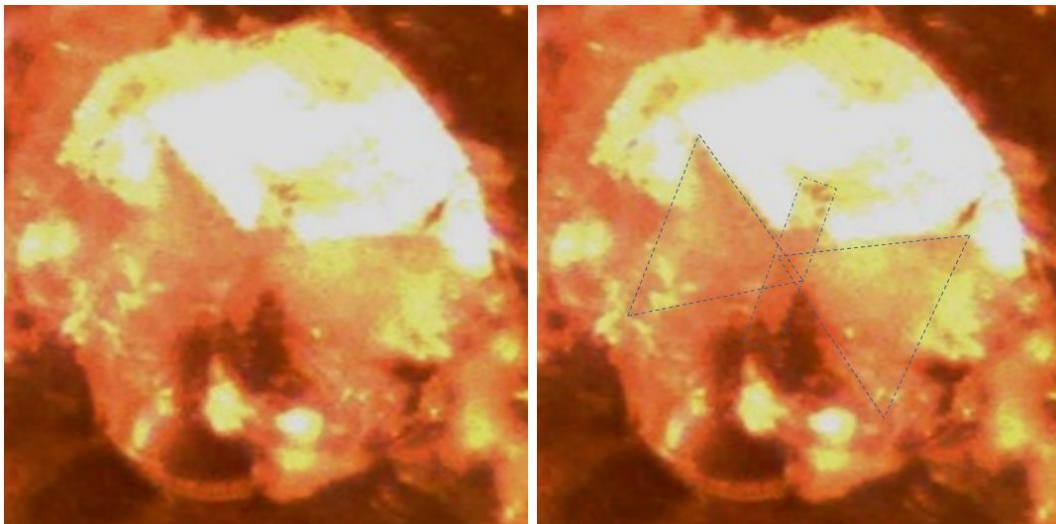


Figure 30: A microscope image of the unstripped, uncleaved MOF. The fiber was cut and put in the setup described above. due to a very rough surface, reflections of the internal microscope light source are too high, and an external light source was provided. The top figure shows the image with scale and the recognized butterfly structure identified. The bottom two pictures clarify the visibility of the butterfly structure.

For three different samples (begin spindle, 20 cm from begin spindle and end spindle) the fiber was cut (not stripped and not cleaved) and put into the microscope setup. With the same calibration as before, two perfect circles were drawn to estimate the circumference of the cladding and the circumference of the fiber itself. In this way we calculated the respected diameters three times, but also the concentricity was determined. It is already clear from Figure 31 that the fiber is not perfectly concentric with its cladding.



Figure 31: The MOF fiber with coating, not stripped and not cleaved. The fiber is clearly not concentric with the coating. To censure the concentricity

The values found for different cross sections were found to be consistent. Over the three measured samples we found an average for the fiber diameter of

$$\varnothing_{fiber} = \frac{(128 + 127 + 127) \mu\text{m}}{3} \approx 127 \pm 0.4 \mu\text{m}$$

with a variance of $0.33 \mu\text{m}^2$, an average for the coating diameter of

$$\varnothing_{coating} = \frac{(219 + 214 + 213) \mu\text{m}}{3} \approx 215 \pm 0.4 \mu\text{m}$$

with a variance of $10.33 \mu\text{m}^2$, and an average of the concentricity of

$$\Delta_{center} = \frac{(10 + 11 + 12)\mu m}{3} = 11 \pm 0.4 \mu m$$

with a variance of $1 \mu m^2$.

The error was calculated by $\delta = \frac{\sqrt{((\delta a)^2 + (\delta b)^2 + (\delta c)^2)}}{3} = \frac{\sqrt{3 \times 0.7^2}}{3} \approx 0.4$ and was only determined with the error on smf-28 calibration [34], not the error by measuring with the dino-lite microscope.

3.3.1.a Orientation of the MOF fiber

A slightly modified setup as in Figure 27 was used to control the orientation of the MOF during the embedding procedure. The setup used now is shown in Figure 32. The MOF with an inscribed FBG is put on the Teflon stage and clamped between an axial rotation stage. The other side of the fiber is not clamped, because the distance between the grating and the fiber end needed to be maximum 4 cm to fit into the composite plate (see Figure 26).

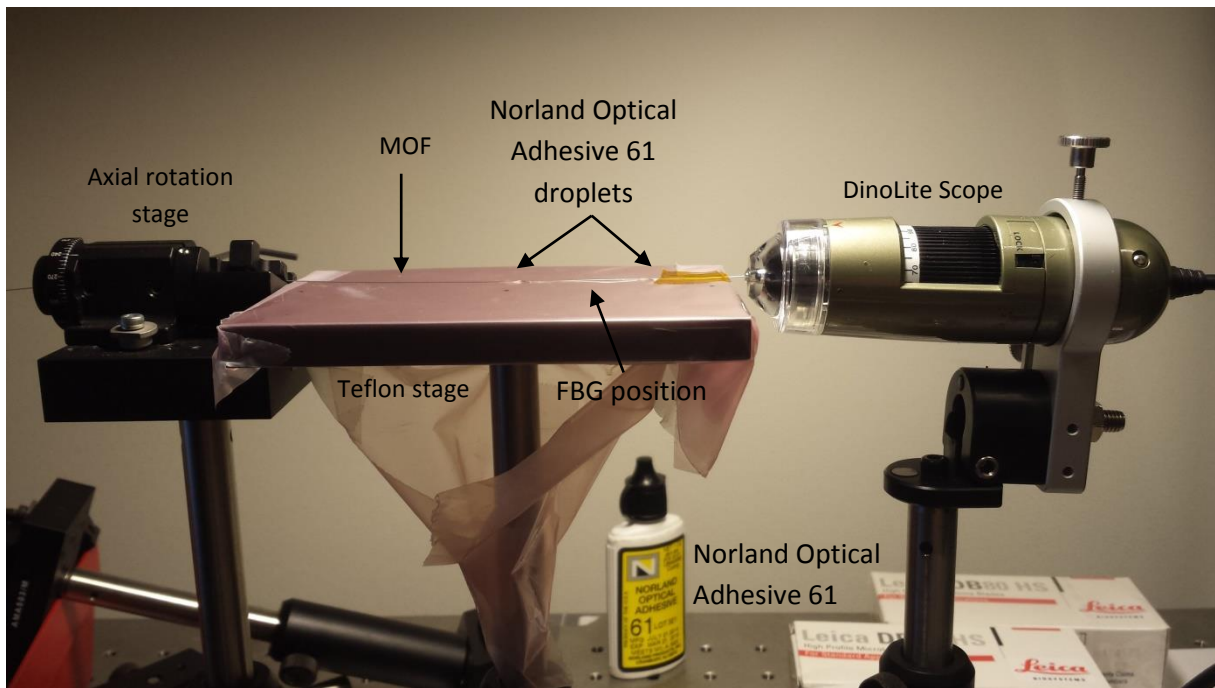


Figure 32: Microscope setup for orienting MOF fibers according to their internal microstructure. The fiber is put in a axial rotation stage on one side. The other side is stripped and cleaved at about 4 cm from the FBG. Because of the small distance between FBG and fiber end, no extra rotation stage is foreseen here. The DinoLite Scope microscope is still used via USB-connection to monitor the orientation of the microstructure in real time on PC.

When the target orientation is obtained through rotation of the stage, the fiber is foreseen of two drops of Norland Optical Adhesive 61 on both sides of the stripped grating with a tweezers. The adhesive is UV curing, so when in place needed to be illuminated with a UV source for about 30 seconds to one minute. This was practiced on Corning SMF-28 many times before used on the FBG-baring MOF samples. An example of such a UV-cured droplet on a SMF is shown in Figure 33. The bottom of the droplet is flat due to the flat Teflon coated stage. In this way is will be easy to put the flat part of the droplet down when embedding the fibers into the composite. If the droplet is small, however, the flat side is sometimes hard to distinguish from the curved top. When this was the case, the top of the droplet was foreseen of a dot by a permanent marker, as in Figure 33.

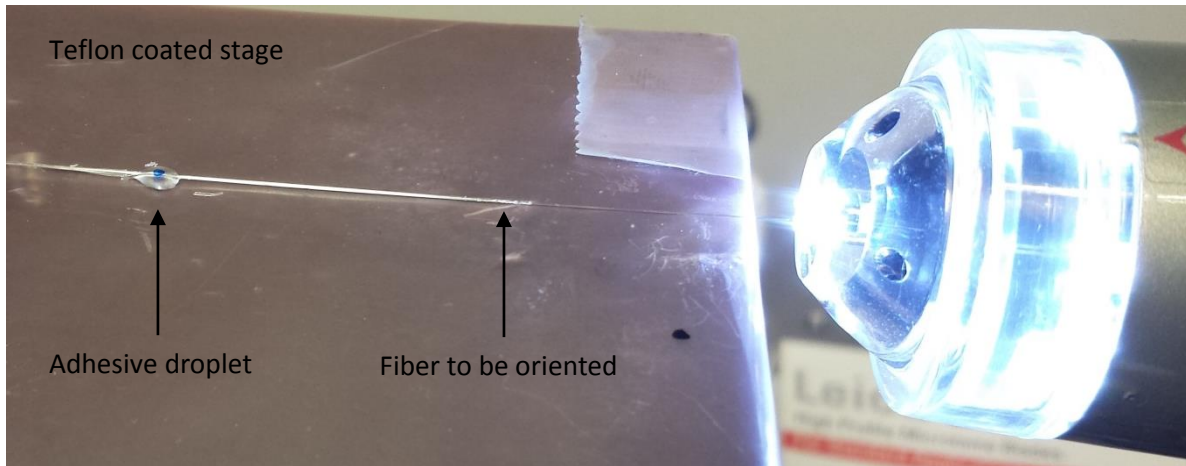


Figure 33: A UV-cured droplet is carefully put onto the oriented fiber by means of a tweezers. When cured, a blue dot is added with permanent marker to indicate the top of the droplet.

3.3.1.b Micro-CT scan

Another method for investigating the orientation of the cross section of the photonic crystal fiber which was explored, was the use of a micro-CT scanner to scan the fiber, whether or not inside a composite. The CT-scan is available for external or internal VUB personnel at the Plant Biology and Nature Management of the Vrije Universiteit Brussel. The objects due for scanning can maximally be 50 x 70 mm, and are best centered at the rotation axis of the scan. The scan uses X-rays to scan the sample. These X-rays are caught by a scintillator and transported to a CCD array with an optical fiber link. [35]



Figure 34: The SkyScan 1172 Micro-CT scan by Bruker. The scan uses X-rays caught on 11Mp, 12-bit cooled CCD fiber-optically coupled to scintillator, and the data is then processed by a computer. [35]

We designed some test holders, fitting the scan. They are shown in Figure 35. The problem with the SkyScan 1172 is the small object chamber (50 x 70 mm), meaning that the entire fiber sample should fit into this small volume. As a fiber sample can have a length of a few meters, the fiber should be wound up around a part of the holder. The FBG, of which the orientation is important, should be isolated from the rest of the fiber to be able to distinguish it from the other wound up fiber. In order to do so, four different designs were made, shown in figure Figure 35.

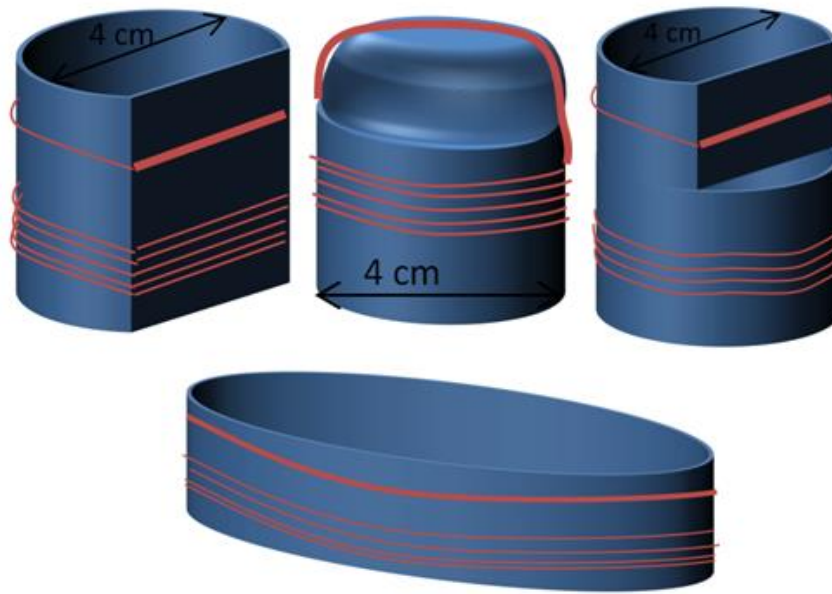


Figure 35: Some test holders to fit the SkyScan μ -CT were designed. The idea still was to put an entire fiber sample of some meters of length into the scanner. This meant the fiber should be able to be wound up around the holder, and the FBG under test should be a straight portion of fiber. The top left holder shows a straight edge for the FBG to be placed. Angles could still be too sharp and might break the fiber. The middle left used the holder's body to wind the fiber, and a curved top to isolate the fiber part containing the FBG. The top right design is a hybrid form and winds the fiber around the hull, while the FBG is placed on a straight edge. Still angles would be too large and might damage the fibers. The bottom structure could solve the problem of too sharp edges by using a flattened cylinder.



Figure 36: The plates designed for the testing of the SkyScan with some small length fiber pieces (length of ~ 6 cm, not wounded). The left design is a rigid one made from perspex, with a drilled hole foreseen of a 6 mm metal rod to fit the rotation stage of the μ -CT scanner. The density of the left design was too high to distinguish between the holder and the fibers. The right holder was a cardboard sandwiched structure with a mousse of light density. The structure was 6.5 by 4.5 cm, which was too large to yield a good resolution. It was therefore afterwards cut to a smaller square of 10 by 10 mm, as shown by the dotted surface.

We started with some test measurements on pieces of different types of fiber (SMF, MOF and plastic optical fiber (POF)). To do this, we made a temporary holder of perspex and one of a cardboard mousse sandwich. They are shown in Figure 36. The perspex holder had a too high density to distinguish between the holder itself and the fibers attached to it. The cardboard holder in its turn was too large to yield a good resolution for the small fiber dimensions. The size was therefore reduced to a square of 1 cm by 1 cm.

Six types of fiber were attached to the 1 by 1 cm cardboard shown in Figure 36 by means double folded tape. The micro-CT image obtained by the SkyScan micro-CT scan is shown in Figure 37. The six types of fiber are shown and numbered from 1 to 6, being: 1) 090921 2) 090727 3) 091006 suspended core 4) 100111/1/700-715 5) and 6) MOF 140321/1/0-100 used in the rest of this thesis.

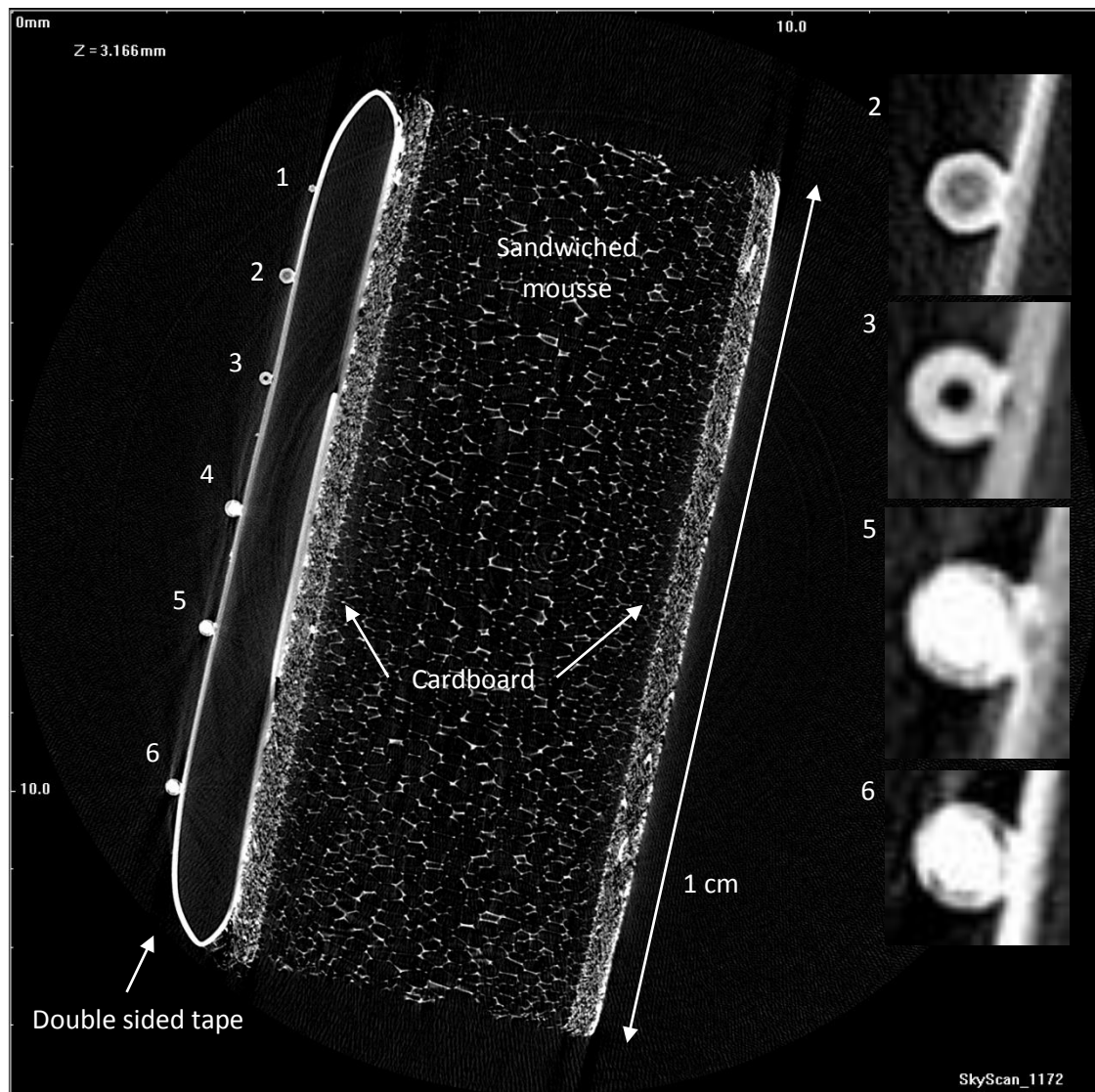


Figure 37: The CT-scan image of the cross section of a 1 x 1 cm holder carrying six types of fiber. The fiber types are numbered from 1 to 6 and for 2, 3, 5 and six a zoomed image is given to the right. The typed of fiber were: 1) 090921 2) 090727 3) 091006 suspended core 4) 100111/1/700-715 and 5) and 6) MOF 140321/1/0-100. The latter two is the fiber type used during the rest of this thesis.

Some of the fibers (number 2, 3, 5 and 6) are zoomed into and shown in more detail. Clearly the resolution of the scan does not suffice to even recognize the internal structure of the fiber. All these

tests tell us that the resolution can be much higher, when the fiber under test is mounted in the rotation middle point of the scan stage, and with no dense material surrounding it. This would imply that to have a successful scan of the cross section of the fiber the fiber core should be positioned in the center of rotation with only a material of light density surrounding it. We first proposed a fiber standing in mid-air, glued to a metal rod with UV-curing adhesive, but due to the rotation of the scan the fiber would vibrate as it was not fixed along the length. To solve former as also latter problem, a holder as in Figure 38 was proposed. The 6 mm metal rod fixes the holder in the SkyScan, the fiber under test is positioned at the same location as the rotation axis of the holder, and the material keeping the fiber in place and keeping it from vibrating is a T-square shaped Styrofoam housing.

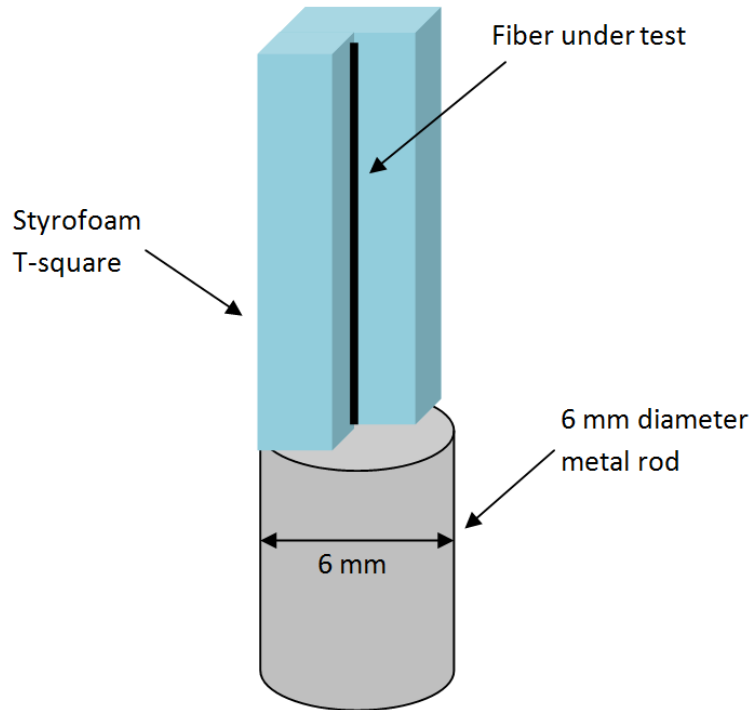


Figure 38: The final design proposal for imaging the cross section of an optical fiber with the SkyScan 1172 μ -CT scan. The fiber part is located at the rotation axis and is kept in place by a T-square shaped Styrofoam housing. The fiber is glued in the angle of the Styrofoam with UV-cured adhesive.

The holder design shown in Figure 38 was e-mailed to the application department of the Bruker ScyScan and positive advice was given for this type of holder. Some other, less feasible alternatives were given (eg. putting the fiber in adhesive wax or gluing it to a curved drinking straw). [35]

We can conclude here that the principle of a micro-CT scan can have an added value to the orientation process of the MOF. The scan used here was dimensionally limited due to the small scanning chamber and the fact that the test object should be positioned at the rotation axis and cannot be surrounded by any other dense material. The search for an appropriate scan continues, but was no more in the scope of this thesis.

3.4. Embedding the fiber sensors in composite material

The manufacturing of the composite plates holding the 3D strain sensor, as shown in Figure 26, was realized at the Department of Materials Science and Engineering of the Universiteit Gent.

3.4 Embedding the fiber sensors in composite material

The composite plate manufactured would be a plate of 44 by 10 cm and later the plate would be cut into two identical pieces of 22 by 10 cm as in Figure 26.

The process is started with cutting the plies foreseen of reinforced fiber from a ply roll. The piece of ply is unfolded on a workbench and the required dimensions are drawn onto the slab. To form a quasi-isotropic composite, equal amounts of horizontal carbon fiber plies are vertical carbon fiber plies were needed. The carbon reinforcements fiber are oriented in the same direction as the ply roll, so plies drawn in the roll direction are called 0° plies are were marked with this number. The same for the other (90°) plies. Figure 39 shows this first step.

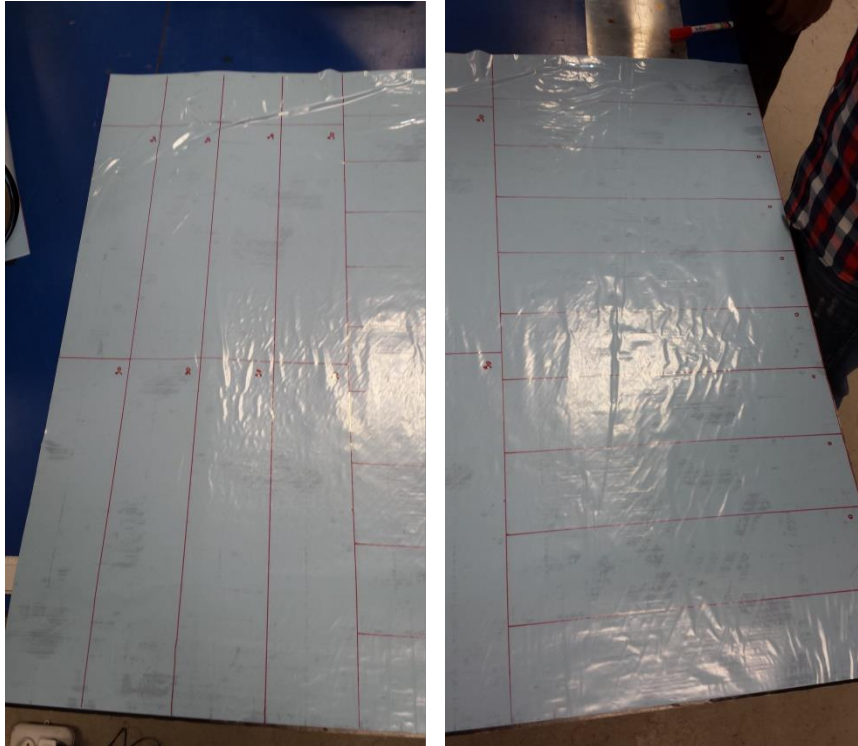


Figure 39: The plies of different orientation are drawn on a part of ply roll. Different orientations of the reinforcement fibers (0°) and (90°) are needed. The orientation of the reinforcement fiber of each ply is written onto it with permanent marker.

The second step is to cut the plies into the prepared sizes with a cutter knife on a hard metal bottom plate, in order not to damage the workbench. Each ply piece is then stripped from the bottom and top protection coating and they are put on top of each other in pairs of two. They have an adhesive nature, yet were pressed tightly together with a rolling pin. The stacking sequence used was

$$\underbrace{0^\circ 0^\circ}_{\text{pair}} \underbrace{90^\circ 90^\circ}_{\text{pair}} \underbrace{0^\circ 0^\circ}_{\text{pair}} \underbrace{90^\circ 90^\circ}_{\text{pair}} \underbrace{90^\circ 90^\circ}_{\text{pair}} \underbrace{0^\circ 0^\circ}_{\text{pair}} \underbrace{90^\circ 90^\circ}_{\text{pair}} \underbrace{0^\circ 0^\circ}_{\text{pair}}$$



Figure 40: The pieces of ply (10 by 44 cm) are then cut with a cutter knife on a hard metal surface (left). The 10 by 44 plies are then stacked onto each other in the right orientation order. Every ply is pressed thoroughly onto the previous by rolling it with a rolling pin. This is done until two ply stacks remain, a top one and a bottom and are this onto two metal plates (right)

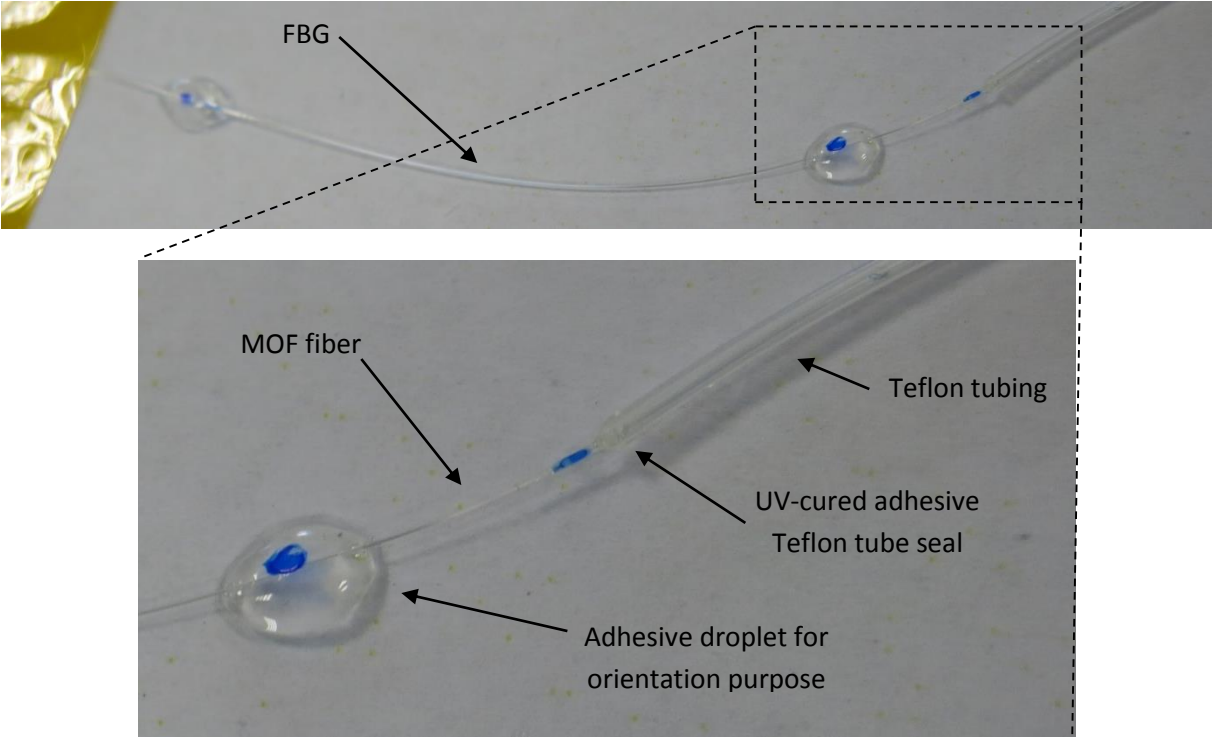


Figure 41: The part of MOF outside of the composite is protected to the epoxy with Teflon tubing. To ensure no epoxy in the tubing, it is sealed off with UV cured glue. In this picture the glue dots for maintaining the fiber orientation are also clearly visible, with a blue dot denoting the top.

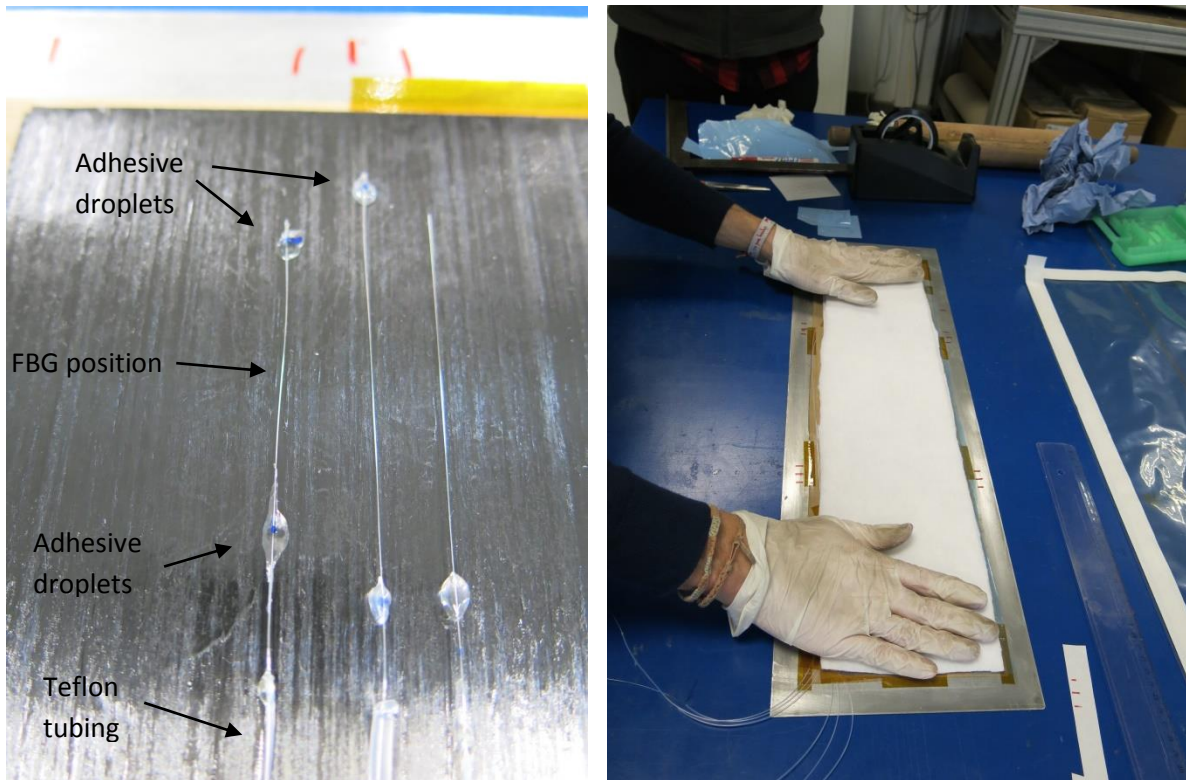


Figure 42: The fibers are put onto the bottom ply stack, with the axial orientation maintained due to the glue droplets. The gratings are located as suggested in the schematical plate design and are separated by 1 cm. This is done two times (left). The top ply is then stacked upon the bottom ply and is thoroughly pressed by hand and with a rolling pin.

The accolades show the pairing of the plies. First two plies of the same orientation are taken and put together. Next two of these stacks, but of different orientation are put together etc.

In order not to damage of soil the MOF fiber coming out of the composite plate during the autoclave curing process, it was foreseen of protective Teflon tubing. As can be seen on Figure 41, this tubing was shoved over the MOF until a few centimeters before the adhesive droplet used to denote the orientation. To be sure the Teflon tubing would not fill up with resin, it was sealed off with the same Norland Optical Adhesive 61 at both sides. Ormocer fiber was spliced to the end of each MOF and is inherently foreseen of a protective coating with the same function as the Teflon tube.

Now the ply stacks are ready and the fibers are protected, the FBGs can be positioned on the composite as in Figure 26. As is seen in the left panel of Figure 42, the adhesive droplets act now as orientation fixers. They are pressed tightly onto the adhesive composite to be kept in place. The second ply stack is now placed on top (as the orientation stated before dictated) and the two stacks are firmly pressed together again also with a rolling pin.

When the plies stick together, a metal plate is put on top followed by a soft piece of fabric. The latter for absorbing a surplus of epoxy matrix resin if need be. Else this resin would end up at the sides of the finished part and need to be cut or broken off. This is displayed in the right panel of Figure 42.

The left panel of Figure 43 shows this as well. On top of the fabric a metal connector is placed. This will connect through the vacuum bag with a tube supplying the epoxy resin. Next to the ply stack the vacuum bag is already visible. The loose Teflon protected fibers are fixed to the metal plate with adhesive tape.

Chapter 3: Preparation of the 3D MOFBGs strain sensors

The vacuum bag is a plastic foil, folded into a bag and placed over the ply stack. The bag is fixed to a metal ground plane by means of an adhesive paste. The paste is pressed tightly to the plate, and possible holes are shut off. This is depicted in Figure 43, on the right panel. One hole in the bag is allowed, above the metal connector, and through this a tube will supply the epoxy resin. To allow for process monitoring, the optical Teflon coated fiber need to be connected to the outside world. The fibers are let through two layers of adhesive gum, as can be seen in the right panel of Figure 43.

Figure 44 shows the whole put inside the autoclave, where the pressure and temperature will be regulated to perform the curing process of the epoxy matrix resin. A thermocouple monitors the temperature inside the chamber and also the air is sucked out of the bag to create a vacuum. The Ormocer coated fibers (connected to the MOF) is spliced to Ormocer coated fiber already present inside the autoclave and connected to the outside. The outside fibers are then also spliced to a APC pigtail to be able to connect the fibers to an interrogator for monitoring the overnight process. The splicing was done with the Ericsson FSU 975 fusion splicer.

3.4 Embedding the fiber sensors in composite material

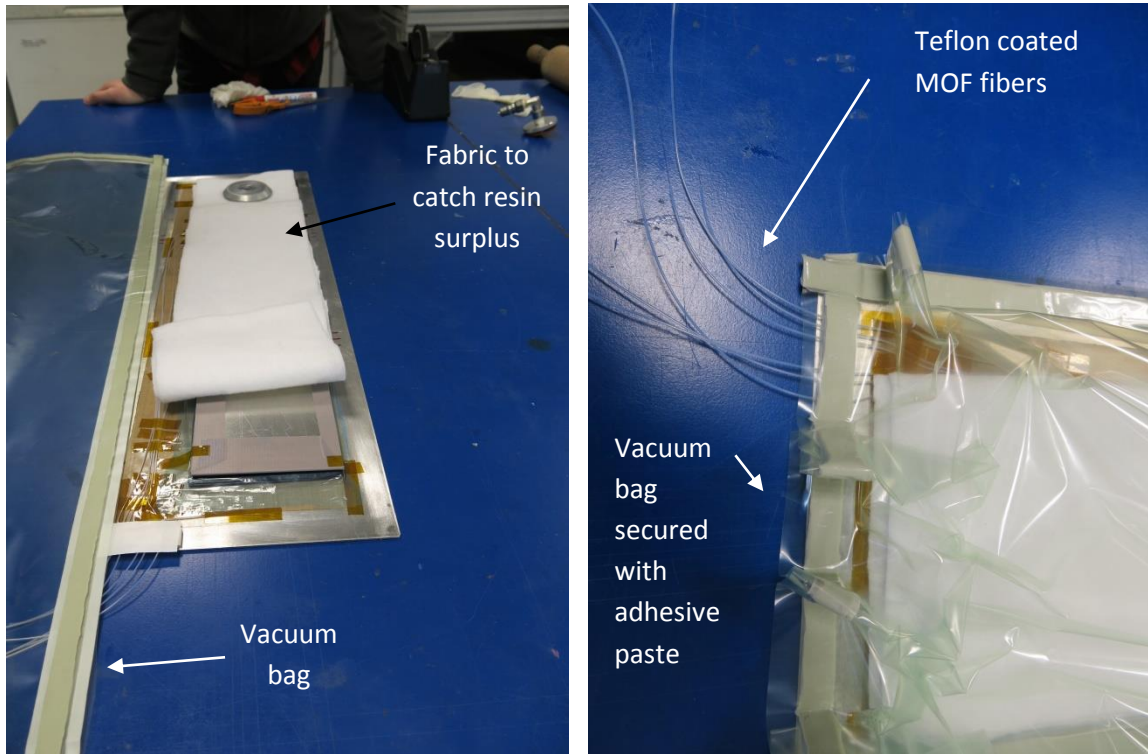


Figure 43: The ply stack is sandwiched between two metal plates and a resin absorber is added on top to absorb the surplus of epoxy resin added during the curing cycle. All optical fibers with or without Teflon tubing are fixed with adhesive tape. (left) Finally a vacuum bag is prepared to shut off the ply stack from the outer world. The bag is fixed with adhesive paste. The fibers are let through the paste in order to monitor the curing cycle. (right)

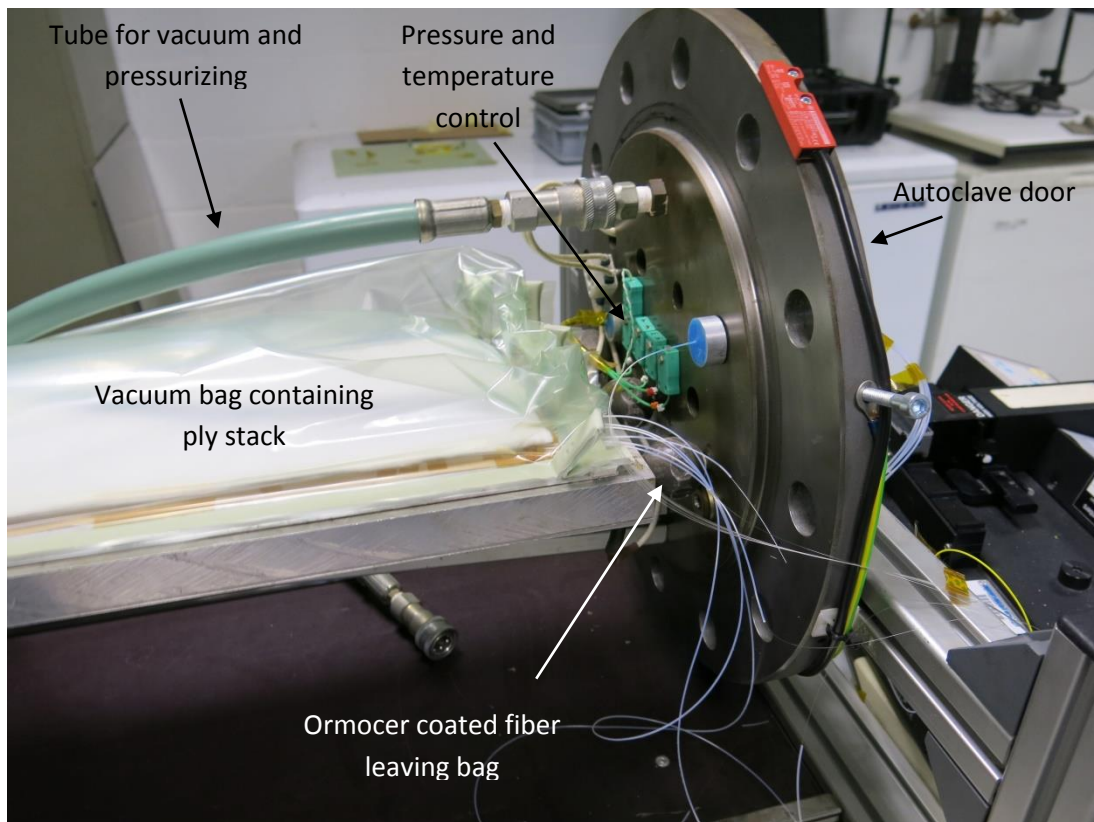


Figure 44: The ply stack inside the vacuum bag is put into the autoclave. All optical fiber are spliced to optical fibers already in place which connect the inside of the autoclave to the outside. The fibers coming out of the autoclave are again spliced to APC-pigtails for easy connection to a Micron Optics interrogator.

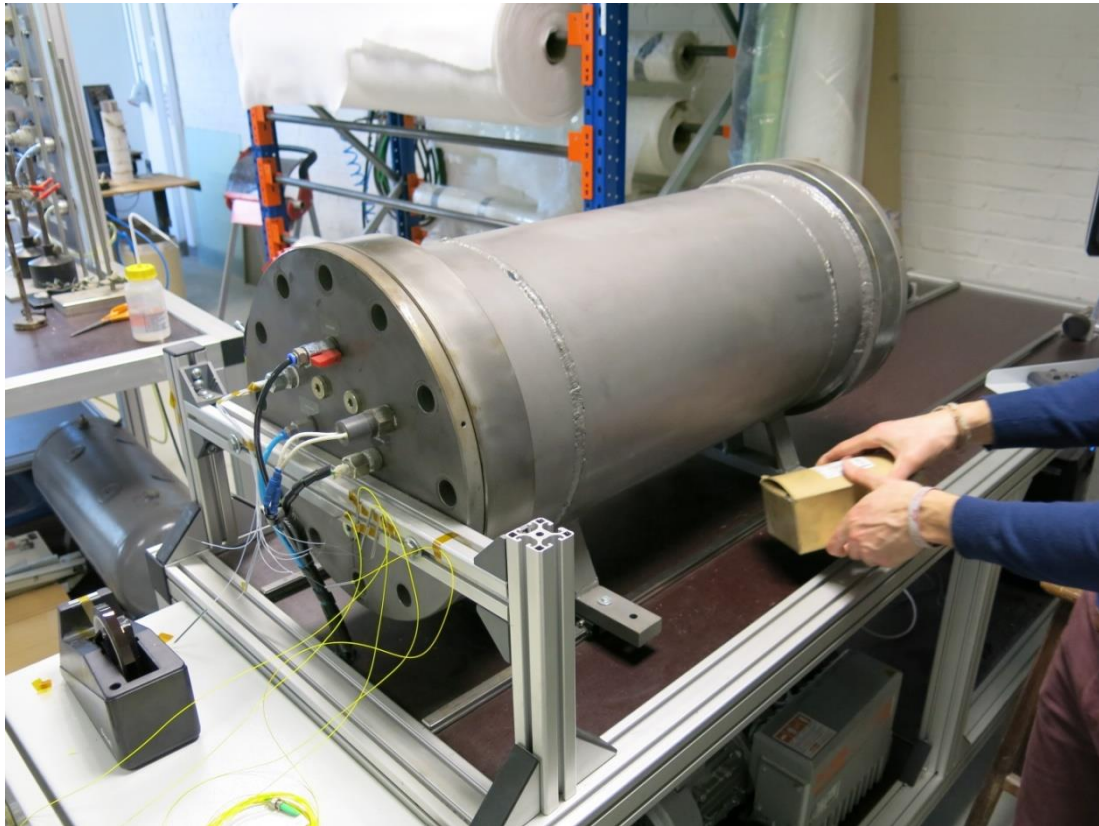


Figure 45: When everything is placed in order and the vacuum of the bag is tested, the autoclave is closed and the curing cycle can begin.

The autoclave can now be closed, as is shown in Figure 45. The cure cycle can be started and the monitoring of the process can commence.

3.5. Cure monitoring

During the overnight curing cycle we monitored the process with the MOFBGs inside the composite plates. Three of the sensors were interrogated with a Micron Optics interrogator (see section 4.3) and the data was stored on a PC left running on the site during the night. Because no post-mortem analysis (see section 3.7) was performed on all of the MOFBGs, the orientation of the MOFs will be treated as their target orientations (being 0° and 90° as in Figure 16).

The peak shifts for all the MOFBGs are shown together with the temperature measured by the thermocouple of the autoclave in Figure 46. All peaks seem to shift simultaneously to higher wavelengths when the temperature increases and vice-versa. When the actual orientation of the MOFs inside the CFRP composite plates are known this raw data can be used to perform strain-transfer calculation and obtain the 3D strain in the composite during the curing. This will allow to visualize the different phases the composite goes through during curing (see section 2.6.3). This was however not in the scope of this text, we only want to show here the temperature sensing abilities of our MOFBGs. The data are raw data determined by the peak detection methods of the SM125 itself, this can mean very small changes in peak shifts or peak separation are not visual.

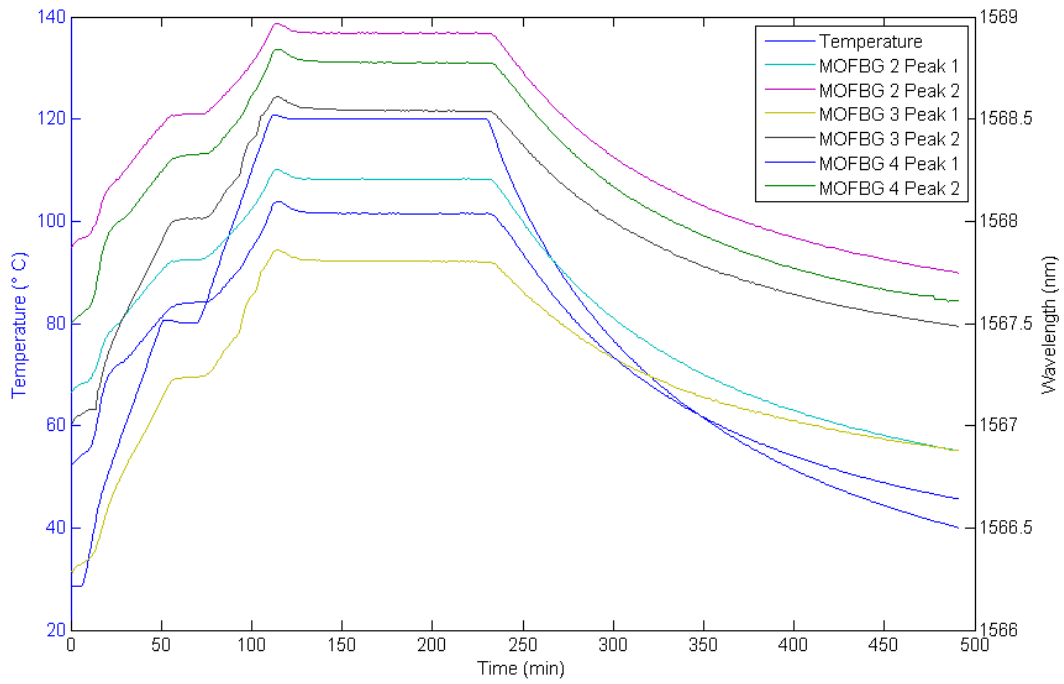


Figure 46: The temperature change measured with the thermocouple of the autoclave and the peak shifts of the three monitored MOFBGs.

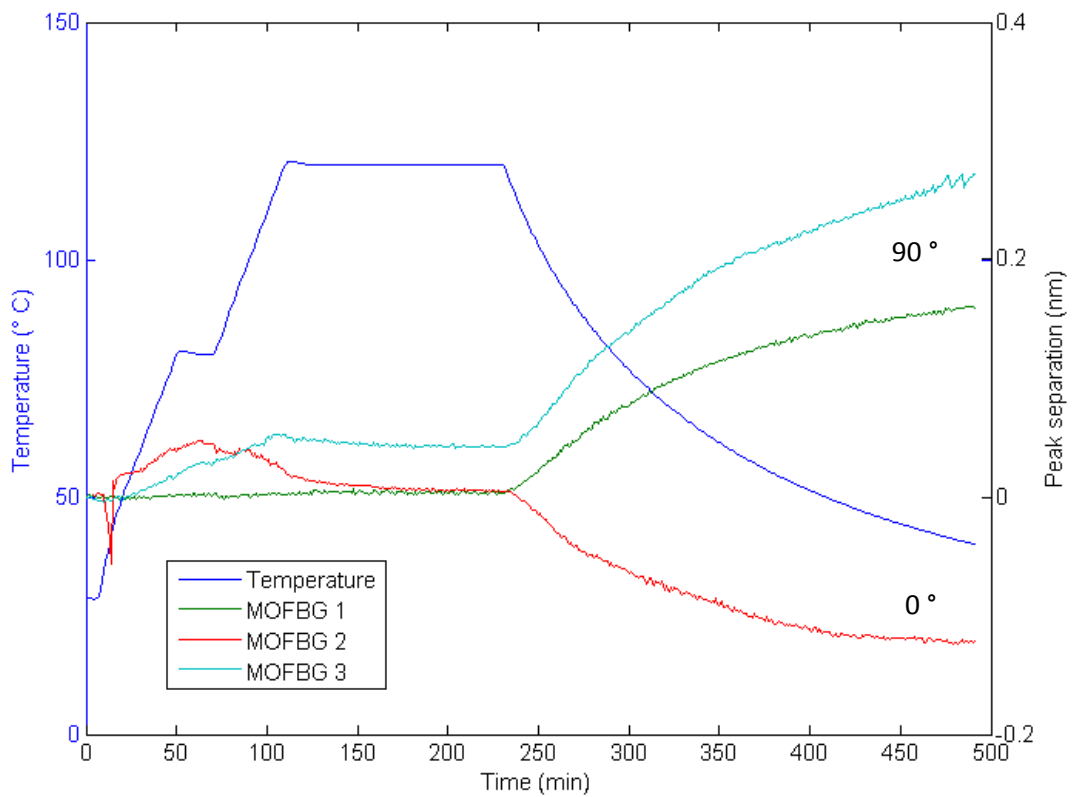


Figure 47: The temperature of the curing process measured with the thermocouple of the MOFBG and the peak separations for each of the MOFBGs

Figure 47 shows the peak separation of the MOFBGs together with the temperature course measured by the thermocouple of the autoclave. Due to the peak detection method of the SM125, small changes in separation are not visible. This prohibited of visualizing the first transition phases of the composite curing. A thorough peak detection analysis could solve the precision of the peak separations, but this was not in the scope of this thesis. Stages that are distinguishable by the peak separation are the isothermal curing stage and the consolation stage.

The isothermal curing stage occurs when the temperature is constant. The slopes of the peak separation are constant here. During this stage the resin evolves from a rubber to a solid material. The consolation stage starts when the autoclave heating is turned off and the temperature starts to fall. During this stage the composite cools down and the residual strain develops within the laminate.

The peak separations we measured are similar to the ones Dr. Camille Sonnenfeld obtained in her PhD. The peak separation here are smaller, however, probably because the orientation of the MOFBGs was not actually 0° and 90° , but something in between.

When the curing cycle was finished, the embedded MOFBGs were all six again characterized with the OSA/ASE setup (see section 4.1). The MOFBGs targeted for orientation at 90° show an average wavelength shift of the left peak of -0.848 nm and of the right peak of -0.619 nm. This means the peak separation has increased with 0.229 nm on average. The standard deviations were respectively 0.0413 , 0.0204 and 0.0213 . Figure 48 shows the spectrum of MOFBG 3 before and after embedding.

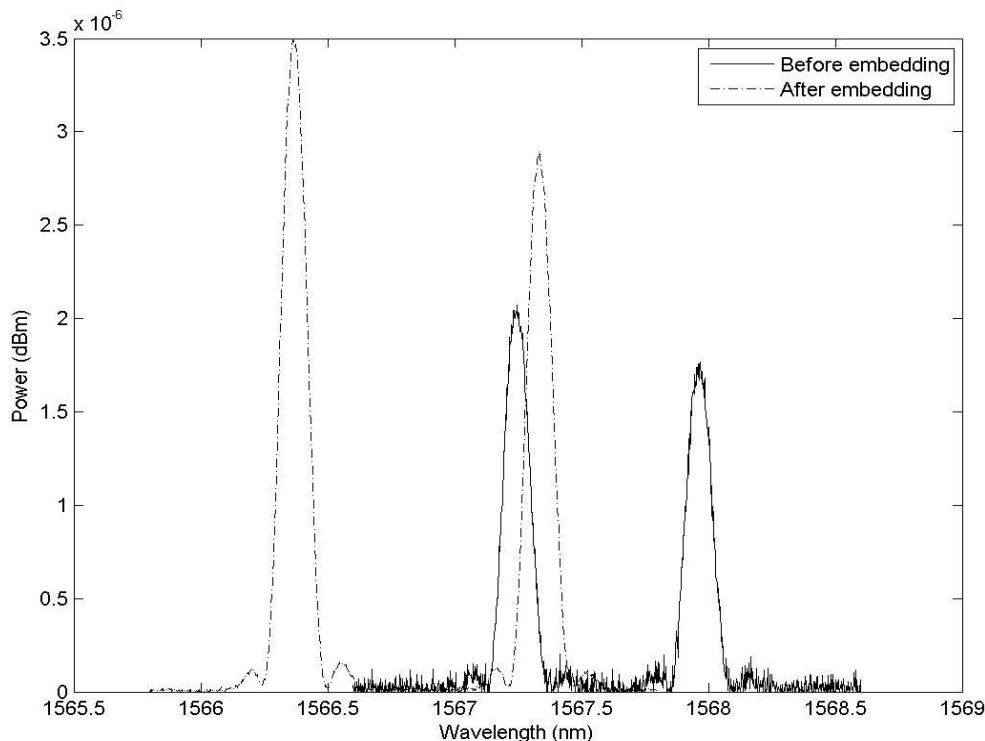


Figure 48: The pre (full line) and post (dashed line) embedding reflection spectra of a MOFBG oriented at a target angle of 0°

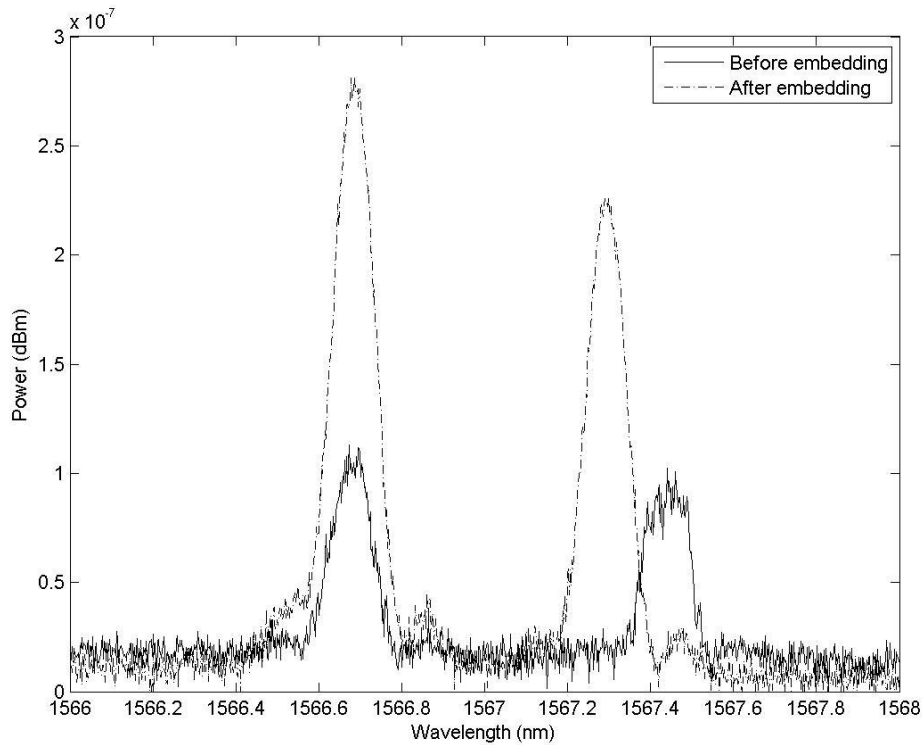


Figure 49: The pre (full line) and post (dashed line) embedding reflection spectra of a MOFBG oriented at a target angle of 90°

The MOFBGs targeted for orientation at 0 ° show an average wavelength shift of the left peak of $5 \cdot 10^{-5}$ nm and of the right peak of -0.161 nm. This means the peak separation has decreased with 0.162 nm on average. The standard deviations were respectively 0.00275, 0.00555 and 0.0028. Figure 49 shows the spectrum of MOFBG 2 before and after embedding.

The peak separations in Figure 48 and Figure 49 are consistent with the SMF125 measurements for a 0 ° MOFBG the peak separation decreased, and for a 90 ° MOFBG it increased, due to the residual strains inside the epoxy matrix.

The peak shifts are in both cases to the left, which would result in a compression along the fiber direction or a decrease in load on the slow axis of the fiber. Comparing this to previous work [1] does not yield the expected result. An elongation of the fiber length or a load in the transversal slow axis direction was expected.

3.6. End result

When the curing cycle was completed, the autoclave could be opened and the vacuum bag removed. This is shown in Figure 50. This figure also shows the epoxy resin that has leaked into the fabric. This epoxy is now hard and has to be removed. In Figure 51 the state of the MOFs coming out of the plates is shown. All fibers survived the curing cycle. Figure 52 shows the finished plate. The only thing remaining was sawing the plate in to two pieces of equal size.

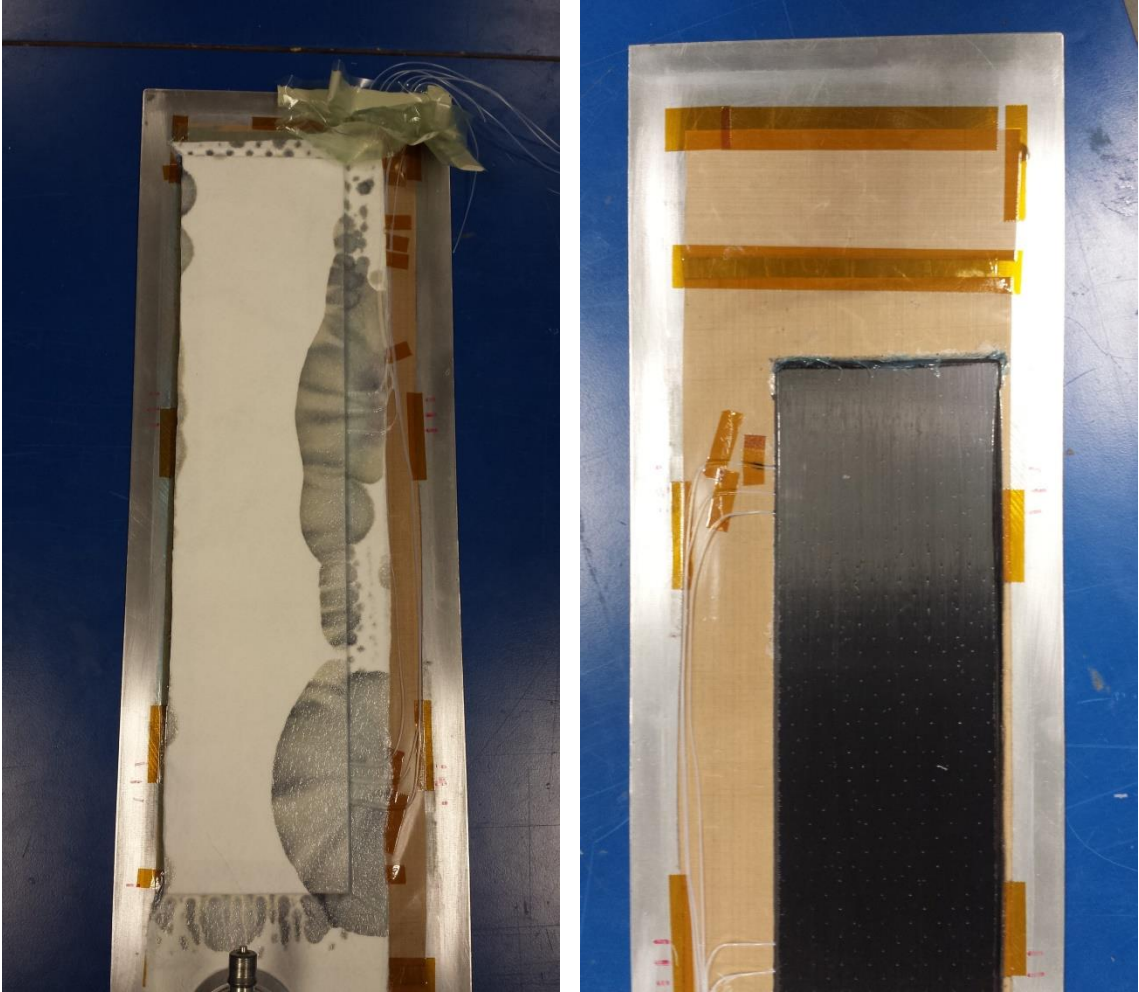


Figure 50: Opened vacuum bag. The fabric did his job absorbing most of the resin residue, but still some ended up next to the composite plate (left) The residue fabric removed shows the composite plate as a finished part. The shiny surface shows the vitrification stage (right)

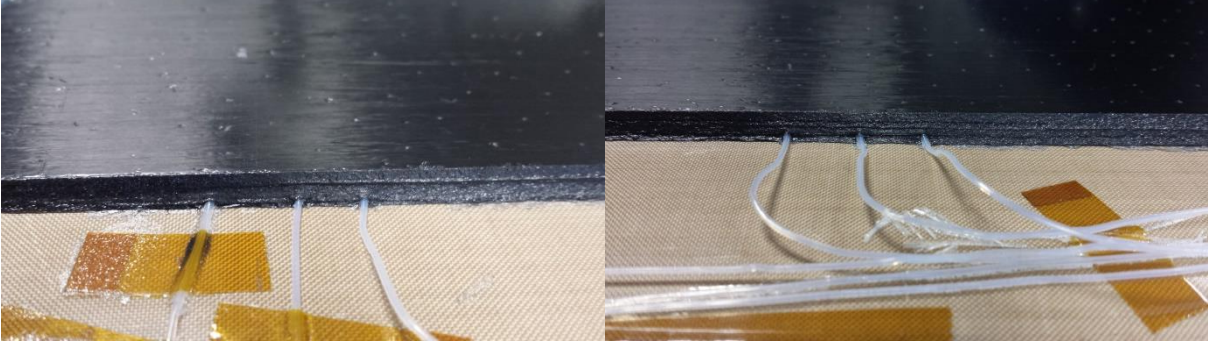


Figure 51: the optical fibers in their protective Teflon tubing coming out of the side of the hardened composite plate. All fibers survived the curing process.

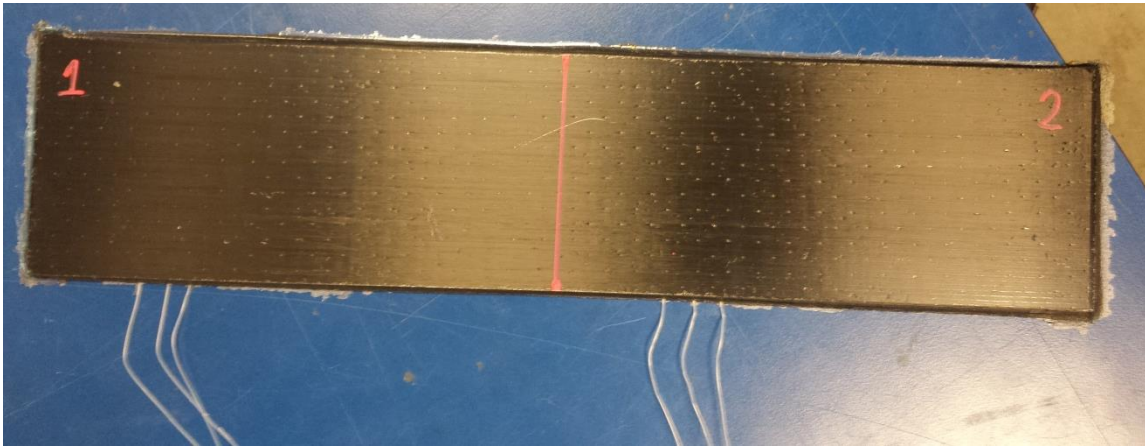


Figure 52: The complete carbon fiber reinforced composite plate with the position of the grating marked. The plate is divided into two parts and the parts are numbered to identify the FBGs. At the line drawn line, the plate will be sawed in half. Some of the residue of resin is still visible at the sides of the plates and will also be sawed off.

3.7. Post-mortem analysis

When the impact measurements were finished, the plate containing the UMon samples which was the most used for measurements, was sawed into pieces to determine the real orientation of the butterfly MOF. The orientation of the MOF could have tilted during the embedding or orientating of the fiber, and not be in the predicted 0° or 90° position. The other composite plate was kept as reserve, in case of necessary complementary measurements. In this section we will describe this post-mortem analysis.

3.7.1. Ultrasound C-scans

The damaged plate was scanned with an ultrasound C-scan to determine damage locations. To perform these scans, the composite plate was clamped into a holder and placed into a water reservoir, as shown in Figure 53. A sound source and detector were positioned above and below the plate on a U-frame holder. This holder was mounted in a computer controlled translation stage. This allowed the motion of the source and detector to be programmed in a predefined horizontal region and also the step size of the stage can be chosen. The source also acts as a detector and vice versa to do the measurement in two directions.

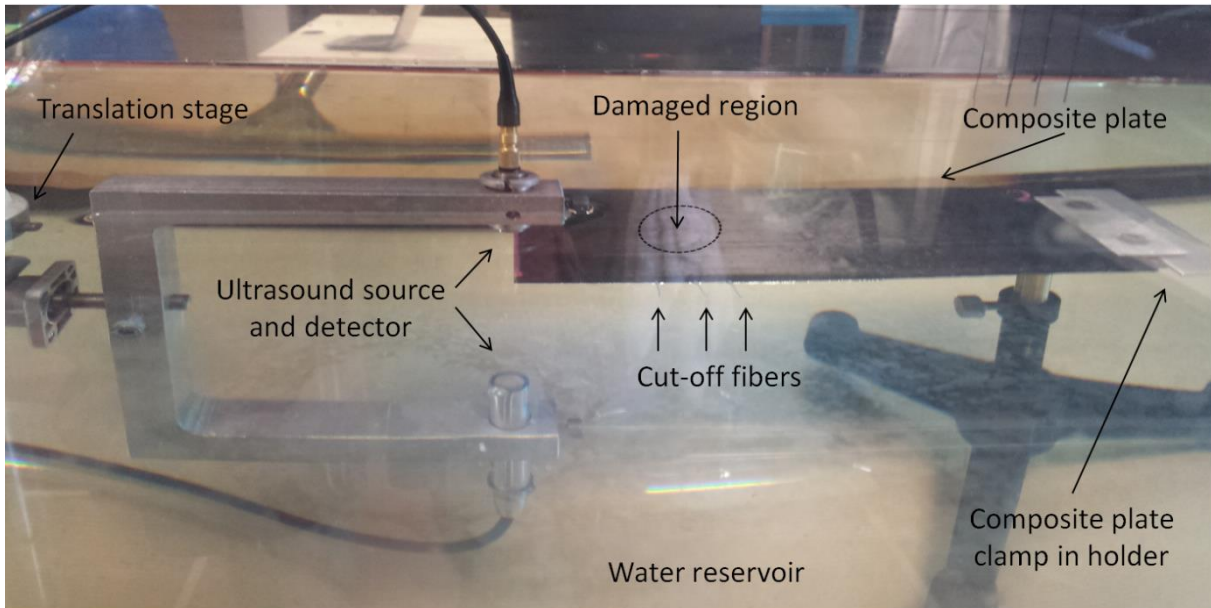
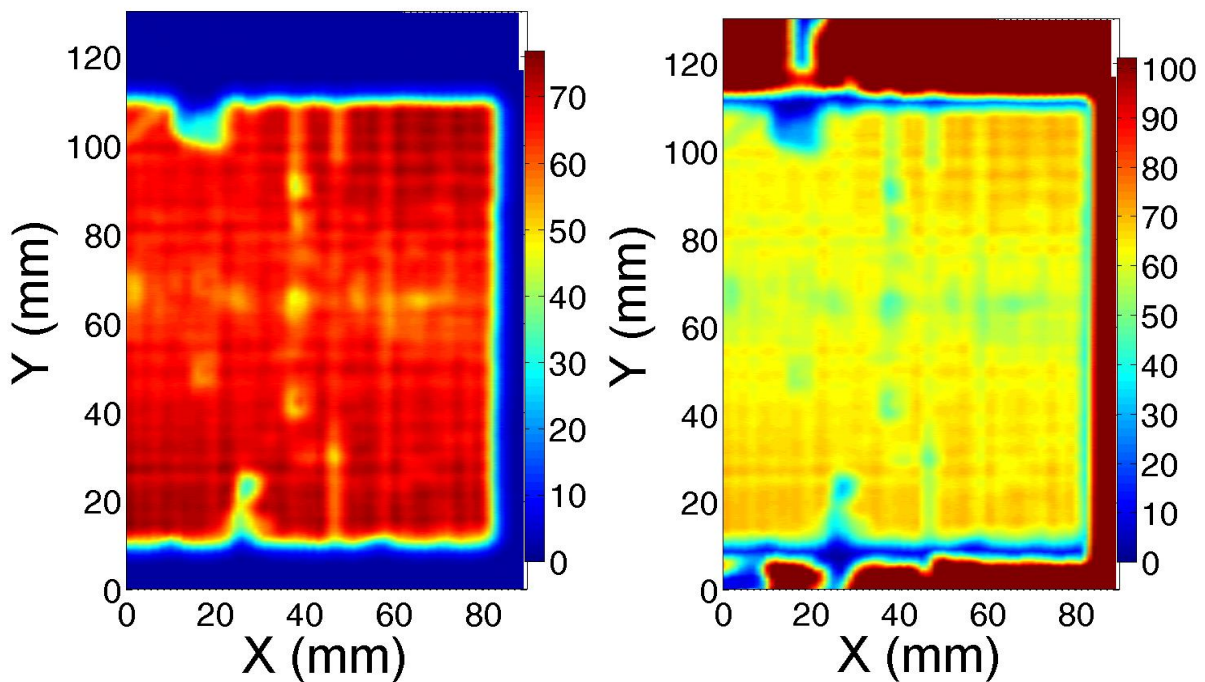


Figure 53: Ultrasound C-scan setup. The damaged composite plate is clamped in a holder and the whole is put into a water reservoir. A sound source sends an ultrasound wave through the composite structure, which is detected by a hydrophone. The detector can also act as source and vice versa, to do the measurement in two directions. Both detector and source are placed above and below the composite plate, on a holder that is mounted on a translation stage. This translation stage is automated with a computer so the X- and Y-extend of the translation as well as the step increase can be programmed.

These C-scans were performed for the two plates containing the IPHT FBGs before impact as a reference. The results of these scans can be found in Figure 54. The position of the fibers and their tubing can be seen at the outside as well as the inside of the plates. Some larger imperfection as air holes or the glue droplets added to the fibers for orientation can be noticed. Also the fibers outside the plates are noticeable with the C-scan.



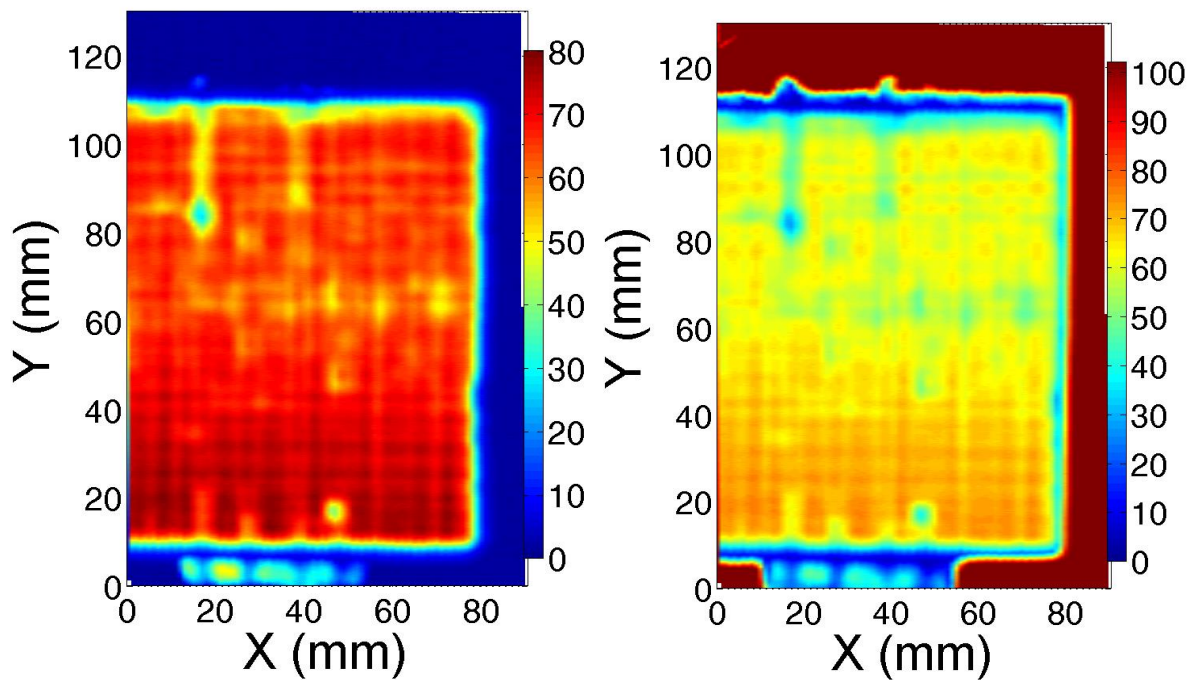


Figure 54: The ultrasound C-scan results for the two plates containing the IPHT FBGs, before impact measurements were conducted. The top panels show the plate AssDoc1 and the bottom panels show the plate AssDoc2. The left panels show the propagation of the sound from top to bottom and the opposite is shown in the right panels. Imperfections as the intrusive fibers, the location of air holes or the glue droplets orienting the fibers can be noticed. The main idea of these images is to compare them with the same images after impact measurements have been performed, and identify delaminated areas that were not previously there.

The ultrasound C-scan was also performed on one of the two composite plates containing MONS FBGs on which impact measurements (see section 5.3) were already performed. In the circled area the impacts occurred, and clearly some damage is visible, probably in the form of delamination.

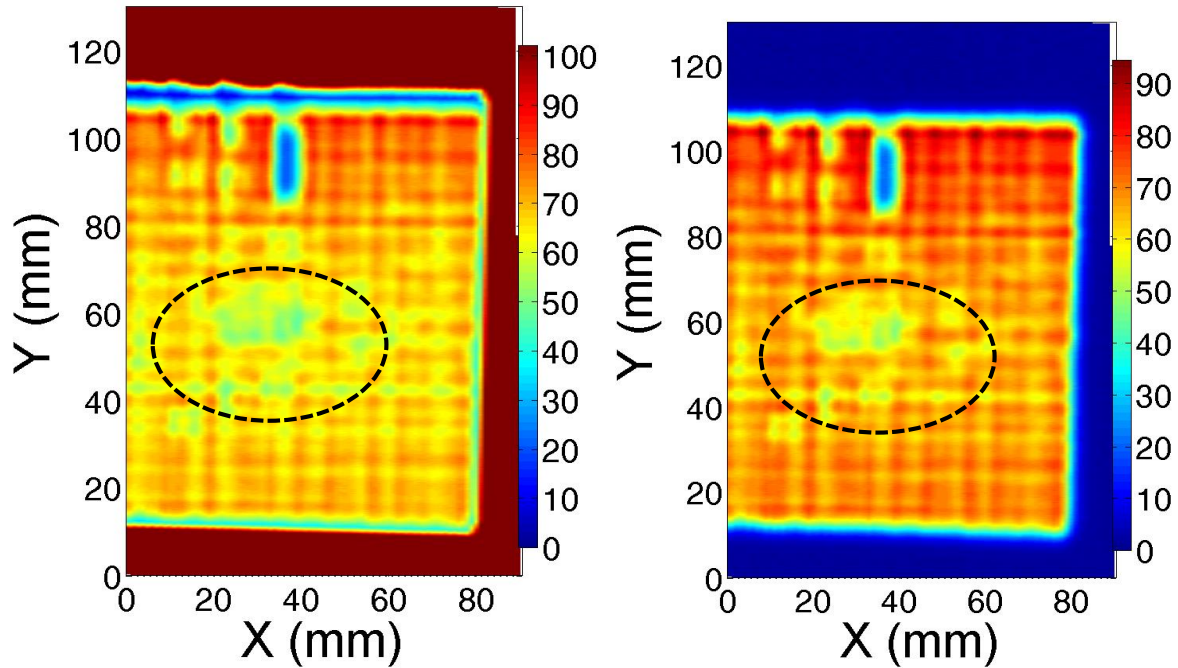


Figure 55: The result of an ultrasound C-scan of the composite plate number 2 holding the UMONS FBGs. Both panels show the same plate, but in the left the sound goes downwards and in the right upwards. X and Y axes show the distance travelled by the translation stage while doing the scan. The color scheme denotes the percentage of sound transmitted. Dark red meaning all the sound is passed (eg. in the water surrounding the plate and dense regions inside it) and dark blue denotes locations where no sound is passing. The latter can be due to imperfections which occurred due to the embedding (eg. the glue droplets or fiber tubing) or due to delamination damage by impact. In the center of the images clearly some delamination is present, when the area circled is compared to the area surrounding it.

3.7.2. Orientation of fibers by polishing and microscope examination

The orientation of a PCF fiber embedded in composite material is important when one has measured FBGs wavelength shifts, but wants to convert these to actual strains and stresses inside the composite material according to the strain-transfer theory explained in section 2.7. The orientation of the fibers is targeted in advance as explained in section 3.3.1. However, during this orientation procedure and the embedding of the fiber the orientation of the fiber can change. When the impact experiments were performed we performed an analysis on the orientation, following the steps explained below.

The first step is to cut the plate where the fibers are located. To be sure of the orientation of the butterfly structure along the entire embedded fiber, we sawed the plate into pieces according to Figure 56. The pieces of which the orientation would be determined we numbered one to three and a mark (^) was added at the side where the orientation would be examined. When the plate was sawed along these lines, the three numbered pieces were carefully positioned into a holder. While trying to keep the pieces parallel and standing upright we poured a liquid epoxy in between the pieces. This second step can be seen in Figure 57.

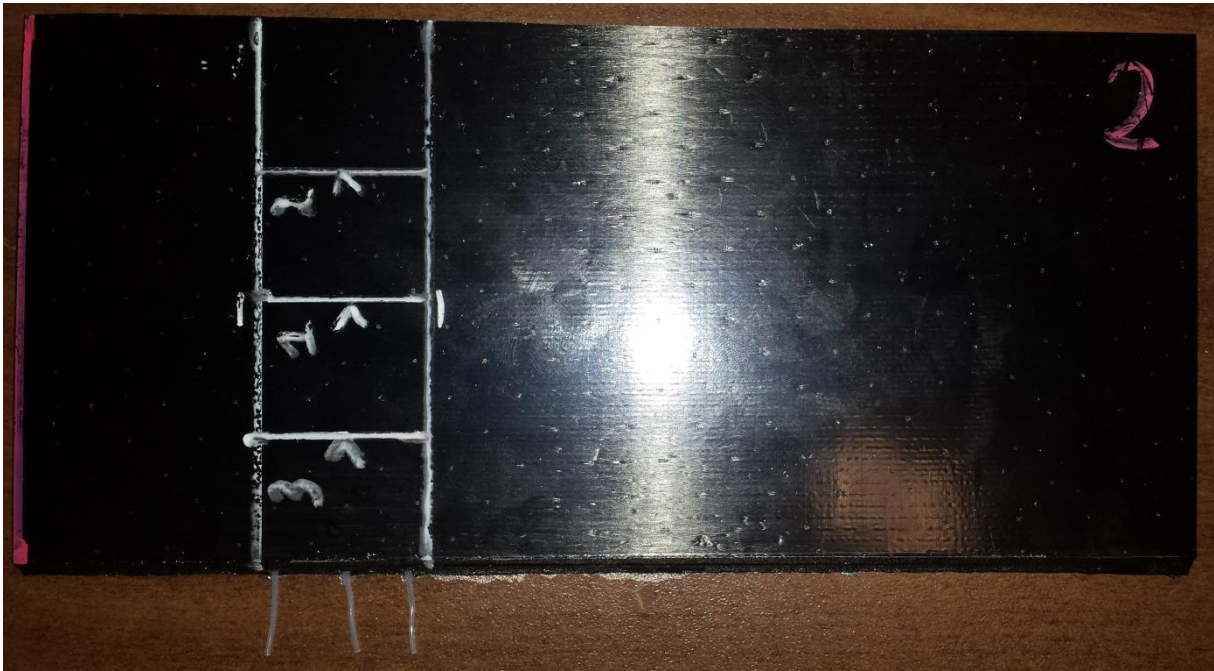


Figure 56: The composite plate containing the embedded MONS FBGs. The tubed fibers can still be seen exiting the plate at the bottom. Lines were drawn parallel with the three fibers to include them all in the three marked rectangles numbered one to three. These three rectangles will also be sawed out. The orientation of the fibers will accordingly be investigated at three different positions inside the composite marked with a (^).



Figure 57: A holder holding the three pieces of composite plate surrounded by a liquid and transparent epoxy.

The epoxy needed to harden overnight, so the polishing process was started some days later. When the (now completely solid) cylinder was taken out of the holder seen in Figure 57, it was ready for polishing. For the polishing of the epoxy cylinder, the steps in the flowchart shown in Figure 58 were followed.

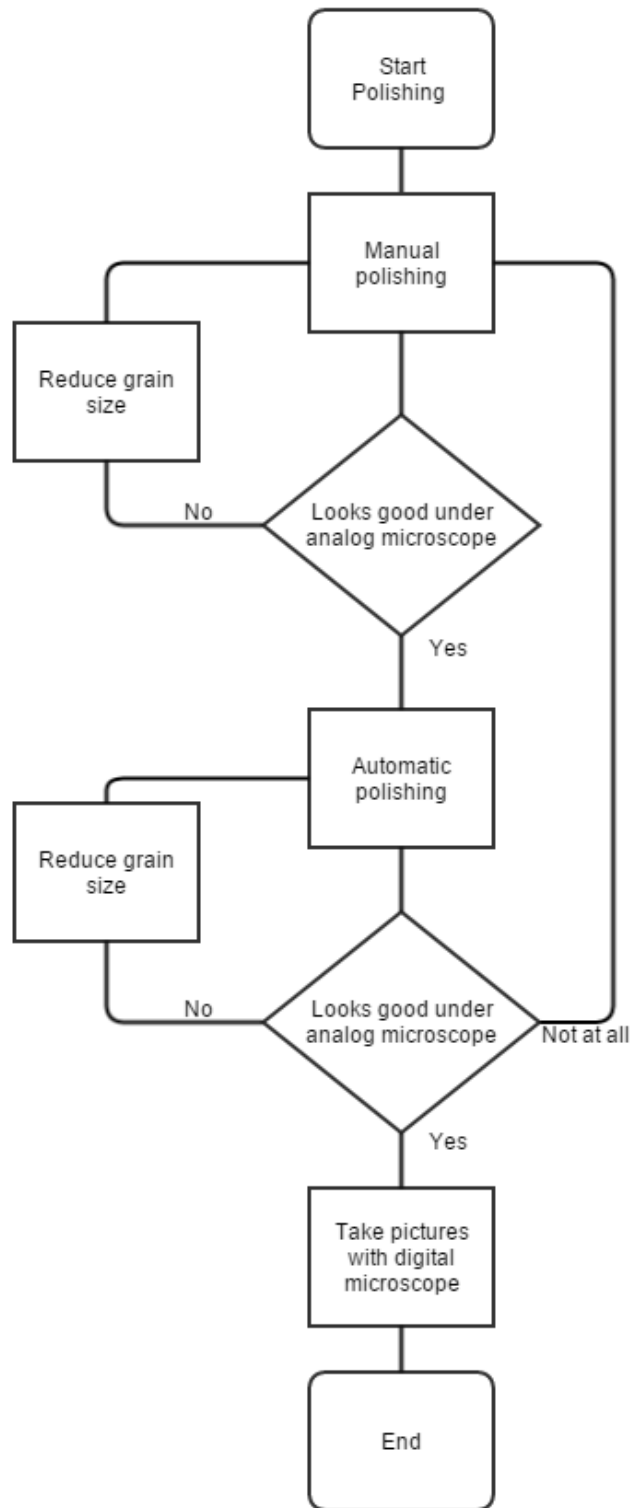


Figure 58: Flow chart displaying the steps followed during the polishing procedure. First a manual polishing was done with different plates, each time reducing the grain size after inspection with an analog microscope. When the polished surface looked good under the analog microscope, we started the automatic polishing. This also included a few steps where the grain size was decreased until a clear image of the butterfly cross section was obtained. If so, a picture was taken with the digital microscope.

First we polished manually with the Struers LaboPol-21. The tables rotate and rinse water constantly while we pressed the epoxy cylinder to the grain plate. Many plates of different grain sizes were

used, starting with the largest grain size (at first to polish off the transparent epoxy and reach the composite pieces) and going down in size each time. The different plates were MD320, MD800, MD1200, MD2400 en MD4000, the number indicating the inverse of the grain size. After some grain size polishing the polished surface of the epoxy cylinder was investigated with an analog microscope. According to the roughness of the surface and the visibility of the fibers, a choice was made to keep polishing with the same grain size, reduce in grain size or switch to automatic polishing.



Figure 59: First manual polishing technique: a Struers LaboPol-21 polishing table with adjustable grain size polishing plates. A constant adjustable supply of water rinses the plate.

The epoxy cylinder underneath the analog microscope is shown in Figure 61 left. To keep the top surface of the cylinder parallel with the translation of the microscope, the cylinder was mounted on a metal surface with a piece of gum and was pressed onto the gum by two horizontal plates. This blue gum can also be seen in both panels of Figure 61.

When the manual polishing looked good enough underneath the analog microscope, we switched to automatic polishing with a Struers Tegramin-30. For the settings we used those programmed by Camille Sonnenfeld during her PhD thesis. Three different steps were used: largo, dac and nap. Each step reduced the grain size of the polishing plate and the size of the diamond grains dissolved in the liquid added. In Figure 60 the green largo plate is shown for example. The black tube regularly adds drops of diamond paste lubricants. Three types of these suspensions were added: DiaP, Mol and Dac. Table 8 summarizes the parameters for all three steps.



Figure 60: Second automatic polishing technique: a Struers Tegramin-30 automatic polishing machine with adjustable spinning sheet and adjustable liquid supply containing diamond or other grains.

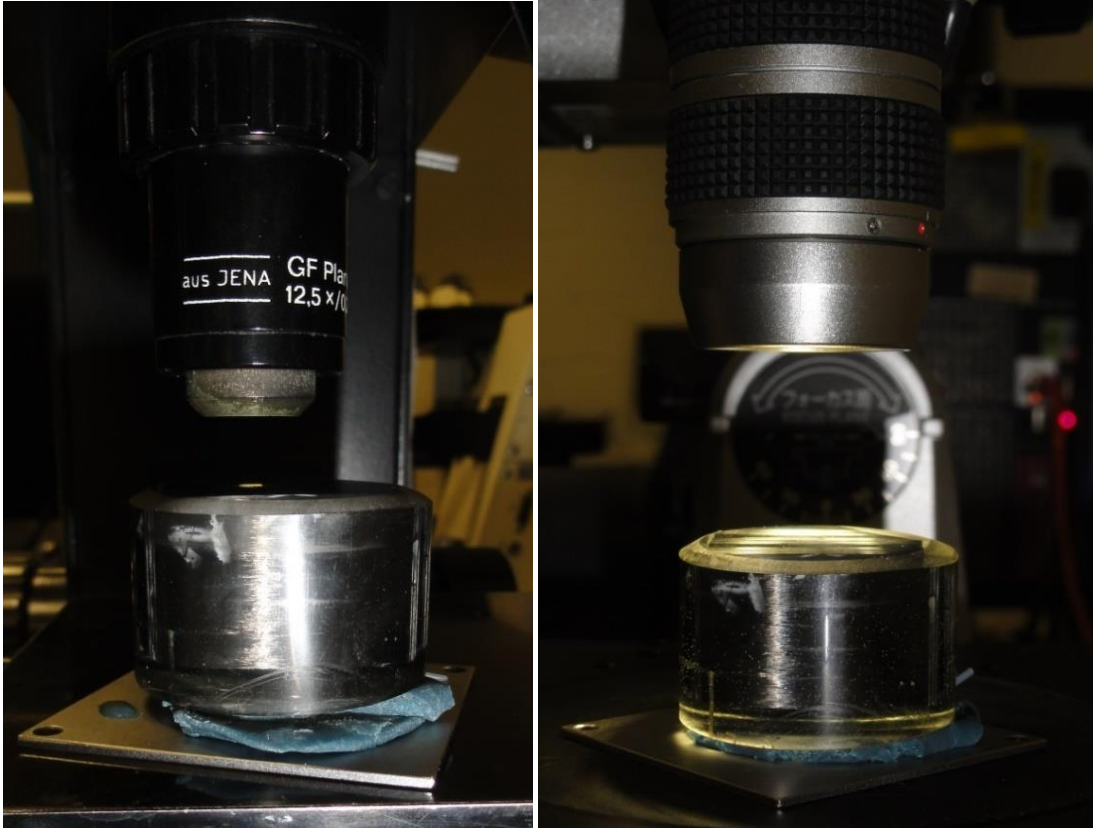


Figure 61: An analog light microscope with interchangeable objectives was used to inspect the fiber cross section visibility in between polishing steps to guide the polishing procedure (left). The VHX-2000 digital microscope was used to take pictures of the polished surface of the composite plate with the orientation of the fibers relative to the composites borders (right). The polished transparent epoxy cylinder was pressed onto a metal substrate with a piece of gum. This

allowed the top surface of the cylinder to be almost parallel with the ground plane of the microscopes and so translation of the substrate would be easier to view under the microscope.

Table 8: Summary of the three grinding steps used for the automatic polishing by the Tegramin-30. The table includes the name of the process, the grain size, the used suspension liquid and the typical time for the process.

Name process	Grain size	Suspension	Typical duration
Largo	9 μm	DiaP, Mol	5 min
Dac	3 μm	DiaP, Mol	2 min
Nap	1 μm	DiaP, Dac	1 min

As was shown in Figure 58, the time durations shown in Table 8 are just guidelines. If the polished surface still looked to rough when examined with the analog microscope, some steps were repeated several times and the duration was sometimes even set to 15 minutes.

When eventually all fiber cross sections were clearly visible under the analog microscope, and their orientation could be determined, the last step is to put the polished cylinder underneath the VHX-2000 digital microscope and take pictures of the butterfly PCF such that their orientation with respect to the borders of the composite pieces can be measured.

It is very important to remember the position of the front and back side of the composite plate in order to determine the angle correctly. Therefore the side of the plate on which the impact was performed, this is the side where the numbers were added, was positioned towards the microscope operator. This means these numbered sides are oriented towards the bottom side of the pictures taken of the polished surface.

3.7.2.a Orientation of butterfly PCFs

Figure 62 shows the orientation of the butterfly PCF with respect to the surrounding composite plate. [1] If the 'wings' of the butterfly are oriented parallel with respect to the composite plate, the orientation of the fiber is said to be 0° . When the fast axis of the fiber is orthogonal (ie. vertical) with respect to the edges of the composite plate, the orientation is said to be 90° .

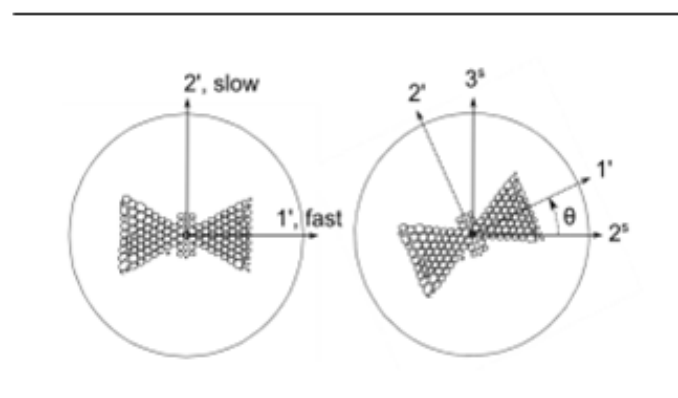


Figure 62: The orientation of the butterfly structure in the PCF cross section relative to the borders of the composite plate. The orientation is determined by the angle between the fast axis (along the 'wings' of the butterfly structure) of

the PCF and the horizontal axis parallel with the borders of the composite plate (shown as two horizontal parallel lines, not to scale with the fibers). [1]

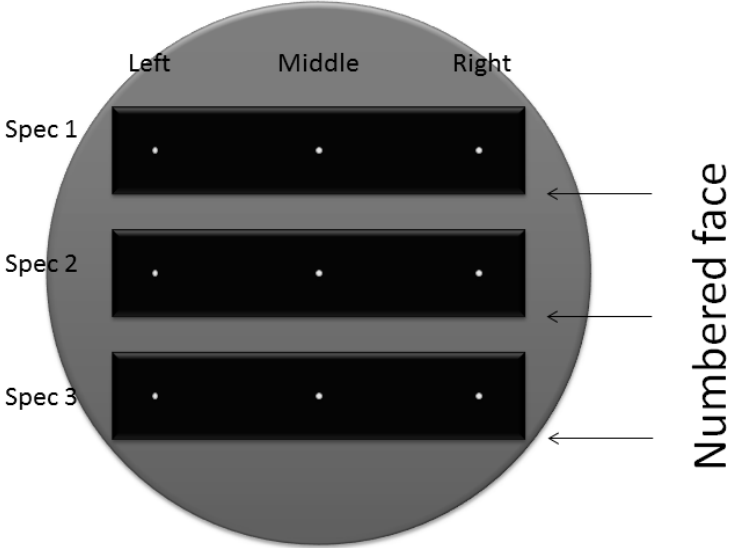


Figure 63: Top view of the polished epoxy cylinder containing the pieces of CFRP as in Figure 56. The pieces are here numbered as Spec 1 to Spec 3, consistent with Figure 56. The sides containing the written numbers denoted as numbered faces. The MOFs are labeled left, middle and right for each specimen.

Figure 63 shows the top view of the polished cylinder containing the specimen. The numbered faces are at the bottom sides of the specimen, as denoted with arrows. It is on this side that the impact occurred. In what follows, the orientation of the MOF butterfly structure was measured with respect to the position of the specimen in Figure 63 and with definition of the angle θ as in Figure 62.

In Figure 64 a picture by the digital microscope is shown. It shows the different ply layers: in the middle four layers of 90° plies, sandwiching the MOFBGs. The carbon fibers are perpendicular to the polished edge. Covering those plies are two layers (two on top and two below) of 0° oriented plies, their carbon fibers can be seen to be parallel with the polished edge. Then again two layers of 90° and two layers of 0° plies, above and below, complete the CFRP plate.

When zoomed into a MOFBG like the one in Figure 64 with the digital microscope, Figure 65 is obtained. For each MOFBG such a detail view was saved. From these pictures, we determined the orientation of the structure of the six different fiber cross sections, with respect to the horizontal axis, which follows the ply edges. The angles of orientation are summarized in Table 9.

Table 9: Orientation of the MOF cross section structure at three different fiber locations and for three different fibers.

	Left MOFBG	Middle MOFBG	Right MOFBG
Spec 1	32 °	109 °	118 °
Spec 2	30 °	111 °	115 °
Spec 3	33 °	109 °	114 °
Average	31.67 °	109.67 °	115.67 °

Standard deviation	1.25	0.94	1.70
Target orientation	0 °	90 °	90 °

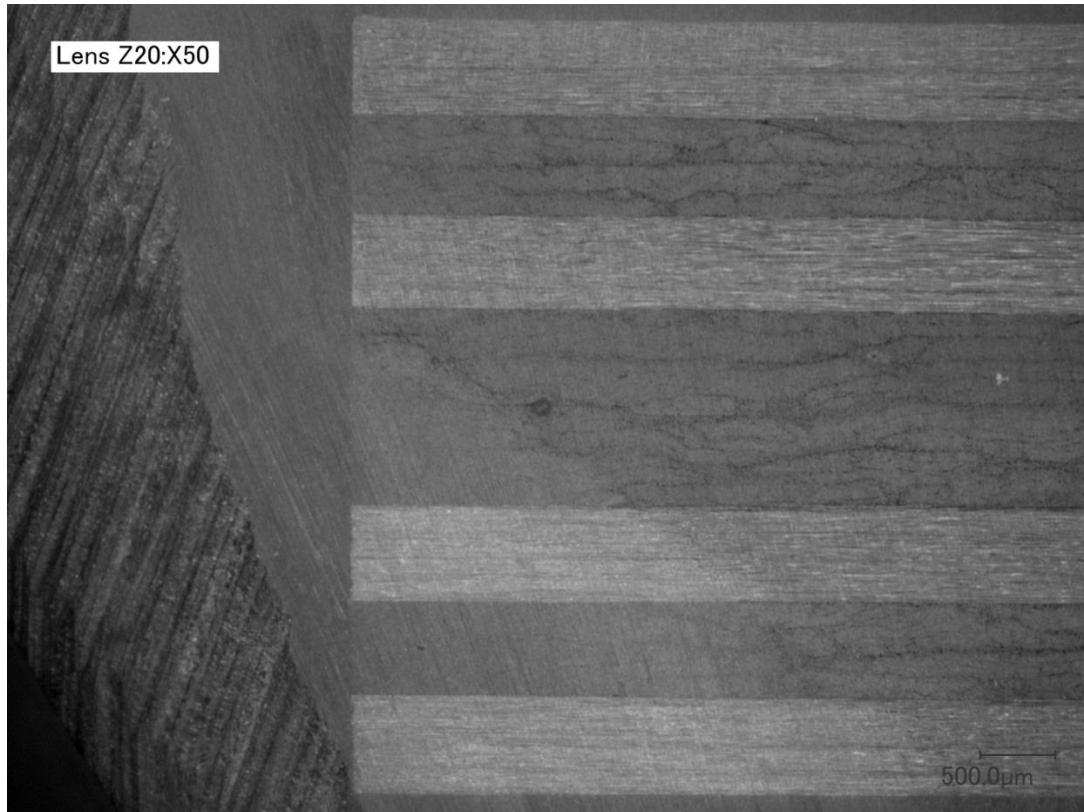
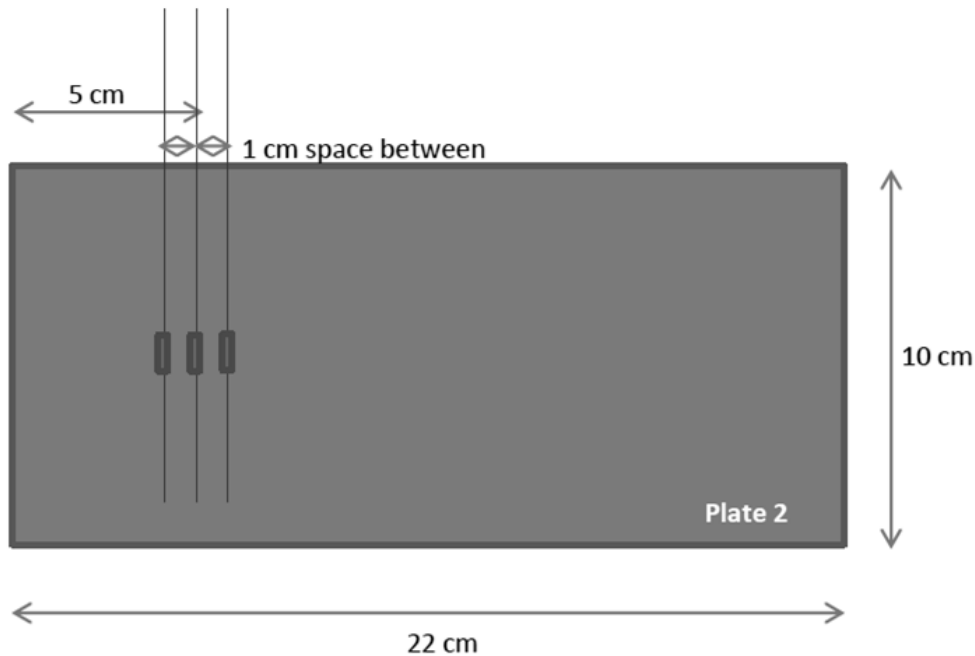


Figure 64: The specimen Spec 1, with the left fiber centered. The different ply orientations of the CFRP are clearly visible. The impact occurred on the specimen at the bottom of this picture.



Figure 65: A zoom of the left fiber in CFRP piece Spec 1. From these detail pictures the orientation of the fiber was determined with respect to the edge of the CFRP plates (ply edges).

A deviation of 31.67° from the targeted 0° orientation was found for an average of three measurements, with a standard deviation of 1.25. For the targeted 90° orientations, a deviation of 19.67° and 25.67° was found for the middle and right fiber, with standard deviations 0.94 and 1.70 respectively. The angle of orientation seemed to be quite consistent over the three positions along the fiber length.



With the real orientation of the MOFBGs known, this can be used for calculating the strains inside the CFRP with the strain transfer method elaborated in section 2.7.

3.8. Conclusion

In this chapter we elaborated on the preparation of the MOFBGs in composite CFRP plates. Two set of MOFBGs were prepared. One set of six fibers was provided of a FBG with a scanning phase mask technique, and embedded in composite CFRP plate for dynamic measurements with the FBG-scan (see section 2.3.1 and 5.3). A second set of 11 samples was provided of two FBGs of a custom wavelength. These wavelengths were in the range of the VCSEL-based interrogator described in section 4.4.

For preparing the MOFBGs, we spliced the MOF to SMF with a unique splicing program and obtained losses of less than 3 dB per splice. These losses are no problem for interrogation of FBGs. We used an orientation procedure to orient the microstructure is the precise way necessary for measuring 3D strains.

We successfully embedded the MOFBGs in a CFRP composite component. During the cure cycle of the epoxy resin a cure monitoring was performed. We were able to show that both peaks on an MOFBG were able to follow the temperature profile of the autoclave process. **With the peak separation of the MOFBGs, we were able to follow the process of consolidation**, when a residual strain builds inside the composite and the material cooled down. **In this way we also showed the ability of the MOFBGs of measuring strain without any temperature influence.**

On the composite component that was used for measurements a post-mortem analysis was performed. With an ultrasound C-scan we showed damage in the plate at the location of the impacts. The actual orientation of the fibers was also determined, and yielded a large error with respect to the target orientation. Possible explanations for this is are 1) a less precise orientation method was used 2) the orientation of the fibers changed during the embedding.

To improve on this orientation method we explored a new way of looking at the microstructure of a MOF and fixing it. This was done with a micro-CT scan, however the scan used showed dimensional difficulties and could not be used. The method itself can certainly be further investigated, and may provide a more precise orientation method.

4. Interrogation methods

There exist many different types of interrogation for measuring the Bragg wavelength of a fiber Bragg grating. One typically has to balance the precision and resolution of the system with the dynamic range and interrogation speed.

In this chapter we will firstly explain the OSA/ASE setup in section 4.1. Next, in section 4.2 the spectrometer based FBGS FBG-scan 700/704D is discussed. In section 4.3 we then elaborate the tunable laser based Micron Optics SM125.

Finally, in section 4.4 we will discuss the working mechanism and characterization of a custom build miniaturized VCSEL-operated interrogation method especially designed for dynamical measurements.

4.1. OSA/ASE Interrogation

The first interrogation setup discussed in this chapter is the one that was used for the characterization of the reflection spectra of the gratings. This because the optical spectrum analyzer (OSA) is the most precise way to determine a spectrum, there it is designed to have a small resolution (0.01 nm). The setup is shown in Figure 66 [36], [37]. A ThorLabs ASE-FL7004 source is used to illuminate the fiber Bragg grating through a circulator., that couples light from gate 1 to gate 2, from gate 2 to gate 3. So, when a part of the light is reflected on the grating (see section 2.2) it will be guided from gate 2 to gate 3, where an ANDO Electric AQ6317 OSA is connected to measure the optical power in function of the wavelength of the light.

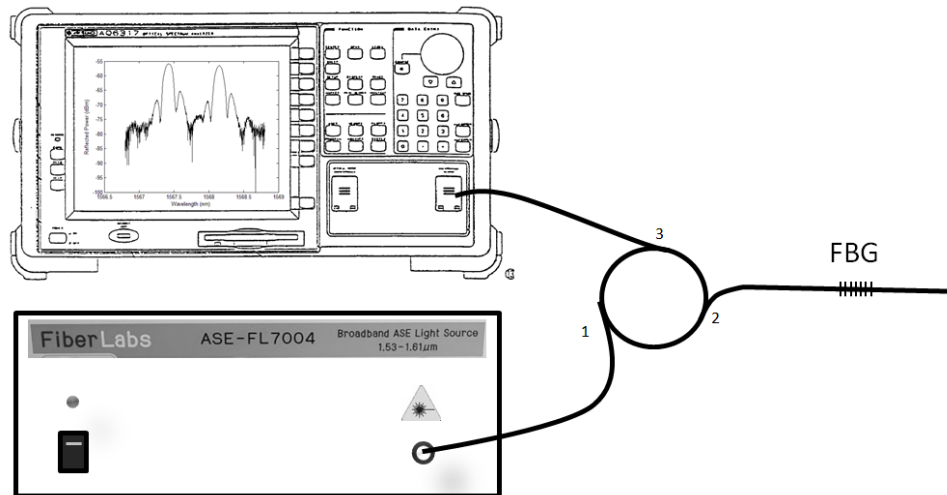


Figure 66: Typical characterization setup used in this thesis. The fiber Bragg grating is interrogated through a circulator with an optical spectrum analyzer (OSA) and an amplified spontaneous emission (ASE) light source. The broadband light of the ThorLabs ASE-FL7004 (1.53 – 1.61 μm) is guided through the circulator to the MOFBG. The light reflected by the FBG will be guided again through the circulator to the ANDO Electric AQ6317 optical spectrum analyzer. [36], [37]

The OSA will measure the reflection spectrum with a monochromator that is shown in Figure 67. The incident light is unpolarized, collimated and incident on a grating mirror. The grating reflects the light at different angles for different wavelengths. The wavelength of interest is reflected to a focusing mirror and focused on an optical sensor through an output slit. By rotating the grating, the wavelength under investigation can be changed. By changing the width the output slit, the resolution can be changed. [37]

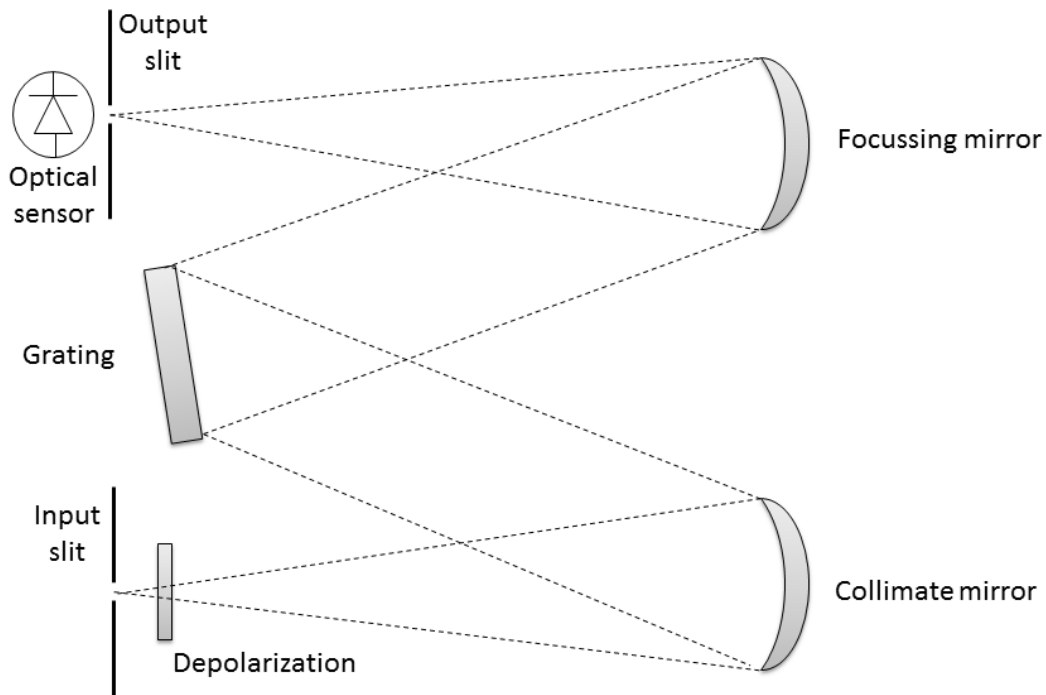


Figure 67: A monochromator like the one in the ANDO Electric explained. The light enters the OSA through an input slit, where the polarization effects are removed, and is incident on a collimate mirror. This mirror collimates the beam onto a grating mirror. By rotating the grating the wavelength reaching the focussing mirror can be changed. This mirror focuses that specific wavelength range onto an optical detector through an output slit that can be changed in width. [37]

We wrote a MATLAB script to control the OSA, of which the foundation was laid by prof. Steve Vanlanduit concerning the GPIB interfaces, and I added the code necessary to save and plot the spectra. The spectra of the OSA were previously transferred by means of a floppy disk, so this MATLAB script increased time efficiency of the measurements considerably. The script was added to this work in Appendix 1.

The advantages of the OSA are the large wavelength range of 600 to 1750 nm, the accuracy of 0.01 nm and the high dynamic range of 70 dB. This makes it excellent for characterizing spectra as Bragg reflection spectra. This accuracy goes at the cost of time, as the OSA takes more than a minute to do an accurate measurement, depending of the resolution, wavelength range, averaging and sensitivity level set. For this reason it cannot be used as dynamic interrogation method.

4.2. FBGS FBG-scan 700/704D interrogation

A second commercially available interrogator used in this work was the FBG-scan from FBGS International. Both the FBG-scan 700 and the FBG-scan 704D were used during this work. The FBG-scan 700 has one operating channel that can be interrogated at 2000 Hz, the 704D has four channels that can be interrogated at 2000 Hz maximum (so 500 Hz per channel when operating four channels).

The FBG-scan 700 consists of an internal superluminescent light emitting diode (SLED) with a spectrum ranging from 1525 to 1565 nm. The light is guided through a coupler to an optical switch which divides the light into one (FBG-scan 700) or four (FBG-scan 704D) channels. The light is then guided through an APC connection to one or multiple fiber Bragg gratings. The reflected light is again guided through the switch and the coupler to an internal spectrometer analyzing the power per wavelength division of 78 pm. Figure 68 shows such an FBG-scan as a device (top) and the internal operating system (bottom).

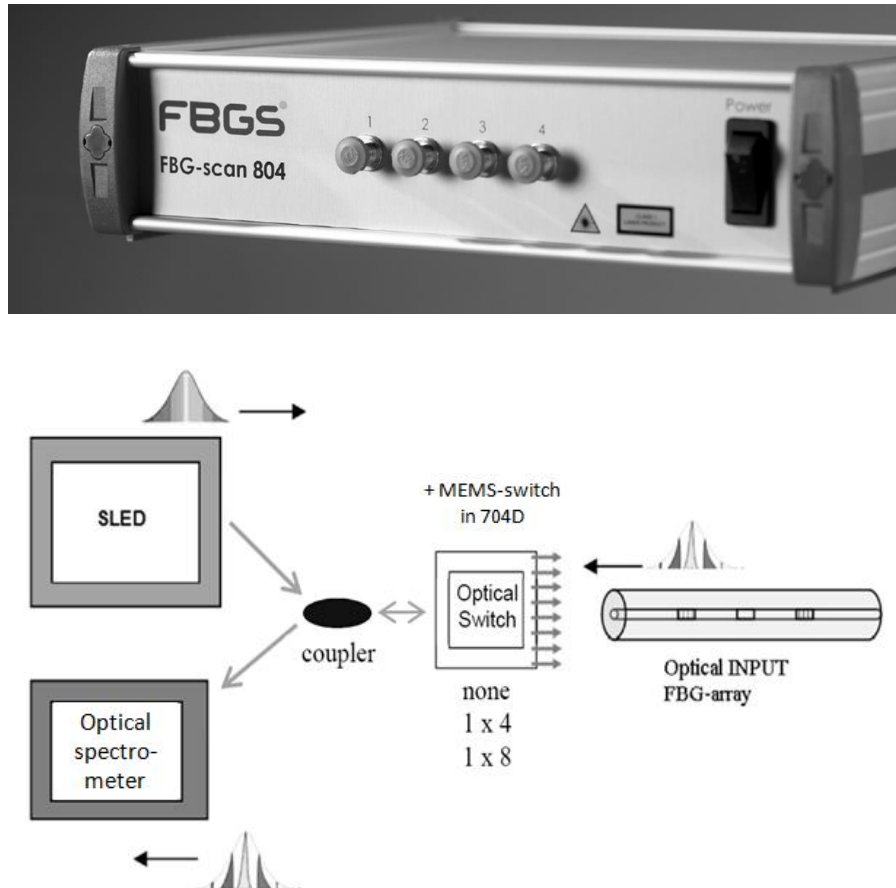


Figure 68: The FBG-scan 804, similar to the 704D, with 4 input channels (top). The FBG-scan 700 had only one input channel. And FBG-scan hardware operation (bottom). A superluminescent diode (SLED) acts as source light (1525-1565 nm). The light is coupled to the optical switches through a circulator. There the light is divided into one (FBG-scan 700) or four (FBG-scan 704D) output channels that can each be connected with an PC/APC connector to a fiber consisting of one or more FBGs. The light that is reflected by the gratings is guided again through the system, but the coupler directs it towards an internal optical spectrum analyzer, analyzing the spectrum with a resolution of 30 pm. [36]

The FBG-scan comes with its own operating software, allowing the read out of the spectra at 2000 Hz and with an automatic Bragg peak recognition. To improve on this interrogation and the data processing, we wrote a MATLAB-script, that allowed interrogating with the FBG-scan at 4266 kHz. In addition the spectrum at each interval is automatically saved and can later be processed with a more precise peak recognition algorithm as the phase correlation algorithm (FPC) explained in section 5.2. The MATLAB-script is added in Appendix 3 and includes data collection and processing of a force sensor during the impact measurements as explained in the next chapter, section 5.3. The Foundations of the script concerning the communication with the devices were laid by Ben De Pauw and Alfredo Lamberti of the Vrije Universiteit Brussel. We added the code for splitting the spectrum into windows and letting loose the FPC algorithm on each window. These shifts were then

automatically plotted for inspection. The maximum force, maximum shift of the maximum wavelength and maximum shift of the centroid (FPC) wavelength were printed in a table for easy saving of the data.

The script not only includes the controlling of the FBG-scan through C++ language commands, but also controls a data acquisition card (DAQ) for reading out a force sensor, as will be explained in section 5.1.

4.3. Micron Optics Optical Sensing Interrogator SM125

During the curing cycle of the autoclave, when embedding the fiber Bragg sensors in composite plates as was explained in section 3.5 of the previous chapter, the monitoring was done with a third interrogation system. This interrogation method is also an commercially available device. The sm125 is shown in Figure 69 and has four channels (all used during cure monitoring), a swept wavelength laser source (1520 – 1580 nm) and a full spectral scanning interrogation core with resolution of 5 pm.



Figure 69: The Micron Optics Optical Sensing Interrogator used during the cure cycle monitoring of the FBGs in embedded composite. This interrogator uses up to four channels (which were all used during the cure monitoring). The source is a high power, low noise swept wavelength laser with fiber Fabry-Perot tunable filter technology. The x25 core allows full spectral scanning and data processing. [38]

The interrogator is controlled via included computer software which can be automated to grab a spectrum from all the four channels at given time intervals, ideal for an overnight monitoring process. The Micron Optics sm125 is not a suitable candidate for dynamic measurements, there the repetition rate is maximally 1 Hz.

4.4. VCSEL-interrogator

Many interrogation methods for reading out the reflection spectra of fiber Bragg gratings exist. From very bulky and expensive, but accurate devices as optical spectrum analyzers (section 4.1) to smaller and faster field units. These eg. include the dynamic, but less precise FBG-scan (section 4.2) or the precise, but slow SM125 (section 4.3).

A dynamic interrogator should be able to measure reflected power of a Bragg peak while the Bragg wavelength shifts rapidly. This can be done with a full-spectrum interrogation, collecting the reflected light over a certain wavelength range, which can be important when not only the peak shifts are important, but information about the impact is also present in the deformation of the reflected Bragg gratings. Doing dynamic measurements in composite materials can reveal indications of damage prior to a static peak shift is induced by the damage, and so predict and help preventing damage inside structures.

Vella et al. demonstrated an interrogator working at 100 kHz for impact loading. They used a broad band ASE source amplified with an erbium doped fiber amplifier (EDFA) which illuminated an FBG in a single mode fiber. The fiber was not embedded in a composite. The interrogation was done with a high-speed driven MEMS filter and a photodiode. The MEMS filter was voltage driven over a range of 10 V to obtain a filter bandwidth between 1540 nm and 1590 nm. [39]

The work of Propst et al. showed a full-spectral interrogation of a 14.9 nm band at 534 Hz interrogation speed with an embedded single mode fiber. They also used a MEMS filter to filter dynamically filter the light of a superluminescent light emitting diode. In this way they show damage indications not visible when doing a static post-damage analysis. [40]

Van Hoe et al. showed a VCSEL-based interrogator, like the one used in this thesis. They demonstrate a low-cost, dynamically tuned (1 kHz) VCSEL-setup to scan the wavelength range of 2.5 nm with a novel coupling technique. [41]

Filtering techniques are also a possibility when interrogating an FBG dynamically. Frieden et al. demonstrated a dynamic interrogator operating at a frequency of 100 kHz. They used a Fabry-Perot filter to relate a measured intensity to a shift in Bragg wavelength of an FBG inscribed in SMF. [42]

Table 10: Characteristics of the different interrogation methods used in this thesis.

Interrogation Method	Wavelength range	Dynamic range	Hardware Resolution	Speed
<i>OSA/ASE</i>	600 – 1750 nm	60 – 70 dB	10 pm	~1 min
<i>FBG-scan 700/704D</i>	1525 – 1565 nm	50 dB	30 pm	4000 Hz
<i>Micron OpticsSM125</i>	1510 – 1590 nm	40 dB	5 pm	1 Hz
<i>VCSEL-interrogation</i>	1540 – 1545 nm		5 pm ²	500 Hz

In this paragraph we suggest a new, small-size dynamic interrogation method based on a vertical-cavity surface-emitting laser (VCSEL) as source and a photodiode (PD) as detector. This principal setup (section 4.4.1) allows the interrogator to be very small, yet precise and able to do dynamic measurements. In the rest of this chapter, the setup and the characterization of the VCSELs available will be discussed.

² Depending on the interrogation rate and the sampling rate of the DAQ.

4.4.1. VCSEL-interrogator Setup

Figure 70 shows the complete setup. The same principle as before is used to guide the light. A circulator guides the light from the source to the fiber Bragg sensor. The reflected part of the spectrum will be guided to a detector by that same circulator. The source is a current controlled TO-65 vertical-cavity surface-emitting laser (VCSEL) by VTEC and the detector a photodiode (PD). The VCSEL is operated by a current source called LDC in Figure 70 (Thorlabs LDC 200 C). The light incident on the PD will generate a current as well, a current amplified by the photodetector amplifier, called PDA in Figure 70 (Thorlabs PDA 200 C). Both PDA and LDC can be manually set and/or read out. To do this at higher frequencies, however, the LDC is in turn controlled by a voltage from a data acquisition card (NI DAQ 6315), and the voltage coming from the PDA is also read in by this DAQ simultaneously. The data processing is done with a custom made script in MATLAB [43].

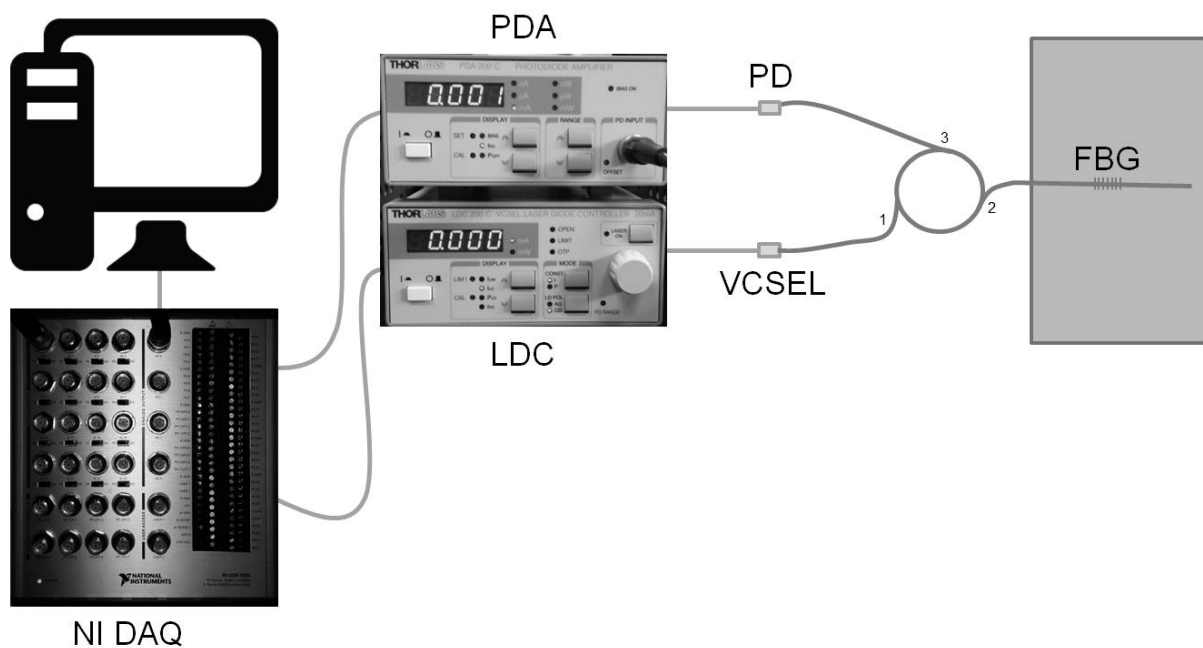


Figure 70: The setup of the custom build VCSEL-source interrogator. The interrogator uses the same basic principles as before in order to guide the light: the light of the source (VCSEL) is coupled to the FBG though a circulator. Light reflected by the FBG will return to the circulator and be guided to a photodiode (PD). The VCSEL is current-driven, meaning a current source is needed to control the VCSEL (LDC). Light power incident on the PD will also generate a current that will have to be amplified by a current amplifier (PDA). Both the VCSEL control and PDA can be manually controlled and/or read out, but in order to do high speed interrogation they are voltage controlled, respectively read out by a data acquisition card (DAQ). This DAQ communicates the data to a PC where it is processed by means of a MATLAB script.

4.4.1.a Vertical-cavity surface-emitting laser (VCSEL)

A vertical cavity surface emitting laser (VCSEL) is a semiconductor laser that emits light perpendicularly to its surface, unlike conventional semiconductor lasers. An advantage of this is that the whole structure can be deposited on a wafer for mass producing them and the VCSEL can be tested during the fabrication for increasing the yield and so decreasing the cost of the process.

Figure 71 shows the layout of a VCSEL schematically. The active gain medium is a thin laser in the middle of the structure. It is surrounded by two oxide layers which form the cavity of the VCSEL. Because of the thin active layer, the gain in one pass is very low. To account for this two stacks of highly reflective Bragg mirrors are added below and on top of the cavity. These mirrors make sure the

light passes through the active layer enough times to have a high amplification. A current is applied perpendicular to the layers to drive the VCSEL through two contacts. A hole needs to be provided in the top contact for the light exiting the structure. [44], [45]

Applying a higher current to the VCSEL will heat the structure and the laser cavity will enlarge. This will result in a higher wavelength emitted by the VCSEL, a property that is used extensively in this thesis.

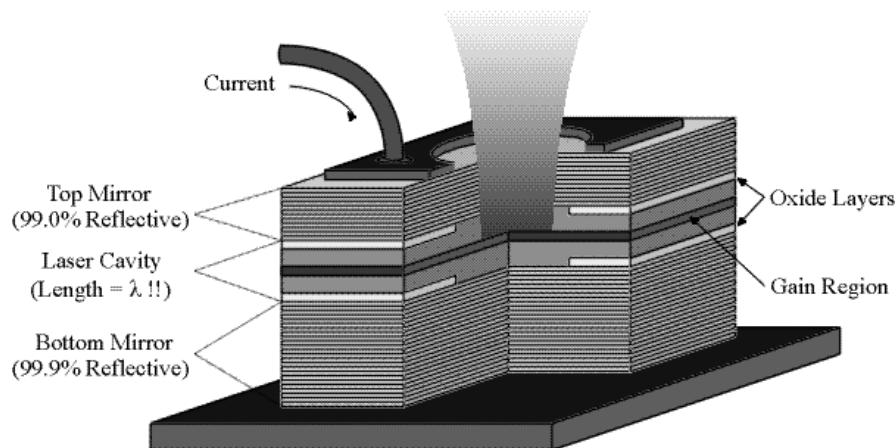


Figure 71: The layout of a vertical cavity surface emitting laser (VCSEL) . The active medium is a very thin layer surrounded on both sides by a stack of highly reflective Bragg mirrors. Unlike a normal semiconductor laser the light the structure vertically at the surface. [44]

4.4.1.b Photodiode (PD)

A photodiode is a semiconductor device consisting out of a reversely biased P-N junction. When light is incident on this junction, an electron-hole pair will be created. This carrier pair is pulled apart by the bias voltage and both carriers reach their oppositely charged contact, generating a current. If more light is incident on the diode, more current is generated.

4.4.1.c MATLAB script and VCSEL control

The data processing is done with a MATLAB script [43] added as appendix 3. The foundation of the script was laid by prof. Steve Vanlanduit, and I adjusted it for the calibrated VCSEL characteristics (section 4.4.2) and for saving and plotting the data. The script tells the DAQ to send a voltage function to the LDC which converts in to a current function and applies it to the VCSEL. A change in current applied to the VCSEL will result in a change of wavelength emitted, as explained in 4.4.1.a. A rapid change in wavelength is coupled through the circulator to the FBG. The reflected part will reach the photodiode, again through the circulator, where the power of the light is converted to a current. By knowing the wavelength emitted by the VCSEL, the current generated at the photodiode at the same time, is proportional to the reflected power of the grating at that wavelength. In this way a sweep over DAQ voltage, will result in a sweep over the LDC current, which will result in a sweep over the emitted wavelength and so a sweep over the reflected Bragg spectrum. The characterization of all these proportionalities is explained in the next section (4.4.2).

4.4.2. VCSEL-characterization

A voltage from the data acquisition card will result in a proportional current applied to the VCSEL by the LDC. The first experiment conducted here was to discover this proportionality. In order to do so, the script in appendix 4 was used to apply a static voltage with the DAQ to the LDC. The current in

turn applied by the LDC could be read off from the LDCs LCD screen as can be seen in Figure 70. This was done for voltages from 0 to 7.5 V in steps of 0.25 V, and this for three different VCSELS attached. The current was the same for each VCSEL at a given voltage applied, so no average needed to be made. When plotting the LDC current in function of the DAQ voltage as in Figure 72, a linear fit could be made, yielding equation (1).

$$I_{LDC} = 2.021 \cdot V_{DAQ} + 0.01465 \quad (43)$$

A maximum current of 20 mA can be applied by the LDC, resulting in maximum 10 V applied to the LDC by equation (43).

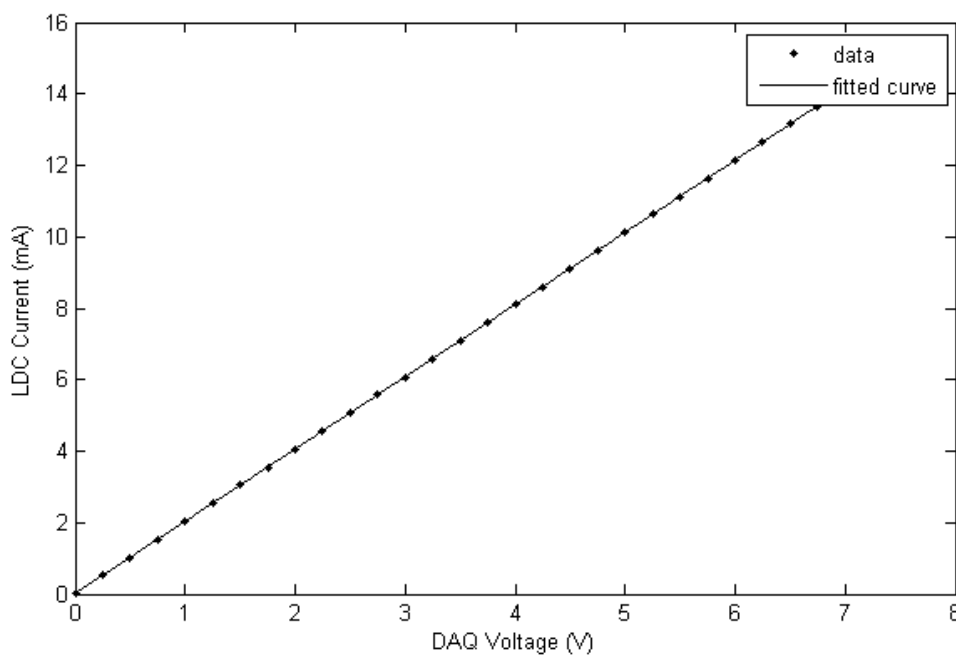


Figure 72: Current applied to the VCSEL by the LDC in function of the voltage applied to the LDC by the DAQ. The data points are shown as dots and the fitted linear is shown as a straight line.

The next characterization is the proportionality between applied voltage by the DAQ (or current by the LDC) and the emitted wavelength of the VCSEL. In order to do so, I used the setup as in Figure 70, but instead of using a photodiode as a detector, the optical spectrum analyzer was attached to gate three of the circulator. By combining parts of the MATLAB scripts for measuring with the OSA (Appendix 3) and controlling the VCSEL-interrogation setup (Appendix 4) I wrote a script that send a voltage to the LDC (sending a current to the VCSEL), and measuring the spectrum with the OSA while waiting to apply a next voltage and repeating the measurement. To be sure the OSA measurement was complete, I chose a waiting time of 180 s in between measurements, resulting in relatively long measuring times. The MATLAB script is added as appendix 5. Such a spectrum of the VCSEL used in this work is shown in Figure 73.

Figure 74 shows the relation of the central wavelength of the spectra of the VCSEL in function of the driving current. The current was increased from 2 mA to 11 mA in steps of 1 mA, using equation (1).

To further be able to work analytically with this wavelength-current relation, a quadratic fit was done, as is also seen in Figure 74. The equation characterizing this fit is shown in (44)

$$\lambda_{VCSEL} = 0.0206 \cdot I_{LDC}^2 + 0.279 \cdot I_{LDC} + 1539 \quad (44)$$

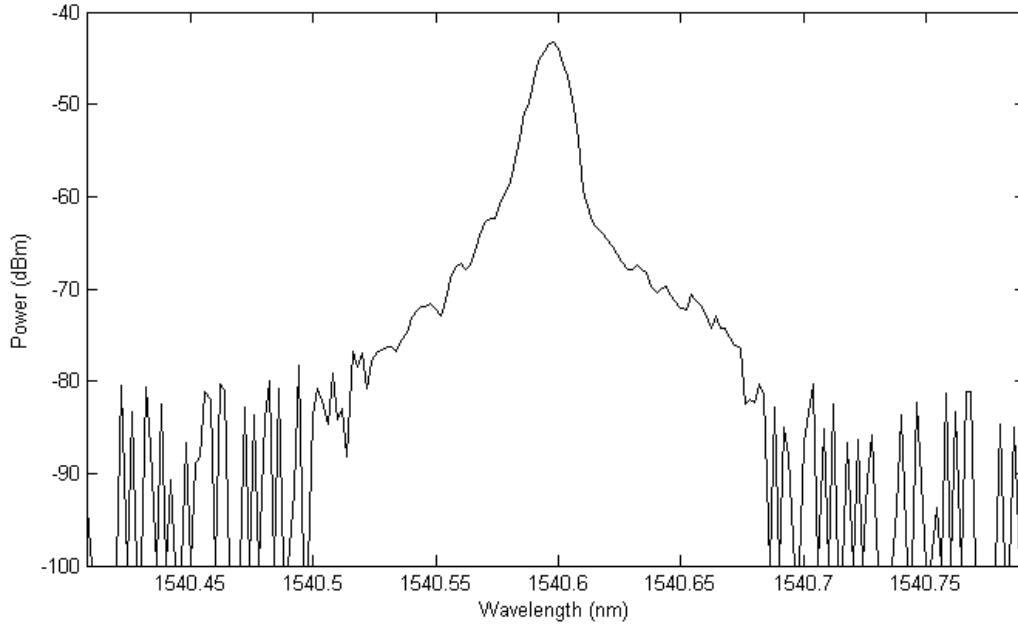


Figure 73: The spectrum of the VCSEL used in this thesis operating at a driving current of 5 mA

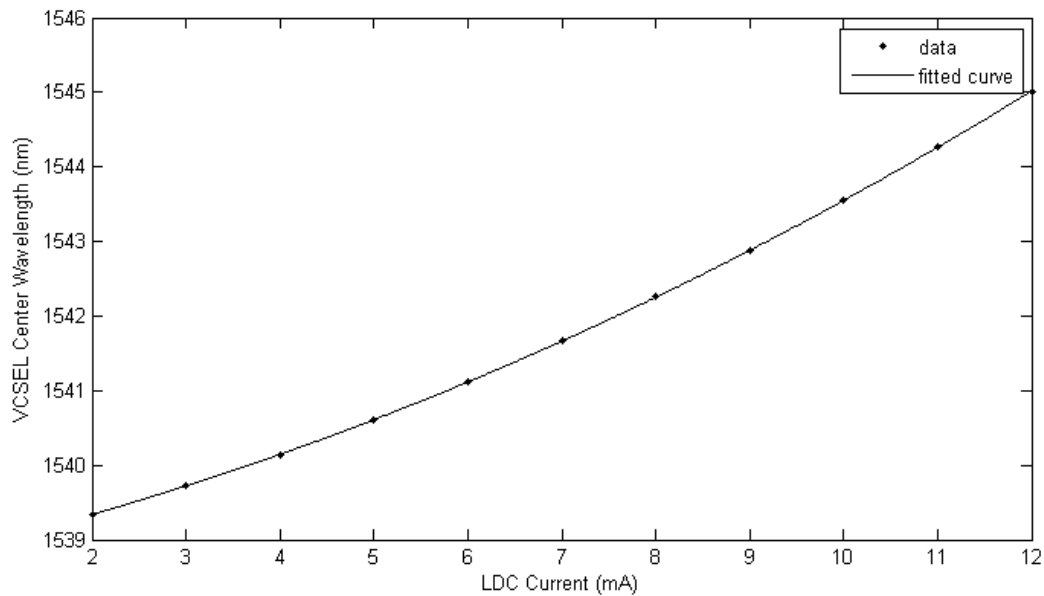


Figure 74: The Emitted central wavelength of the VCSEL used in this work in function of the current applied to it by the LDC. A quadratic fit was made, to predict the wavelength behavior of the VCSEL analytically.

Equation (44) and Figure 74 a valid for static VCSEL operation. It was observed that the center wavelength of the VCSEL changed when it was operated dynamically. This means an accurate full spectrum measurement cannot be done at high interrogation speeds, without this calibration. When however only the relative peak position and peak separation are of interest, as is the case here.

The VCSEL used above and during the measurements was VCSEL RC320161-FFP-01323217. This VCSEL had a wavelength range from about 1539.5 to 1545 nm. The MOFBGs inscribed with a Talbot interferometric setup were chosen to be in this range. Two gratings per MOF with target values 1541 nm and 1543.5 nm were ordered.

This same analysis was done for seven more VCSELs that were available. If the VCSEL above was lost due to damaging or ageing another VCSEL whose wavelength range also includes 1541 nm and 1543.5 nm could still be used. Figure 75 shows the same wavelength analysis, but for fewer currents (2, 7 10 and 12 mA respectively). The five bottom VCSELs in this figure show to have corresponding wavelength range as the VCSEL investigated above, so four VCSELs acted as reserve, although not needed.

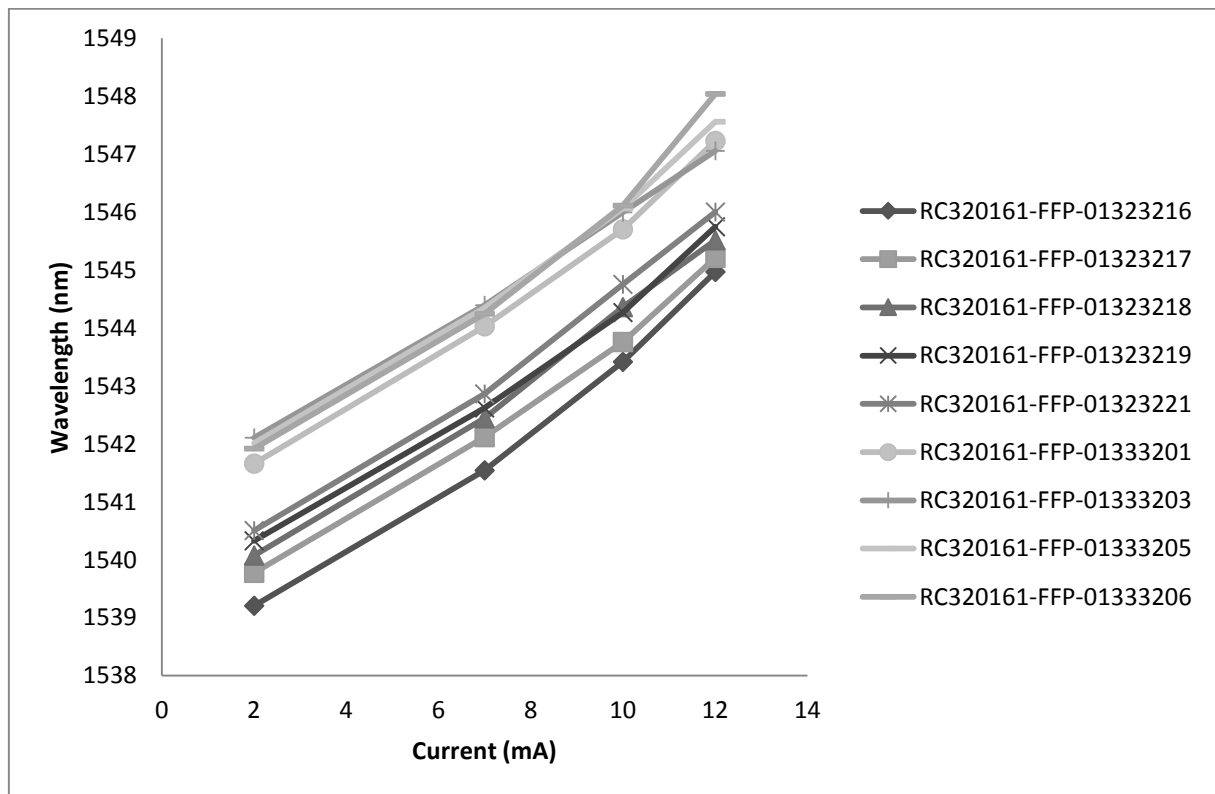


Figure 75: The central wavelength for the eight different VCSELs available in function of their driving current. The bottom five VCSELs cover the wavelength range from about 1540.5 to 1545 nm.

The full width at half maximum (FWHM) of these eight VCSELs, measured at four different currents, had an average value of 0.0163 nm with a standard deviation of 0.0048. For the maximum power of the VCSEL spectra an average value of 0.0745 mW with standard deviation of 0.0533 was measured.

4.5. Conclusion

Different interrogation techniques were discussed in this chapter. We explained their working principles and advantages or disadvantages. The ASE/OSA-interrogator showed to be a good way for characterizing FBGs due to its polarization independence and high dynamic range. Micron Optics SM125 was an excellent interrogator for the cure monitoring of composite materials, because it allowed automatically measuring and saving data at high precision, at different time intervals.

A drawback of these interrogators, with an eye on dynamic measurements, was their slow operation (1 Hz or less). We described an FBGS International FBG-scan 700/704D which allowed doing full-spectral dynamic measurements at 4266 Hz.

As a last interrogator, we successfully developed and calibrated a miniaturized VCSEL-based interrogator consisting of only one VCSEL and a photodiode as photonic components, especially design for dynamic measurements in MOFBGs.

5. 3D strain Measurements with MOFBGs sensors

In this chapter we present our results for dynamic measurements of strains and stresses with microstructured fiber Bragg gratings in composite materials.

First, in section 5.1, we will discuss the custom build setup designed to create a dynamical excitation on the composite plates discussed in section 3.3 in the form of an impact. Then we will elaborate on the theory behind the selected Bragg peak recognition algorithm, which detects the peak wavelengths in consecutive measured spectra and determines the wavelength shift with respect to a reference measurement in section 5.2. With the impact setup, the peak detection algorithm and the FBG-scan interrogator (see section 4.2) and the VCSEL interrogator (see section 4.4), we will then measure the dynamic excitation on wavelength peak shifts and elaborate on the results in sections 5.3, 5.4 and 5.5.

5.1. Impact setup

In order to generate the dynamic excitation, we proposed an impact setup. The setup impacts the composite plate with a metal tip at the location of the FBGs. The design schematic is depicted in Figure 76. The tip is connected to a steel arm that is in his turn mounted to a thicker steel post. The post is fixed to a cross of two steel beams at the bottom of the setup.

In order to clamp the composite plates into the setup, two steel plates are mounted parallel to each other on the steel post. The composite plate can be easily inserted between the two plates. The impact occurs on the part of the composite plate not sandwiched by the two metal plates. In order not to break the composite plate during an impact, the composite was supported with an aluminum plate.

To be able to do reproducible measurements, a protractor was added to the top of the setup. This protractor allowed measuring the angle of the arm with respect to the rest position. To repeat a measurement, the arm was dropped from the same angle.

The arm of the setup contains equally spaced drilled holes. These holes are there to

1. move the arm with respect to its center position, where it is connected to the post
2. place and move weights to change the impact force
3. move the impact tip position

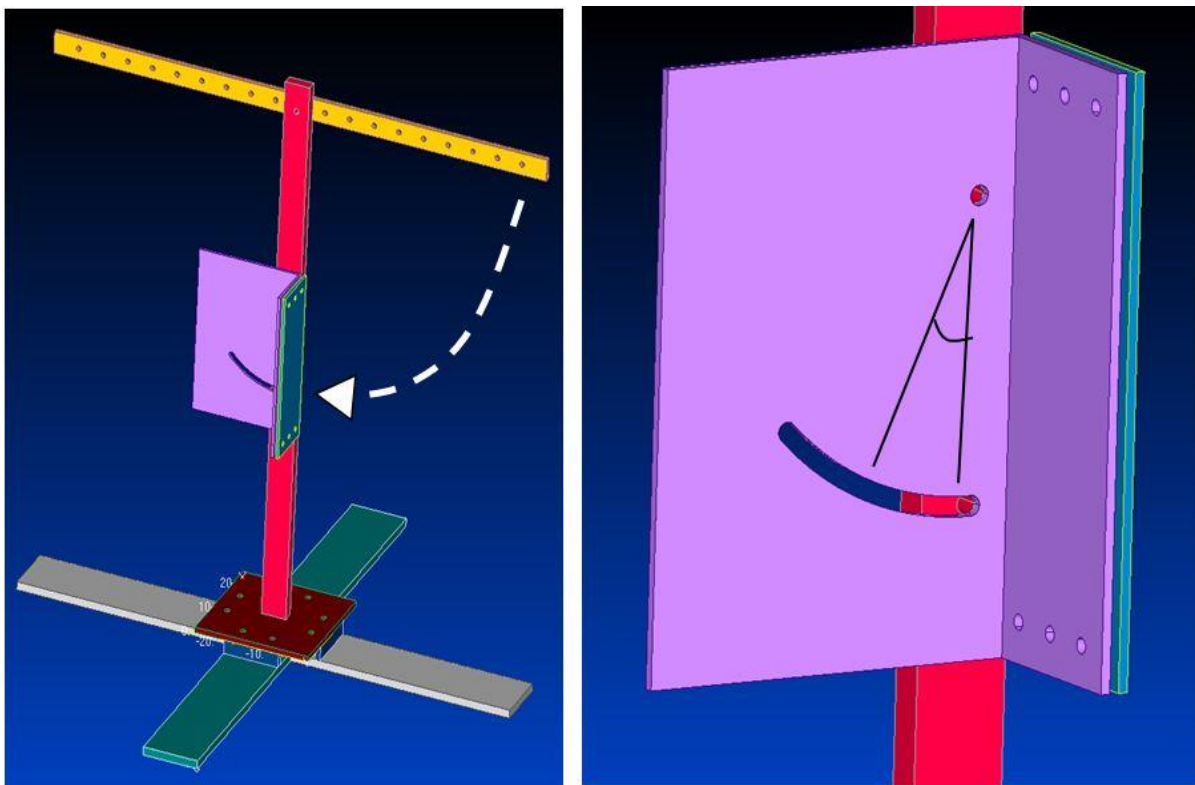


Figure 76: The complete setup (left). An impacting steel arm (yellow) can rotate around a bolt that connects it to the steel mount (red). The mount is stabilized with a steel cross of thick and wide beams. The holes drilled into the arm allow it to be laterally moved and to add weights in order to change the impact force. The composite plate will be clamped between steel plates (violet and dark green). This part of the setup is enlarged (right). The composite plate can be easily clamped between them. The curved slit allows tilting the composite plate.

The excitation occurred with an aluminum tip hitting the surface of the plate on top of the (estimated) position of the MOFBG. An enlarged profile image of the aluminum tip is displayed in Figure 77. The surface of the tip was about 20 mm^2 , but because it was curved less of the surface will touch the composite plate during an impact. The image was enlarged with a Nikon 6C-2 profile projector. Attached to the aluminum tip was a Piezotronics 208B02 voltage output force transducer. This force sensor measured the force during the impact.

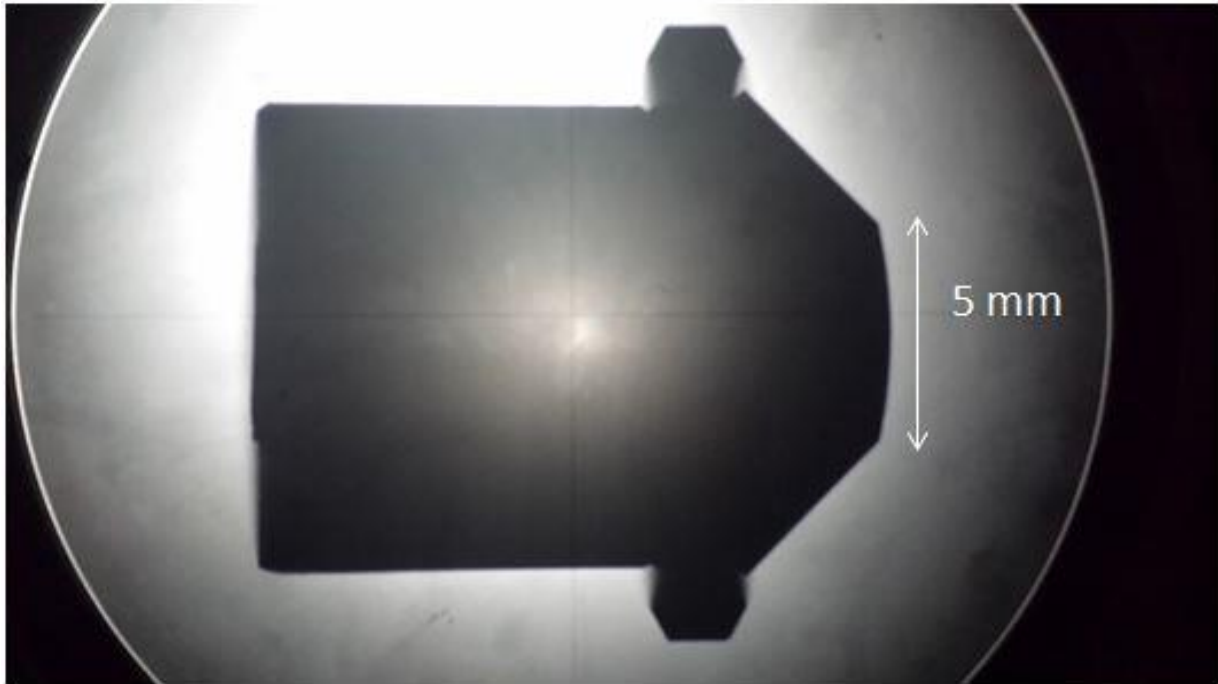


Figure 77: A contour image of the aluminum tip used in the impact setup obtained with a Nikon 6C-2 profile projector. The diameter of the circular surface is about 5 mm, but the surface hitting the composite plate will be lower, because the tip is slightly curved.

5.2. Fast phase correlation algorithm

In this thesis strain are measured by the shift of the Bragg wavelength of an FBG. To measure the Bragg shifts we use an innovative peak detection algorithm called the fast phase correlation (FPC) algorithm [46], [47]. In the algorithm, we start from a reference spectrum and calculate the shift in subsequent spectra with respect to the reference spectrum. In this work we used the algorithm in a MATLAB-script form, which is added in appendix 6. We now explain the working principle of this algorithm.

The reference power spectrum is noted as $R(\lambda_j)$. λ_j denotes the j^{th} element of the wavelength vector with $j = 1, 2, \dots, (N - 1)$. N is the number of samples and is given the wavelength range of the interrogator ($\lambda_{\max} - \lambda_{\min}$) and its hardware resolution $\delta\lambda$:

$$\frac{\lambda_{\max} - \lambda_{\min}}{\delta\lambda} \quad (45)$$

When a strain is acting on the FBG and the second wavelength vector is stored by the interrogator as

$R'(\lambda_j)$, with $j = 1, 2, \dots, (N - 1)$. Assuming that the peak has only shifted and not deformed, the new spectrum can be written as in (46):

$$R'(\lambda_j) = R(\lambda_j - \Delta\lambda) \quad (46)$$

$\Delta\lambda$ is the shift of the Bragg wavelength, and in the assumption of a spectrum with the same form, can be seen as the wavelength shift of the entire spectrum $R(\lambda_j)$. To obtain $\Delta\lambda$, the fast Fourier transform is applied on both spectra. This results in $\Re(k)$ for $R(\lambda_j)$ and $\Re'(k)$ for $R'(\lambda_j)$ respectively, as shown in (47).

$$\Re(k) = \sum_{j=1}^{N-1} R(\lambda_j) e^{\frac{-2\pi i}{N}(j-1)(k-1)}, \quad k = 1, 2, \dots, M \ll N \quad (47)$$

$$\Re'(k) = \sum_{j=1}^{N-1} R'(\lambda_j) e^{\frac{-2\pi i}{N}(j-1)(k-1)}, \quad k = 1, 2, \dots, M \ll N \quad (48)$$

Here k is the generic Fourier spectral line and M the maximum amount of spectral lines considered. An estimation of the wavelength shift $\widehat{\Delta\lambda}$ is then calculated as

$$\widehat{\Delta\lambda}(k-1) = \left(\angle \Re'(k) - \angle \Re(k) \right) \left(\frac{Nk\delta\lambda}{2\pi} \right), \quad k = 2, \dots, M \ll N \quad (49)$$

with $\angle \Re'(k)$ and $\angle \Re(k)$ being the phase of the complex numbers. The real wavelength shift $\Delta\lambda$ is then taken as the median value of the previously calculated estimates as in equation (49), because the median is less sensitive to outliers than eg. the mean.

$$\Delta\lambda = \underset{2 \leq k \leq M}{\text{median}} \left(\widehat{\Delta\lambda}(k-1) \right) \quad (50)$$

5.3. Impact on MONS-samples with FBG-scan

The first dynamical measurements I performed were done with MOFBGs gratings inscribed with a scanning phase mask technique in UMons. Three MOFBGs were embedded in a CFRP composite plate. On top of the position of the gratings I impacted the plate with an aluminum tip, with the setup explained in section 5.1. Impact forces ranged between 100 N and 1200 N.

5.3.1.a Setup

To interrogate the MOFBGs I used the FBG-scan 700 and 704D with an external C&L-band ASE source (NP Photonics). The source was coupled to the FBG-scan with a patch chord. Since the ASE source has a higher power than the internal FBG-scan source, and also because the FBG-scan 704D had no internal source due to reparations. FBGS international added an input channel to the FBG-scan to couple an ASE source as shown in the setup illustrated in Figure 78.

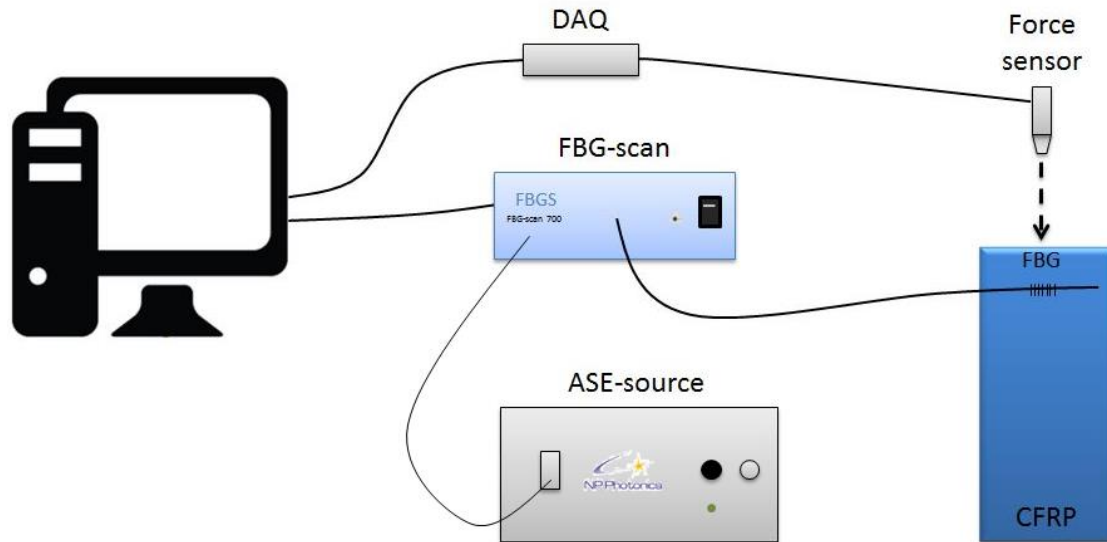


Figure 78: The setup used during the first dynamic measurements. The ASE source is coupled to the FBG-scan which in its turn couples the light to the MOFBG. This MOFBG is embedded in a CFRP plate. The light reflected by the MOFBG returns back to the FBG-scan. The FBG-scan is read out with a custom made MATLAB script at 4266 Hz. The impacts occur on the CFRP plate on top of the MOFBG under test, with an aluminum tip attached to the arm of the setup shown in Figure 76. To this impact tip a force sensor is attached which measures the force and is read out by a DAQ, controlled by the same MATLAB script.

The layout of the CFRP plate on which the impacts were performed is shown in Figure 79. The gratings were numbered 1 to 3. MOFBG 1 had Bragg wavelengths of 1566.685 nm and 1567.688 nm. The post-mortem analysis in section 3.7 showed the orientation of the butterfly structure was 31.67 °. MOFBG 2 had Bragg wavelengths at 1566.366 nm and 1567.368 nm and was oriented under an angle of 109.67 °. The third MOFBG had Bragg wavelengths of 1566.368 nm and 1567.370 nm and had an orientation angle of 115.67 °. Figure 16 shows the definition of these angles with respect to the composite plate.

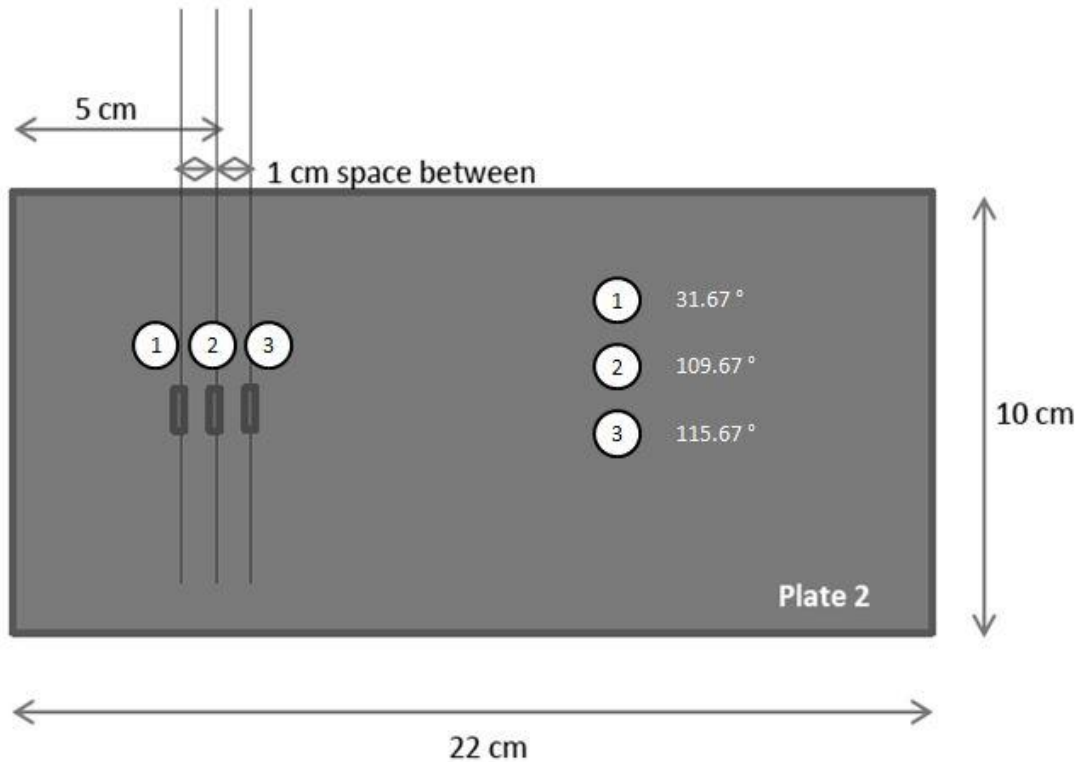


Figure 79: The CFRP plate on which impact measurements were performed. The plate is embedded with three MOFBG labeled 1 to 3. The orientation angles measured during the post-mortem analysis are noted to be respectively 31.67 °, 109.67 ° and 115.67 °. Impact occurred on top of the grating that was interrogated.

5.3.1.b Peak shifts during the impact

As an example we show the results of an impact measured with MOFBG 2 at a drop angle of 60 °. Figure 80 shows the course of the force measured with the force sensor on the impact tip. The maximum force measured in this case was 1429.4 N. Figure 81 shows the peak shifts and separation change during this impact force. The left peak shifted 94.7 pm to the left, and the right peak 36.6 pm to the left. The peak separation increased with 58.2 pm. This is larger than the measuring accuracy, so we have shown that this impact is indeed a measurable quantity. An increase in peak separation is also expected for a rating oriented at ~90 °.

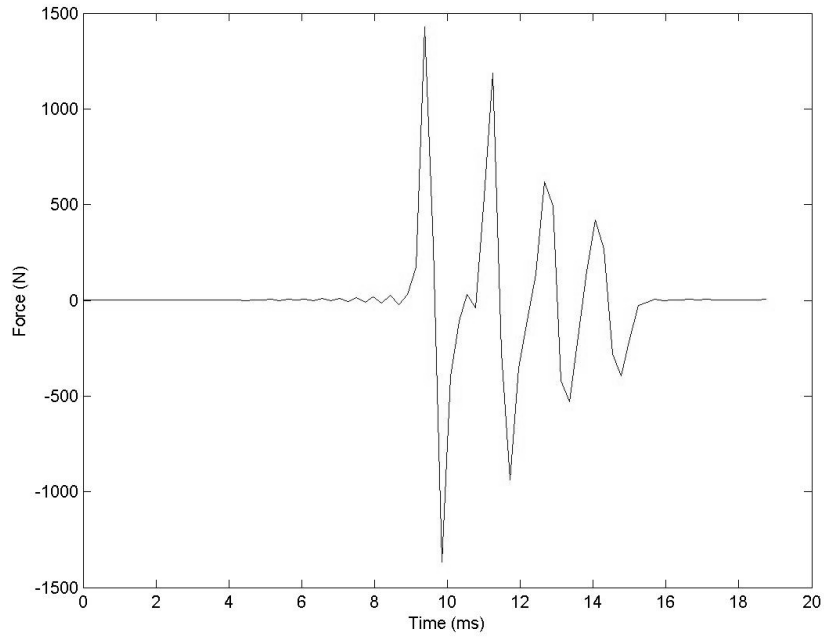


Figure 80: The force course measured with the force sensor during an impact on MOFBG 2 with a drop angle of 60°. A maximum force of 1429.4 N was measured during this specific measurement.

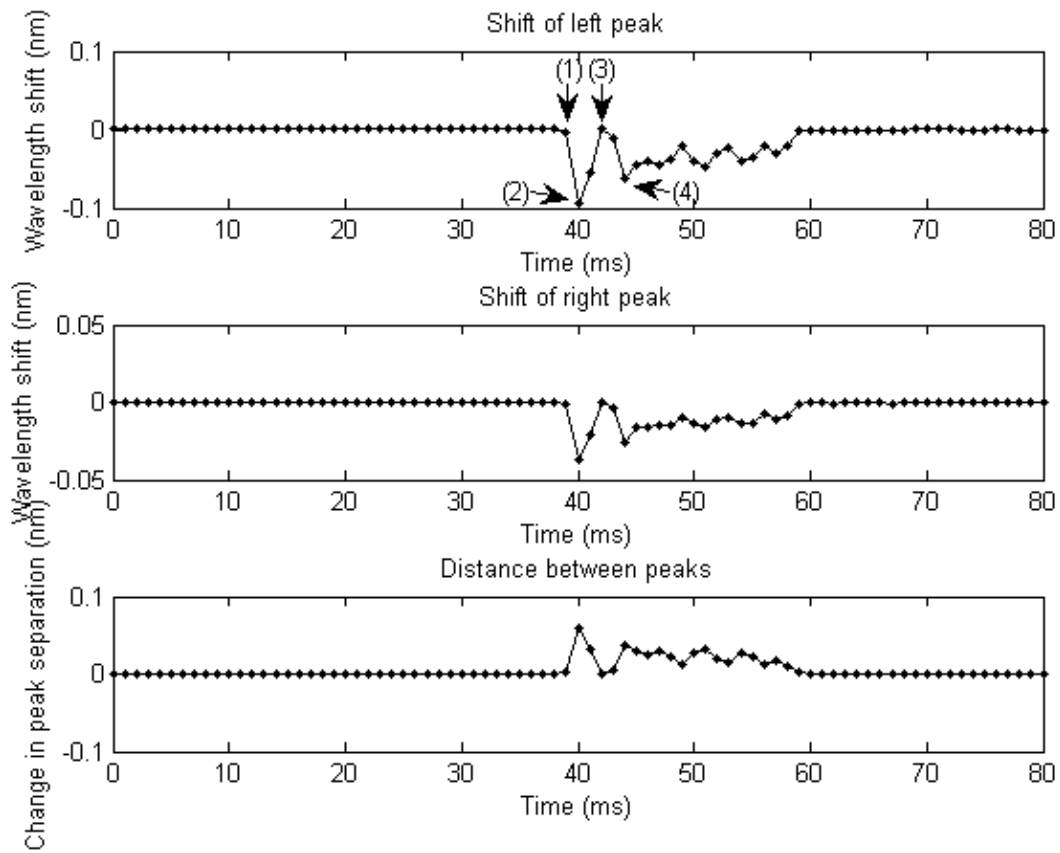


Figure 81: The peak shifts and separation during the same measurement as shown in Figure 80 for MOFBG 2 oriented at 109.67°. The left peak sifted 94.7 pm to the left, the right peak 36.6 pm to the left and the separation increased with 58.2 pm.

The full spectrum showing the positions of the peaks in function of the wavelength was measured and saved at each data point in Figure 81. To have a closer look at some interesting spectra, the spectra corresponding to the wavelength shifts denoted with (1) to (4) in Figure 81, are displayed in Figure 82.

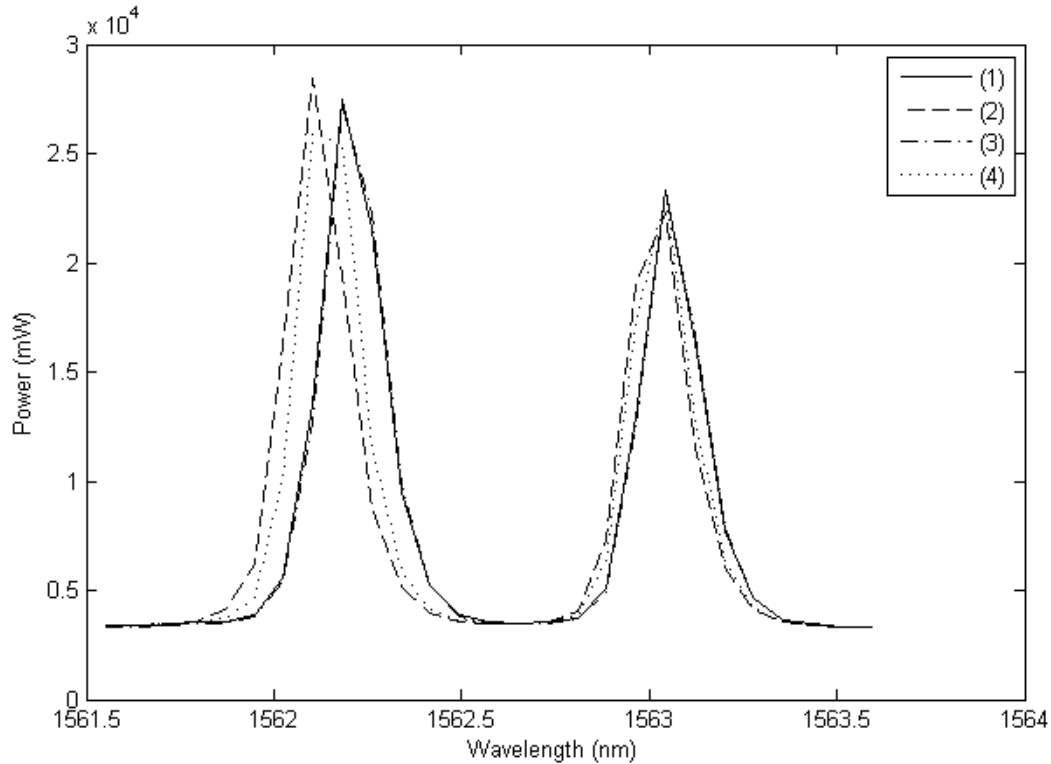


Figure 82: The spectra showing the two Bragg peaks of MOFBG 2. The full line corresponds to the rest position of the Bragg wavelength (no load applied) in point (1) of the previous figure. The dashed line corresponds to number (2) in the previous figure. The wavelength shifts are maximal here (as expected from Figure 81). The dash-dot line shows the spectrum of number (3), which is at the same shift as number (1), and indeed the spectra coincide. The dotted line corresponds to number (4) and is in between spectrum (1) and spectrum (2), as also in Figure 81.

The spectra are consistent with the shifts in Figure 81. The full line (1) denotes the spectra of the MOFBG being in its rest position (no load is applied). The largest shift (2) also corresponds to the largest shift of the spectrum for both peaks to the left. In (3) the shift returns to 0 nm, and so does the dash-dotted line coincide with the full line (1) again. From the shift seen in Figure 81, the spectrum of point number (4) is expected to be in between spectrum (1) and spectrum (2), as is the case.

5.3.1.c Force calibration

Measurements like the one discussed above were performed four times for each impact angle and averaged. This was done for all three MOFBGs. During all impacts, the force sensor on the tip of the impact arm measured the force. The maximum force was set out in function of the drop angle. As expected the force increases with increasing start angle of the arm. A quadratic fit was done on this curve, and is shown in equation (1).

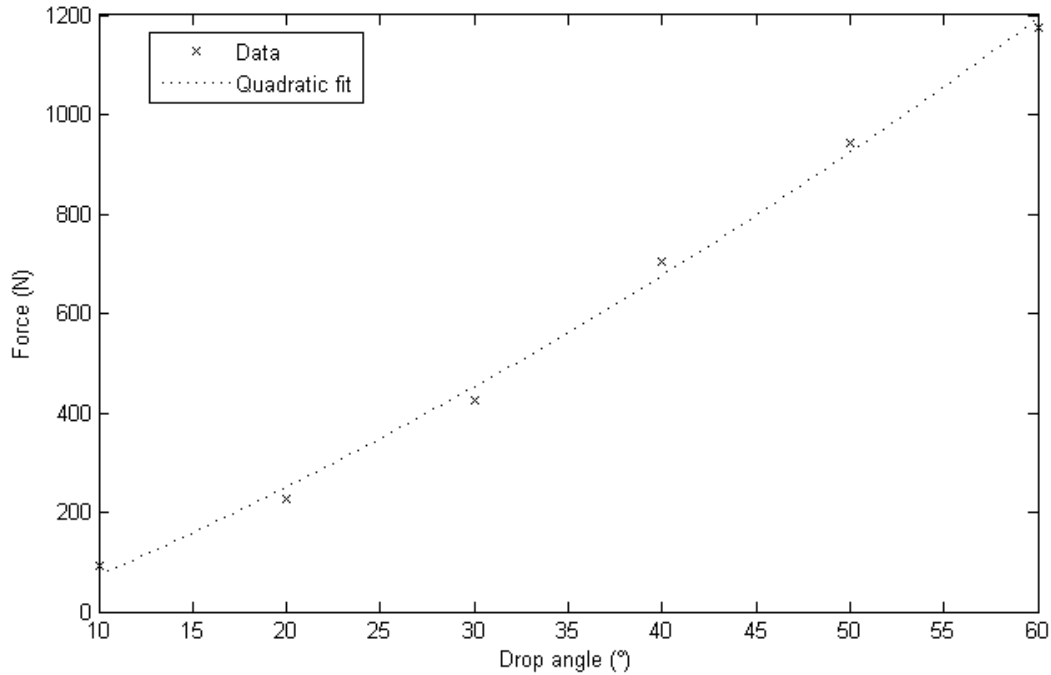


Figure 83: The force measured with the force sensor on the tip during impact with a quadratic fit.

$$F = 0.1144 \cdot \theta^2 + 14.41 \cdot \theta - 83.08 \quad (51)$$

Here F is the force in Newton and θ is the drop angle of the impact arm in degrees.

5.3.1.d Measurements on MOFBG 1

The plate was positioned in the setup such that the impact occurred right on top of MOFBG 1. This grating had Bragg wavelengths of 1566.685 nm and 1567.688 nm and an orientation of the butterfly structure of 31.67°. Impacts were performed with forces between 200 N and 900 N. With the protractor as reference, each impact was done four times and the average of the force and peak shifts was taken over these four measurements.

Figure 84 shows the data of these averaged measurements. The x-marker denotes the left peak shift, which was between -40 pm and -100 pm from rest position. A full line shows the linear fit that was done on the data. The equation of this fit is given in equation (52). $\Delta\lambda_{b,L}$ is the shift of the Bragg wavelength of the left peak (1566.685 nm in rest), and F is the applied force measured with force sensor.

The +-marker denotes the right peak shift and was between 0 and -20 pm from rest position. Here a dotted line shows the linear fit, which equation is shown in equation (53). $\Delta\lambda_{b,R}$ stands for the shift of the Bragg wavelength of the right peak (1567.688 nm) in rest.

Lastly also the peak separation change is shown with an o-marker. The peak separation changes are between 40 pm and 100 pm from rest separation of 1.003 nm. Also here a linear fit was done and is shown with a dotted line in Figure 84 and in equation (54).

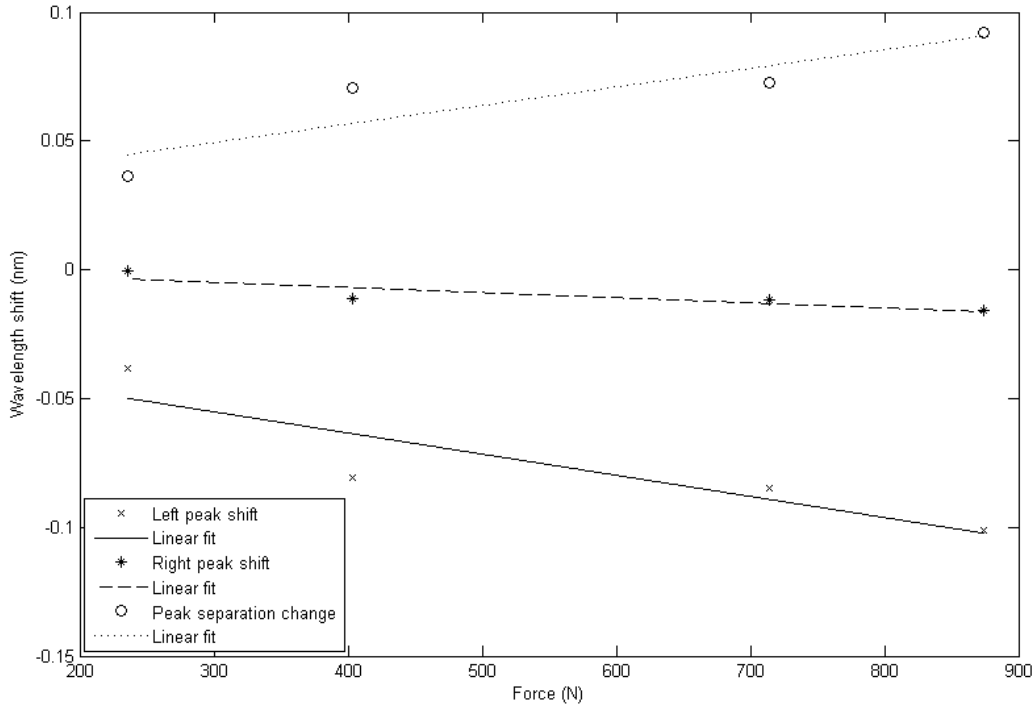


Figure 84: The left and right peak shifts and peak separation change for MOFBG 1, oriented at 31.67 °. Measurements were averaged four times and this at five different drop angles from 20 ° to 60 °. The x-marker shows the data points for the averaged left peak change, the +marker for the right peak change, and the o-marker for the change in peak separation. For each dataset a linear fit was provided.

$$\Delta\lambda_{b,L} = -8.21 \cdot 10^{-5} \cdot F - 0.0305 \quad (52)$$

$$\Delta\lambda_{b,R} = -1.99 \cdot 10^{-5} \cdot F + 0.00109 \quad (53)$$

$$(\Delta\lambda_{b,L} - \Delta\lambda_{b,R}) = 7.21 \cdot 10^{-5} \cdot F + 0.0278 \quad (54)$$

The raw data of this measurement can be found in appendix 6.

5.3.1.e Measurements on MOFBG 2

The same procedure was followed for the sensor MOFBG 2. This MOFBG had Bragg wavelengths of 1566.366 nm and 1567.368 nm and was oriented under an angle of 109.67 °.

The averaged results are displayed in Figure 85. The same legend is used as in Figure 84, 'x' for the left peak, '+' for the right peak and 'o' for the peak separation. The wavelength shift of the left peak is between -20 pm and -120 pm. The shift of the right peak is between -10 pm and -40 pm. The change in peak separation is between 10 pm and 80 pm.

All datasets were fitted with a linear trend line as shown in Figure 85 as a full line for the left peak, a dashed line for the right peak and a dotted line for the peak separation. Their equations are given in equation (55) to (57) respectively.

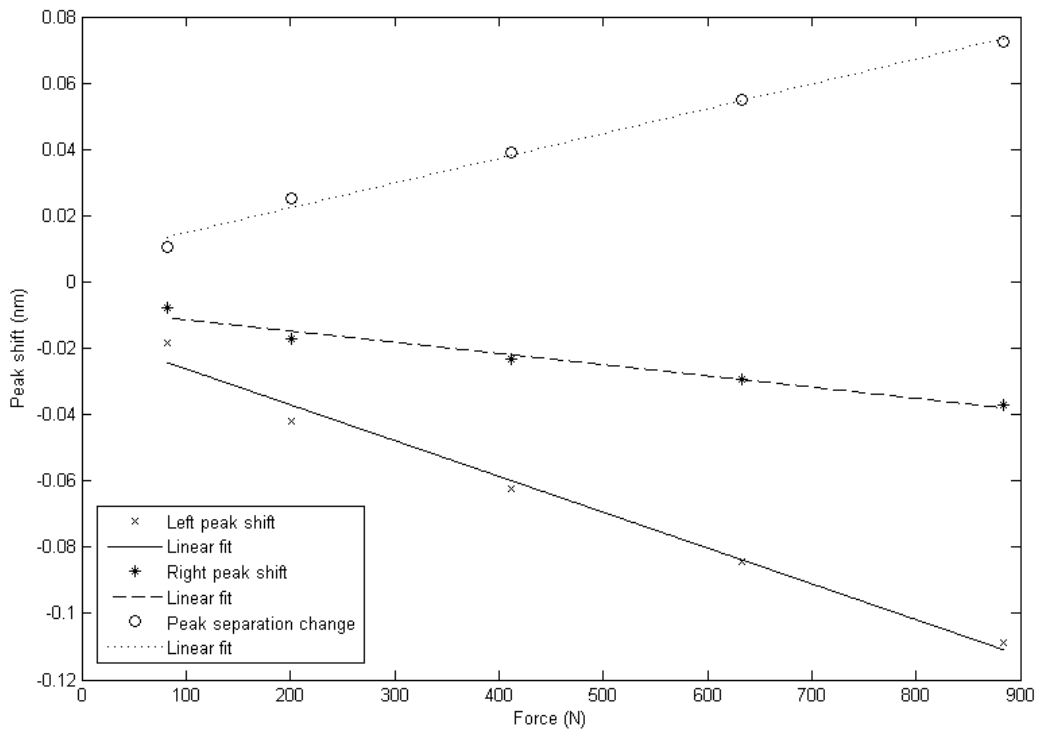


Figure 85: The left and right peak shifts and peak separation change for MOFBG 2 oriented at 109.67 °. Measurements were averaged four times and this at six different drop angles from 10 ° to 60 °. The x-marker shows the data points for the averaged left peak change, the +marker for the right peak change, and the o-marker for the change in peak separation. For each dataset a linear fit was provided.

$$\Delta\lambda_{b,L} = -1.08 \cdot 10^{-4} \cdot F - 0.0154 \quad (55)$$

$$\Delta\lambda_{b,R} = -3.39 \cdot 10^{-5} \cdot F - 0.00802 \quad (56)$$

$$(\Delta\lambda_{b,L} - \Delta\lambda_{b,R}) = 7.48 \cdot 10^{-5} \cdot F + 0.00738 \quad (57)$$

The raw data of this measurement can be found in appendix 7.

5.3.1.f Measurements on MOFBG 3

Also the third MOFBG in the CFRP plate was subjected to the same impacts. MOFBG has Bragg wavelengths of 1566.368 nm and 1567.370 nm and an orientation angle of 115.67 °. The peak shifts are measured for impact forces between 100 N and 1400 N in this case. As can be seen in Figure 86 the Bragg wavelength of the left peak ('x') shifts between -30 pm and -150 pm, the right peak ('+') shifts between -10 pm and -50 pm and the peak separation changes are between 20 pm and 130 pm.

A full line denotes the linear fit made for the left peak shifts and its equation is shown in equation (58). The dashed line does the same for the right peak shifts and has equation (59). Lastly the dotted line fits the linearity of the change in peak separation and is also shown in equation (60).

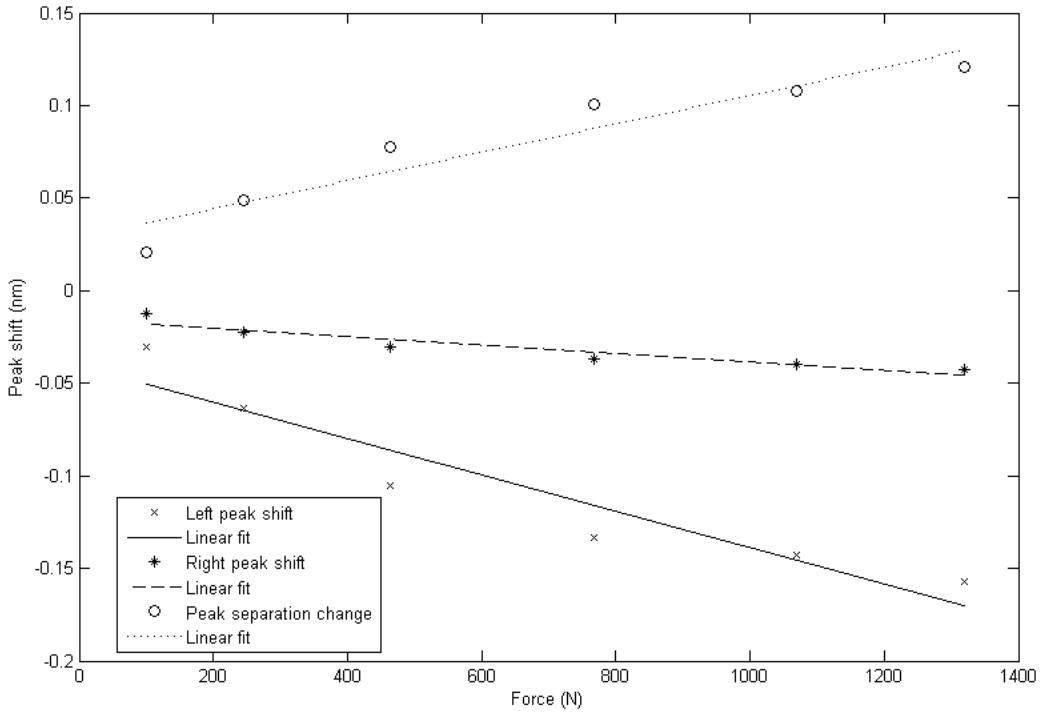


Figure 86: The left and right peak shifts and peak separation change for the MOFBG oriented at 115.67 °. Measurements were averaged four times and this at six different drop angles from 10 ° to 60 °. The x-marker shows the data points for the averaged left peak change, the +marker for the right peak change, and the o-marker for the change in peak separation. For each dataset a linear fit was provided.

$$\Delta\lambda_{b,L} = -9.81 \cdot 10^{-5} \cdot F - 0.0406 \quad (58)$$

$$\Delta\lambda_{b,R} = -2.27 \cdot 10^{-5} \cdot F - 0.0157 \quad (59)$$

$$(\Delta\lambda_{b,L} - \Delta\lambda_{b,R}) = 7.65 \cdot 10^{-5} \cdot F + 0.0288 \quad (60)$$

The raw data of this measurement can be found in appendix 8.

The three gratings show similar sensitivities when measuring the Bragg wavelength shifts. For MOFBG 2 and MOFBG 3, oriented at 109.67 ° and 115.67 ° respectively, a positive sensitivity in the peak separation is indeed as we expect. For MOFBG 1 the orientation was slightly below 45 ° (32.67 °), and consequently a slightly negative sensitivity was expected. This is however not the case as the sensitivity of $7.21 \cdot 10^{-5} \text{ nm/N}$ is not just positive, but of the same order as the ones obtained for MOFBG 2 and MOFBG 3. This could possibly be explained by a discontinuity in the composite material around the MOF. However it was not seen at the immediate position of MOFBG 1 (see Figure 64), Figure 87 shows the cross section of the MOF inside the composite at location 3 specified in Figure 56. A few centimeters from the MOFBG a relatively large discontinuity is present. It is not sure what the origin of this discontinuity is, but it could have had an influence on the strain transfer from the composite to the MOF for MOFBG 1.



Figure 87: The embedded MOF containing MOFBG 1 about 2 cm from the MOFBG. A discontinuity in the matrix of the composite plate is clearly visible around the MOF.

5.3.1.g Strain transfer

The orientation of the MOFBGs was 31.67° , 109.67° and 115.67° respectively. These orientations deviate considerably from the respectively targeted 0° , 90° and 90° orientations. In order to do a strain-transfer analysis, we should first do a FE-simulation for calculating the correct transfer matrix to convert wavelength shifts into 3D strains. This was however not in the scope of this thesis.

However, to have an idea of the order of strains we used the $45^\circ - 90^\circ$ transfer matrix calculated by dr. Camille Sonnenfeld in her PhD thesis, as it was closest to the orientation of the MOFBGs in this thesis. This transformation is shown in equation (61). The strains ε_1^h , ε_2^h and ε_3^h are along the directions defined in Figure 15. [1]

$$\begin{bmatrix} \varepsilon_1^h \\ \varepsilon_2^h \\ \varepsilon_3^h \end{bmatrix} = \begin{bmatrix} 1.90 & -0.715 & 0.054 \\ 5.89 & -0.952 & -5.28 \\ 5.91 & -11.7 & 5.47 \end{bmatrix} \cdot \begin{bmatrix} \Delta\lambda_{B1,1'}/\lambda_{B1,1'} \\ \Delta\lambda_{B1,2'}/\lambda_{B1,2'} \\ \Delta\lambda_{B2,1'}/\lambda_{B2,1'} \end{bmatrix} \quad (61)$$

To perform this strain transfer, we need wavelength shift information of both Bragg peak of MOFBG 1 (31.67°) and the first Bragg peak of MOFBG 2 (109.67°). Their respective Bragg wavelengths are shown in equation (62) to (64). Because the impact measurements on each MOFBG were performed independently, we used a measurement of which the force measured by the force sensor was similar. This was a measurement at an impact force of 861 N on MOFBG 1 and 910 N on MOFBG 2. Both forces are depicted in Figure 88.

$$\lambda_{B1,1'} = 1566.685 \text{ nm} \quad (62)$$

$$\lambda_{B1,2'} = 1567.688 \text{ nm} \quad (63)$$

$$\lambda_{B2,1'} = 1566.366 \text{ nm} \quad (64)$$

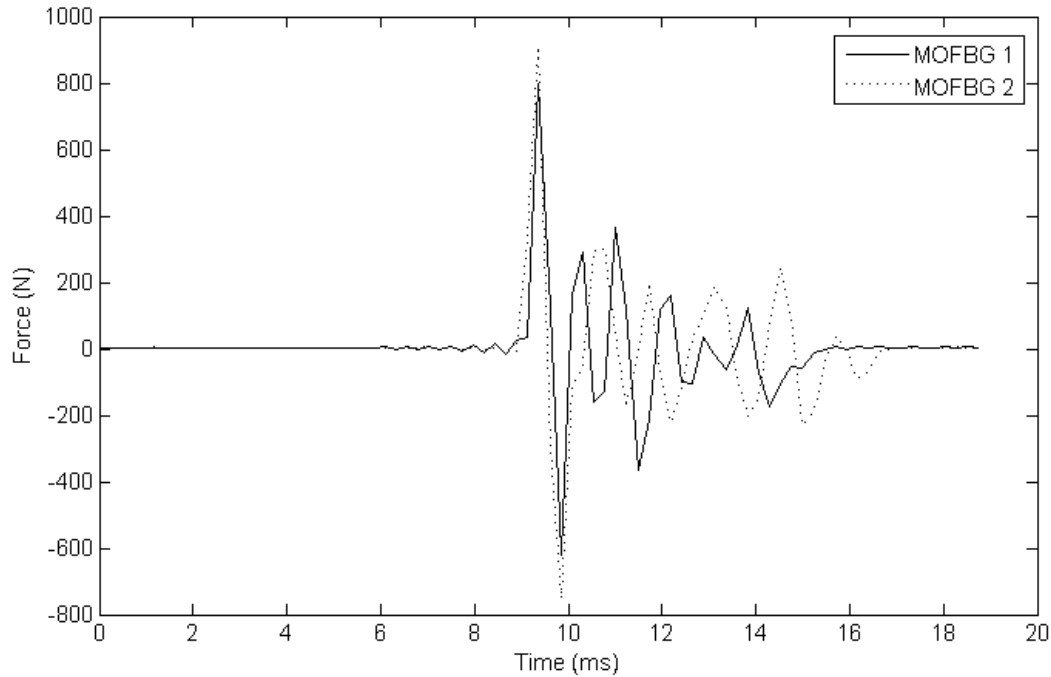


Figure 88: The force measured by the force sensor on applied by an impact on MOFBG 1 (full line) and on MOFBG 2 (dotted line). Both impacts showed similar maximum force around 800 N and course of the curve during the first main interactions with the composite plate.

Force these two similar impacts we calculated the strains ε_1^h , ε_2^h and ε_3^h in function of time during the impact on MOFBG 1 and MOFBG 2. Figure 89 (top) shows the Bragg wavelength shifts for the three peaks and (bottom) the strain course in the three axes of the composite plate as defined in Figure 15.

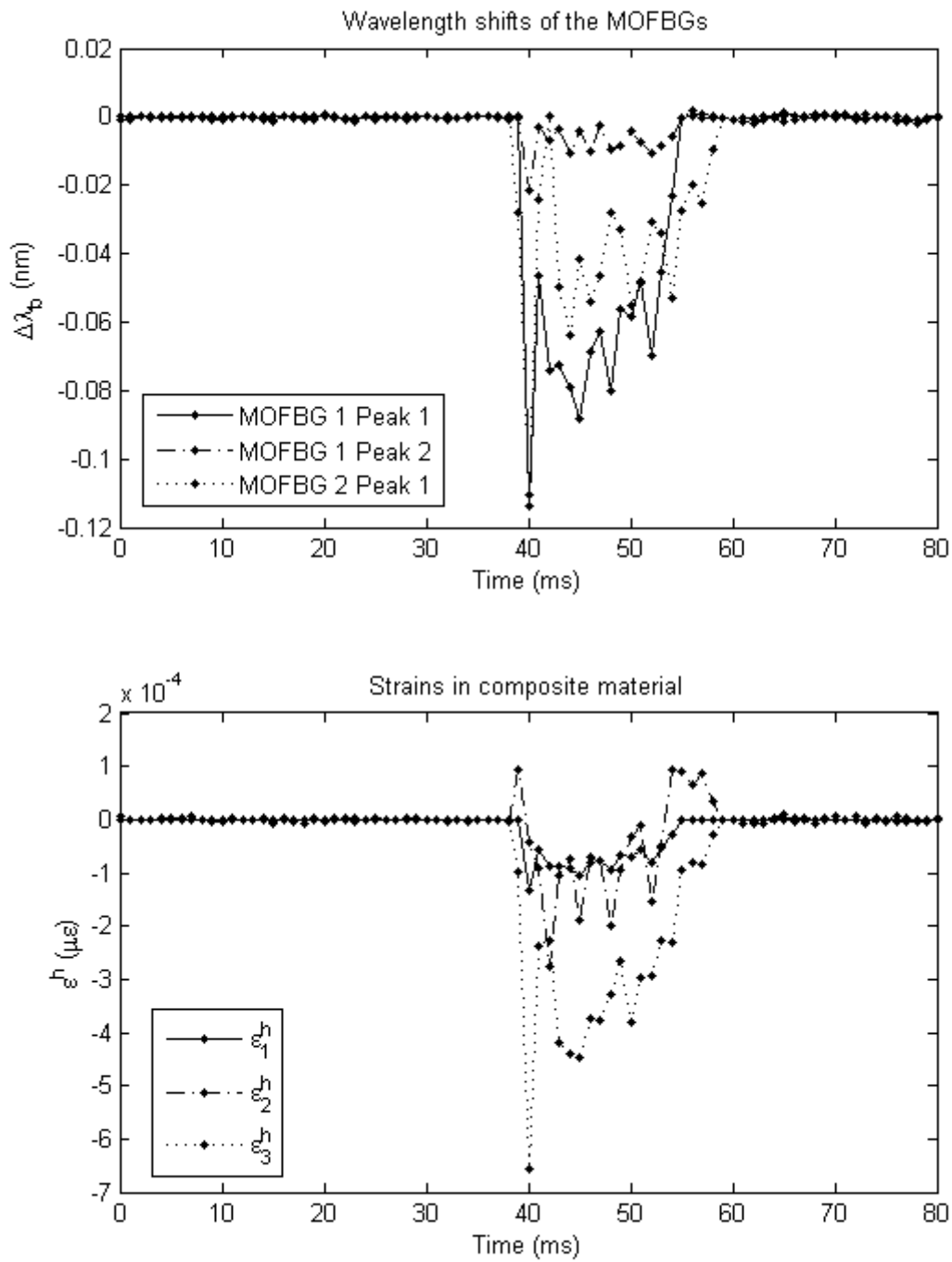


Figure 89: The wavelength shifts of the two peaks of MOFBG 1 (32.67 °) and one peak of MOFBG 2 (109.67 °) during an impact of N measured with the FBG-scan at 4266 Hz. (top) The three axial strains in function of time as determined with the transfer method performed on the three Bragg wavelength shown in the top panel.

We see that the in plane strains ε_1^h and ε_2^h (full line and dash-dotted line respectively) show a corresponding course and the transversal component ε_3^h shows much higher strain (about 5 times) at the maximum wavelength shift. This is indeed as we expected, as the impact is symmetrical for the two in-plane directions and the highest strain is expected in the direction of the impact (transversal).

We have thereby proven that our MOFBGs are able to measure 3D strains in a dynamic way, something that has not been shown before.

5.4. Impacts on IHPT-samples with FBG-scan

Dynamic measurements were also performed with the MOFBGs inscribed at the IPHT in JENA. These MOFBGs were embedded in composite plates with the same layout as the CFRP plates containing the UMons MOFBGs. The difference with the UMons MOFBGs was in first instance the wavelength of the gratings (targeted 1541 nm and 1543.5 nm to be interrogated with the VCSEL setup explained in section 4.4). A second difference was the sensor layout, as now two gratings are inscribed into one fiber for simultaneous interrogation. The layout of the plates is illustrated in Figure 90. It was the MOFBG called 'Sidney6' in this layout that was interrogated during the impacts in this section.

Figure 91 shows the reflection spectrum of the MOFBGs in rest labeled 'Sidney6' in Figure 90, which was interrogated during impact measurements in this section.

The same procedure was followed as in sections 5.1 and 5.3 with the interrogation by the FBG-scan as explained in section 5.3.1.a and shown in Figure 78.

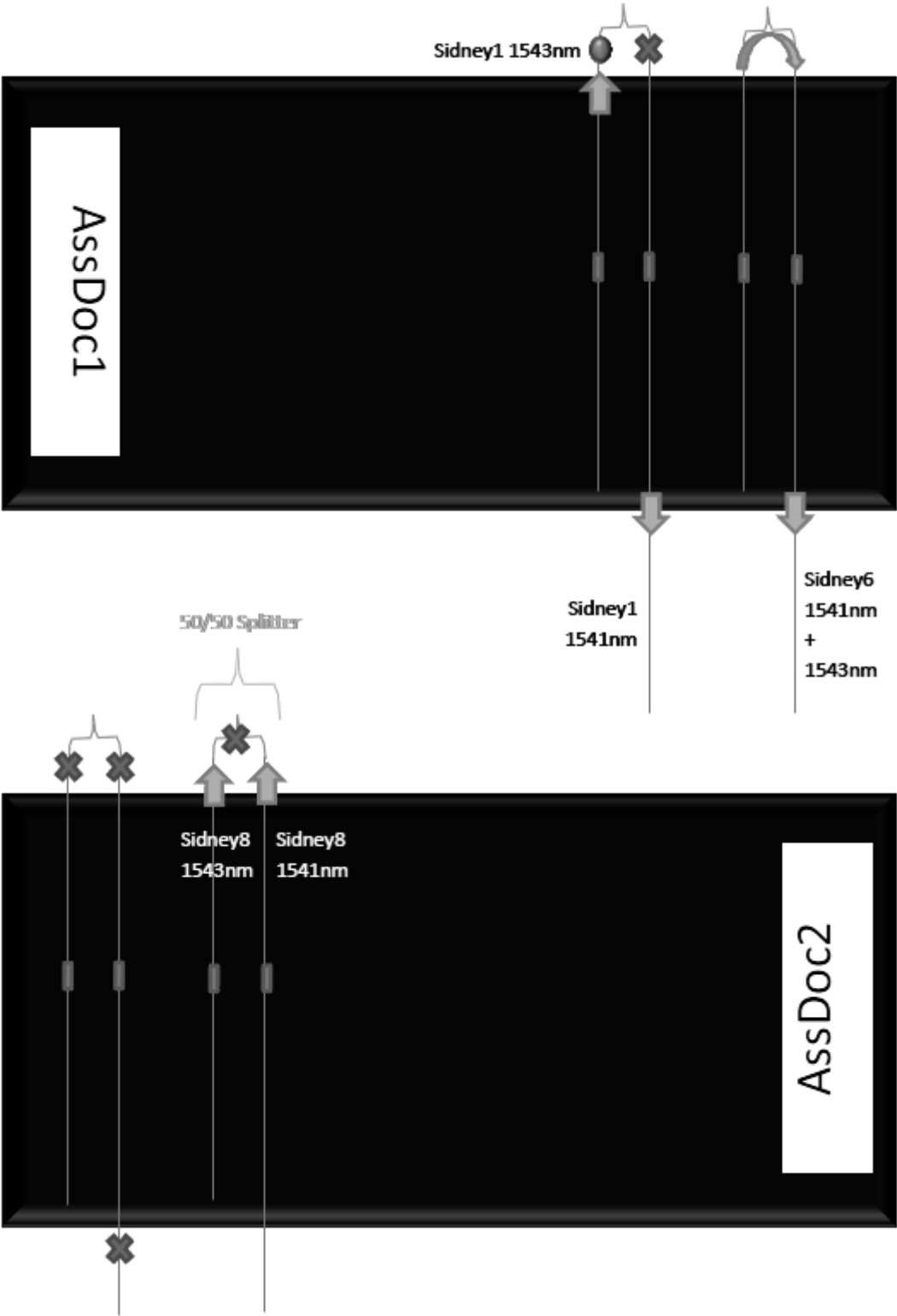


Figure 90: Layout of the IPHT MOFBGs embedded in CFRP. The MOFBG 'Sidney6' in plate 'AssDoc1' was used for performing measurements. The crosses show the fibers that were lost during the removing of the vacuum bag. The arrows suggest ways to still interrogate the MOFBG. The plates were labeled AssDoc1 and AssDoc2

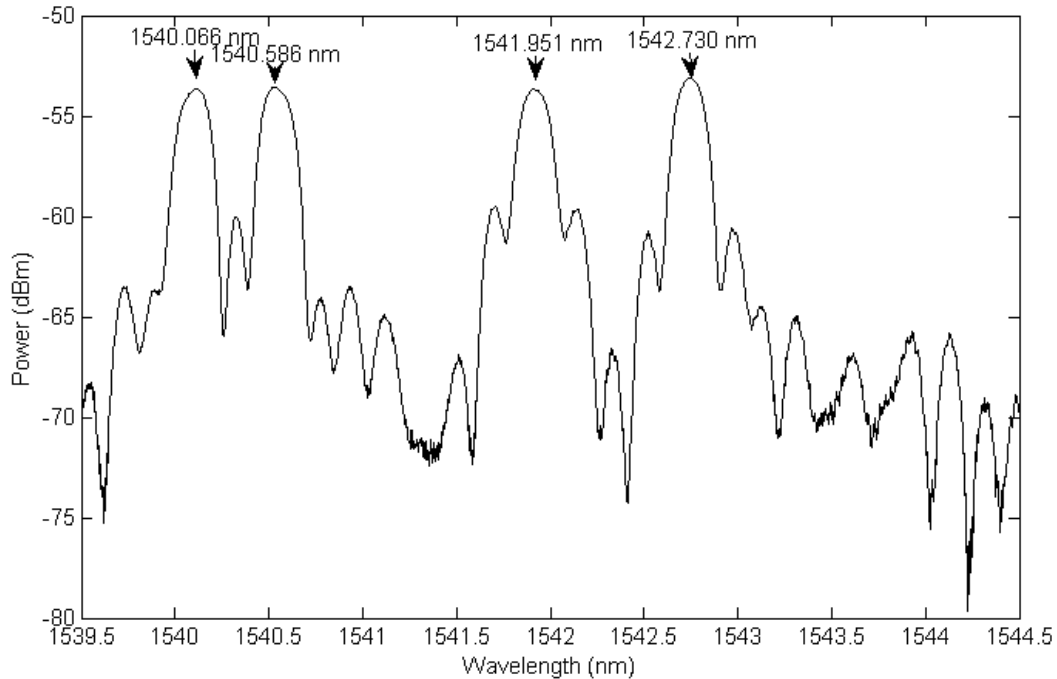


Figure 91: Reflection spectrum of the MOFBG used in this section. The spectrum was measured with the ASE/OSA setup as explained in section 4.1.

As in sections 5.3.1.d to 5.3.1.f the force was measured during the impact, and so was the Bragg wavelength shift of the left peak, the right peak and the change in peak separation. All were averaged over four measurements.

Figure 92 shows the averaged Bragg wavelength shifts of the first MOFBG at wavelengths 1540.066 nm and 1540.586 nm. The legend denotes 'x' for the left peak, '+' for the right peak and 'o' for the peak separation.

A full line denotes the linear fit made for the left peak shifts and its equation is shown in equation (65). The dashed line does the same for the right peak shifts and has equation (66). Lastly the dotted line fits the linearity of the change in peak separation and is also shown in equation (67).

The data in this graph show an unexpected trend, which could be due to an unfavorably orientation of the MOFBG sensor in the CFRP. As in section 5.3, a linear increase (or decrease) is expected when the impact force is increased, but this was not the case. Further research is needed to determine the cause of inconsistent data. For this reason the CFRP plate was not sawed open to perform a post-mortem analysis on the orientation of the MOFBGs.

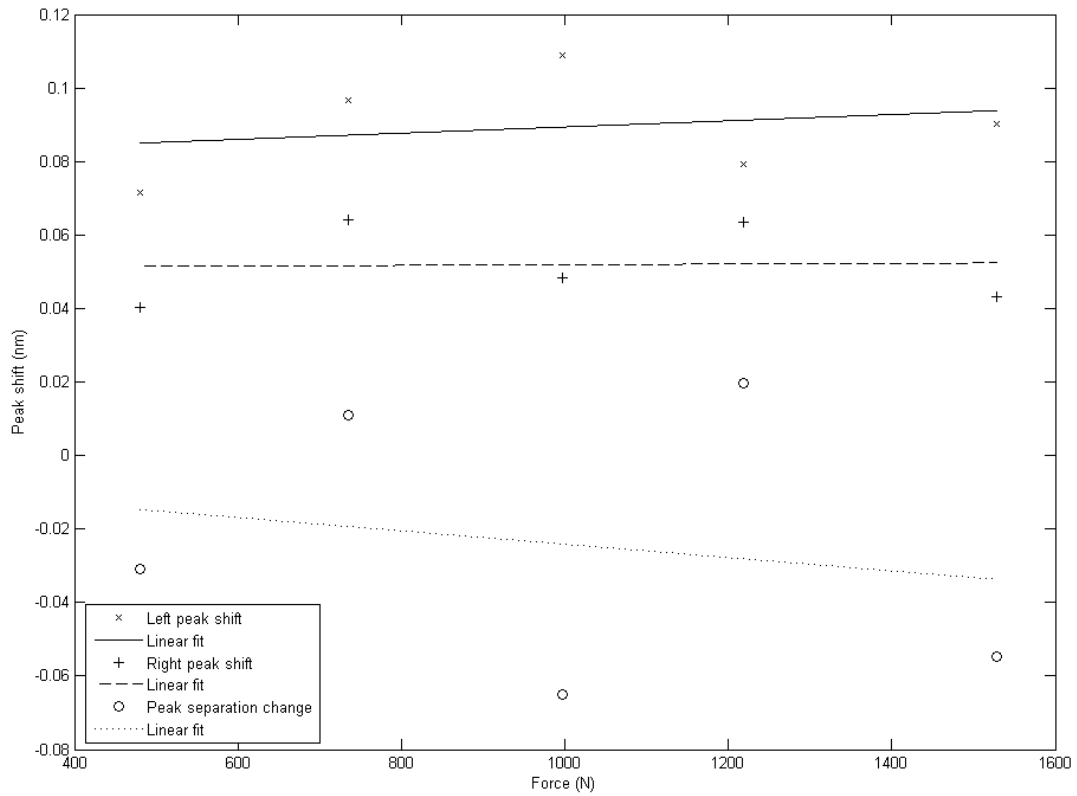


Figure 92: The left and right peak shifts and peak separation change for the first MOFBG with Bragg wavelengths and . Measurements were averaged four times and this at five different drop angles from 20 ° to 60 °. The x-marker shows the data points for the averaged left peak change, the +-marker for the right peak change, and the o-marker for the change in peak separation. For each dataset a linear fit was provided.

$$\Delta\lambda_{b,L} = 8.43 \cdot 10^{-6} \cdot F + 0.0810 \quad (65)$$

$$\Delta\lambda_{b,R} = 9.12 \cdot 10^{-7} \cdot F + 0.0510 \quad (66)$$

$$(\Delta\lambda_{b,L} - \Delta\lambda_{b,R}) = -1.82 \cdot 10^{-5} \cdot F - 0.00594 \quad (67)$$

The impact results of the second grating with Bragg wavelengths 1541.951 nm and 1542.730 nm are shown in Figure 93. The peak shifts are measured for impact forces between 400 N and 1600 N in this case. The Bragg wavelength of the left peak ('x') shifts between -20 pm and -60 pm, the right peak ('+') shifts between -10 pm and -40 pm and the peak separation changes are between 10 pm and 20 pm.

A full line denotes the linear fit made for the left peak shifts and its equation is shown in equation (68) (58). The dashed line does the same for the right peak shifts and has equation (69). Lastly the dotted line fits the linearity of the change in peak separation and is also shown in equation (70).

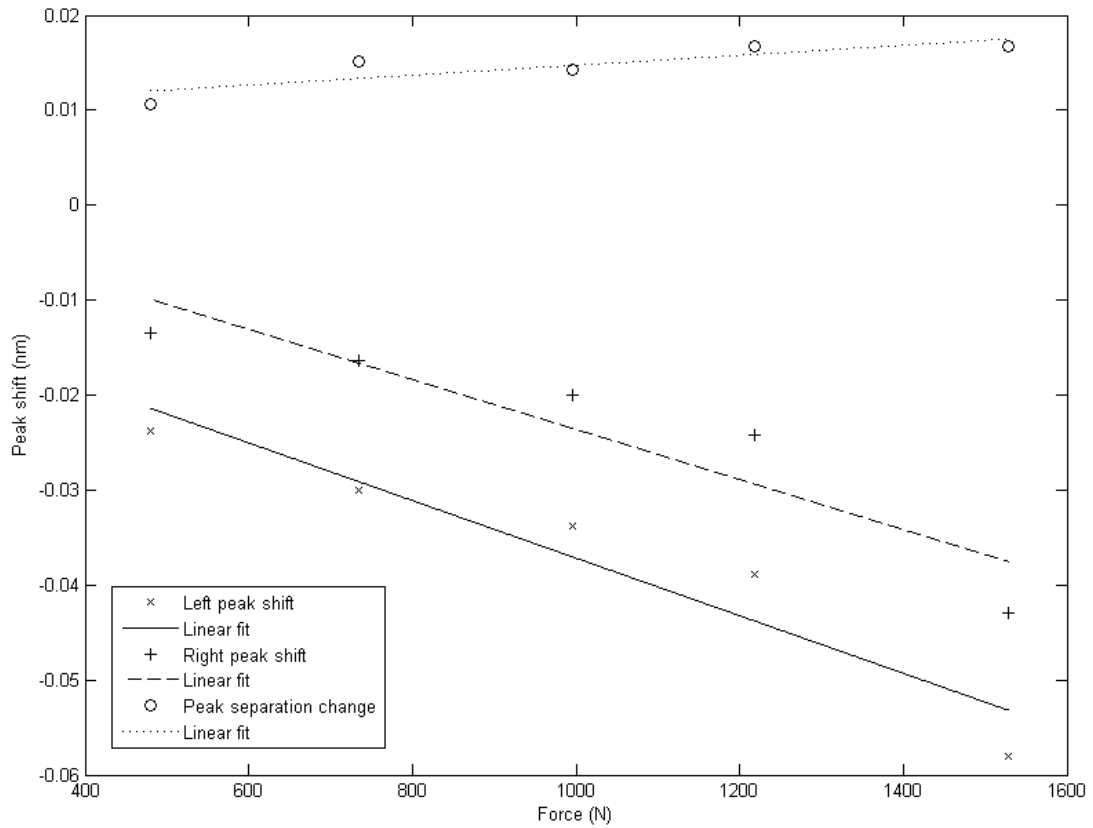


Figure 93: The left and right peak shifts and peak separation change for the second MOFBG with Bragg wavelengths and . Measurements were averaged four times and this at five different drop angles from 20 ° to 60 °. The x-marker shows the data points for the averaged left peak change, the +-marker for the right peak change, and the o-marker for the change in peak separation. For each dataset a linear fit was provided.

$$\Delta\lambda_{b,L} = -3.03 \cdot 10^{-5} \cdot F - 0.00682 \quad (68)$$

$$\Delta\lambda_{b,R} = -2.63 \cdot 10^{-5} \cdot F + 0.00273 \quad (69)$$

$$(\Delta\lambda_{b,L} - \Delta\lambda_{b,R}) = 5.23 \cdot 10^{-6} \cdot F + 0.00951 \quad (70)$$

The peak shift values here are of the same order as the ones found in sections 5.3.1.d to 5.3.1.f, and also the trends of the shifts is consistent with what is expected. Because, however, no post-mortem analysis is performed, so the angle of orientation of the two MOFBGs is unknown, it requires more research to do a full 3D strain analysis. As there was no more time, this was not in the scope of this thesis, but is a future prospect.

5.5. Impacts on IHPT-samples with VCSEL-interrogator

The IPHT MOFBGs were inscribed with a Talbot interferometric setup especially to have targeted Bragg wavelengths around 1541 nm and 1543.5 nm. This to be used by the VCSEL-interrogator as explained in section 4.4. Figure 70 shows the setup of the interrogator.

We started testing the VCSEL-interrogator on the IPHT MOFBGs at low interrogation frequencies (10 Hz). At these frequencies the four Bragg peaks were clearly visible with the VCSEL-interrogator. The VCSEL was driven between currents of 2.20 mA and 10.30 mA. These values were obtained from the VCSEL calibration in order to have a spectrum sweep between 1540 nm and 1545 nm. As illustration we show the reflection spectra of the MOFBGs 'Sidney1', 'Sidney6' and 'Sidney8', which are the ones embedded in CFRP and able to be read out, as displayed in the layout in Figure 90. The spectra are compared to the spectra measured with the ASE/OSA-interrogator (section 4.1) and displayed respectively in Figure 94, Figure 95 and Figure 96.

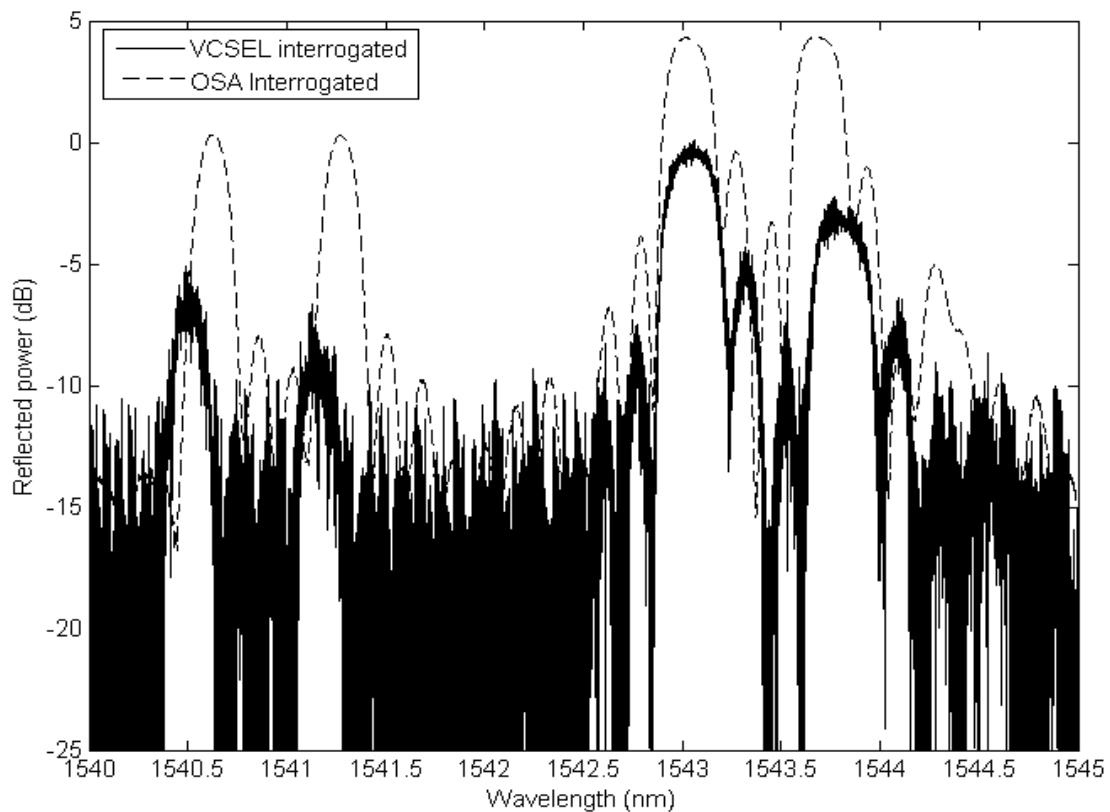


Figure 94: Reflection spectrum of MOFBG 'Sidney1' in Figure 90. The full line shows the VCSEL-interrogated spectrum and the dashed line the comparison with the ASE/OSA-interrogator.

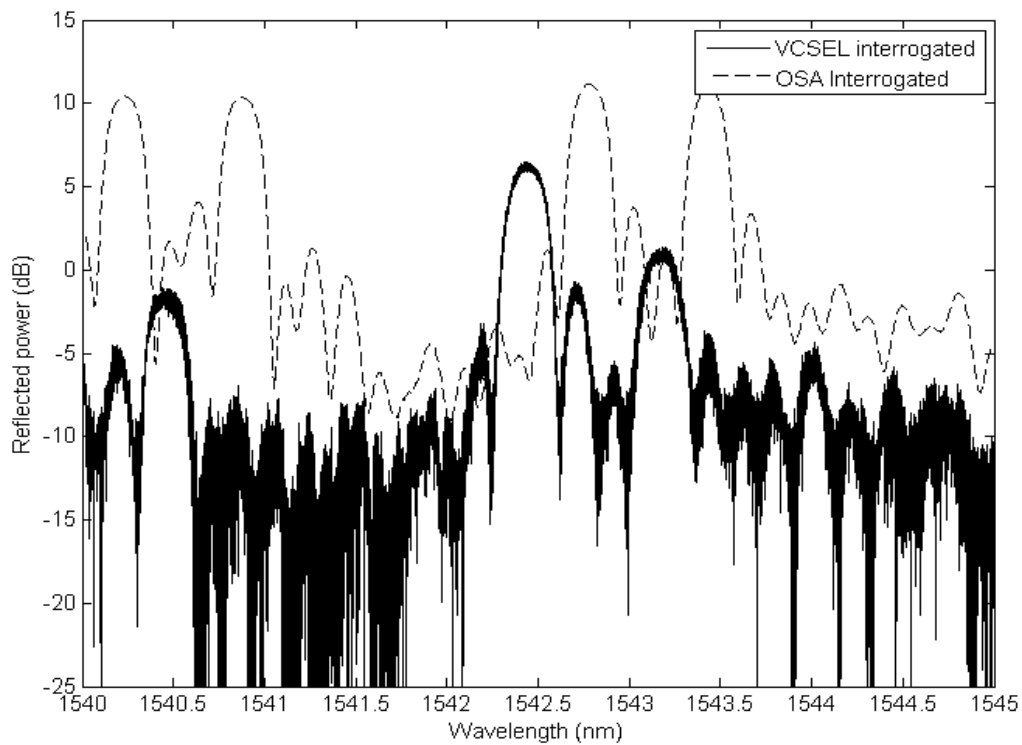


Figure 95: Reflection spectrum of MOFBG 'Sidney6' in Figure 90, it was this MOFBG that was used in the other measurements in this section. The full line shows the VCSEL-interrogated spectrum and the dashed line the comparison with the ASE/OSA-interrogator.

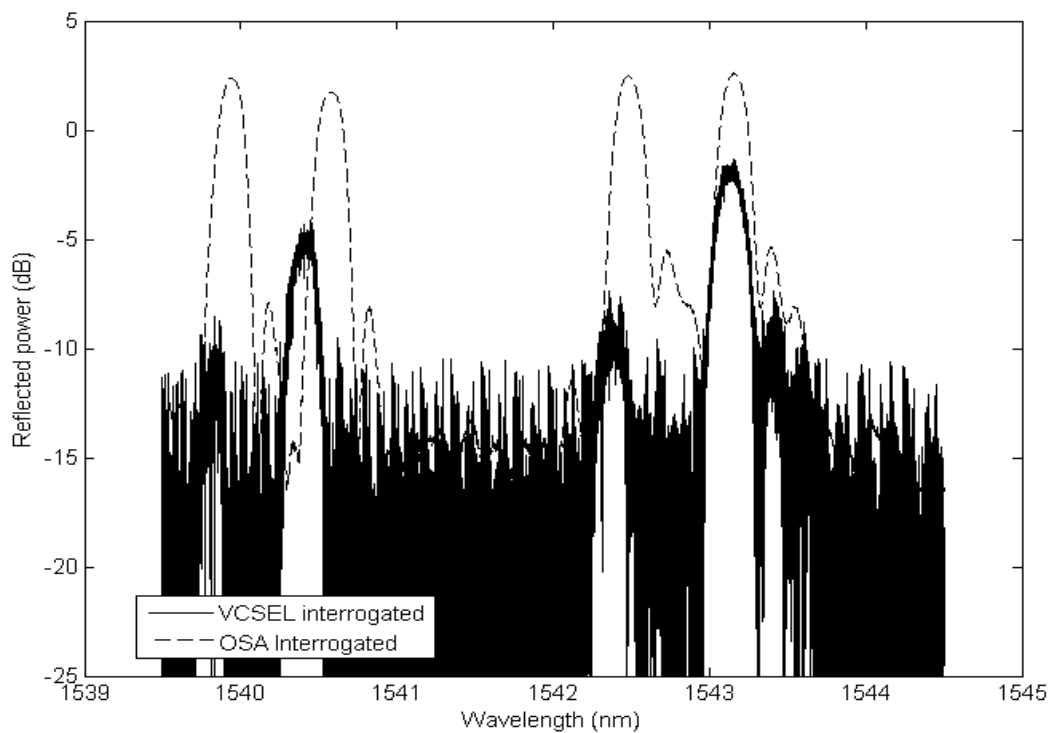


Figure 96: Reflection spectrum of MOFBG 'Sidney8' in Figure 90. The full line shows the VCSEL-interrogated spectrum and the dashed line the comparison with the ASE/OSA-interrogator.

We conclude that the spectra of the IPHT MOFBGs can indeed be read out with the VCSEL-interrogator and are consistent with the spectra read out by the ASE/OSA.

The VCSEL-interrogated spectra are however not identical to the spectra measured by the ASE/OSA-interrogator. This is possibly by temperature effect inside the VCSEL, which made the VCSEL – wavelength shift with respect to the wavelength it was calibrated for. When only looking at relative wavelength shifts, like the shifts in Bragg wavelength we are interested in, this should however not form a problem. As mentioned in section 4.4.2, the wavelength of the VCSEL also changes when the scanning speed is increased. Because it was not possible to perform a calibration of the emission spectrum of the VCSEL, when the VCSEL was operated at fast current sweeps, we will also have to look at relative Bragg peak position when doing a full spectrum measurement.

A second artifact that needs to be noted is the fact the light from a VCSEL is polarized. Depending on the way the polarized light is coupled into the MOF, more light could be traveling in one mode than in the other. This will automatically imply that the Bragg peak of one mode will be clearer than the Bragg peak of the other mode containing less light power. The coupling of the VCSEL light into the MOF was not in the scope of this thesis. During the measurements this problem was solved by changing the position of the optical fibers until a quasi-equal amount of light was traveling in both modes, whenever possible.

5.5.1. Full spectrum measurements

When measuring the full spectrum of the MOFBG denoted as ‘Sidney1’ in Figure 90 at interrogation rates higher than 500 Hz, we noticed that the number of data points per spectrum became insufficient to represent the reflection peaks. Figure 97 to Figure 99 show the spectrum interrogated with the VCSEL-interrogator for repetition rates of 500 Hz, 1000 Hz and 2000 Hz respectively (dashed lines). All spectra are compared with the spectrum obtained by interrogation at 100 Hz (full line).

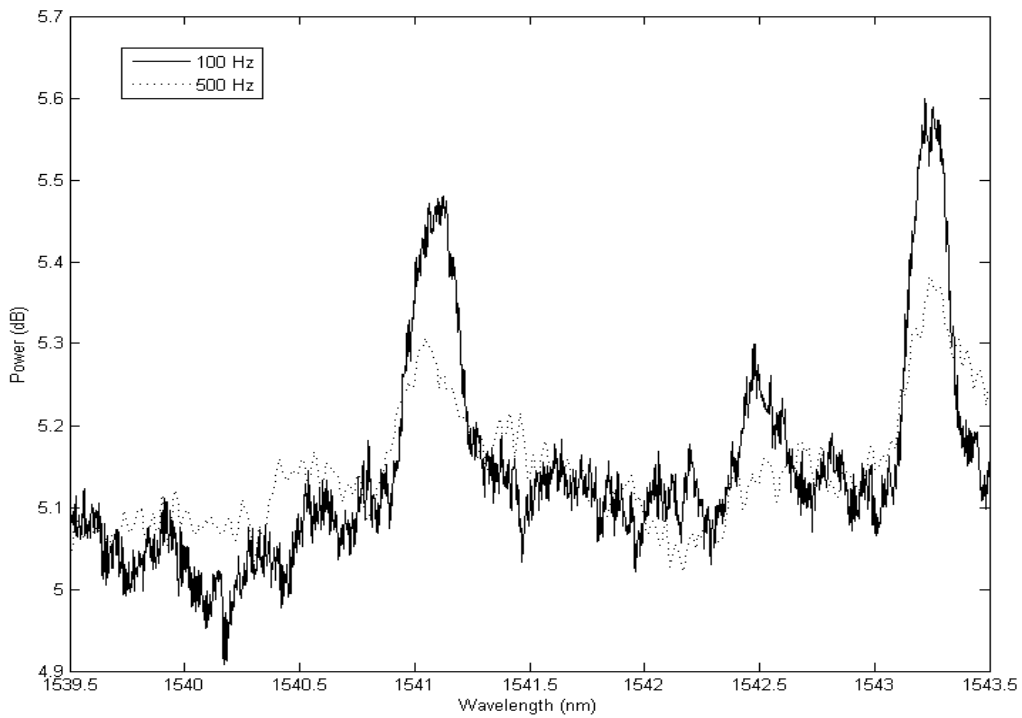


Figure 97: The spectrum of the MOFBG interrogated with the VCSEL setup at 500 Hz (dashed) compared with the interrogation at 100 Hz (full line). The spectrum at the higher frequency seems deformed compared to the one at the lower frequency.

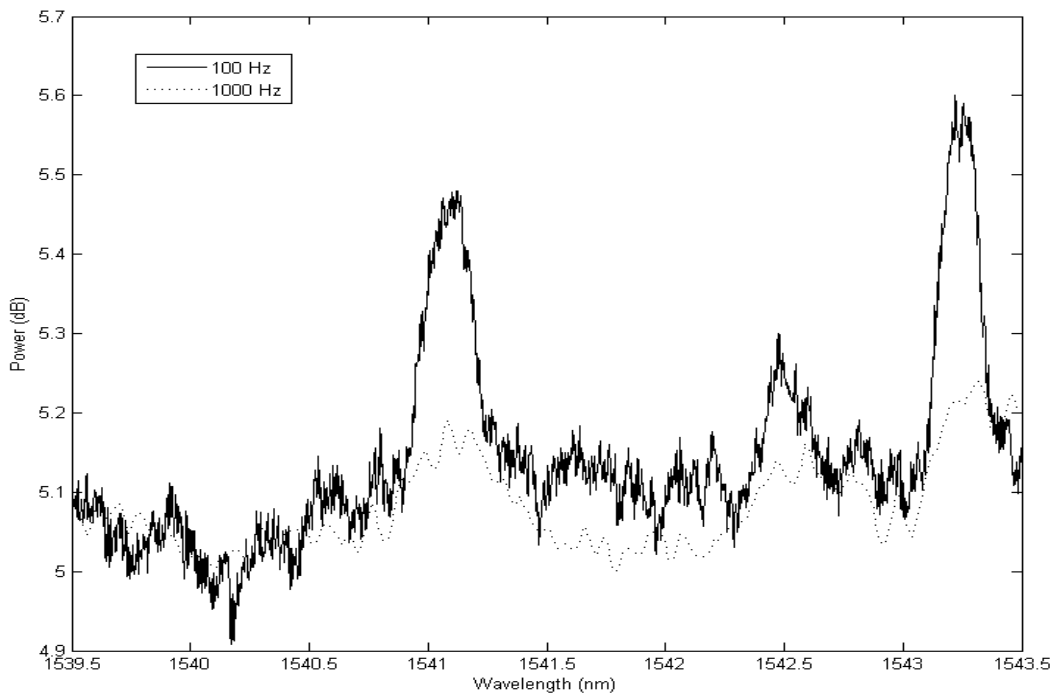


Figure 98: The spectrum of the MOFBG interrogated with the VCSEL setup at 1000 Hz (dashed) compared with the interrogation at 100 Hz (full line). The spectrum at the higher frequency seems deformed compared to the one at the lower frequency.

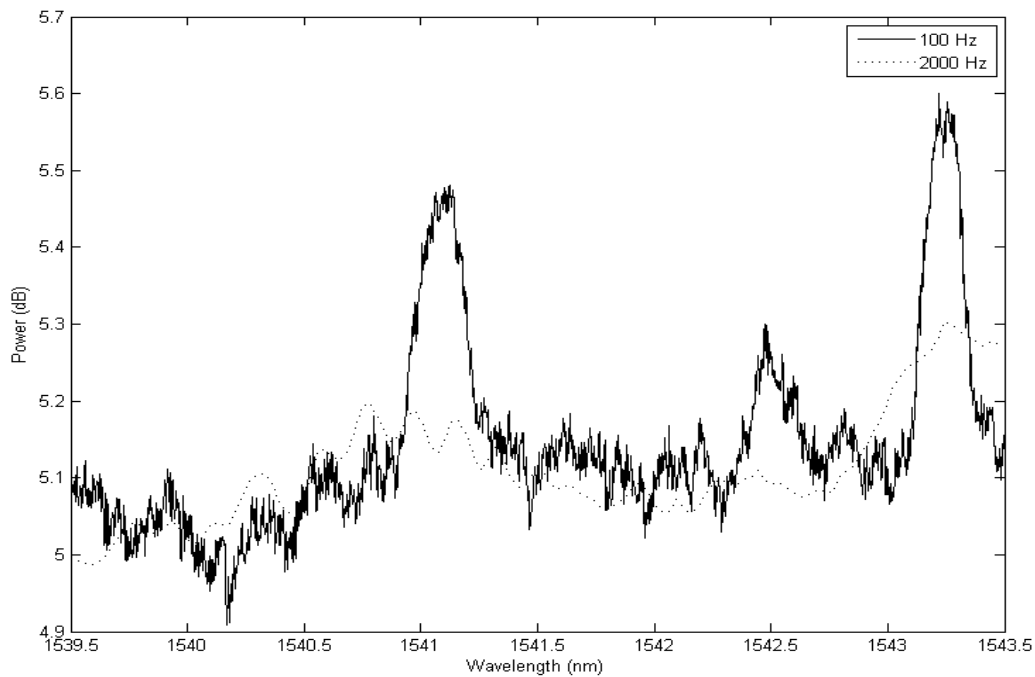


Figure 99: The spectrum of the MOFBG interrogated with the VCSEL setup at 2000 Hz (dashed) compared with the interrogation at 100 Hz (full line). The spectrum at the higher frequency seems deformed compared to the one at the lower frequency.

At 100 Hz the four Bragg peaks are clearly visible, although the left peaks of each grating are lower in power, because of polarization effects. At 500 Hz (Figure 97) the peaks are still clearly distinguishable, however lower in power. This is still the case at 1000 Hz (Figure 98), but more pronounced. At a higher interrogation repetition of 2000 Hz, the spectrum is deformed in a way that the peaks are no longer visible. At even higher repetition rates, the peaks were no longer visible.

A reason for this deformation of the spectrum is possibly found in the sampling rate of the data acquisition card (DAQ) used. This NI USB-6343 DAQ was operating at a maximal sampling rate of 500 kHz, so 500000 samples per second were obtained. When, however, the repetition rate of the VCSEL was set to eg. 4000 kHz, this means only 125 points remained for a full spectral analysis of a wavelength span of 4 nm (see Figure 99). This gave a hardware resolution of maximally 32 pm, which, together with polarization effects and wavelength shifting (and possibly even deformation) of the VCSEL-spectrum at higher repetition rates, made a full spectral analysis with the VCSEL-interrogator not possible.

Possible solutions, which were not in the scope of this thesis, are using a DAQ with higher sampling rates, or look at other than full-spectrum interrogation techniques. An example is given in the next section.

5.5.2. Future prospect: edge filtering

A possible way to solve the high-speed interrogation problems explained in section 5.5.1 above, is to use the VCSEL-interrogator in an edge-filtering techniques. The concept of edge-filtering is shown in Figure 100. In this technique the VCSEL is driven at a constant current, and so the VCSEL spectrum is fixed in time. By choosing the driving current in such a way that the VCSEL-spectrum is located at an

edge of the FBG peak, the amount of light reflected by the FBG will change when the Bragg wavelength changes and the peak shifts to the left or the right.

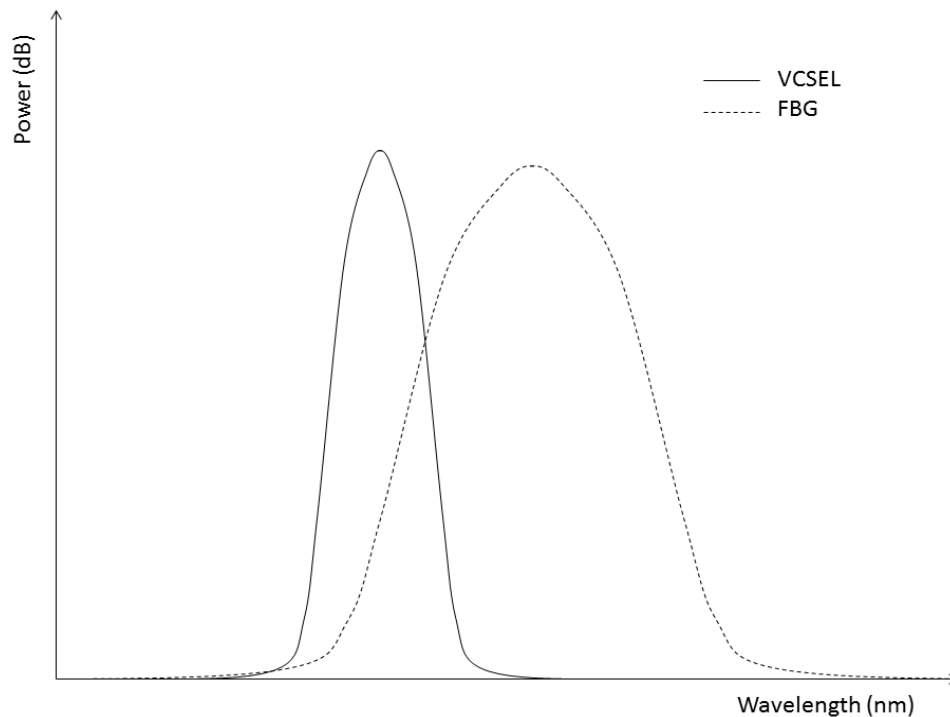


Figure 100: The principle of edge-filtering of a FBG with a VCSEL. The VCSEL-spectrum is stationary in time, but when the Bragg peak shifts to the left more power is reflected, and when it shifts to the right, less power is reflected.

In this way the VCSEL spectrum will not deform due to high repetition rates, and the sampling can occur at full sampling rate of the DAQ. A drawback of this technique is the fact that per Bragg peak a VCSEL and photodiode is needed. Implementation of this edge-filtering technique was however not in the scope of this thesis outline, and is a future prospect.

5.6. Conclusion

In this chapter we show the results of the dynamic strain measurements with microstructured optical fiber sensors embedded in composite CFRP plates. The 3D strain field inside a CFRP composite plate was measured during an impact excitation on the plate.

An impact setup is proposed to act as a dynamic excitation by impacting the surface of the CFRP plate with an aluminum tip. During this very short impact of a few milliseconds the 3D strain was measured at a repetition rate of 4266 Hz with a commercially available FBG-scan 700. At the same time the impact force was measured with a force sensor, attached to the impact tip.

This was done for three distinct embedded MOFBGs oriented at 21.67° , 109.67° and 115.67° inside a composite plate. **We were able to measure the impacts in a dynamic way with our MOFBGs, something that was not done before.**

Two of these MOFBGs, oriented under 32.67° and $109,67^\circ$ were used to perform a strain transfer method. **We obtained the strains in three dimensions during a dynamic excitation, and the results**

were as we expected. The two in-plane strains were in the same order of magnitude and the transversal component of the strain, in the direction of the impact, was 5 times higher.

The same impact measurements were performed on MOFBGs fabricated at IPHT and embedded in CFRP plates with the same layout as the UMons samples. A first grating yielded unexpected data, possibly due to orientation errors of the MOF. A second MOFBG in the plate yielded values in the same order as those of the UMons measurements. Because no post-mortem analysis was performed, no transfer matrix method could be applied to calculate the 3D strain field inside the CFRP during an impact.

A miniaturized VCSEL-based interrogator was tested to also measure the same impacts. **We showed proof of concept of the VCSEL interrogator and were able to do a full-spectrum measurement with it at frequencies of 10 Hz.** Due to wavelength shifts of the VCSEL during high speed driving, polarization effects and an insufficient sampling rate of the data acquisition, a full-spectrum analysis of a four-peak MOFBG was not possible. Future prospects include optimizing the data acquisition or switching to a edge-filtering technique to also allow this VCSEL-based interrogator to do dynamic measurements at frequencies higher than 500 Hz.

6. Conclusion and future prospects

The main objective of my master thesis was to enable dynamic 3D measurements of strain with microstructured optical fiber Bragg gratings (MOFBGs) embedded in structural composite components. This thesis combined the strain sensing properties of fiber Bragg gratings (FBGs) together with the high birefringence of a specific type of microstructured optical fiber (MOF) embedded inside a carbon fiber reinforce polymer (CFRP) composite structure to create a sensor capable of measuring the 3D strain field inside that component. Using a high speed interrogator we were able to measure impact forces onto a composite component.

To achieve this objective we tackled the following challenges. First we had to prepare a 3D MOFBG sensor. This included using a special splicing procedure for splicing PCF to single mode fiber (SMF), developing a method for orienting the microstructure of the MOF, inscribing an FBG with a scanning phase mask technique and choosing a sensor layout. Second, we had to embed the MOFBGs in composite materials and perform a cure monitoring of the composite. Subsequently we had to carry out dynamic measurements on these embedded MOFBGs with a custom built impact setup and derive the 3D strain field from these measurements. Finally, we also had to design a miniaturized VCSEL-based interrogator for 3D MOFBG sensors.

6.1. Accomplishments

6.1.1. Preparing the 3D strain MOFBGs for embedding

We succeeded in designing two types of 3D strain sensors with MOFBGs. The first type of sensors used differently oriented MOFBGs with the same Bragg wavelength in different MOFs. The second type used two MOFBGs in the same MOF, which were wavelength division multiplexed. In this way 3D MOFBGs could be interrogated with one channel.

We used a special splicing program to fusion splice the MOF to standard SMF, and succeeded in doing so. We proposed a simple method, including a USB microscope and UV-curing adhesive, order to fix the orientation of the fiber. Furthermore, we succeeded in inscribing six FBGs into six different MOFs with a UV scanning phase ask technique.

6.1.2. Embedding the MOFBGs in CFRP composite materials

We successfully embedded our MOFBGs into CFRP composite stacks. We performed a monitoring of the cure cycle with our FBGs and showed that the sensors were able to follow the temperature course and the residual strain developed during the cooling of the composite. We characterized the FBGs and we showed that the Bragg peak separation had decreased or that the spectrum had shifted, depending on the orientation of the MOF. This did not have any negative consequences on the interrogation of the gratings and the processing of the Bragg peak shifts.

6.1.3. Dynamic 3D strain sensors

With a custom built impact setup for generating dynamical excitations, we showed that our 3D MOFBG sensors succeeded in measuring dynamical excitations generated in a composite CFRP material. We obtained the strains in three dimensions during a dynamic excitation, and the results were as we expected. The two in-plane strains were in the same order of magnitude and the transversal component of the strain, in the direction of the impact, was 5 times higher. **It is the first time that MOFBGs were used to monitor dynamic events and also the first time that 3D strain measurements during an impact were measured with these sensors.**

6.1.4. Miniaturized VCSEL-based interrogator

We successfully developed a miniaturized VCSEL-based interrogator consisting of only one VCSEL and a photodiode as photonic components. We calibrated the interrogator and we showed evidence that it could be used for measuring the reflection spectra of our 3D MOFBGs. **This was the first time to our knowledge that a VCSEL-based interrogator with the potential to be miniaturized at low cost was successfully applied to the interrogation of MOFBGs at 1550nm.**

6.2. Future prospects

6.2.1. Orientation of MOFBGs in composite materials

We believe that it is interesting to further explore the possibility of using a micro-CT scan for determining the orientation of a MOF inside a composite material without destroying the component, or for orienting the MOF prior to embedding it in the composite.

We investigated a micro-CT scan method to determine the orientation of the MOF, but due to limitations imposed by the available CT-scan device, it could not be used for characterizing the orientation of a long MOF sample or a composite structure embedded with MOFBGs.

The concept of using a micro-CT scan could still be promising for fixing or determining the orientation of MOFBGs. In this way orientation of MOFBGs would be possible along the entire fiber (not only at the end) and the orientation of the MOF embedded in a composite material could be determined without having to destroy the component.

6.2.2. Custom VCSEL-based interrogator

The custom built VCSEL-based interrogator proposed in this master thesis showed proof-of-concept at low interrogation rates, but did not allow operating at higher interrogation speeds due to the limited sampling rate of the data acquisition and possibly also due to polarization effects and deformation of the VCSEL spectrum at higher driving rates. We believe that it would be valuable to have a look at higher sampling rates of the data acquisition by using another data acquisition card (DAQ) with a sampling rate exceeding 500 kHz.

In case this does not solve the problem of the deformed reflection spectrum, the VCSEL setup could be used in an edge filtering technique, where the spectrum of the VCSEL is located at the edge of the FBG spectrum. Whenever the Bragg wavelength shifts, more or less light will be reflected, and the sampling can be done at 500 kHz. A disadvantage of this technique is that each FBG will require a separate VCSEL and photodiode.

6.2.3. Further impact measurements

Impact measurements were performed on two types of embedded samples, the first fabricated at the University of Mons and the second at the Leibniz Institute of Photonic Technology. The last set showed inconsistent data for one grating. Finding the reason requires carrying out more measurements and possibly improve the orientation of the MOFBG inside the composite.

A post-mortem analysis of the CFRP composite plate would give an answer to this question as it will allow determining the orientation of all the MOFBGs in order to do perform a correct transfer matrix operation and correct calculation of the 3D strain field.

6.2.4. Industrial prospects

Many companies fabricating structural components with composite materials start using FBGs in the fabricated parts. An interesting future prospect is the embedding of a MOFBG into a real component of an aircraft wing fabricated in composite material by the company ASCO. Their component showed weakness along a seam combining two different shapes, and it would be interesting to investigate if a MOFBG can be embedded in this component for doing 3D strain measurements and if it can measure or even predict damage in this component at the anticipated location. This experiment is planned in July.

References

- [1] C. Sonnenfeld, "Microstructured Optical Fibre Bragg Grating Sensors for Production and Health Monitoring of Carbon Reinforced Polymer Materials and Structures," PHD Dissertation, Vrije Universiteit Brussel, Brussel, Belgium, 2013.
- [2] F. Berghmans, *Optical Sensor Course*. Brussel: Vrije Universiteit Brussel, 2015.
- [3] L. Thévenaz, *Advanced Fiber Optics: Concepts and Technology*. EPFL Press, 2011.
- [4] A. Othonos, "Bragg Gratings in Optical Fibers: Fundamentals and Applications," in *Optical Fiber Sensor Technology*, K. T. V. Grattan and B. T. Meggitt, Eds. Springer US, 2000, pp. 79–187.
- [5] T. Geernaert, "Microstructured Fiber Bragg Grating Sensors," PHD Dissertation, Vrije Universiteit Brussel, Brussel, 2010.
- [6] K. O. Hill, "Photosensitivity in optical fiber waveguides: from discovery to commercialization," *IEEE J. Sel. Top. Quantum Electron.*, vol. 6, no. 6, pp. 1186–1189, Nov. 2000.
- [7] E. A. Al-Fakih, N. A. A. Osman, A. Eshraghi, and F. R. M. Adikan, "The Capability of Fiber Bragg Grating Sensors to Measure Amputees' Trans-Tibial Stump/Socket Interface Pressures," *Sensors*, vol. 13, no. 8, pp. 10348–10357, Aug. 2013.
- [8] C. Voigtländer, R. G. Becker, J. Thomas, D. Richter, A. Singh, A. Tünnermann, and S. Nolte, "Ultrashort pulse inscription of tailored fiber Bragg gratings with a phase mask and a deformed wavefront [Invited]," *Opt. Mater. Express*, vol. 1, no. 4, p. 633, Aug. 2011.
- [9] FBGS, "Draw Tower Gratings, <http://www.fbgs.com/>," May 2015.
- [10] A. Yariv and P. Yeh, *Optical Waves in Crystals: Propagation and Control of Laser Radiation*. Wiley, 2002.
- [11] A. Bertholds and R. Dandliker, "Determination of the Individual Strain-Optic Coefficients in Single-Mode Optical Fibers," *J. Light. Technol.*, vol. 6, no. 1, pp. 17–20, Jan. 1988.
- [12] P. Russell, "Photonic Crystal Fibers," *Science*, vol. 299, no. 5605, pp. 358–362, Jan. 2003.
- [13] P. Yeh, A. Yariv, and E. Marom, "Theory of Bragg fiber," *J. Opt. Soc. Am.*, vol. 68, no. 9, pp. 1196–1201, Sep. 1978.
- [14] D. M. Atkin, T. J. Shepherd, T. A. Birks, P. S. J. Russell, and P. J. Roberts, "Full 2-D photonic bandgaps in silica/air structures," *Electron. Lett.*, vol. 31, no. 22, pp. 1941–1943, Oct. 1995.
- [15] NKT Photonics, "<http://www.nktphotonics.com/>," May 2015.
- [16] P. S. J. Russell, "Photonic-Crystal Fibers," *J. Light. Technol.*, vol. 24, no. 12, pp. 4729–4749, Dec. 2006.
- [17] C. Sonnenfeld, S. Sulejmani, T. Geernaert, S. Eve, N. Lammens, G. Luyckx, E. Voet, J. Degrieck, W. Urbanczyk, P. Mergo, M. Becker, H. Bartelt, F. Berghmans, and H. Thienpont, "Microstructured Optical Fiber Sensors Embedded in a Laminate Composite for Smart Material Applications," *Sensors*, vol. 11, no. 12, pp. 2566–2579, Feb. 2011.
- [18] F. C. Campbell, *Introduction to composite materials*. ASM International, 2010.
- [19] P. K. Mallick, *Fiber-reinforced composites: materials, manufacturing, and design*, 3rd ed., [expanded and rev. ed.]. Boca Raton, FL: CRC Press, 2008.
- [20] J.-P. Pascault, H. Sautereau, J. Verdu, and R. J. J. Williams, *Thermosetting Polymers*. CRC Press, 2002.
- [21] J. K. Gillham, "Formation and properties of thermosetting and high tg polymeric materials," *Makromol. Chem. Macromol. Symp.*, vol. 7, no. 1, pp. 67–74, Jan. 1987.
- [22] E. Turi, *Thermal Characterization of Polymeric Materials*. Elsevier, 2012.
- [23] G. Jr and R. E., "Existing technologies for condition monitoring of construction materials and bridges," *FIBER Opt. Sens. Constr. Mater. Bridg. - Proc. Int. Workshop HELD MAY 1998*, 1998.
- [24] V. Karbhari and V. M. Karbhari, "Health monitoring, damage prognosis and service-life prediction - Issues related to implementation," *Sens. Issues Civ. Struct. Health Monit.*, p. 301, 2005.

- [25] G. Housner, L. Bergman, T. Caughey, A. Chassiakos, R. Claus, S. Masri, R. Skelton, T. Soong, B. Spencer, and J. Yao, "Structural Control: Past, Present, and Future," *J. Eng. Mech.*, vol. 123, no. 9, pp. 897–971, 1997.
- [26] G. F. Fernando, "Fibre optic sensor systems for monitoring composite structures," *Reinf. Plast.*, vol. 49, no. 11, pp. 41–49, Dec. 2005.
- [27] SPIE, "www.optics.org, visited on 2015-05-14." .
- [28] T. Geernaert, S. Sulejmani, C. Sonnenfeld, K. Chah, G. Luyckx, N. Lammens, E. Voet, M. Becker, H. Thienpont, and F. Berghmans, "Internal strain monitoring in composite materials with embedded photonic crystal fiber Bragg gratings," 2014, p. 92260D.
- [29] J. A. Guemes and J. M. Menendez, "Response of Bragg grating fiber-optic sensors when embedded in composite laminates," *Compos. Sci. Technol.*, vol. 62, no. 7, pp. 959–966, 2002.
- [30] M. S. Mueller, H. J. El-Khozondar, T. C. Buck, and A. W. Koch, "Analytical solution of four-mode coupling in shear strain loaded fiber Bragg grating sensors," *Opt. Lett.*, vol. 34, no. 17, pp. 2622–2624, Sep. 2009.
- [31] M. S. Willer, L. Hoffmann, A. Sandmair, and A. W. Koch, "Full Strain Tensor Treatment of Fiber Bragg Grating Sensors," *IEEE J. Quantum Electron.*, vol. 45, no. 5–6, pp. 547–553, Jun. 2009.
- [32] Ericsson Cables AB, "User's manual for the FSU 975 single fiber fusion splicer by Ericsson," *Sundbyberg Swed.*
- [33] T. Geernaert, K. Chah, T. Nasilowski, H. Ottevaere, F. Berghmans, and H. Thienpont, "Fiber Bragg Grating Inscription in Highly Asymmetric HiBi PCF with a Low Intensity UV CW laser," presented at the Proceedings Symposium IEEE/LEOS Benelux Chapter, Brussel, Belgium, 2007.
- [34] Corning Incorporated, "Corning SMF-28 ULL Optical Fiber Datasheet," 2014.
- [35] Bruker, "<http://www.skyscan.be/products/1172.htm>," 18-May-2015.
- [36] FBGS, "Hardware Manual FBG-Scan X00-X04D-X08D Dynamic Units," Geel, Belgium.
- [37] ANDO Electric CO., LTD, "AQ6317 Optical Spectrum Analyzer Instruction Manual," 1999.
- [38] Micron Optics, "Datasheet Optical Sensing interrogator sm125," *Atlanta GA 30345 USA*, 2009.
- [39] T. Vella, S. Chadderdon, R. Selfridge, S. Schultz, S. Webb, C. Park, K. Peters, and M. Zikry, "Full-spectrum interrogation of fiber Bragg gratings at 100 kHz for detection of impact loading," *Meas. Sci. Technol.*, vol. 21, no. 9, p. 094009, Sep. 2010.
- [40] A. Propst, K. Peters, M. A. Zikry, W. Kunzler, Z. Zhu, M. Wirthlin, R. Selfridge, and S. Schultz, "Dynamic, full-spectral interrogation of fiber Bragg grating sensors for impact testing of composite laminates," 2009, p. 75030G–75030G–4.
- [41] B. Van Hoe, E. Bosman, J. Missinne, S. Kalathimekkad, G. Lee, Z. Yan, K. Sugden, D. J. Webb, G. Van Steenberge, and P. Van Daele, "Low-cost fully integrated fiber Bragg grating interrogation system," 2012, p. 83510U–83510U–8.
- [42] J. Frieden, J. Cugnoni, J. Botsis, T. Gmür, and D. Ćorić, "High-speed internal strain measurements in composite structures under dynamic load using embedded FBG sensors," *Compos. Struct.*, vol. 92, no. 8, pp. 1905–1912, Jul. 2010.
- [43] The MathWorks Inc., *MATLAB R2013a (8.1.0.604)*. USA, 2013.
- [44] G. Verschaffelt, "LASERs course: Semiconductor lasers," Brussel: Vrije Universiteit Brussel, 2014.
- [45] N. G. Basov, "Semiconductor lasers," *Nobel Lect. Phys. 1963 Ę 1970*, p. 89, 1998.
- [46] A. Lamberti, S. Vanlanduit, B. De Pauw, and F. Berghmans, "Influence of Fiber Bragg Grating Spectrum Degradation on the Performance of Sensor Interrogation Algorithms," *Sensors*, vol. 14, no. 12, pp. 24258–24277, Dec. 2014.
- [47] A. Lamberti, S. Vanlanduit, B. De Pauw, and F. Berghmans, "A novel fast phase correlation algorithm for peak wavelength detection of fiber Bragg grating sensors," *Opt. Express*, vol. 22, no. 6, p. 7099, Mar. 2014.

Appendix 1: MATLAB script for OSA READOUT

Reads out the ANDO Electric Optical Spectrum Analyzer AQ6317 with a GPIB-interface automatically.

```
% Steve Vanlanduit  
% Sidney Goossens  
% 2014-2015
```

Initialize

```
clear all;  
close all;
```

Set GP-IB address parameters

```
daqreset;  
instrreset;  
GPIBAddress = 1; % see <MY ADRS> of the [SYSTEM] switch (between 0 and 30)  
g = gpib('ni',0,GPIBAddress);  
fopen(g);
```

Set numerical parameters

```
LambdaC=1542; % Choose central wavelength (nm)  
Span=5; % Choose wavelength span (nm)  
Res=0.01; % Choose resolution ( between 0.01 and 2.0 nm)  
avg=2; % Choose averaging (1 to 1000)  
MeasureTime=180; % Choose time to wait for OSA measuring (sec)  
sample=' Sample name'; % Choose a name for the data
```

Using auto measurement to determine maximum wavelength and center it

```
% fprintf(g,'AUTO'); % Start auto measurement  
% pause(16.5); % Wait for OSA to measure  
% fprintf(g,'STP'); % Stop auto measurement  
  
% fprintf(g,'PKSR'); % Let OSA determine max of spectrum  
% fprintf(g,'MKR?'); % Markers ?  
% marker=fscanf(g); % Scan for marker  
%  
% LambdaC=str2num(marker)
```

Set Parameters for OSA

```

CentralString=strcat('CTRWL',num2str(LambdaC));
fprintf(g,CentralString) % set central wavelength (nm)
SpanString=strcat('SPAN',num2str(Span));
fprintf(g,SpanString) % Set wavelength span (nm)
ResString=strcat('RESOLN',num2str(Res));
fprintf(g,ResString) % Set wavelength span (nm)
fprintf(g,'ZSWPT10') % set sweep time in sec: 0 to 50 in 1sec steps
AvgString=strcat('AVG',num2str(avg));
fprintf(g,AvgString) % set averaging 1 to 1000
fprintf(g,'TRFMT2') % select a record format: 0=binary, 2=text
fprintf(g,'SD1') % set string delimiter to CRLF
fprintf(g,'ATREF1') % Set automatic reference level for power
fprintf(g,'LSCL5.0') % Set power scale
fprintf(g,'SHI1'); % Set sensitivity

```

Acquire sweep data

```

fprintf(g,'SGL') % AUTO or SGL (single) or STP (stop)
pause(MeasureTime); % Set time (sec) to wait for measurement

LambdaB=LambdaC-Span/2; % Define begin and end wavelength
LambdaE=LambdaC+Span/2; % from central wavelength and span
fvec = ([LambdaB:0.002:LambdaE]); % Define wavelength range vector
Nf = length(fvec);

```

Read out data

```

aa=zeros(1,Nf+1);
fprintf(g,'LDATA')
for i=1:(Nf+1)
    a=fscanf(g);
    a=str2num(a);
    aa(i)=a;
end;

spectrumDBM = aa(2:end);
spectrum=10.^(spectrumDBM./10);

Data=[fvec; spectrum]'; % Row1 wavelength Row2 power
DataDBM=[fvec; spectrumDBM]'; % Row1 wavelength Row2 dBm

```

Save and plot data

```

% Titles of figures
titlePower=strcat('OSA Spectrum Sample ',sample);
titleDBM=strcat('dBm OSA Spectrum Sample ',sample);

%Plotting

```

Appendix 1: MATLAB script for OSA READOUT

```
f=figure
plot(fvec,spectrumDBM,'k');
xlabel('wavelength (nm)');
ylabel('Power (dBm)');

%Saving data as a mat file
titleDataMat=strcat('OSA Spectrum Sample',sample,'.mat');
save(titleDataMat,'DataDBM');

% Saving data as a figure in three file formats
titleFig=strcat('OSA Spectrum Sample ',sample);
saveas(f,titleFig,'fig');
saveas(f,titleFig,'eps');
saveas(f,titleFig,'jpg');
```

End

Sidney Goossens 2014-2015

[Published with MATLAB® R2013a](#)

Appendix 2: MATLAB script Impact Measurements with FBG-scan (700/704D) and the Piezotronics 208B02 Force Sensor

Ben De Pauw, Alfredo Lamberti, Sidney Goossens - Vrije Universiteit Brussel - 2014-2015

Initialization

```
clear all
clc
close all
```

Set parameters

```
% Choose a file name for saving
filename = 'MONS_2_3_00_2015-04-22_2_7_60_4.mat';

% Set folders for data saving
FBGSfolder = 'D:\Dropbox\Vrije Universiteit Brussel (2011 - 2014)\Thesis\2015-04-20 Mons Impact Measurements - External Source'; addpath(FBGSfolder);% folder that contains toolbox for FBG Scan
MatlabdataDir = 'D:\Dropbox\Vrije Universiteit Brussel (2011 - 2014)\Thesis\2015-04-20 Mons Impact Measurements - External Source\FBGs';
addpath(MatlabdataDir);
```

Setting variables for FBG-scan Interrogator

```
Tacq=5; %acquisition time in sec
prev_index = 1; %refers to the first spectrum
int_time =250; % integration time
line_rate = 4e3; % sampling frequency
num_spectra=Tacq*line_rate; % number of spectra to acquire
process_mode = 3; % ring processing mode
channel=1;
```

Settings for the FBG reflection Spectra

```
lambda_min=1525;
lambda_max=1565;
wavelength_range=lambda_max-lambda_min; % wavelength range in nm of the FBGs 700
samples=512; % number of points for the entire reflection spectrum
```

Appendix 2: MATLAB script Impact Measurements with FBG-scan (700/704D) and the Piezotronics 208B02 Force Sensor

```
res=wavelength_range/samples; % resolution
lambda=linspace(lambda_min,lambda_max,samples);

width=1; % nm % window width around each Bragg wavelength
nwind=round(width/res); % samples per window
```

Settings of the acquisition with the NI DAQ

```
Nacq = Tacq*4266.6667; % number of time samples of acquisition
Fsample = 1./(Tacq./Nacq); % sample frequency
Nchans = 1; % number channels
Nchansinput=1;
% channel 0 Force vibration signal ----> ai0
```

Create data acquisition objects

```
devs = daq.getDevices;
s = daq.createSession('ni');
s.DurationInSeconds=Tacq; % Set acquisition time
s.Rate=4000;
ai = s.addAnalogInputChannel( devs.ID,[0:(Nchansinput-1)], 'voltage'); % see 'devs' DEVICE IDs

cd(FBGSfolder)
mex fbgs.cpp Sense2020D11.lib
pause(1);
fbgs('open');
fbgs('load_calibration');
fbgs('set_channel',channel);
beep
fbgs('start_grabbing_constantly',3);

fbgs('set_int_time_and_line_rate',int_time,line_rate);
previous=fbgs('get_last_spectrum_index');

data = s.startForeground();

% fbgs('set_int_time_and_line_rate',int_time,line_rate);
last_index = fbgs('get_last_spectrum_index');

try
    spectdata = fbgs('indexspectra',prev_index,last_index-previous);
catch
    disp('Error occured in FBG acquisition');
end;

a=size(spectdata,2);
b=size(data,1);
difference=abs(b-a);

spectdata=spectdata(:,difference:end).';
fbgs('stop_grabbing_constantly');
```

```
pause(0.5);  
fbgs('close');
```

Save workspace

```
save(filename);  
  
token = strtok(filename, '.');
```

Force data

```
force=data.*11241; % Force in Newton  
timeforce=[0:length(data)-1]'/4266.6667; % Time in seconds  
  
% Plotting  
h=figure;  
plot(timeforce,force);  
xlabel('Time (s)');  
ylabel('Force (N)');
```

Script for deviding the FBG-relection spectrum into two parts and letting the FPC-algorithm loose on both.

Sidney Goossens - Vrije Universiteit Brussel - 2014-2015

Defining parameters

```
cut_point=482;  
%res=;  
flag=0;  
num_spec=5;
```

Determining the two peaks

```
[A index_left]=max(spectdata(1,cut_point-20:cut_point));  
[B index_right]=max(spectdata(1,cut_point:end));  
  
index_left=index_left+cut_point-20;  
index_right=index_right+cut_point;  
  
Half_peak_diff=round((index_right-index_left)/2);
```

Defining two parts

```
spectdata_left=spectdata(:,index_left-Half_peak_diff:index_left+Half_peak_diff);  
spectdata_right=spectdata(:,index_right-Half_peak_diff:index_right+Half_peak_diff);
```

```
lambda_left=lambda(:,index_left-Half_peak_diff:index_left+Half_peak_diff);  
lambda_right=lambda(:,index_right-Half_peak_diff:index_right+Half_peak_diff);
```

Letting loose FPC

```
Y_L=FPC(spectdata_left,res,flag,num_spec);  
Y_R=FPC(spectdata_right,res,flag,num_spec);
```

Plotting

```
f=figure;  
subplot(3,1,1)  
plot(Y_L,'k');  
xlabel('Time');  
ylabel('wavelength shift (nm)');  
title('Shift of left peak');  
subplot(3,1,2)  
plot(Y_R,'k');  
xlabel('Time');  
ylabel('wavelength shift (nm)');  
title('Shift of right peak');  
subplot(3,1,3)  
plot(Y_R-Y_L,'k');  
xlabel('Time');  
ylabel('wavelength shift (nm)');  
title('Distance between peaks');
```

Saving plot

```
token = strtok(filename, '.');  
  
titleFig=strcat('Peak shifts of measurement ',token);  
saveas(f,titleFig,'fig');  
saveas(f,titleFig,'eps');  
saveas(f,titleFig,'jpg');
```

Taking impact part

```
[M1 I1]=max(Y_L);  
[Mi1 Ii1]=min(Y_L);  
[M2 I2]=max(Y_R);  
[Mi2 Ii2]=min(Y_R);  
[M3 I3]=max(Y_R-Y_L);  
[Mi3 Ii3]=min(Y_R-Y_L);
```

Calculating highest maximum or lowest minimum

```
if -(Mi1)>M1
    M1=Mi1;
    I1=Ii1;
end

if -(Mi2)>M2
    M2=Mi2;
    I2=Ii2;
end

if -(Mi3)>M3
    M3=Mi3;
    I3=Ii3;
end

M4=M2-M1;

Y_L_section=Y_L(I1-40:I1+40);
Y_R_section=Y_R(I1-40:I1+40);

time_fbg_section=(0:length(Y_L_section)-1);
```

Plotting

```
j=figure;
subplot(3,1,1)
plot(time_fbg_section,Y_L_section,'k');
xlabel('Time (ms)');
ylabel('wavelength shift (nm)');
title('Shift of left peak');
subplot(3,1,2)
plot(time_fbg_section,Y_R_section,'k');
xlabel('Time (ms)');
ylabel('wavelength shift (nm)');
title('Shift of right peak');
subplot(3,1,3)
plot(time_fbg_section,Y_R_section-Y_L_section,'k');
xlabel('Time (ms)');
ylabel('wavelength shift (nm)');
title('Distance between peaks');
```

Saving plot

```
token = strtok(filename, '.');

titleFig=strcat('Peak shifts of measurement ',token);
saveas(j,titleFig,'fig');
saveas(j,titleFig,'eps');
saveas(j,titleFig,'jpg');
```

Calculating maximum shift (Additional option for also calculating maxima)

```
% [Y_L_max, MmL, ImL]=maximumshift(spectdata_left,res);
% Y_L_max_section=Y_L_max(abs(ImL-40):abs(ImL+40),1);
%
% [Y_R_max, MmR, ImR]=maximumshift(spectdata_right,res);
% Y_R_max_section=Y_R_max(abs(ImL-40):abs(ImL+40),1);
%
% %% Plotting
% k=figure;
% subplot(3,1,1)
% plot(Y_L_max_section,'k');
% xlabel('Time');
% ylabel('Wavelength shift (nm)');
% title('Shift of maximum left peak');
% subplot(3,1,2)
% plot(Y_R_max_section,'k');
% xlabel('Time');
% ylabel('Wavelength shift (nm)');
% title('Shift of maximum right peak');
% subplot(3,1,3)
% plot(Y_R_max_section-Y_L_max_section,'k');
% xlabel('Time');
% ylabel('Wavelength shift (nm)');
% title('Distance between maxima of peaks');
%
% %% Saving plot
%
% token = strtok(filename, '.');
%
% titleFig=strcat('Peak shifts of maxima measurement ',token);
% saveas(k,titleFig,'fig');
% saveas(k,titleFig,'eps');
% saveas(k,titleFig,'jpg');
```

Plotting Peaks (Additional option for also plotting all peak on top of each other and spotting differences.

```
% g=figure
% subplot(2,1,1)
% plot(spectdata_left');
% xlabel('Wavelength (nm)');
% ylabel('Amplitude');
% title('Left peaks');
% subplot(2,1,2)
% plot(spectdata_right');
% xlabel('Wavelength (nm)');
% ylabel('Amplitude');
% title('Right peaks');
%
% %% Saving peak plot
```

```
%  
% titleFig=strcat('Peaks of measurement ',token);  
% saveas(g,titleFig,'fig');  
% saveas(g,titleFig,'eps');  
% saveas(g,titleFig,'jpg');
```

Processing Force Data

```
[M I]=max(force); % Determine maximum force  
force_section=force(I-40:I+40,:); % Take out section of impact  
  
time_section=(0:length(force_section)-1)/4266.6667*1000; % Define time axis in ms  
  
i=figure; % Plot section of impact  
plot(time_section,force_section)  
xlabel('Time (ms)');  
ylabel('Force (N)');  
  
titleFig=strcat('Force during impact ',token);  
saveas(i,titleFig,'fig');  
saveas(i,titleFig,'eps');  
saveas(i,titleFig,'jpg');
```

Displaying maximum values in a table form

```
M  
D=[M1 M2 M3 M4]  
  
%E=[MmL MmR (MmR-MmL)]
```

Let me know when you are done

```
beep
```

End

Sidney Goossens - Vrije Universiteit Brussel - 2014-2015

[Published with MATLAB® R2013a](#)

Appendix 3: FBG Sensor Readout with VCSEL SETUP

Steve Vanlanduit, Sidney Goossens - Vrije Universiteit Brussel - 2014-2015

INIT

```
clear all;
close all;
title=strcat('test');
Freq=100;
```

NI DAC Parameters setting

```
if 1 % Set 1 on first time run to 1, else 0

% NI outputs
Dev = daq.getDevices;
session=daq.createSession('ni');
session.addAnalogOutputChannel(Dev.ID, {'ao0'}, 'voltage');
session.addAnalogInputChannel(Dev.ID, {'ai0'}, 'voltage');
% Set measurement channel properties
%session.Channels(3).InputType='Differential';
%session.Channels(3).Range=[-0.1 0.1];
InputRange = 10;
session.Channels(2).Range=[-InputRange InputRange];
%session.Channels(3).Range=[-InputRange InputRange];
%session.Channels(4).Range=[-InputRange InputRange];
```

Set output channels properties

```
OutputRange = 10;
session.Channels(1).Range=[-OutputRange OutputRange];

end;
```

Definitions of parameters

```
Rate = 5000; % Samples per second
session.Rate=Rate;
Ttot = 1; % Total measurement time [Seconds]
N = Ttot*Rate; % Total number of samples
%Freq = 100; % Ramp repetition frequency in Hz (sample frequency)
Nsamples = Ttot.*Freq; % Sweeps in measuring time
Nlambda = N./Nsamples; % Points per sweep (per ramp)
```

Sawtooth VCSEL current from inverse wavelength relation

```
Vstart = 1.0764;Vend = 5.0494;

DeltaLambda = (Vend-Vstart). *1200./Nlambda*2      % Wavelength Res in pm
```

Data acquisition

```
RampUP=linspace(Vstart,Vend,Nlambda./2);
RampDOWN=linspace(Vend,Vstart,Nlambda./2);

OutputData = repmat([RampUP RampDOWN],1,Nsamples).';
session.queueOutputData([OutputData(:)]);
data = session.startForeground;

% Only one column
data=data(:,1);
% Only one ramp
%data=data(1: numel(data)/2,1);

% dlmwrite('data.txt',data)           % Saves data to text
% Spec=dlmread('spectrum','\t',17,1); % Opens ref. FBG data
```

Plotting

```
OutputLambda=0.1074.*OutputData.*OutputData+0.3489.*OutputData+1539;
datadB=mag2db(data)./2;

% Clipping at -25 dB
datadB(datadB<-25)=-25;

% Plot axis setup
s=10; % Number of ticks on x-axis
num=numel(OutputData);
step=num/s;
Tick=1:step:num;
OutputLambdaTick=OutputLambda(1:step:end);

f=figure;
plot(data,'k')
xlabel('wavelength (nm)')
set(gca,'xtick',Tick,'xticklabel',OutputLambdaTick);
ylabel('10*log10(voltage)')
title('VCSEL interrogator (VCSEL 217)')

% Saving

saveas(f,title,'fig');
saveas(f,title,'eps');
saveas(f,title,'jpg');

VCSELData=[OutputLambda 10*log10(data(:,1))];
```

```
save(title, 'VCSELData');
```

Taking one repeat

```
tick=round(N/Freq);  
section=data(1+50:tick+50,1);  
g=figure  
plot(section);  
  
s1='_section';  
s = strcat(title,s1);  
  
saveas(g,s,'fig');  
saveas(g,s,'eps');  
saveas(g,s,'jpg');
```

End

[Published with MATLAB® R2013a](#)

Appendix 4: Automatic Reading Out of VCSEL-spectra with the OSA

Sidney Goossens - Vrije Universiteit Brussel - 2015-03-05

Init

```
clear all;
close all;
clc;
```

Define current range to drive VCSEL (mA) and scan range for OSA

```
I_start=2;
I_end=12;
I_step=1;

Span=1;
LambdaS=1539.1; % Estimated central wavelength to start with for OSA
```

Calculating DAQ drive voltage vector

```
RICO=2.021;

I_drive=[I_start:I_step:I_end];
V_drive=[I_start:I_step:I_end]/2.021;

L=length(V_drive);
LambdaP=zeros(1,L);
PeakP=zeros(1,L);
FWHM=zeros(1,L);
```

Sending vector to DAQ and reading out OSA

```
for i = 1:L

% First send data to DAQ
```

INIT DAQ

```
Dev = daq.getDevices;
session=daq.createSession('ni');
session.addAnalogOutputChannel(Dev.ID, {'ao0'}, 'voltage');
session.addAnalogInputChannel(Dev.ID, {'ai0','ai1','ai2'}, 'voltage');
% Set measurement channel properties
```

```

session.Channels(3).InputType='Differential';
%session.Channels(3).Range=[-0.1 0.1];
InputRange = 10;
session.Channels(2).Range=[-InputRange InputRange];
session.Channels(3).Range=[-InputRange InputRange];
session.Channels(4).Range=[-InputRange InputRange];
% Set output channels properties
OutputRange = 10;
session.Channels(1).Range=[-OutputRange OutputRange];

OutputData=V_drive(i).';
session.queueOutputData([OutputData]);
data=session.startForeground;

```

Acquire sweep data

```

LambdaC=LambdaS+0.558*(I_drive(i)-I_drive(1)); % Intelligently estimate central wavelength

LambdaB=LambdaC-Span/2; % Define begin and end wavelength
LambdaE=LambdaC+Span/2; % from central wavelength and span
fvec = ([LambdaB:0.002:LambdaE]); % Define wavelength range vector
Nf = length(fvec);

```

INIT OSA

```

daqreset;
instrreset;
 GPIBAddress = 1; % see <MY ADRS> of the [SYSTEM] switch (between 0 and 30)
  g = gpib('ni',0,GPIBAddress);
fopen(g);

CentralString=strcat('CTRWL',num2str(LambdaC));
fprintf(g,CentralString) % set central wavelength (nm)
SpanString=strcat('SPAN',num2str(Span));
fprintf(g,SpanString) % set wavelength span (nm)
fprintf(g,'RESOLNO.01') % set resolution between 0.01 and 2.0 (1-2-5 steps)
fprintf(g,'ZSWPT10') % set sweep time in seconds 0 to 50 in 1sec steps
fprintf(g,'AVG2') % set averaging 1 to 1000
fprintf(g,'TRFMT2') % select a record format: 0=binary, 2=text
fprintf(g,'SD1') % set string delimiter to CRLF
%fprintf(g,'REFL-56.1') % set the reference level in dBm (-90 to 20 dBm)
fprintf(g,'ATREF1')
fprintf(g,'LSCL5.0')
fprintf(g,'SHI1');

```

Measure

```

fprintf(g,'SGL');
pause(60);

aa=zeros(1,Nf+1);

```

```

fprintf(g,'LDATA')
for k=1:(Nf+1)
    a=fscanf(g);
    a=str2num(a);
    aa(k)=a;
end;

spectrumDBM = aa(2:end);

DataDBM=[fvec; spectrumDBM]';           % Row1 wavelength Row2 dBm

```

Save spectrum

```

titleDataMat=strcat('OSA Reflection Spectrum VCSEL 217 at current ',num2str(I_drive(i)),
mA.mat');
save(titleDataMat,'DataDBM');

```

From this spectrum we then determine the peak

```

res=fvec(2)-fvec(1);

index=PeakDetectQuadratic(spectrumDBM,10);
roundindex=round(index);
CentralWavelength=fvec(roundindex)+Res*(index-roundindex)

LambdaP(i)=CentralWavelength;

```

Maximum Power

```

MaxPower=max(spectrumDBM);
PeakP(i)=MaxPower;

```

FWHM

```

Peakwidth=fwhm(fvec,10.^(spectrumDBM./10));
FWHM(i)=Peakwidth;

```

```
end
```

Make a matrix with the voltage and wavelength values and plotting

```

VCSELData=[V_drive; LambdaP]';

% Save data
titleDataMat=strcat('OSA Peak values of VCSEL 217 in function of the drive voltage.mat');
save(titleDataMat,'VCSELData');

```

Appendix 4: Automatic Reading Out of VCSEL-spectra with the OSA

```
% plot and save plot
f=figure;
plot(V_drive,LambdaP,'k');    % Plot data logarithmic
xlabel('Drive voltage (V)');
ylabel('Peak wavelength (nm)');

titleFig=strcat('OSA Peak values of VCSEL 217 in function of the drive voltage');
saveas(f,titleFig,'fig');
saveas(f,titleFig,'eps');
saveas(f,titleFig,'jpg');
```

Fitting

```
[Lambda2,stats]=fit(V_drive',LambdaP','poly2')

figure
plot(Lambda2,'k',V_drive,LambdaP,'xk');
xlabel('Drive voltage (V)');
ylabel('Peak wavelength (nm)');
legend(['fitted curve with R^2=',num2str(0.9997)],'Measured data');

titleFig=strcat('OSA Peak values of VCSEL 217 in function of the drive voltage');
saveas(f,titleFig,'fig');
saveas(f,titleFig,'eps');
saveas(f,titleFig,'jpg');
```

Make a matrix with the voltage and power values and plotting

```
VCSELPowerData=[V_drive; PeakP]';

% Save data
titleDataMat=strcat('OSA Peak Power of VCSEL 217 in function of the drive voltage.mat');
save(titleDataMat,'VCSELPowerData');

% plot and save plot
f=figure;
plot(V_drive,PeakP,'k');    % Plot data logarithmic
xlabel('Drive voltage (V)');
ylabel('Peak power (dBm)');

titleFig=strcat('OSA Peak Power of VCSEL 217 in function of the drive voltage');
saveas(f,titleFig,'fig');
saveas(f,titleFig,'eps');
saveas(f,titleFig,'jpg');
```

Fitting

```
[Peak2,stats]=fit(V_drive',PeakP','poly2')

figure
plot(Peak2,'k',V_drive,PeakP,'xk');
```

```

xlabel('Drive voltage (V)');
ylabel('Peak wavelength (nm)');
legend(['fitted curve'],'Measured data');

titleFig=strcat('OSA Peak values of VCSEL 217 in function of the drive voltage');
saveas(f,titleFig,'fig');
saveas(f,titleFig,'eps');
saveas(f,titleFig,'jpg');

figure
plot(fvec,PeakP,'k');
xlabel('Drive voltage (V)');
ylabel('Peak wavelength (nm)');
legend(['fitted curve'],'Measured data');

titleFig=strcat('OSA Peak values of VCSEL 217 in function of the wavelength');
saveas(f,titleFig,'fig');
saveas(f,titleFig,'eps');
saveas(f,titleFig,'jpg');

```

Make a matrix with the voltage and FWHM-values and plotting

```

VCSELFWHMData=[V_drive; FWHM]';

% Save data
titleDataMat=strcat('OSA FWHM of VCSEL 217 in function of the drive voltage.mat');
save(titleDataMat,'VCSELFWHMData');

% plot and save plot
f=figure;
plot(V_drive,FWHM,'k');
xlabel('Drive voltage (V)');
ylabel('FWHM (nm)');

titleFig=strcat('OSA FWHM of VCSEL 217 in function of the drive voltage');
saveas(f,titleFig,'fig');
saveas(f,titleFig,'eps');
saveas(f,titleFig,'jpg');

f=figure;
plot(fvec,FWHM,'k');
xlabel('wavelength (nm)');
ylabel('FWHM (nm)');

titleFig=strcat('OSA FWHM of VCSEL 217 in function of the wavelength');
saveas(f,titleFig,'fig');
saveas(f,titleFig,'eps');
saveas(f,titleFig,'jpg');

```

End

Sidney Goossens - Vrije Universiteit Brussel - 2014-2015

[Published with MATLAB® R2013a](#)

Appendix 5: MATLAB script for the Phase Correlation Algorithm

version 2.0
author: Alfredo Lamberti
PhD candidate at Vrije Universiteit Brussel

This function computes the spectral shift of FBG sensors using a Phase correlation approach.

The inputs are the following:

X:

matrix of the input spectra stacked in different rows.
For instance, if the interrogator acquire N spectra using M wavelength lines, then X is a matrix of dimension N x M.

res:

wavelength resolution. If res is in picometer then the output will be in picometer. Default res=1.

flag:

is a boolean value which determine either to use piecewise phasecorrelation or not. flag=0 means that no piecewise phase correlation will be used and so the wavelength shift will be computed with respect the first spectrum X(1,:).
flag=1 means that a piecewise phase correlation is used and the shifts between consecutive spectra is computed. Default flag=0.

num_spec:

number of spectral line to be used in the phase correlation
The best value of num_spec depends on the shape of the input spectra. Suggested range 3-15. Note that num_spec has to be higher than 1. If the inserted value of num_spec is <2, then the script automatically assumes num_spec=2.

The output is

y: cumulative wavelength shift with respect to initial spectrum X(1,:). y is a row vector.

```
function [y] = FPC(X, res, flag, num_spec)

%check the input variables and set default res and flag if nedded.
if nargin<4
    num_spec=3; %default value if no num_spec is given in input
if nargin<3
    flag=0; %default value if no flag is given in input
    if nargin<2
        res=1; %default value if no res is given in input
```

```

    end
end
end
if num_spec<2
    num_spec=2;
    disp('... the selected number of spectral lines is too low. ')
    disp('... num_spec has been changed to 2')
end

[n,m] = size(X);           %n=number of spectra
                           %m=number of wavelength lines

if flag ==0
disp('... FPC is executed')
FFTSpectra = fft(X.').'; %compute the FFT of the Spectra

%Phase Correlation
for i=1:num_spec

%compute the phase
Phase = unwrap(angle(FFTSpectra(:,i+1))));

%compute the wavelength at each spectral line
Y(:,i)=Phase./(2.*pi).*(m)./i;

%compute the wavelength shift at each spectral line
y(:,i)=Y(:,i)-Y(1,i);
end

%compute the median on the selected num_spec spectral lines
y=(median(y.')).';

%compute wavelength shift vector. It is a row vector
y=-y.'*res;

else
disp('... piecewise FPC is executed')

for j=1:n;
%the FPC is executed between pairs
%of consecutive Spectra [X(i,:),X(i+1,:)]
    if j==1
        XX(1,:)=X(j,:);
        XX(2,:)=X(j+1,:);

    else
        XX=X(j-1:j,:);

    end

    FFTSpectra = fft(XX.').';

for i=1:num_spec
%compute the phase
Phase = unwrap(angle(FFTSpectra(:,i+1))));
%compute the wavelength at each spectral line
YY(:,i)=Phase./(2.*pi).*(m)./i;
%compute the wavelength shift at each spectral line

```

Appendix 5: MATLAB script for the Phase Correlation Algorithm

```
yy(:,i)=YY(:,i)-YY(1,i);
end
%compute the median on the selected num_spec spectral lines
yy=(median(yy.')).';
y(j,:)=yy*res;
end
%compute wavelength shift vector. It is a row vector
y=y(:,end);
y=cumsum(y).';

end
```

[Published with MATLAB® R2013a](#)

Appendix 6: Raw data for impact measurements on MOFBG 1 at 31.67 °

Table 11: The raw data of the impact measurements on MOFBG 1 oriented under 31.67 °. The table gives the angle of impact, the maximum force measured, the maximum shift in left and right wavelength and the maximum is peak separation. Every measurements is repeated 4 times and an average is made.

<u>Angle of incidence</u> <i>In degrees</i>	<u>#</u> <i>#</i>	<u>Max force</u>			
		<u>1</u> <i>Newton</i>	<u>Shift PL</u> <i>nm</i>	<u>Shift PR</u> <i>nm</i>	<u>Shift Diff</u> <i>nm</i>
20	1	260.4856	-0.031	-0.007	0.0295
20	2	249.1175	-0.0272	0.0063	0.0212
20	3	240.0929	-0.0458	0.0052	0.0448
20	4	194.5451	-0.0501	-0.0071	0.0489
20	AVG	236.060275	-0.03853	-0.00065	0.0361
20	STDEV	25.0342737	0.009641	0.006412	0.011237
30	1	398.3965	-0.076	-0.0123	0.0655
30	2	391.1193	-0.0759	-0.0084	0.0709
30	3	360.1054	-0.0828	-0.0124	0.0713
30	4	465.2963	-0.0879	-0.0123	0.0756
30	AVG	403.729375	-0.08065	-0.01135	0.070825
30	STDEV	38.3438098	0.005034	0.001704	0.003584
40	1	707.7951	-0.1017	-0.0115	0.0902
40	2	692.5829	-0.0898	-0.0109	0.0789
40	3	739.0077	-0.0837	-0.0088	0.0749
40	4	719.1358	-0.0632	-0.0164	0.0467
40	AVG	714.630375	-0.0846	-0.0119	0.072675
40	STDEV	16.9363881	0.013948	0.002785	0.016012
50	1	931.1142	-0.101	-0.0077	0.0967
50	2	861.3364	-0.1236	-0.0108	0.1161
50	3	908.0079	-0.0664	-0.0227	0.0641
50	4	795.5741	-0.114	-0.0229	0.0911
50	AVG	874.00815	-0.10125	-0.01603	0.092
50	STDEV	51.7917884	0.02166	0.006863	0.018588
60	1	1017.6803	-0.0916	-0.0251	0.0852
60	2	1217.6327	-0.0619	-0.00966	0.05227
60	3	1153.62	-0.0666	-0.0101	0.0579
60	4	950.0404	-0.0686	-0.0259	0.0663
60	AVG	1084.74335	-0.07218	-0.01769	0.065418
60	STDEV	106.120108	0.011476	0.007817	0.012465

Appendix 7: Raw data for impact measurements on MOFBG 2 at 109.67 °

Table 12: The raw data of the impact measurements on MOFBG 2 oriented under 109.67 °. The table gives the angle of impact, the maximum force measured, the maximum shift in left and right wavelength and the maximum is peak separation. Every measurements is repeated 4 times and an average is made.

<u>Angle of incidence</u>	#	<u>Max force</u>	FPC		
			<u>Shift PL</u>	<u>Shift PR</u>	<u>Shift Diff</u>
<i>In degrees</i>	<i>#</i>	<i>Newton</i>	<i>nm</i>	<i>nm</i>	<i>nm</i>
10	1	97.9906	-0.0196	-0.0085	0.0111
10	2	89.4091	-0.0177	-0.0077	0.01
10	3	70.1607	-0.0187	-0.0081	0.0106
10	4	72.936	-0.0175	-0.0075	0.0102
10	AVG	82.6241	-0.01838	-0.00795	0.010475
10	STDEV	11.5256363	0.000841	0.000384	0.000421
20	1	209.7437	-0.041	-0.0173	0.0237
20	2	212.5189	-0.0474	-0.0186	0.0288
20	3	196.4501	-0.0399	-0.0168	0.0232
20	4	184.8353	-0.0403	-0.0161	0.0258
20	AVG	200.887	-0.04215	-0.0172	0.025375
20	STDEV	11.0802232	0.003057	0.000914	0.002205
30	1	406.9689	-0.0611	-0.0248	0.0363
30	2	389.3034	-0.0629	-0.025	0.0379
30	3	392.017	-0.0611	-0.0211	0.04
30	4	459.4992	-0.0646	-0.0225	0.0421
30	AVG	411.947125	-0.06243	-0.02335	0.039075
30	STDEV	28.2662817	0.001455	0.001629	0.002184
40	1	548.957	-0.0782	-0.0279	0.0502
40	2	671.2034	-0.0808	-0.0288	0.0519
40	3	646.9323	-0.0854	-0.0292	0.0563
40	4	665.2145	-0.0927	-0.032	0.0607
40	AVG	633.0768	-0.08428	-0.02948	0.054775
40	STDEV	49.3826514	0.005505	0.001532	0.004081
50	1	788.2147	-0.1071	-0.0392	0.0679
50	2	885.3129	-0.123	-0.0355	0.0875
50	3	953.2679	-0.0947	-0.0368	0.0612
50	4	910.0568	-0.1104	-0.0365	0.0739

Appendix 7: Raw data for impact measurements on MOFBG 2 at 109.67

50	AVG	884.213075	-0.1088	-0.037	0.072625
50	STDEV	60.5255413	0.010073	0.001358	0.009692
60	1	1030.4	-0.1037	-0.0407	0.0631
60	2	1122.2	-0.1118	-0.0407	0.0711
60	3	1183.1	-0.1036	-0.0406	0.0629
60	4	1157.9	-0.0947	-0.0366	0.0582
60	AVG	1123.4	-0.10345	-0.03965	0.063825
60	STDEV	57.8895068	0.006049	0.001761	0.004635

Appendix 8: Raw data for impact measurements on MOFBG 2 at 115.67 °

Table 13: The raw data of the impact measurements on MOFBG 1 oriented under 115.67 °. The table gives the angle of impact, the maximum force measured, the maximum shift in left and right wavelength and the maximum is peak separation. Every measurements is repeated 4 times and an average is made.

<u>Angle of incidence</u>	#	<u>Max force</u>	FPC		
			<u>Shift PL</u>	<u>Shift PR</u>	<u>Shift Diff</u>
<i>In degrees</i>	<i>#</i>	<i>Newton</i>	<i>nm</i>	<i>nm</i>	<i>nm</i>
10	1	111.275	-0.0305	-0.0122	0.0208
10	2	91.5196	-0.0309	-0.012	0.021
10	3	90.9097	-0.0301	-0.0119	0.0202
10	4	107.4377	-0.0304	-0.0127	0.0201
10	AVG	100.2855	-0.03048	-0.0122	0.020525
10	STDEV	9.17428067	0.000286	0.000308	0.000383
20	1	220.406	-0.0661	-0.0208	0.0513
20	2	266.8446	-0.0613	-0.023	0.0456
20	3	250.5359	-0.06	-0.022	0.0467
20	4	243.5739	-0.0679	-0.0242	0.0516
20	AVG	245.3401	-0.06383	-0.0225	0.0488
20	STDEV	16.6903315	0.003271	0.001253	0.00268
30	1	475.986	-0.0996	-0.0285	0.0711
30	2	497.9342	-0.1242	-0.0325	0.0918
30	3	411.5394	-0.0953	-0.0309	0.071
30	4	467.6672	-0.1017	-0.0308	0.0779
30	AVG	463.2817	-0.1052	-0.03068	0.07795
30	STDEV	31.853937	0.01121	0.001425	0.008471
40	1	816.4122	-0.1399	-0.0381	0.1072
40	2	705.3009	-0.1427	-0.0387	0.104
40	3	766.4035	-0.1191	-0.0329	0.0924
40	4	785.3572	-0.1316	-0.0383	0.099
40	AVG	768.36845	-0.13333	-0.037	0.10065
40	STDEV	40.5530407	0.009171	0.002377	0.005588
50	1	1153	-0.1407	-0.0403	0.1069
50	2	1113.8	-0.146	-0.0408	0.1053
50	3	1056.6	-0.1436	-0.0394	0.1108
50	4	954.7412	-0.1412	-0.0389	0.1091

Appendix 8: Raw data for impact measurements on MOFBG 2 at 115.67

50	AVG	1069.5353	-0.14288	-0.03985	0.108025
50	STDEV	74.6169002	0.002111	0.000743	0.002094
60	1	1235.5	-0.1543	-0.0412	0.1195
60	2	1183.1	-0.1536	-0.0436	0.115
60	3	1432.3	-0.1605	-0.0426	0.124
60	4	1429.4	-0.1604	-0.042	0.1241
60	AVG	1320.075	-0.1572	-0.04235	0.12065
60	STDEV	112.318173	0.00326	0.000876	0.003754